



Delft University of Technology

Multiwavelength observations of active galactic nuclei Using current facilities and development of enabling technologies

Janssen, Reinier

DOI

[10.4233/uuid:8b277229-6a8c-4e8f-942f-9c485da1e1ce](https://doi.org/10.4233/uuid:8b277229-6a8c-4e8f-942f-9c485da1e1ce)

Publication date

2017

Document Version

Final published version

Citation (APA)

Janssen, R. (2017). *Multiwavelength observations of active galactic nuclei: Using current facilities and development of enabling technologies*. [Dissertation (TU Delft), Delft University of Technology].
<https://doi.org/10.4233/uuid:8b277229-6a8c-4e8f-942f-9c485da1e1ce>

Important note

To cite this publication, please use the final published version (if applicable).
Please check the document version above.

Copyright

Other than for strictly personal use, it is not permitted to download, forward or distribute the text or part of it, without the consent of the author(s) and/or copyright holder(s), unless the work is under an open content license such as Creative Commons.

Takedown policy

Please contact us and provide details if you believe this document breaches copyrights.
We will remove access to the work immediately and investigate your claim.

Multiwavelength Observations of Active Galactic Nuclei

Using current facilities and
development of enabling technologies

R. M. J. Janssen

PROPOSITIONS

accompanying the Ph. D. thesis

MULTIWAVELENGTH OBSERVATIONS OF ACTIVE GALACTIC NUCLEI USING CURRENT FACILITIES AND DEVELOPMENT OF ENABLING TECHNOLOGIES

by

REINIER MAARTEN JOHANNES JANSSEN

1. Blue low excitation radio galaxies are the result of recent galaxy interactions. (Chapter 3 and 4)
2. Comparing the measured and expected photon noise limited NEP is the preferred method to determine the detector efficiency of MKIDs. (Chapters 6 through 8)
3. Far-infrared observations are the key to reliably separating the mid-infrared contributions of dust heated by AGN and stellar activity in a galaxy SED. (This thesis)
4. Observational astronomers buy instruments to make new discoveries. Experimental astronomers make instruments to create new discovery space.
5. Astronomy is the best replacement of war when it comes to driving the development of new technology.
6. The first goal in any interdisciplinary collaboration should be to understand each other's language.
7. The only way to really understand a subject, is to explain it to an interested layman.
8. Feeling at home somewhere depends more on the people surrounding you there than the material aspects of the location.
9. Propositions stimulate doctoral candidates to become a reflective practitioner.
10. The increase in board game popularity is the result of an increased adherence by game designers to Nolan Bushnell's law: "All the best games are easy to learn and difficult to master."

These propositions are considered opposable and defensible and have been approved as such by the supervisor prof. dr. ir. T. M. Klapwijk.

Multiwavelength observations of active galactic nuclei

Using current facilities and development of enabling technologies

Multiwavelength observations of active galactic nuclei

Using current facilities and development of enabling technologies

Proefschrift

ter verkrijging van de graad van doctor
aan de Technische Universiteit Delft,
op gezag van de Rector Magnificus prof. ir. K.C.A.M. Luyben,
voorzitter van het College voor Promoties,
in het openbaar te verdedigen op donderdag 26 januari 2017 om 12:30 uur

door

Reinier Maarten Johannes JANSSEN

natuurkundig ingenieur en doctorandus in de sterrenkunde
geboren te Delft.

Dit proefschrift is goedgekeurd door de

promotors: prof. dr. ir. T. M. Klapwijk en prof. dr. H. J. A. Röttgering

copromotor: dr. ir. J. J. A. Baselmans

Samenstelling promotiecommissie:

Rector Magnificus

voorzitter

Prof. dr. ir. T. M. Klapwijk

Technische Universiteit Delft, promotor

Prof. dr. H. J. A. Röttgering

Universiteit Leiden, promotor

Dr. ir. J. J. A. Baselmans

SRON Stichting Ruimte Onderzoek Nederland &
Technische Universiteit Delft, copromotor

Onafhankelijke leden:

Prof. dr. J. Zmuidzinas

California Institute of Technology, Verenigde Staten

Prof. dr. P. N. Best

University of Edinburgh, Verenigd Koninkrijk

Prof. dr. B. R. Brandl

Universiteit Leiden &

Technische Universiteit Delft

Prof. dr. ing. A. Neto

Technische Universiteit Delft

Prof. dr. ir. H. S. J. van der Zant

Technische Universiteit Delft, reservelid



Universiteit
Leiden



SRON
Netherlands Institute for Space Research



Published by: R. M. J. Janssen

Printed by: GVO printers & designers B.V. — Ponsen & Looijen, Ede, The Netherlands

Cover design: Observations of the night sky by the KiloDegree Survey (KiDS) projected onto an array of microwave kinetic inductance detectors (KIDs). On the backside of the cover we observe a merging galaxy pair which is the host of a radio-loud AGN. Also shown is the William Herschel Telescope in La Palma used for observations performed in the context of this thesis.

An electronic version of this thesis is available at: <http://repository.tudelft.nl>

Copyright © 2017 by R. M. J. Janssen. All rights reserved.

Casimir PhD Series, Delft-Leiden, 2016–40

ISBN 978–90–8593–285–7

Contents

1	Introduction	1
1.1	Galaxy evolution	1
1.1.1	AGN feedback	3
1.2	Technology of multiwavelength observations	4
1.2.1	Microwave kinetic inductance detectors	6
1.3	Outline of this thesis	8
2	Radio-loud active galactic nuclei	15
2.1	Radiative-mode AGN	16
2.2	Jet-mode AGN	19
2.3	AGN feedback	21
3	The triggering probability of radio-loud AGN: A comparison of high- and low-excitation radio galaxies in hosts of different colours	27
3.1	Introduction	29
3.2	The radio-loud AGN sample	29
3.3	The radio-loud AGN fraction	32
3.4	Dependence on AGN excitation	33
3.5	Dependence on galaxy colour	34
3.6	Discussion	37
3.7	Conclusion	38
4	Morphology of radio-loud AGN hosted by massive blue galaxies	43
4.1	Introduction	43
4.2	Jet-mode AGN hosted by blue galaxies	45
4.3	Deep optical imaging	47
4.4	Optical morphology	49
4.5	Radio morphology	54
4.6	Discussion	55
4.7	Conclusion	57

5	Classification of radio galaxies using broadband mid-infrared observations	63
5.1	Introduction	64
5.2	Low-redshift sample of radio-loud AGN	65
5.2.1	Volume-limited sample	66
5.3	The mid-IR luminosity of radio-loud AGN	67
5.3.1	Influence of star formation	68
5.3.2	Influence of redshift and host galaxy mass	70
5.4	Comparison between radio-loud AGN and inactive galaxies	72
5.5	Discussion	75
5.5.1	K-correction	75
5.5.2	High-excitation radio galaxies	76
5.5.3	Low-excitation radio galaxies	79
5.5.4	Broadband separation methods	79
5.6	Conclusion	81
6	Controlled illumination of microwave kinetic inductance detectors	85
6.1	Microwave kinetic inductance detectors	85
6.2	Electrical conductivity	86
6.2.1	Metals, insulators and semiconductors	86
6.2.2	Superconductivity	90
6.3	Superconducting microwave resonator	99
6.3.1	Superconducting transmission line	99
6.3.2	Superconducting $\lambda/4$ resonator	101
6.3.3	Response	102
6.3.4	Noise	104
6.4	Experimental setup	106
6.4.1	Illumination source	108
6.4.2	Lens-antenna system	109
6.4.3	Microwave setup	110
6.5	Coupling radiation into an MKIDs	112
6.5.1	Geometrical throughput	112
6.5.2	Lens-antenna coupling	114
6.6	Photon noise limited performance by MKIDs	119
6.6.1	Sensitivity	119
6.6.2	Radiation efficiency	121
6.7	Fabrication of hybrid MKIDs	122
7	High optical efficiency and photon noise limited sensitivity of microwave kinetic inductance detectors using phase readout	133
7.1	Introduction	134

7.2	Device design	134
7.3	Photon noise limited performance	137
7.4	Readout	138
7.5	Aperture efficiency	138
7.6	Conclusion	142
8	Equivalence of optical and electrical noise equivalent power of hybrid NbTiN-Al microwave kinetic inductance detectors	145
8.1	Introduction	146
8.2	Measurement setup	147
8.3	Optical noise equivalent power	148
8.4	Electrical noise equivalent power	149
8.5	Optical versus electrical noise equivalent power	151
8.6	Discussion	152
8.7	Conclusion	153
9	Conclusions and future perspectives	157
9.1	Conclusions	157
9.1.1	Radio-loud AGN in the local universe	157
9.1.2	Performance of hybrid NbTiN-Al MKIDs	158
9.2	Future perspectives: tracing the co-evolution of galaxies and black holes	159
9.2.1	AGN in the visible high-redshift universe	159
9.2.2	AGN in the dust-obscured high-redshift universe	160
A	Mid-IR classification of radio-loud AGN: A comparison between high and low radio power samples.	167
B	Spherical coordinate systems	171
B.1	ISO80000 definition	171
B.2	Mathematics	172
B.2.1	Converting physics into math, and back	173
B.3	Matlab	173
B.3.1	Conversion between ISO and Matlab coordinates	174
B.4	CST Microwave Studio	175
B.4.1	Conversion between CST MWS and the ISO8000 norm	175
B.5	Alternative coordinate systems	176
	Summary	179
	Samenvatting	183
	Curriculum Vitae	189

List of publications	191
Acknowledgements	193

Chapter 1

Introduction

1.1 Galaxy evolution

The galaxies we observe today in the local universe are the result of over 13 billion years of galaxy formation and evolution. This evolution has occurred in a universe which consists of [1]: $\sim 69\%$ dark energy, $\sim 26\%$ dark matter and only $\sim 5\%$ baryonic matter. Dark energy drives the expansion of the universe. Because of this expansion, the electromagnetic (EM) radiation (or light) emitted by distant objects at wavelength λ_{emit} is observed at a wavelength $\lambda_{\text{obs}} = \lambda_{\text{emit}} \times (1 + z)$. Here z is called the redshift, because the increased wavelength makes the EM radiation more red. In addition to being redshifted, it takes time for light to reach earth due to the finite speed of light. Light from the Andromeda galaxy, the nearest neighbour of the Milky Way, takes 2.5 million years to reach earth. Thus observations of the distant universe are observations into the history of the universe. The relation between redshift and the age of the universe is shown by the two horizontal axes in Fig. 1.1.

Dark matter (DM) is called dark because it does not absorb, reflect or emit EM radiation. However, it does have mass and exerts a gravitational attraction on other masses. Because DM constitutes 85% of the mass in the universe, it dominates the gravitational interactions on cosmological scales. Over the past 13 billion years the small initial clumps of DM (or DM halos) have continued to grow in a hierarchical way [2]. Through mergers with other halos the massive DM halos observed locally are assembled from the bottom-up.

Baryonic matter is the ordinary matter we know and includes atoms, molecules, gas and dust. Inside the ever more massive and dense DM halos, the baryonic matter has formed stars and galaxies. A simple model to describe galaxy evolution [3] is to see a galaxy as a reservoir of stars and gas inside a DM halo. In this reservoir the inflow of gas into the halo must be balanced by the formation of stars and the ejection of gas from the halo. The inflow in most galaxies is governed by the gravitational attraction of cold gas from the dense filaments that make up the cosmic web. Galaxies that are slowly but steadily forming stars from this inflow are associated with the main sequence

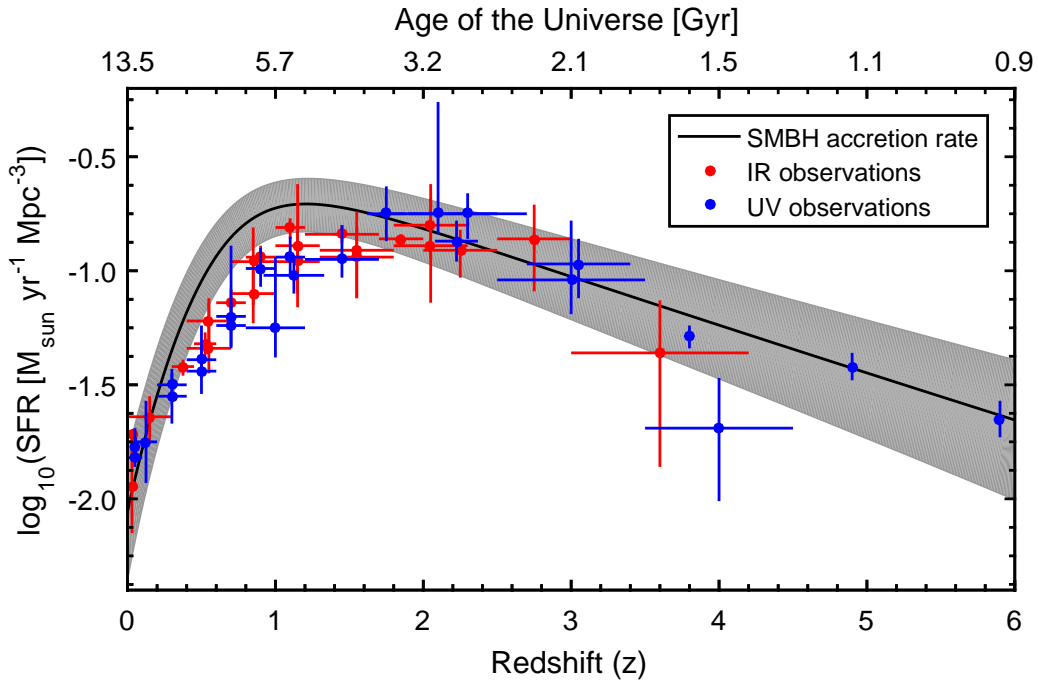


Figure 1.1: Evolution of the global star formation rate as measured using infrared (red dots) or ultraviolet (blue dots) observations [9, and references therein]. Also shown is the black hole accretion rate (solid black line; 1σ uncertainty is given by grey shaded area) modelled by luminosity and density evolution [10]. The black hole accretion rate is scaled up by a factor 5000, which is approximately the same mass ratio found between the central black hole and the mass of the galaxy bulge in its host galaxy [11, 12].

of star formation [4]: a strong (almost) linear correlation between the mass, M_* (and therefore gravitational attraction on gas) and star formation rate, SFR , of a galaxy. In the local universe the main sequence of star formation is populated by spiral galaxies. These spiral galaxies generally have a $M_* \lesssim 10^{10.5} M_\odot$ and a blue colour in the visible (VIS) light. The latter is the result of their young stellar population.

Alternatively, galaxies can grow through mergers just like their DM halos. While major mergers are rare, they can have a dramatic effect on the evolution of a galaxy. The tidal torques acting on the mass inside a galaxy can efficiently transport the large supply of new gas to the centres of the galaxies [5, 6], which in turn triggers star formation [e.g. 7]. Therefore, major mergers are often seen as the triggering event for starburst galaxies. Mergers can also convert spiral galaxies into elliptical galaxies [e.g. 8]. As such, merging events are thought to have produced the population of massive ($M_* \gtrsim 10^{10.5} M_\odot$) elliptical galaxies in the local universe. These massive ellipticals have little star formation and an old stellar population, which gives them a red colour.

Fig. 1.1 shows the global star formation density throughout the history of the universe. The SFR has been measured by observing both the ultraviolet (UV, blue dots) and the far-infrared (far-IR) emission (red dots) of galaxies. In the UV the emission of

massive young stars can be seen directly. Stars with a mass of $10 M_{\odot}$ only live for 30 million years, which means their emission is a good indication of the ‘current’ SFR of a galaxy. At high redshift the UV emission of galaxies is observable at VIS and near-IR wavelengths. This has enabled Bouwens et al. [13, 14], among others, to determine the global SFR out to $z \sim 8$ using the Hubble (Ultra) Deep Fields. The observations show that the SFR increases by an order of magnitude between the local universe at $z = 0$ and $z \sim 1$ as shown in Fig. 1.1. After a peak between $1 < z < 2$ the SFR declines again. The decrease in the global SFR since $z \sim 1$ is the result of a decreasing amount of cold gas. The large supply of cold gas at $1 < z < 2$ allowed galaxies on the main sequence of star formation to achieve a higher specific star formation rate, $sSFR = SFR/M_*$. This has allowed galaxies on the main sequence of star formation to dominate the global SFR for at least the last 10 billion years [15].

With the increased gas content there is also an increased amount of dust at $1 < z < 5$. UV radiation is very sensitive to absorption by dust. The absorption of UV radiation heats the dust which re-emits the absorbed energy at far-IR wavelengths. Through this process half of the total energy generated by stars since the Big Bang reaches earth in the IR as dust emission [16]. As such far-IR observations complement those of the UV radiation in determining the star formation history. Surveys done using the Herschel Space Observatory [e.g. 17–19] have resolved 75% of the cosmic IR background into individual galaxies. In particular, a large population of galaxies with a very high IR luminosity ($\geq 10^{12} L_{\odot}$) and no visible optical counterpart was discovered at $z > 1$. This population of galaxies was first identified in extragalactic sub-mm surveys using the SCUBA camera [e.g. 20] and are thus called sub-mm galaxies (SMGs). The large amount of dust in these galaxies reprocesses the UV and VIS radiation of the hundreds of solar masses of young stars formed each year and re-emits it at far-IR wavelengths [21]. SMGs are rare in the local universe; only the brightest starburst galaxies resulting from major mergers have the high IR luminosities and $SFR > 100 M_{\odot}/\text{yr}$ associated with SMGs. However, at $z \sim 2$ the main sequence of star formation is located at a higher sSFR and is dominated by SMGs [22] instead of the blue spiral galaxies seen locally.

1.1.1 AGN feedback

Large scale cosmological simulations [23, 24] show that processes are required that suppress or even terminate star formation [25] in order to reproduce

- the shape of global star formation rate shown in Fig. 1.1.
- the bimodality in the local galaxy population (blue star forming spirals vs red quiescent ellipticals).
- the local galaxy luminosity function.

The two prime candidates to provide this feedback are core collapse supernova explosions (SNe) and active galactic nuclei (AGN) [26]. SNe are the explosions in which the most massive ($> 8M_{\odot}$) stars end their life. These explosions inject kinetic energy into the surrounding medium and can drive galactic winds [27]. The winds create an gas flow out of the galaxy.

AGN are the result of matter being accreted by the super-massive ($10^6 < M_{\text{BH}} < 10^9 M_{\odot}$) black hole (SMBH) which is thought to be present at the centre of every galaxy [28]. This process can release enormous amounts of energy: the brightest AGN are 100 times more luminous than all the stars in their host galaxy combined. The radiation pressure from the AGN emission can drive powerful winds. These winds are thought to expel the gas out off the galaxy, thereby terminating star formation and AGN activity [e.g. 29]. Alternatively, AGN may provide feedback by means of their radio jet: streams of charged particles that are accelerated along magnetic fields, which can be observed at radio wavelengths. Because of this, AGN with a radio jet are often classified as radio-loud. The largest radio jets are seen far outside the visible extend of the host galaxy. Both inside and outside the host galaxy, radio jets can heat gas through shocks. This heating can regulate the inflow of gas from the halo of hot X-ray gas seen around many elliptical galaxies and prevent them from growing any further [30].

1.2 Technology of multiwavelength observations

To investigate the co-evolution of galaxies and AGN through cosmic time, observations across the EM spectrum are required. The EM spectrum is the collection of all EM radiation, which as a function of decreasing wavelength includes radio, millimetre (mm) and sub-mm, IR, VIS, UV, X-rays and gamma-rays.

- At radio wavelengths the synchrotron emission of electrons can be observed. These are produced by the radio jet of AGN and the SNe with which massive stars end their life. Radio observations are an important tool to find AGN, because dust is transparent at radio wavelengths.
- About half the energy generated by stellar and accretion processes since the Big Bang reaches earth at far-IR and sub-mm wavelengths [16]. This far-IR emission is from dust, which has been heated by the aforementioned processes. Far-IR observations enable us to measure the dust emission of galaxies. In particular, they allow us to see a population of heavily dust obscured galaxies, which have no or a very faint optical counterpart.
- The near-IR, VIS and UV part of the spectrum is dominated by emission from stars. In addition, AGN can be identified at these wavelengths by their optical

emission lines or the UV emission from the accretion process. However, VIS and UV emission are sensitive to absorption by gas and dust.

- X-ray emission is (just like radio emission) primarily produced by SNe and AGN. In the latter X-ray emission is produced close to the SMBH. X-ray emission is also emitted by the hot halo gas observed in galaxy clusters.

To efficiently map the night sky at these different wavelengths astronomers use telescopes in combination with large format imaging cameras. At the heart of any astronomical camera are detectors (or sensors) that have the same function as the rods and cones in the human eye: they absorb the incoming radiation, which changes the electrical properties of the detector. This change can be measured, digitized and stored on a computer where further image analysis can be performed. Throughout the EM spectrum astronomers use different types of detectors to detect the radiation from the universe.

- Radio telescopes which receive radiation at frequencies $\nu \lesssim 20$ GHz, use semiconductor transistors to directly amplify the incoming signal before it is digitized on integrated circuits similar to those found in modern computers [e.g. 31].
- At far-IR, sub-mm and mm wavelengths most astronomical instruments use bolometer arrays to detect radiation. A bolometer consists of a membrane on which an absorber and a thermometer are present. The absorber heats up when radiation is absorbed, which changes the electrical resistance of the adjacent thermometer. The classic astronomical bolometer uses a highly-doped semiconductor as temperature dependent resistance (thermistor). For example, the PACS and SPIRE instruments on the Herschel Space Observatory launched in 2009 used bolometers made from doped germanium [32, 33]. New state-of-the-art instruments instead use arrays of Transition Edge Sensors (TES) [e.g. 34, 35]. TES use a superconductor biased at the superconducting transition as a temperature-dependent resistance. At this transition the electrical resistance of a superconducting material drops from a finite value to 0 in a very small temperature range, which allows TES to have a very high electrical response to a very small temperature change.
- Astronomical observations in the near-IR, VIS and UV are almost exclusively done using semiconducting CCD imaging sensors [36]. The CCD chips in astronomical instruments are very similar to the ones found in smartphones and consumer digital cameras and generally contain over a million pixels. When light is absorbed in the semiconductor it excites an electron, a so-called photo-electron. By counting the number of electrons after a given integration time, the IR, VIS or UV flux can be determined.

- The two main X-ray telescopes, which are currently operational, are Chandra [37] and XMM Newton [38]. Both telescopes employ multiple CCD imaging sensor arrays to detect X-rays in their instruments [39–41]. In contrast to IR or VIS CCDs, the absorption of an X-ray photon creates a number of photo-electrons proportional to the frequency of the radiation. By counting the number of photo-electrons generated in the CCD these instruments can achieve a spectroscopic resolution of $\frac{\nu}{\Delta\nu} \sim 50$.

As can be seen from the above list, astronomers rely on semiconducting detectors for observations in a large part of the EM spectrum. The advantage of CCDs over many other detectors is that millions of pixels can be read out using just a single amplifier located at the corner of the CCD chip. Reading out many pixels efficiently in terms of complexity, mass, power and cost is the key to achieving large format detector arrays. A good measure for this efficiency is the multiplexing (MUX) factor, which is defined as the number of detectors per readout channel [42]. Large format imaging systems can more easily be achieved using detectors that can achieve high MUX factors, such as the pixels in a CCD sensor.

For the cryogenic detectors used at far-IR and sub-mm wavelengths achieving high MUX factors is both more pressing and more complex as a result of their sub-K operation temperatures: every wire going from sub-K to room temperature is a thermal link through which the warm environment can heat the sub-K environment. While TES can meet the high sensitivities required for astronomical space applications, they suffer, like all bolometers, from the problem that it is hard to read many detectors simultaneously using just a few readout lines. To reduce the number of readout chains TES detector arrays are connected to cryogenic multiplexing chips. A MUX factor of 128 pixels per readout line will be achieved this way by the next generation readout systems [43]. Using these specifications a 10.000 pixel TES instrument would still require at least 20.000 interconnects between the detector and MUX chip and 80 readout lines going from sub-K temperatures to 80 readout systems at room temperature. Furthermore, the TES MUX is based on Superconducting Quantum Interference Devices (SQUIDS) that are highly sensitive to changes in the external magnetic field such as generated by electromotors or motion with respect to the earths magnetic field.

1.2.1 Microwave kinetic inductance detectors

Over the last 15 years Microwave Kinetic Inductance Detectors (MKIDs) have seen a rapid development from a new detector concept [44] to operational instruments on astronomical mm-wave [45] and optical [46] telescopes. Across the world research groups have been striving to turn MKIDs into usable astronomical imaging arrays at far-IR and sub-mm wavelengths [47]. However, MKIDs are also being developed for the detection of near-IR/VIS/UV photons [48] and X-rays [49] as well as particle detection [50] and

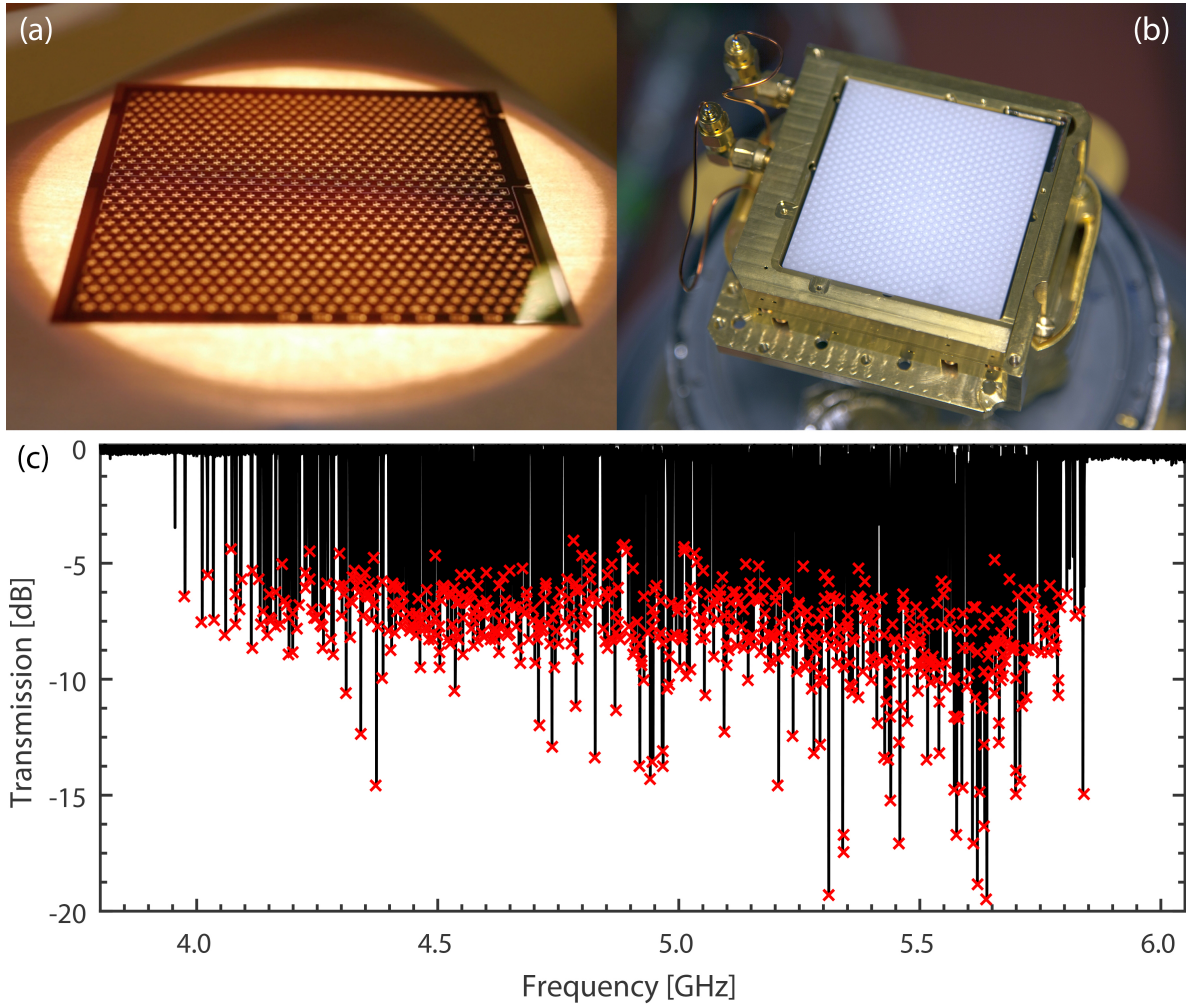


Figure 1.2: (a) photograph of a 1000 pixel MKID array. Each MKID is given a slightly different length, thereby changing its resonance frequency. (b) The array mounted in the test cryostat. Clearly visible is the cable pair used to read out the array and the lenslet array mounted on top of the array. The lenslet array is used to focus light onto the most sensitive part of each MKID. (c) Transmission of the readout line of a 1000 pixel MKID array. Here the red crosses show the resonance frequency of the individual MKIDs. Images courtesy of SRON.

for observation of the cosmic microwave background [51].

MKIDs are superconducting resonators optimized for the detection of radiation. The main advantage of MKIDs is that their resonance frequency can be changed by small changes in the design. The 1000 pixel MKID array shown in Fig. 1.2 has been constructed such that each individual MKID creates a resonance signature at a different read out frequency as shown in Fig. 1.2(c). This means all pixels in the array can be read out using a single pair of co-axial cables and one set of room temperature electronics. This inherent potential for frequency-domain multiplexing enables MKID arrays to achieve MUX factors of 1000–8000 at read out frequencies of a few GHz. This,

in combination with the high sensitivity MKIDs can achieve [52], makes them a very attractive detector technology.

1.3 Outline of this thesis

Understanding the co-evolution of galaxies and their SMBHs through cosmic time is one of the main goals of modern astronomy. There is increasing evidence that supports a co-evolution. The growth rate of SMBHs, as measured by the AGN activity, through cosmic time closely matches the growth of galaxies through star formation as shown in Fig. 1.1 [9, 10]. In addition, the mass of the central SMBH strongly correlates with the stellar mass of the galactic bulge in which the SMBH is located [11, 12]. The ratio between these two masses is remarkably similar to the factor 5000 by which the SMBH mass accretion rate in Fig. 1.1 has been scaled. However, many open questions remain: Do SMBHs and galaxies grow simultaneously or does the growth of one precede the other? How does AGN activity affect the star formation inside the host galaxy, and vice versa? Or, is their growth independent and are the correlations observed between SMBHs and their host galaxies the result of having the same ‘fuel’ source, the availability of gas?

To answer these question we need to know which galaxies host AGN and how these change through cosmic time. This requires multiwavelength observations of both AGN and their host galaxies. Observations at radio wavelengths are an important means to identify AGN activity, because it is unaffected by dust obscuration, while the host galaxies can be identified in VIS and far-IR observations. Far-IR observations become particularly important at redshifts $1 < z < 5$ where dust obscuration makes an increasing fraction of galaxies faint at VIS wavelengths. However, since the Herschel Space Observatory has stopped its operation, no instruments are available to efficiently perform blind large area far-IR surveys.

This thesis consists of two parts. In the first part (Chapters 2–5) we will make use of existing large area VIS, IR and radio surveys to investigate:

- Which galaxies host radio-loud AGN in the local ($z \sim 0.1$) universe?
- How can radio-loud AGN be efficiently detected and classified at higher redshifts?

To understand the properties of AGN in dust obscured host galaxies, a new generation of far-IR instruments is required that can create a large 3D map of the dust obscured universe. MKIDs are the technology of the future for far-IR imaging and spectroscopy. Hence, we will investigate the performance of hybrid NbTiN-Al MKIDs in the second part of this thesis (Chapters 6–8) and answer the question:

- Can MKIDs meet the requirements to enable a new generation of large format far-IR cameras and spectrometers?

Chapter 2 gives an overview of the properties of AGN observed in the local universe. Particular attention is given to radio-loud AGN, which exist in two modes. 1) Radiative-mode AGN or high-excitation radio galaxies (HERGs) accrete matter at a high rate in a radiatively efficient manner. They are thought to follow the orientation-based unification model of AGN [53]. 2) Jet-mode AGN or low-excitation radio galaxies (LERGs) are thought to have a much lower accretion rate and as a result are radiatively inefficient. Observationally, only the presence of a radio jet gives the presence of these AGN away. At the end of *Chapter 2* we will also give a more detailed description of the feedback each of these AGN modes provides and how this can influence the evolution of their host galaxy.

In *Chapter 3* we investigate the population of radio-loud AGN in greater detail. For this we use a (large) sample of approximately 7000 local radio-loud AGN, which have been identified in a sample of more than half a million galaxies observed by the Sloan Digital Sky Survey (SDSS). We investigate the probability that a galaxy in the local universe hosts a jet-mode or radio-loud radiative-mode AGN as a function of the host galaxies stellar mass, SFR, colour and radio power.

In *Chapter 4* we take a closer look at the optical and radio morphology of the jet-mode AGN hosted by massive blue galaxies identified in *Chapter 3*. For this we use morphological classification by Galaxy Zoo [54]: an online citizen science project, in which the general public classifies the morphology of galaxies in SDSS. In addition, we have obtained deep optical imaging from public surveys and observations at the William Herschel Telescope in La Palma. These are used to identify merger signatures. The morphology of the radio jets is classified using images from the FIRST radio survey [55]. In *Chapter 5* we continue to analyse our sample of local radio-loud AGN. The difference between radiative-mode and jet-mode AGN is investigated using mid-IR observations by the WISE satellite [56]. Our aim is to identify a broadband classification method that capitalizes on the difference in mid-IR torus emission, which is only expected in radiative-mode AGN.

Chapter 6 gives an introduction to MKIDs. It gives an introduction to superconductivity and explains the operational principle of MKIDs. It also discusses the experimental setup required to accurately measure the optical sensitivity, expressed as the Noise Equivalent Power (NEP), and optical coupling efficiency of antenna-coupled MKIDs.

In *Chapter 7* we present optical measurements of hybrid NbTiN-Al MKIDs using the experimental setup described in *Chapter 6*. We illuminate a small array of hybrid MKIDs with a range of sub-mm powers and determine at which loading levels the noise spectra are consistent with photon noise limited performance. Furthermore, a detailed analysis of the optical throughput gives us the optical efficiency of the system and MKIDs.

In *Chapter 8* we compare the response of hybrid NbTiN-Al MKIDs to sub-mm radiation and temperature. Both responses are used to determine the NEP of the detectors. Furthermore, we determine the error on both measurements. If sub-mm radiation and temperature have an equivalent effect and give the same measure for the NEP, this will

greatly simplify sensitivity measurements of large MKID arrays; thermal sensitivity measurements can be performed in a closed cryostat in which disturbances can be more easily eliminated.

In *Chapter 9* conclusions are drawn from the research presented in this thesis. We will discuss their implications for research of AGN and galaxy evolution outside our local universe.

References

- [1] Planck Collaboration, P. A. R. Ade, N. Aghanim, M. Arnaud, M. Ashdown, et al., *Planck 2015 results. XIII. Cosmological parameters*, ArXiv e-prints, 1502.01589 (2015).
- [2] S. D. M. White and M. J. Rees, *Core condensation in heavy halos - A two-stage theory for galaxy formation and clustering*, Monthly Notices of the Royal Astronomical Society **183**, 341 (1978).
- [3] S. J. Lilly, C. M. Carollo, A. Pipino, A. Renzini, and Y. Peng, *Gas Regulation of Galaxies: The Evolution of the Cosmic Specific Star Formation Rate, the Metallicity-Mass-Star-formation Rate Relation, and the Stellar Content of Halos*, The Astrophysical Journal **772**, 119 (2013).
- [4] J. Brinchmann, S. Charlot, S. D. M. White, C. Tremonti, G. Kauffmann, et al., *The physical properties of star-forming galaxies in the low-redshift Universe*, Monthly Notices of the Royal Astronomical Society **351**, 1151 (2004).
- [5] J. E. Barnes and L. Hernquist, *Transformations of Galaxies. II. Gasdynamics in Merging Disk Galaxies*, The Astrophysical Journal **471**, 115 (1996).
- [6] T. Naab, R. Jesseit, and A. Burkert, *The influence of gas on the structure of merger remnants*, Monthly Notices of the Royal Astronomical Society **372**, 839 (2006).
- [7] T. J. Cox, P. Jonsson, R. S. Somerville, J. R. Primack, and A. Dekel, *The effect of galaxy mass ratio on merger-driven starbursts*, Monthly Notices of the Royal Astronomical Society **384**, 386 (2008).
- [8] J. E. Barnes, *Encounters of disk/halo galaxies*, The Astrophysical Journal **331**, 699 (1988).
- [9] P. Madau and M. Dickinson, *Cosmic Star-Formation History*, Annual Review of Astronomy and Astrophysics **52**, 415 (2014).
- [10] J. Aird, K. Nandra, E. S. Laird, A. Georgakakis, M. L. N. Ashby, et al., *The evolution of the hard X-ray luminosity function of AGN*, Monthly Notices of the Royal Astronomical Society **401**, 2531 (2010).

- [11] A. Marconi and L. K. Hunt, *The Relation between Black Hole Mass, Bulge Mass, and Near-Infrared Luminosity*, The Astrophysical Journal Letters **589**, L21 (2003).
- [12] N. Häring and H.-W. Rix, *On the Black Hole Mass-Bulge Mass Relation*, The Astrophysical Journal Letters **604**, L89 (2004).
- [13] R. J. Bouwens, G. D. Illingworth, P. A. Oesch, M. Trenti, I. Labbé, et al., *Lower-luminosity Galaxies Could Reionize the Universe: Very Steep Faint-end Slopes to the UV Luminosity Functions at $z \geq 5 - 8$ from the HUDF09 WFC3/IR Observations*, The Astrophysical Journal Letters **752**, L5 (2012).
- [14] R. J. Bouwens, G. D. Illingworth, P. A. Oesch, M. Franx, I. Labbé, et al., *UV-continuum Slopes at $z \sim 4 - 7$ from the HUDF09+ERS+CANDELS Observations: Discovery of a Well-defined UV Color-Magnitude Relationship for $z \geq 4$ Star-forming Galaxies*, The Astrophysical Journal **754**, 83 (2012).
- [15] G. Rodighiero, E. Daddi, I. Baronchelli, A. Cimatti, A. Renzini, et al., *The Lesser Role of Starbursts in Star Formation at $z = 2$* , The Astrophysical Journal Letters **739**, L40 (2011).
- [16] H. Dole, G. Lagache, J.-L. Puget, K. I. Caputi, N. Fernández-Conde, et al., *The cosmic infrared background resolved by Spitzer. Contributions of mid-infrared galaxies to the far-infrared background*, Astronomy & Astrophysics **451**, 417 (2006).
- [17] D. Lutz, A. Poglitsch, B. Altieri, P. Andreani, H. Aussel, et al., *PACS Evolutionary Probe (PEP) - A Herschel key program*, Astronomy & Astrophysics **532**, A90 (2011).
- [18] E. E. Rigby, S. J. Maddox, L. Dunne, M. Negrello, D. J. B. Smith, et al., *Herschel-ATLAS: first data release of the Science Demonstration Phase source catalogues*, Monthly Notices of the Royal Astronomical Society **415**, 2336 (2011).
- [19] S. J. Oliver, J. Bock, B. Altieri, A. Amblard, V. Arumugam, et al., *The Herschel Multi-tiered Extragalactic Survey: HerMES*, Monthly Notices of the Royal Astronomical Society **424**, 1614 (2012).
- [20] I. Smail, R. J. Ivison, and A. W. Blain, *A Deep Sub-millimeter Survey of Lensing Clusters: A New Window on Galaxy Formation and Evolution*, The Astrophysical Journal Letters **490**, L5 (1997).
- [21] B. Magnelli, D. Lutz, P. Santini, A. Saintonge, S. Berta, et al., *A Herschel view of the far-infrared properties of submillimetre galaxies*, Astronomy & Astrophysics **539**, A155 (2012).
- [22] P. F. Hopkins, J. D. Younger, C. C. Hayward, D. Narayanan, and L. Hernquist, *Mergers, active galactic nuclei and ‘normal’ galaxies: contributions to the distribution of star formation rates and infrared luminosity functions*, Monthly Notices of the Royal Astronomical Society **402**, 1693 (2010).

- [23] V. Springel, S. D. M. White, A. Jenkins, C. S. Frenk, N. Yoshida, et al., *Simulations of the formation, evolution and clustering of galaxies and quasars*, Nature **435**, 629 (2005).
- [24] J. Schaye, R. A. Crain, R. G. Bower, M. Furlong, M. Schaller, et al., *The EAGLE project: simulating the evolution and assembly of galaxies and their environments*, Monthly Notices of the Royal Astronomical Society **446**, 521 (2015).
- [25] S. D. M. White and C. S. Frenk, *Galaxy formation through hierarchical clustering*, The Astrophysical Journal **379**, 52 (1991).
- [26] J. Schaye, C. Dalla Vecchia, C. M. Booth, R. P. C. Wiersma, T. Theuns, et al., *The physics driving the cosmic star formation history*, Monthly Notices of the Royal Astronomical Society **402**, 1536 (2010).
- [27] S. Veilleux, G. Cecil, and J. Bland-Hawthorn, *Galactic Winds*, Annual Review of Astronomy and Astrophysics **43**, 769 (2005).
- [28] J. Kormendy and L. C. Ho, *Coevolution (Or Not) of Supermassive Black Holes and Host Galaxies*, Annual Review of Astronomy and Astrophysics **51**, 511 (2013).
- [29] M. J. Page, M. Symeonidis, J. D. Vieira, B. Altieri, A. Amblard, et al., *The suppression of star formation by powerful active galactic nuclei*, Nature **485**, 213 (2012).
- [30] A. C. Fabian, *Observational Evidence of Active Galactic Nuclei Feedback*, Annual Review of Astronomy and Astrophysics **50**, 455 (2012).
- [31] P. J. Napier, A. R. Thompson, and R. D. Ekers, *The Very Large Array - Design and performance of a modern synthesis radio telescope*, IEEE Proceedings **71**, 1295 (1983).
- [32] M. J. Griffin, A. Abergel, A. Abreu, P. A. R. Ade, P. André, et al., *The Herschel-SPIRE instrument and its in-flight performance*, Astronomy & Astrophysics **518**, L3 (2010).
- [33] A. Poglitsch, C. Waelkens, N. Geis, H. Feuchtgruber, B. Vandenbussche, et al., *The Photodetector Array Camera and Spectrometer (PACS) on the Herschel Space Observatory*, Astronomy & Astrophysics **518**, L2 (2010).
- [34] J. E. Austermann, K. A. Aird, J. A. Beall, D. Becker, A. Bender, et al., *SPTpol: an instrument for CMB polarization measurements with the South Pole Telescope*, Proceedings of the SPIE **8452**, 84521E (2012).
- [35] W. S. Holland, D. Bintley, E. L. Chapin, A. Chrysostomou, G. R. Davis, et al., *SCUBA-2: the 10 000 pixel bolometer camera on the James Clerk Maxwell Telescope*, Monthly Notices of the Royal Astronomical Society **430**, 2513 (2013).
- [36] C. D. Mackay, *Charge-coupled devices in astronomy*, Annual Review of Astronomy and Astrophysics **24**, 255 (1986).

- [37] M. C. Weisskopf, B. Brinkman, C. Canizares, G. Garmire, S. Murray, et al., *An Overview of the Performance and Scientific Results from the Chandra X-Ray Observatory*, Publications of the Astronomical Society of the Pacific **114**, 1 (2002).
- [38] F. Jansen, D. Lumb, B. Altieri, J. Clavel, M. Ehle, et al., *XMM-Newton observatory. I. The spacecraft and operations*, Astronomy & Astrophysics **365**, L1 (2001).
- [39] L. Strüder, U. Briel, K. Dennerl, R. Hartmann, E. Kendziorra, et al., *The European Photon Imaging Camera on XMM-Newton: The pn-CCD camera*, Astronomy & Astrophysics **365**, L18 (2001).
- [40] A. D. Turner, J. J. Bock, J. W. Beeman, J. Glenn, P. C. Hargrave, et al., *Silicon nitride micromesh bolometer array for submillimeter astrophysics*, Applied Optics **40**, 4921 (2001).
- [41] G. P. Garmire, M. W. Bautz, P. G. Ford, J. A. Nousek, and G. R. Ricker Jr., *Advanced CCD imaging spectrometer (ACIS) instrument on the Chandra X-ray Observatory*, Proceedings of the SPIE **4851**, 28 (2003).
- [42] S. W. Henderson, J. R. Stevens, M. Amiri, J. Austermann, J. A. Beall, et al., *Readout of two-kilopixel transition-edge sensor arrays for Advanced ACTPol*, Proceedings of the SPIE **9914**, 99141G (2016).
- [43] D. Prêle, F. Voisin, M. Piat, T. Decourcelle, C. Perbost, et al., *A 128 Multiplexing Factor Time-Domain SQUID Multiplexer*, Journal of Low Temperature Physics **184**, 363 (2016).
- [44] P. K. Day, H. G. LeDuc, B. A. Mazin, A. Vayonakis, and J. Zmuidzinas, *A broadband superconducting detector suitable for use in large arrays*, Nature **425**, 817 (2003).
- [45] A. Monfardini, A. Benoit, A. Bideaud, L. Swenson, A. Cruciani, et al., *A Dual-band Millimeter-wave Kinetic Inductance Camera for the IRAM 30 m Telescope*, The Astrophysical Journal Supplement **194**, 24 (2011).
- [46] M. J. Strader, M. D. Johnson, B. A. Mazin, G. V. Spiro Jaeger, C. R. Gwinn, et al., *Excess Optical Enhancement Observed with ARCONS for Early Crab Giant Pulses*, The Astrophysical Journal Letters **779**, L12 (2013).
- [47] B. A. Mazin, *Microwave Kinetic Inductance Detectors: The First Decade*, American Institute of Physics Conference Series **1185**, 135 (2009).
- [48] B. A. Mazin, B. Bumble, S. R. Meeker, K. O'Brien, S. McHugh, et al., *A superconducting focal plane array for ultraviolet, optical, and near-infrared astrophysics*, Optics Express **20**, 1503 (2012).
- [49] G. Ulbricht, B. A. Mazin, P. Szypryt, A. B. Walter, C. Bockstiegel, et al., *Highly multiplexible thermal kinetic inductance detectors for x-ray imaging spectroscopy*, Applied Physics Letters **106**, 251103 (2015).

-
- [50] L. J. Swenson, A. Cruciani, A. Benoit, M. Roesch, C. S. Yung, et al., *High-speed phonon imaging using frequency-multiplexed kinetic inductance detectors*, Applied Physics Letters **96**, 263511 (2010).
 - [51] J. Goupy, A. Adane, A. Benoit, O. Bourrion, M. Calvo, et al., *Microfabrication Technology for Large Lkic Arrays: From Nika2 to Future Applications*, Journal of Low Temperature Physics **184**, 661 (2016).
 - [52] P. J. de Visser, J. J. A. Baselmans, J. Bueno, N. Llombart, and T. M. Klapwijk, *Fluctuations in the electron system of a superconductor exposed to a photon flux*, Nature Communications **5**, 3130 (2014).
 - [53] C. M. Urry and P. Padovani, *Unified Schemes for Radio-Loud Active Galactic Nuclei*, Publications of the Astronomical Society of the Pacific **107**, 803 (1995).
 - [54] C. Lintott, K. Schawinski, S. Bamford, A. Slosar, K. Land, et al., *Galaxy Zoo 1: data release of morphological classifications for nearly 900 000 galaxies*, Monthly Notices of the Royal Astronomical Society **410**, 166 (2011).
 - [55] R. H. Becker, R. L. White, and D. J. Helfand, *The FIRST Survey: Faint Images of the Radio Sky at Twenty Centimeters*, The Astrophysical Journal **450**, 559 (1995).
 - [56] E. L. Wright, P. R. M. Eisenhardt, A. K. Mainzer, M. E. Ressler, R. M. Cutri, et al., *The Wide-field Infrared Survey Explorer (WISE): Mission Description and Initial On-orbit Performance*, The Astronomical Journal **140**, 1868 (2010).

Chapter 2

Radio-loud active galactic nuclei

Active galactic nuclei (AGN) are the result of a super-massive black hole (SMBH) that is growing through the accretion of matter. This accretion process can result in: an increased infrared (IR), ultraviolet (UV) or X-ray emission with respect to the host galaxy. In addition, one may observe broad emission lines from highly ionized elements at visible (VIS) wavelengths. Moreover, some AGN have a bright radio nucleus and/or extended radio emission. Furthermore, AGN show variability of over two orders of magnitude of luminosity on timescales of days [1]. The presence or absence of the above emission characteristics has resulted in a wide taxonomy of AGN based upon their observational characteristics. A few examples are given in Table 2.1.

Detailed studies of the AGN population in the local universe have shown that AGN can be divided in two populations based on their SMBHs mass accretion rate, \dot{M}_{BH} , with respect to the SMBHs mass, M_{BH} [2–4]. AGN with a high accretion rate can efficiently turn the kinetic and potential energy of the accreted gas into electromagnetic (EM) radiation. This results in a galactic nucleus which is bright across the entire EM spectrum. As such, AGN of this population are often called ‘radiative-mode’ AGN. Observationally the brightest of these sources are identified with quasars. At low accretion rates the emission of EM radiation is inefficient and the primary method to release energy is through a radio jet. The presence of a radio jet is often also the only observational indication of such AGN. Therefore this population of AGN is called ‘jet-mode’ AGN.

A useful quantity in this respect is the Eddington-scaled accretion rate or Eddington ratio, λ_{Edd} :

$$\lambda_{\text{Edd}} = (L_{\text{rad}} + L_{\text{mech}})/L_{\text{Edd}} \quad (2.1)$$

Here L_{rad} is the bolometric AGN luminosity and L_{mech} the mechanical work of the AGNs radio jets on the surrounding gas. This combined energy output is expected to be related to \dot{M}_{BH} . L_{Edd} is the Eddington luminosity, which is a theoretical upper limit on the AGN luminosity. L_{Edd} can be estimated using [5]:

$$L_{\text{Edd}} = \frac{4\pi G m_{\text{p}} c}{\sigma_{\text{T}}} M_{\text{BH}} \approx 1.3 \times 10^{31} \frac{M_{\text{BH}}}{M_{\odot}} \text{ W} \quad (2.2)$$

Here G is the gravitational constant, c the speed of light, m_p the proton mass and σ_T the Thomson cross-section of an electron. Above the Eddington luminosity the radiation pressure will exceed the gravitational attraction of the SMBH on the gas it is accreting, thereby effectively terminating its food supply.

Fig. 2.1 shows the distribution of λ_{Edd} for two samples of radio-loud AGN [3]. Radiative-mode AGN generally have a $\lambda_{\text{Edd}} \gtrsim 0.01$, while jet-mode AGN typically have a $\lambda_{\text{Edd}} \lesssim 0.01$. Fig. 2.2 illustrates the difference in central engines driving the two AGN populations [4, 6, 7], which will be further discussed in the following Sections.

2.1 Radiative-mode AGN

The SMBH at the centre of a radiative-mode AGN accretes matter at a high rate. At high accretion rates the accreted material can form an optically thick, geometrically thin accretion disk around the SMBH. This accretion disk is heated by internal friction to an effective temperature of $T_{\text{eff}} \sim 10^6$ K, which makes it a very bright source of UV and X-ray emission. The total accretion luminosity, L_{acc} , of this process is given by:

$$L_{\text{acc}} = \epsilon \dot{M}_{\text{BH}} c^2 \quad (2.3)$$

ϵ is the mass to energy conversion efficiency, which for radiative-mode AGN is found to be $\epsilon \approx 0.1$ [10].

Radiative-mode AGN are thought to follow the classical unification scheme of AGN [9] which uses AGN luminosity and inclination angle to explain the presence or absence

Table 2.1: Various (radiative-mode) AGN taxonomies and their observational properties. Table reproduced from Krolik [8].

AGN Type	Point-like	Broad-band EM	Broad Lines	Narrow Lines	Radio	Variable Luminosity
Radio-loud quasars	Yes	Yes	Yes	Yes	Yes	Some
Radio-quiet quasars	Yes	Yes	Yes	Yes	Weak	Weak
Broad line radio galaxies (Fanaroff-Riley II only)	Yes	Yes	Yes	Yes	Yes	Weak
Narrow line radio galaxies (FRI and FRII)	No	No	No	Yes	Yes	No
OVV quasars (Optically violently variable)	Yes	Yes	Yes	Yes	Yes	Yes
BL Lac objects	Yes	Yes	No	No	Yes	Yes
Seyfert type I	Yes	Yes	Yes	Yes	Weak	Some
Seyfert type II	No	Yes	No	Yes	Weak	No
LINERs	No	No	No	Yes	No	No

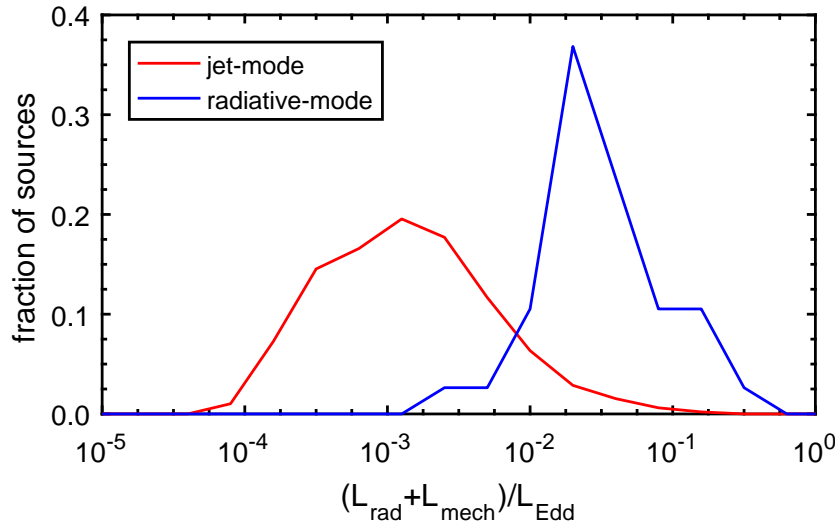


Figure 2.1: The distribution of Eddington-scaled accretion rates for jet-mode and radiative-mode radio galaxies. Original image from Best and Heckman [3].

of broad emission lines and highly energetic radiation in Type I and Type II AGN, respectively. Fig. 2.2(a) shows a sketch of the gaseous and dust structures thought to surround radiative-mode AGN. At the centre are the SMBH and the accretion disk. When a radiative-mode AGN is observed ‘face-on’ (Type 1 AGN) the emission of the accretion disk and the surrounding corona of hot X-ray gas is observed directly and will dominate the UV and X-ray continuum of the AGN as shown in Fig. 2.3. Type 1 AGN are observed through the ionization cone of the AGN. In the ionization cone the emission of the disk irradiates the gas clouds of the broad-line region and narrow-line region. The gas is ionized by the radiation and emits characteristic emission lines at visible wavelengths. Due to the random motion of the clouds the emission lines of these highly ionized atoms are Doppler broadened. The higher velocities in the broad-line region explain the increased linewidth of its emission. In addition to optical line emission, Type 1 AGN often show a high variability due to the stochastic nature of the accretion which is observed directly.

When the AGN is viewed ‘edge-on’ (Type 2 AGN) the broad-line region as well as the emission from the accretion disk are obscured by a toroidal structure of gas and dust. The exact mass, shape and composition of this torus is an open question (see Netzer [11] for a review). Particular uncertainty exists with regards to the physical mechanism that enables the torus to maintain its thick gaseous shape over a long period of time. However, some general trends are seen within both hydrodynamical simulations and phenomenological models used to explain the observed mid- and near-IR spectral energy distributions (SEDs) observed at the centre of nearby AGN. The accretion disk, broad-line region and torus are hypothesized to all be part of the accretion flow bringing gas and dust from galactic scales (~ 100 pc) to the SMBH ($\sim 10^{-4}$ pc). This accretion

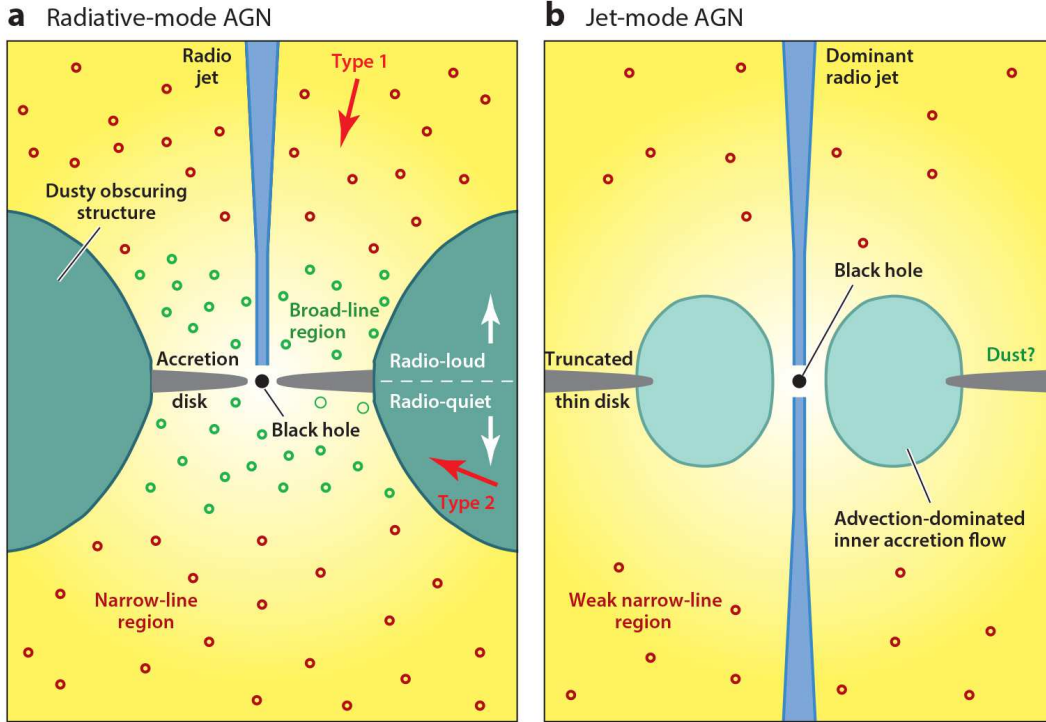


Figure 2.2: A schematic drawing of the central engine for (a) radiative-mode and (b) jet-mode AGN (not to scale). Radiative-mode AGN follow the unification scheme by Urry and Padovani [9]. Matter in the accretion disk accretes onto the super-massive black hole and releases its kinetic and potential energy in the form of ultraviolet and X-ray radiation. This radiation heats the surrounding structures of gas and dust. These structures re-radiate this energy in the form of optical emission lines, in case of the broad- and narrow-line region, or broadband infrared emission, in the case of the dusty obscuring structure (torus). About 5% of the radiative-mode AGN also host radio jets: streams of electrons accelerated by magnetic fields, which can be observed at radio wavelengths. Radio jets can extend to far outside the host galaxy. Jet-mode AGN have an advection dominated accretion flow (ADAF), which is geometrically thick and optically thin. Gas can not cool efficiently in these disks and therefore does not produce the EM radiation seen in radiative-mode AGN. However, theoretical models show that the increased vertical structure of the accretion disk could be beneficial to launching a radio jet. Figure from Heckman and Best [4].

flow is thought to consist of high density gas and dust clumps moving in a much lower density continuous gas medium. Inside the self-gravity radius (~ 0.05 pc) the vertical component of the SMBH's gravity exceeds the local gravity and the clumps will collapse into the thin, radiatively efficient accretion disk described above. The radiation from the accretion disk will irradiate the outer accretion flow. Because dust is opaque to wavelengths below $1 \mu\text{m}$, the absorption of all this radiation heats the gas and dust clouds. At a radius of ~ 1 pc temperatures will reach just over 1000 K, the dust sublimation temperature. This creates an inner region between 0.05 pc and 1 pc of

dust-free gas clouds, which are thought to be the broad-line region. Beyond 1 pc the gas clouds will contain dust, which continues to absorb the radiation and provide the classical obscuration of the torus. The gas in the outer dust rich accretion flow will reach typical temperatures of a few hundred K due to absorption of radiation. This makes the torus a very bright source of IR radiation. Up to 50% of the total AGN luminosity can be observed in the IR due to this process. A typical SED of the torus emission is shown in Fig. 2.3 by the dashed red line. However, due to the many free parameters in the various torus models such SED observation do not constrain them significantly. The use of mid-IR interferometry could improve the constraints on torus model. Burtscher et al. [12] used MIDI to observe 23 nearby AGN with a milliarcsecond resolution. This equates to a few pc in linear distance at the source. Burtscher et al. [12] showed that 18 sources had two components: a point-source component or compact disk and an extended component with an elongation along the polar axis, i.e. along the ionization cone. These new insights do raise questions with regards to the more extended torus model, which is not observed. The results of Burtscher et al. [12] suggest a small, more central torus of hot dust near the sublimation temperature. The extended component is most likely emission of warm dust in polar AGN winds.

In addition to the above sources of EM radiation, about 5% of the radiative-mode AGN can also be observed at radio wavelengths. These radio-loud AGN have so-called radio jets which can extend up to a few megaparsec outside the host galaxy. Radio jets are streams of charged particles that are accelerated out off the galaxy along magnetic field lines and emit synchrotron emission in this process. This synchrotron emission produces a characteristic power-law spectral energy distribution, $S_\nu \propto \nu^\alpha$, at radio wavelengths [13]. For local radio-loud AGN a typical spectral index $\alpha \approx -0.8$ is found [e.g. 14]. Even though both the magnetic field and the charged particles are thought to originate from the galactic nucleus [15], the exact launching mechanism of the radio jets is unknown. The parameters governing the presence or absence of a radio jet as well as its morphology would further complete the AGN unification scheme.

Radiative-mode AGN have a wide nomenclature depending on their orientation and luminosity. In addition to the variations given in Table 2.1, radiative-mode AGN may be called ‘quasar-mode’, ‘cold-mode’, ‘high-excitation’, ‘radiatively efficient’ or ‘quenching-mode’ AGN.

2.2 Jet-mode AGN

In the local universe the bulk of the radio-loud AGN are from the jet-mode population [22]. Observationally, jet-mode AGN lack the IR torus emission, optical emission lines, and UV and X-ray emission associated with radiative-mode AGN [23–25]. On the other hand, a survey of ~ 150 low-luminosity AGN by Nagar et al. [26, 27] shows that at

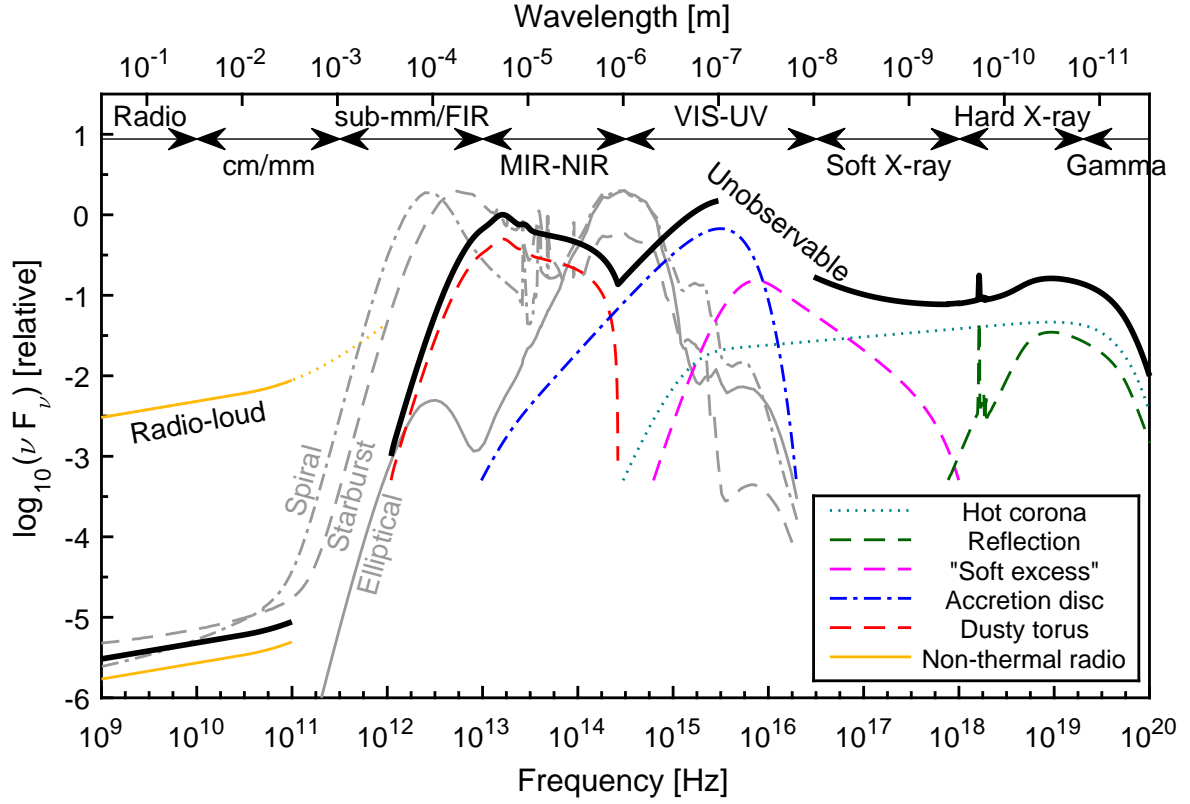


Figure 2.3: A schematic representation of the spectral energy distribution (SED) of a radiative-mode AGN loosely based on observations of radio-quiet quasars [e.g. 16, 17]. The solid black curve represents the total of all six AGN components. The emission of each component is given by the coloured curves, which have been offset for clarity. The emission from the AGN accretion disk (blue dashed line) can be described by a modified blackbody spectrum at $T \sim 60000$ K and peaks in the UV. Interaction of these UV photons with the corona of hot gas around the accretion disk produces the X-ray emission. The torus a bright source in the mid- and near-IR (red dashed line) [18]. Radio-loud AGN also have emission from their radio jets that can be several orders of magnitude higher than radio-quiet AGN (labelled yellow line). The extreme UV is, even with space telescopes, effectively unobservable because the interstellar medium is opaque in this wavelength range at interstellar distances [19]. Furthermore, in the mm–far-IR regime the AGN emission is widely believed to be negligible compared to the emission of dust heated by star formation. For comparison the SED of a local spiral galaxy, elliptical galaxy and starburst galaxy from GRASIL [20] are shown in grey. In all these galaxy SEDs the stellar emission (near-IR–VIS) and dust emission (mm–far-IR) is clearly distinguishable. Note that the relative strength of the AGN SED components with respect to the host galaxy SED or each other can vary with the AGN and galaxy luminosity as well as AGN type. Image courtesy of Harrison [21].

least 40% has a radio core or radio jet. Deeper radio observations for smaller samples find a radio jet in over 70% of the jet-mode AGN [28, 29]. This high fraction of radio jets in low-luminosity AGN is thought to be the result of a different accretion structure as shown in Fig. 2.2(b) [30]. The low accretion rates in jet-mode AGN result in an advection-dominated accretion flow (ADAF), which is geometrically thick and optically thin. Gas can not cool efficiently in these disks and therefore does not produce the EM radiation seen in radiative-mode AGN. However, theoretical models show that the increased vertical structure of the accretion disk could be beneficial to launching a radio jet [5]. Jet-mode AGN release the bulk of their energy in the form of kinetic energy carried by their radio jets. Some jet-mode AGN have been associated with LINERs (Low Ionisation Nuclear Emission Line Regions) which would indicate that a weak narrow-line region is present in some of these galactic cores. Jet-mode AGN nomenclature includes ‘radio-mode’, ‘hot-mode’, ‘low-excitation’, ‘radiatively inefficient’ or ‘maintenance-mode’ AGN.

2.3 AGN feedback

In the local universe radiative-mode AGN are predominantly found in galaxies at the massive end ($M_* \sim 10^{10.5} M_\odot$) of the main sequence of star formation [31]. At these masses the cold gas supply for star formation is large enough that also the SMBH can accrete a significant amount of cold gas and form a radiative-mode AGN. The radiation from this AGN can exert pressure on the surrounding medium and drive powerful winds. Blue shifted absorption lines in the VIS/UV spectra of Type 1 AGN show winds with velocities between a few hundred to a few tens of thousands kilometres per second [32, and references therein]. These winds are thought to expel the gas out off the galaxy, thereby quenching the star formation and terminating the AGN activity [e.g. 33]. The quenching of star formation in galaxies is thought to be quick, based on the dearth of galaxies in the green valley [34, 35]. Using mm-interferometry these gas outflows have been resolved in nearby quasars on kiloparsec scales [e.g. 36]. They carry enough mass to compensate the accretion onto the galaxy. As such luminous radiative-mode AGN are the kill switch which terminates star formation and limits the formation of overly massive galaxies [37]. However, the observational evidence is not as strong for lower luminosity radiative-mode AGN. For example, a sample of Type 2 Seyfert galaxies by Krug et al. [38] shows no evidence of high-velocity outflows.

Major mergers are often seen as the triggering event for starburst galaxies and the most powerful radiative-mode AGN. During a merger the tidal torques acting on the mass inside a galaxy can efficiently transport the large supply of new gas to the centres of the galaxies [39, 40], which in turn triggers star formation [e.g. 41] and AGN activity [e.g. 42]. However, recent observations suggest that mergers do not dominate the total cosmic star formation and AGN activity [4, 43].

Jet-mode AGN have a strong preference to be hosted by the most massive galaxies [44]. About 30% of the most massive ($M_* \gtrsim 10^{11.5} M_\odot$) red elliptical galaxies shows signatures of a radio-loud AGN. These massive galaxies are often located in the centre of groups and clusters and are associated with a halo of hot X-ray gas. Both numerical simulations and multiwavelength observations show that radio jets can blow bubbles in the hot halo gas of a galaxy [e.g. 45, 46]. The mechanical energy of the jets can continuously heat the X-ray gas and balance the gas cooling [e.g. 47]. Because jet-mode AGN are thought to slowly accrete halo gas as their fuel [7] we observe a negative feedback loop which regulates the total amount of halo gas that is allowed to cool into the galaxy. Thereby the AGN prevents further growth through star formation in massive red elliptical galaxies. However, also positive feedback from radio jets has been observed [e.g. 48–50]. In this scenario the radio jet compresses the gas inside the host galaxy. In these increased densities new stars are able to form.

References

- [1] M.-H. Ulrich, L. Maraschi, and C. M. Urry, *Variability of Active Galactic Nuclei*, Annual Review of Astronomy and Astrophysics **35**, 445 (1997).
- [2] G. Kauffmann and T. M. Heckman, *Feast and Famine: regulation of black hole growth in low-redshift galaxies*, Monthly Notices of the Royal Astronomical Society **397**, 135 (2009).
- [3] P. N. Best and T. M. Heckman, *On the fundamental dichotomy in the local radio-AGN population: accretion, evolution and host galaxy properties*, Monthly Notices of the Royal Astronomical Society **421**, 1569 (2012).
- [4] T. M. Heckman and P. N. Best, *The Coevolution of Galaxies and Supermassive Black Holes: Insights from Surveys of the Contemporary Universe*, Annual Review of Astronomy and Astrophysics **52**, 589 (2014).
- [5] A. Kembhavi and J. Narlikar, *Quasars and Active Galactic Nuclei*, Cambridge University Press, New York (1999).
- [6] D. J. Croton, V. Springel, S. D. M. White, G. De Lucia, C. S. Frenk, et al., *The many lives of active galactic nuclei: cooling flows, black holes and the luminosities and colours of galaxies*, Monthly Notices of the Royal Astronomical Society **365**, 11 (2006).
- [7] M. J. Hardcastle, D. A. Evans, and J. H. Croston, *Hot and cold gas accretion and feedback in radio-loud active galaxies*, Monthly Notices of the Royal Astronomical Society **376**, 1849 (2007).
- [8] J. Krolik, *Active galactic nuclei: from the central black hole to the galactic environment*, Princeton University Press, New Jersey (1999).

-
- [9] C. M. Urry and P. Padovani, *Unified Schemes for Radio-Loud Active Galactic Nuclei*, Publications of the Astronomical Society of the Pacific **107**, 803 (1995).
 - [10] A. Marconi, G. Risaliti, R. Gilli, L. K. Hunt, R. Maiolino, et al., *Local supermassive black holes, relics of active galactic nuclei and the X-ray background*, Monthly Notices of the Royal Astronomical Society **351**, 169 (2004).
 - [11] H. Netzer, *Revisiting the Unified Model of Active Galactic Nuclei*, Annual Review of Astronomy and Astrophysics **53**, 365 (2015).
 - [12] L. Burtscher, K. Meisenheimer, K. R. W. Tristram, W. Jaffe, S. F. Hönig, et al., *A diversity of dusty AGN tori. Data release for the VLTI/MIDI AGN Large Program and first results for 23 galaxies*, Astronomy & Astrophysics **558**, A149 (2013).
 - [13] I. J. Klammer, R. D. Ekers, J. J. Bryant, R. W. Hunstead, E. M. Sadler, et al., *A search for distant radio galaxies from SUMSS and NVSS - III. Radio spectral energy distributions and the z - α correlation*, Monthly Notices of the Royal Astronomical Society **371**, 852 (2006).
 - [14] C. De Breuck, W. van Breugel, H. J. A. Röttgering, and G. Miley, *A sample of 669 ultra steep spectrum radio sources to find high redshift radio galaxies*, Astronomy & Astrophysics Supplement Series **143**, 303 (2000).
 - [15] M. J. Rees, *Relativistic jets and beams in radio galaxies*, Nature **275**, 516 (1978).
 - [16] M. Elvis, B. J. Wilkes, J. C. McDowell, R. F. Green, J. Bechtold, et al., *Atlas of quasar energy distributions*, The Astrophysical Journal Supplement Series **95**, 1 (1994).
 - [17] G. T. Richards, M. Lacy, L. J. Storrie-Lombardi, P. B. Hall, S. C. Gallagher, et al., *Spectral Energy Distributions and Multiwavelength Selection of Type 1 Quasars*, The Astrophysical Journal Supplement Series **166**, 470 (2006).
 - [18] J. R. Mullaney, D. M. Alexander, A. D. Goulding, and R. C. Hickox, *Defining the intrinsic AGN infrared spectral energy distribution and measuring its contribution to the infrared output of composite galaxies*, Monthly Notices of the Royal Astronomical Society **414**, 1082 (2011).
 - [19] L. H. Aller, *Some Aspects of Ultraviolet Satellite Spectroscopy*, Publications of the Astronomical Society of the Pacific **71**, 324 (1959).
 - [20] L. Silva, G. L. Granato, A. Bressan, and L. Danese, *Modeling the Effects of Dust on Galactic Spectral Energy Distributions from the Ultraviolet to the Millimeter Band*, The Astrophysical Journal **509**, 103 (1998).
 - [21] C. M. Harrison, *Observational constraints on the influence of active galactic nuclei on the evolution of galaxies*, Springer International Publishing, Switzerland (2016).

- [22] P. N. Best, G. Kauffmann, T. M. Heckman, and Ž. Ivezić, *A sample of radio-loud active galactic nuclei in the Sloan Digital Sky Survey*, Monthly Notices of the Royal Astronomical Society **362**, 9 (2005).
- [23] R. A. Laing, C. R. Jenkins, J. V. Wall, and S. W. Unger, *Spectrophotometry of a Complete Sample of 3CR Radio Sources: Implications for Unified Models*, Astronomical Society of the Pacific Conference Series **54**, 201 (1994).
- [24] D. A. Evans, D. M. Worrall, M. J. Hardcastle, R. P. Kraft, and M. Birkinshaw, *Chandra and XMM-Newton Observations of a Sample of Low-Redshift FR I and FR II Radio Galaxy Nuclei*, The Astrophysical Journal **642**, 96 (2006).
- [25] D. Whysong and R. Antonucci, *Thermal Emission as a Test for Hidden Nuclei in Nearby Radio Galaxies*, The Astrophysical Journal **602**, 116 (2004).
- [26] N. M. Nagar, H. Falcke, A. S. Wilson, and L. C. Ho, *Radio Sources in Low-Luminosity Active Galactic Nuclei. I. VLA Detections of Compact, Flat-Spectrum Cores*, The Astrophysical Journal **542**, 186 (2000).
- [27] N. M. Nagar, H. Falcke, A. S. Wilson, and J. S. Ulvestad, *Radio sources in low-luminosity active galactic nuclei. III. “AGNs” in a distance-limited sample of “LLAGNs”*, Astronomy & Astrophysics **392**, 53 (2002).
- [28] S. D. van Dyk and L. C. Ho, *Radio emission from low-luminosity active galactic nuclei*, IAU Symposium **184**, 489 (1998).
- [29] L. C. Ho and C. Y. Peng, *Nuclear Luminosities and Radio Loudness of Seyfert Nuclei*, The Astrophysical Journal **555**, 650 (2001).
- [30] L. C. Ho, *Nuclear Activity in Nearby Galaxies*, Annual Review of Astronomy and Astrophysics **46**, 475 (2008).
- [31] T. M. Heckman, G. Kauffmann, J. Brinchmann, S. Charlot, C. Tremonti, et al., *Present-Day Growth of Black Holes and Bulges: The Sloan Digital Sky Survey Perspective*, The Astrophysical Journal **613**, 109 (2004).
- [32] D. M. Crenshaw, S. B. Kraemer, and I. M. George, *Mass Loss from the Nuclei of Active Galaxies*, Annual Review of Astronomy and Astrophysics **41**, 117 (2003).
- [33] M. J. Page, M. Symeonidis, J. D. Vieira, B. Altieri, A. Amblard, et al., *The suppression of star formation by powerful active galactic nuclei*, Nature **485**, 213 (2012).
- [34] K. Schawinski, C. M. Urry, B. D. Simmons, L. Fortson, S. Kaviraj, et al., *The green valley is a red herring: Galaxy Zoo reveals two evolutionary pathways towards quenching of star formation in early- and late-type galaxies*, Monthly Notices of the Royal Astronomical Society **440**, 889 (2014).

- [35] J. W. Trayford, T. Theuns, R. G. Bower, R. A. Crain, C. d. P. Lagos, et al., *It is not easy being green: the evolution of galaxy colour in the EAGLE simulation*, Monthly Notices of the Royal Astronomical Society **460**, 3925 (2016).
- [36] C. Feruglio, R. Maiolino, E. Piconcelli, N. Menci, H. Aussel, et al., *Quasar feedback revealed by giant molecular outflows*, Astronomy & Astrophysics **518**, L155 (2010).
- [37] R. G. Bower, J. Schaye, C. S. Frenk, T. Theuns, M. Schaller, et al., *The dark nemesis of galaxy formation: why hot haloes trigger black hole growth and bring star formation to an end*, Monthly Notices of the Royal Astronomical Society **465**, 32 (2017).
- [38] H. B. Krug, D. S. N. Rupke, and S. Veilleux, *Neutral Gas Outflows and Inflows in Infrared-faint Seyfert Galaxies*, The Astrophysical Journal **708**, 1145 (2010).
- [39] J. E. Barnes and L. Hernquist, *Transformations of Galaxies. II. Gasdynamics in Merging Disk Galaxies*, The Astrophysical Journal **471**, 115 (1996).
- [40] T. Naab, R. Jesseit, and A. Burkert, *The influence of gas on the structure of merger remnants*, Monthly Notices of the Royal Astronomical Society **372**, 839 (2006).
- [41] T. J. Cox, P. Jonsson, R. S. Somerville, J. R. Primack, and A. Dekel, *The effect of galaxy mass ratio on merger-driven starbursts*, Monthly Notices of the Royal Astronomical Society **384**, 386 (2008).
- [42] P. F. Hopkins, L. Hernquist, T. J. Cox, T. Di Matteo, P. Martini, et al., *Black Holes in Galaxy Mergers: Evolution of Quasars*, The Astrophysical Journal **630**, 705 (2005).
- [43] G. Rodighiero, E. Daddi, I. Baronchelli, A. Cimatti, A. Renzini, et al., *The Lesser Role of Starbursts in Star Formation at $z = 2$* , The Astrophysical Journal Letters **739**, L40 (2011).
- [44] P. N. Best, G. Kauffmann, T. M. Heckman, J. Brinchmann, S. Charlot, et al., *The host galaxies of radio-loud active galactic nuclei: mass dependences, gas cooling and active galactic nuclei feedback*, Monthly Notices of the Royal Astronomical Society **362**, 25 (2005).
- [45] L. Birzan, D. A. Rafferty, B. R. McNamara, M. W. Wise, and P. E. J. Nulsen, *A Systematic Study of Radio-induced X-Ray Cavities in Clusters, Groups, and Galaxies*, The Astrophysical Journal **607**, 800 (2004).
- [46] W. English, M. J. Hardcastle, and M. G. H. Krause, *Numerical modelling of the lobes of radio galaxies in cluster environments - III. Powerful relativistic and non-relativistic jets*, Monthly Notices of the Royal Astronomical Society **461**, 2025 (2016).

-
- [47] P. N. Best, C. R. Kaiser, T. M. Heckman, and G. Kauffmann, *AGN-controlled cooling in elliptical galaxies*, Monthly Notices of the Royal Astronomical Society **368**, L67 (2006).
 - [48] M. Krause, *Very light jets II: Bipolar large scale simulations in King atmospheres*, Astronomy & Astrophysics **431**, 45 (2005).
 - [49] S. W. Allen, R. J. H. Dunn, A. C. Fabian, G. B. Taylor, and C. S. Reynolds, *The relation between accretion rate and jet power in X-ray luminous elliptical galaxies*, Monthly Notices of the Royal Astronomical Society **372**, 21 (2006).
 - [50] R. J. H. Dunn and A. C. Fabian, *Investigating AGN heating in a sample of nearby clusters*, Monthly Notices of the Royal Astronomical Society **373**, 959 (2006).

Chapter 3

The triggering probability of radio-loud AGN: A comparison of high- and low-excitation radio galaxies in hosts of different colours

Low-luminosity radio-loud active galactic nuclei (AGN) are generally found in massive red elliptical galaxies, where they are thought to be powered through gas accretion from their surrounding hot halos in a radiatively inefficient manner. These AGN are often referred to as ‘low-excitation’ radio galaxies (LERGs). When radio-loud AGN are found in galaxies with a young stellar population and active star formation, they are usually high-power radiatively efficient radio AGN (‘high-excitation’, HERG). Using a sample of low-redshift radio galaxies identified within the Sloan Digital Sky Survey (SDSS), we determine the fraction of galaxies that host a radio-loud AGN, f_{RL} , as a function of host galaxy stellar mass, M_* , star formation rate, colour (defined by the 4000 Å break strength), radio luminosity and excitation state (HERG/LERG).

We find the following: 1. LERGs are predominantly found in red galaxies. 2. The radio-loud AGN fraction of LERGs hosted by galaxies of any colour follows a $f_{RL}^{LE} \propto M_*^{2.5}$ power law. 3. The fraction of red galaxies hosting a LERG decreases strongly for increasing radio luminosity. For massive blue galaxies this is not the case. 4. The fraction of green galaxies hosting a LERG is lower than that of either red or blue galaxies, at all radio luminosities. 5. The radio-loud AGN fraction of HERGs hosted by galaxies of any colour follows a $f_{RL}^{HE} \propto M_*^{1.5}$ power law. 6. HERGs have a strong preference to be hosted by green or blue galaxies. 7. The fraction of galaxies hosting a HERG shows only a weak dependence on radio-luminosity cut. 8. For both HERGs and LERGs, the hosting probability of blue galaxies shows a strong dependence on star formation rate. This is not observed in galaxies

of a different colour.

Our interpretation of these results is that the presence of cold gas in a LERG enhances the probability that its super-massive black hole becomes a luminous radio-loud AGN compared to the typical ‘model’ LERG in a red elliptical galaxy. If enough cold gas can be transported to the SMBH a HERG can be created. However, the presence of cold gas does not automatically imply a HERG will be created. We speculate that feedback of the enhanced AGN activity in blue galaxies is responsible for the reduced probability of green galaxies to host a LERG.

3.1 Introduction

It has been known for a long time that low-luminosity radio-loud (RL) active galactic nuclei (AGN) are predominantly hosted by massive red elliptical galaxies [e.g. 1]. These AGN are thought to be the result of an accretion process in which hot gas from the red elliptical's X-ray halo is falling at low Eddington rates into the super-massive black hole (SMBH) at its centre [e.g. 2]. Because this accretion process is radiatively inefficient, halo-fed radio galaxies often lack the luminous emission lines, X-ray emission and infrared torus emission generally associated with AGN [e.g. 3–5]. Therefore, they have been referred to as ‘radio-mode’ or ‘low-excitation’ radio galaxies (LERGs). A limited number of LERGs have also been found in massive galaxies with a younger stellar population [bluer colour; e.g. 6]. Because young stars require cold gas to form, a young stellar population is often associated with the presence of a cold-gas reservoir in the galaxy. If gas from this reservoir reaches the SMBH, it can be accreted at higher rates in a radiatively efficient process, creating an AGN with many luminous emission lines. This accretion process is more similar to the ‘standard’ AGN accretion mode found in quasars. Hence, the population of emission line rich RL AGN is referred to as ‘quasar-mode’ or ‘high-excitation’ radio galaxies (HERGs).

High- and low-excitation radio galaxies were shown to be two independent populations [7–9] in which HERGs are typically hosted by lower mass, bluer galaxies [10] located in less dense environments. Despite this preference, LERGs have been identified in blue galaxies and HERGs in red galaxies. Because these populations are rare, the number of observed examples has not been large enough for a statistical study. However, using the Sloan Digital Sky Survey (SDSS) [11, 12, and references therein] in combination with all sky radio surveys, a sample of radio galaxies can now be constructed that contains the number statistics to analyse the host galaxies of RL AGN in detail. Hereby we aim to achieve new insights into the effect of the presence or absence of an internal reservoir of cold gas on the creation of a RL AGN.

The sample of galaxies and RL AGN used to investigate this is described in Sect. 3.2. After defining the RL AGN fraction in Sect. 3.3, we use this parameter in Sect. 3.4 and 3.5 to investigate the probability of hosting a RL AGN as a function of host galaxy mass, SFR, colour and the RL AGN's radio luminosity and excitation. An interpretation of these results is discussed in Sect. 3.6 before we summarize our conclusions in Sect. 3.7. Throughout this paper we assume the cosmological parameters $H_0 = 70 \text{ km s}^{-1} \text{ Mpc}^{-1}$, $\Omega_m = 0.3$, and $\Omega_\Lambda = 0.7$.

3.2 The radio-loud AGN sample

In this research we use the sample of RL AGN defined by Best and Heckman [10]. It was constructed by cross-comparing the positions of galaxies in the seventh data release (DR7) [14] of the SDSS spectroscopic sample with data from the National Radio As-

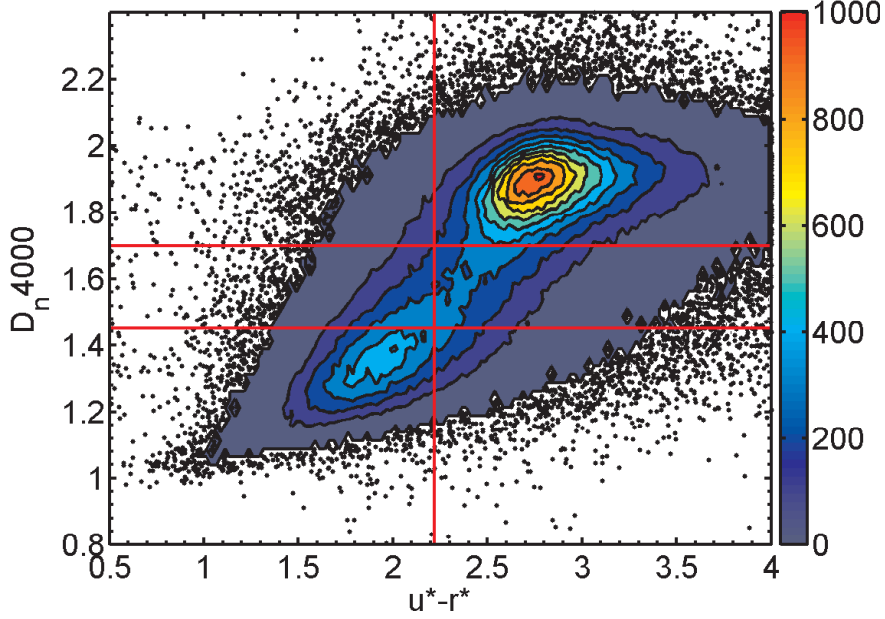


Figure 3.1: A contour plot showing the distribution of galaxies with a mass $10^{10.25} M_{\odot} \leq M_{*} \leq 10^{12.0} M_{\odot}$ within the $u^{*} - r^{*}$ vs D_n4000 plane. The colourbar on the right indicates the number of galaxies per bin of width 0.025 in both $u^{*} - r^{*}$ and D_n4000 . If the number of galaxies per bin is less than 5, these galaxies are shown as black dots instead. The vertical red line indicates the optimum separation in the Petrosian colour, $u^{*} - r^{*} = 2.22$, proposed by Strateva et al. [13]. Although this does indeed separate galaxies of the blue cloud and red sequence, the separation between the two populations is more pronounced in D_n4000 . Therefore the horizontal separation lines $D_n4000 = 1.45$ and $D_n4000 = 1.7$ are adopted in this research. Galaxies between these two values are classified as green.

tronomy Observatory (NRAO) Very Large Array (VLA) Sky Survey (NVSS) [15] and the Faint Images of the Radio Sky at Twenty centimetres survey (FIRST) [16]. The optical parent sample consists of all galaxies in the value-added spectroscopic catalogues (VASC) created by the Max Planck Institute for Astrophysics and Johns Hopkins University group [cf. 17]. These objects are either targets from the SDSS main galaxy sample [18] with a usable spectrum, or QSOs with a spectrum that is clearly dominated by the emission of stars in the host galaxy. For each galaxy the VASC contains a number of derived quantities such as the stellar mass, M_{*} , and star formation rate, SFR [19, 20]. Within the 927522 galaxies of the VASC, Best and Heckman [10] identified a magnitude-limited sample of 18286 radio sources. This sample was shown to have a completeness of 95% and a reliability of 99% [21]. Besides RL AGN, it also contains radio sources in which the radio emission is associated with star formation. Best and Heckman [10] separated the RL AGN and star forming galaxies using three different criteria: emission line ratio diagnostics, such as the ‘BPT’ diagram [22]; the radio luminosity, $L_{1.4\text{GHz}}$, versus $H\alpha$ emission line luminosity [23]; the $L_{1.4\text{GHz}}/M_{*}$ vs

D_n4000 plane [21]. Where possible, Best and Heckman [10] also classified each true RL AGN as a ‘low-excitation’ (9863 sources) or ‘high-excitation’ (481 sources) radio galaxy, using emission line properties. We will use these classification in the research presented below.

From all the galaxies in the VASC we select the best observations of all unique objects with a reliable redshift in the range $0.03 \leq z \leq 0.3$. This redshift range is narrow enough to exclude most evolutionary effects, whilst it is wide enough to keep the number statistics required for this work. We only consider galaxies in the mass range $10^{10.25} M_\odot \leq M_* \leq 10^{12.0} M_\odot$, because of the limited number of RL AGN available outside this mass range. Within the galaxy population a small contamination of stars and QSOs was found. These objects were removed based on their point-source nature, because galaxy parameter estimation is unreliable for these sources. Visual inspection showed that our method removed all stars and QSOs.

A separation between galaxies of the red sequence, green valley and blue cloud is made using the rest frame 4000 Å break value (D_n4000) [24]. In previous works this has typically been done using broadband colours. For example, Strateva et al. [13] show that the optimal separation in the $u^* - r^*$ colour based on Petrosian magnitudes is $u^* - r^* = 2.22$. This separation is indicated by the vertical red line in Fig. 3.2, which shows the distribution of galaxies in the $u^* - r^*$ vs D_n4000 plane. However, from this figure it is clear that the galaxy colour bimodality has a wider separation in D_n4000 than $u^* - r^*$. Therefore we define galaxies with $D_n4000 \geq 1.7$ as ‘red’ and galaxies with $D_n4000 \leq 1.45$ as ‘blue’. Any galaxy with an intermediate value ($1.45 < D_n4000 < 1.7$) is considered a ‘green’ galaxy. These two separation values are shown as horizontal red lines in Fig. 3.2.

The number of galaxies (including those hosting a RL AGN) of each colour can be found in Table 3.1. This table also gives the number of red, green and blue HERGs and LERGs for 2 different radio luminosity cuts ($L_{1.4\text{GHz}} \geq L_{1.4\text{GHz}}^{\min}$).

Table 3.1: The number of red, green and blue galaxies and radio-loud AGN with a mass $10^{10.25} M_\odot \leq M_* \leq 10^{12.0} M_\odot$. The number of high- and low-excitation radio galaxies is given for 2 radio-luminosity cuts, $L_{1.4\text{GHz}} \geq L_{1.4\text{GHz}}^{\min}$. Here $L_{1.4\text{GHz}}^{\min}$ is given in W Hz^{-1} . Note that the number of galaxies includes the galaxies that host a radio-loud AGN.

Colour	Galaxies	LERG		HERG	
		$L_{1.4\text{GHz}} \geq 10^{23.0}$	$L_{1.4\text{GHz}} \geq 10^{24.5}$	$L_{1.4\text{GHz}} \geq 10^{23.0}$	$L_{1.4\text{GHz}} \geq 10^{24.5}$
Red	295523	6157	1546	94	40
Green	114210	363	89	98	51
Blue	114947	171	83	60	40

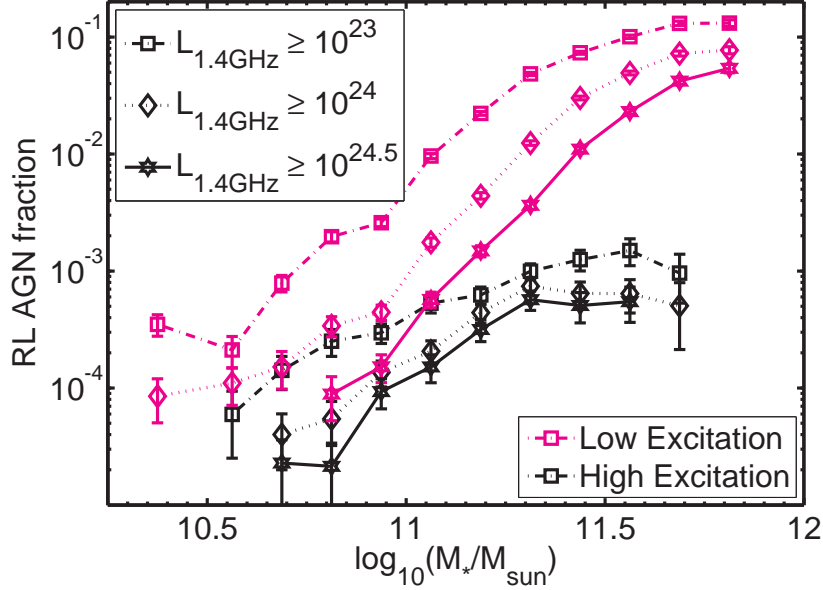


Figure 3.2: The fraction of galaxies hosting a high- (black) or low-excitation (magenta) radio galaxy as a function of host galaxy stellar mass. Three radio-luminosity cuts are given for each excitation. The error bars are determined by Poissonian statistics.

3.3 The radio-loud AGN fraction

We will investigate which galaxies preferentially host RL AGN by determining the fraction of RL AGN, f_{RL} , as a function of host galaxy mass, SFR, colour (x) and the RL AGN's radio luminosity and excitation (y). $f_{RL}^{y,x}$ is defined as

$$f_{RL}^{y,x} = \left(\sum_{i \in A_{y,x}} \frac{1}{V_{\max}^i} \right) \left(\sum_{j \in G_x} \frac{1}{V_{\max}^j} \right)^{-1} \quad (3.1)$$

Here A and G are all RL AGN and galaxies (including AGN), respectively, in a particular bin. V_{\max} is the maximum volume in which each galaxy can be observed, as defined by the V_{\max} -formalism [25]. This takes into account the redshift limits from both the radio and optical selection criteria, as well as the limits due to the redshift range being analysed. Previous works [e.g. 7] limited the volume studied at each radio luminosity to produce a volume-limited sample. This allowed them to use simple fractions defined as:

$$f_{RL}^{y,x} = N_A^{y,x} / N_G^x \quad (3.2)$$

Here N_A and N_G are the number of RL AGN and galaxies in a bin. Such analysis produces results that are equivalent to the results presented below, within the errors. We estimate the error on the RL AGN fraction, $\sigma(f_{RL})$, using Poissonian statistics [26].

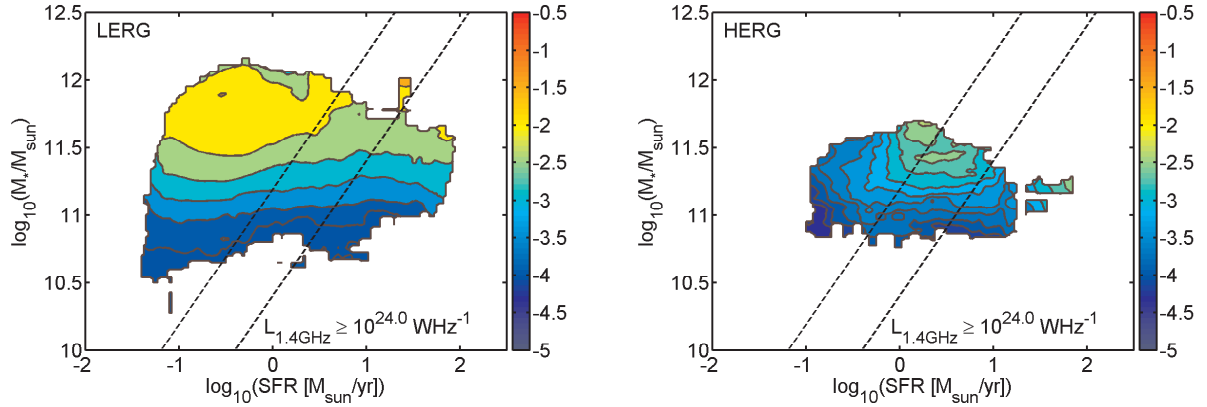


Figure 3.3: This contour plot shows the fraction of galaxies hosting a RL AGN in the stellar mass versus star formation rate plane. The value of $\log_{10}(f_{RL}^y)$ for low-excitation (left panel) and high-excitation (right panel) radio galaxies is given by colour gradients for which the legend is found in the colorbars on the right. Only radio-loud AGN with a $L_{1.4\text{GHz}} \geq 10^{24.0} \text{ W Hz}^{-1}$ were considered in the determination of f_{RL}^y . As the specific star formation rate (SFR/ M_*) is broadly correlated with the D_n4000 value of a galaxy, each panel contains 2 diagonals, which are a guide to the eye on where the red, green and blue galaxy population are located.

3.4 Dependence on AGN excitation

Figure 3.2 shows the fraction of galaxies hosting either a HERG (black) or LERG (magenta) more luminous than a given radio power, as a function of host galaxy mass. At all radio luminosities the LERG population shows an increase in the RL AGN fraction that is consistent with $f_{RL}^{LE} \propto M_*^{2.5}$. The fraction of galaxies hosting a LERG saturates at high masses ($M_* > 10^{11.6} M_\odot$) at a value of $\sim 10\%$. These results are similar to what was found by Best et al. [7]. Compared to the LERGs, HERGs have a far more shallow dependence on mass, $f_{RL}^{HE} \propto M_*^{1.5}$. In addition, the level of f_{RL}^{HE} is much less dependent on the radio luminosity cut. Over the 1.5 orders of magnitude in radio luminosity shown in Fig. 3.2, the fraction of galaxies hosting a HERG typically decreases by a factor of 3. This is significantly less than the factor of 10 decrease found at masses $M_* < 10^{11.5} M_\odot$ between f_{RL}^{LE} at the highest and lowest radio-luminosity cuts.

As discussed in the introduction, the presence or absence of cold gas is thought to be of strong influence on the creation of either a HERG or LERG. Therefore it is of interest to consider the fraction of galaxies hosting a HERG or LERG as a function of SFR. Fig. 3.3 shows the SFR vs M_* plane in which coloured contours are used to indicate the value of $\log_{10}(f_{RL}^y)$. The value of $\log_{10}(f_{RL}^y)$ corresponding to each colour can be found in the colorbars on the right of each panel. In the determination of f_{RL}^y only RL AGN with a $L_{1.4\text{GHz}} \geq 10^{24.0} \text{ W Hz}^{-1}$ are considered.

The ‘colourbands’ of the LERG population are all horizontally aligned over the considered range of SFR, as can be seen in the left-hand panel of Fig. 3.3. Only for galaxies

with both a high mass ($M_* \geq 10^{11.5} M_\odot$) and a high SFR ($\text{SFR} \geq 10 M_\odot/\text{yr}$) is the SFR independence lost. However, given that there is little data in this region, this could very well be due to the scarceness of high mass, high SFR galaxies in general. The right-hand panel in Fig. 3.3 shows the probability to host a HERG. From this figure it is clear that HERGs are preferentially hosted by a population of massive, $M_* \approx 10^{11.5} M_\odot$, galaxies with a typical $\text{SFR} = 3 M_\odot/\text{yr}$. From this maximum the hosting probability rapidly decreases to both lower mass and lower SFR.

The correlation between specific star formation rate ($\text{sSFR} = \text{SFR}/M_*$) and D_n4000 [17] allows us to give a guide to the eye on where the red, green and blue galaxy population approximately lie in the (SFR, M_*) -plane. The left and right dashed diagonal lines roughly correspond to $D_n4000 = 1.7$ and $D_n4000 = 1.45$, respectively. However, there is considerable overlap between galaxies of the three colours. Therefore, we will investigate the properties of the HERG and LERG population in red, green and blue galaxies individually in the next section.

3.5 Dependence on galaxy colour

The left-hand panel of Fig. 3.4 shows the fraction of red, green and blue galaxies that host a LERG as a function of host galaxy stellar mass and radio-luminosity cut. For all combinations of colour and radio-luminosity cut the fraction of galaxies hosting a LERG is consistent with the $f_{RL}^{LE,x} \propto M_*^{2.5}$ power law dependence typical for LERGs. A saturation at high masses similar to Fig. 3.2 is found as well. However, the most striking feature of Fig. 3.4 (left panel) is that for an increasing value of the radio-luminosity cut the fraction of LERGs in the red and green galaxy population drops strongly, while in the blue population it is relatively unchanged. The left-hand panel of Fig. 3.5 shows this effect in more detail. It shows the fraction of galaxies with a mass $10^{11.25} \leq M_*/M_\odot \leq 10^{11.5}$ that host a LERG with a radio luminosity above a given $L_{1.4\text{GHz}}^{\min}$. The mass range $10^{11.25} \leq M_*/M_\odot \leq 10^{11.5}$ was chosen because it has the highest number of LERGs in green (36) and blue (28) hosts. Because of their scarceness, these LERG populations limit our statistics. At low $L_{1.4\text{GHz}}^{\min}$ the probability of finding a LERG in a red galaxy is significantly greater than the probability of finding one in a blue galaxy. However, for increasing values of $L_{1.4\text{GHz}}^{\min}$, $f_{RL}^{LE,red}$ decreases, while $f_{RL}^{LE,blue}$ remains almost constant out to $L_{1.4\text{GHz}}^{\min} \approx 10^{24.5} \text{ W Hz}^{-1}$. As a result, there is a cross-over at $L_{1.4\text{GHz}}^{\min} \approx 10^{24.25} \text{ W Hz}^{-1}$. At higher radio luminosities the RL AGN fraction can be higher for the blue galaxy population than it is for the red. For example, at a $L_{1.4\text{GHz}} \geq 10^{24.5} \text{ W Hz}^{-1}$ the fraction of RL AGN in a blue host, $f_{RL}^{LE,blue}$, with a mass in the range $10^{11.25} M_\odot < M_* < 10^{11.5} M_\odot$, is 1.58 ± 0.31 times higher than $f_{RL}^{LE,red}$. As can be seen in Fig. 3.4 and particularly in Fig. 3.5, the green population has a LERG fraction, $f_{RL}^{LE,green}$, which is generally lower than $f_{RL}^{LE,red}$ and equal to or lower

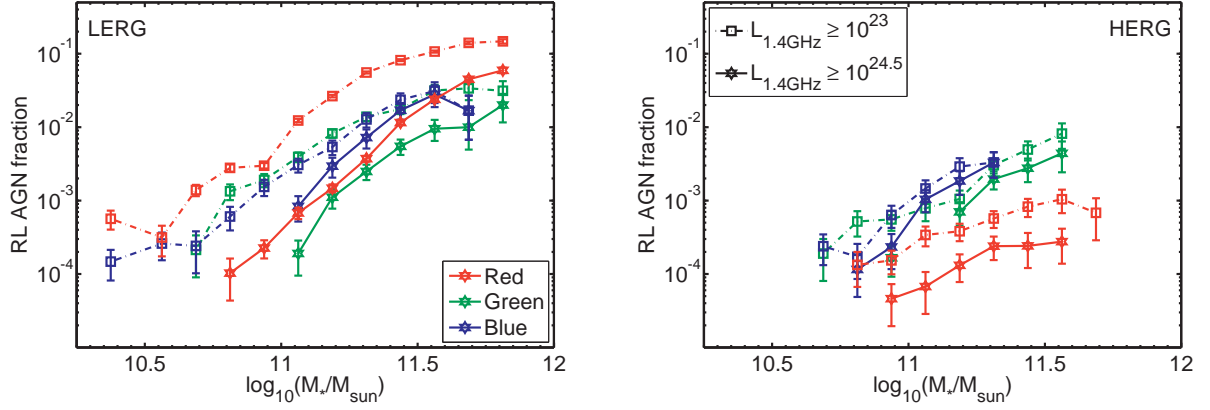


Figure 3.4: The fraction of red, green and blue galaxies hosting a LERG (left panel) or HERG (right panel) as a function of stellar mass. In both panels two radio-luminosity cuts are shown per colour. The error bars are determined by Poissonian statistics.

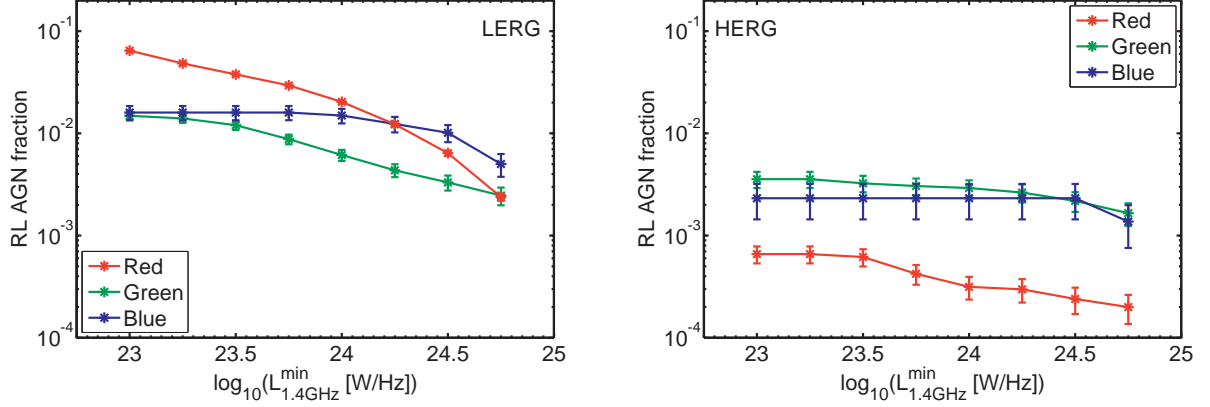


Figure 3.5: The fraction of red, green and blue galaxies with a mass $10^{11.25} \leq M_*/M_\odot \leq 10^{11.5}$, which host a LERG (left panel) or HERG (right panel), as a function of radio-luminosity cut. The error bars are determined by Poissonian statistics.

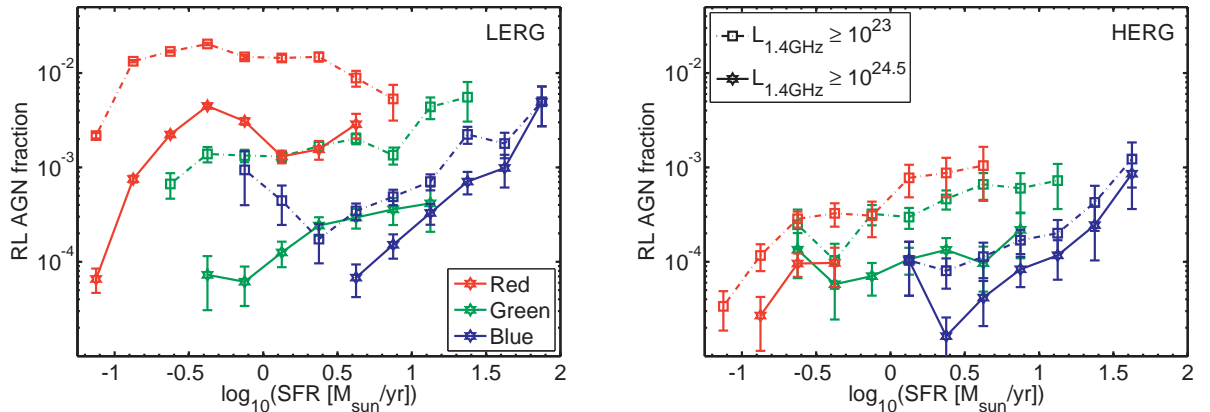


Figure 3.6: The fraction of red, green and blue galaxies hosting a LERG (left panel) or HERG (right panel) as a function of star formation rate. In both panels two radio-luminosity cuts are shown per colour. The error bars are determined by Poissonian statistics.

than $f_{RL}^{LE,blue}$. Green galaxies are less likely to host LERGs than either blue or red galaxies. In the example given above $f_{RL}^{LE,green}/f_{RL}^{LE,red} = 0.52 \pm 0.09$. Only at the highest radio-luminosity cut considered, $L_{1.4\text{GHz}} \geq 10^{24.75} \text{ W Hz}^{-1}$, is there an indication of a cross-over between $f_{RL}^{LE,red}$ and $f_{RL}^{LE,green}$. This is the result of the LERG fraction in green galaxies decreasing more slowly with increasing radio luminosity than that in red galaxies.

The right-hand panels of Fig. 3.4 and 3.5 are graphs equivalent to the left-hand panels, only for the HERG population. Fig. 3.4 shows that HERGs have a preference for galaxies with a bluer colour. The mass dependence of $f_{RL}^{HE,x}$ seems fairly similar for all three colours. However, the probability of finding a HERG in a blue or green galaxy is significantly higher than for a red galaxy, particularly at high masses. This preference is illustrated even more clearly in Fig. 3.5. For galaxies with a mass $10^{11.25} M_{\odot} < M_* < 10^{11.5} M_{\odot}$ green and blue galaxies are most likely to host a HERG. The probability of a red galaxy hosting a HERG is significantly lower at all radio luminosities. At $L_{1.4\text{GHz}}^{\min} = 10^{24} \text{ W Hz}^{-1}$ the difference in hosting probability between green and red is a factor of $f_{RL}^{HE,green}/f_{RL}^{HE,red} = 9.3 \pm 2.9$. It can also be clearly seen in the right-hand panel of Fig. 3.5 that the fraction of galaxies hosting a HERG is almost independent of radio-luminosity cut for blue and green galaxies. For the LERGs this was only observed in blue galaxies. The fraction of red galaxies hosting a HERG shows a slope, but this is significantly shallower than that of the LERG hosting fraction of red and green galaxies.

Fig. 3.6 shows the RL AGN fraction as a function of SFR and colour for LERGs (left panel) and HERGs (right panel). The fraction of blue galaxies hosting a RL AGN of either excitation increases strongly with increasing SFR. A linear least squares fit of the data at a radio luminosity cut $L_{1.4\text{GHz}} \geq 10^{24} \text{ W Hz}^{-1}$ shows $f_{RL}^{LE,blue} \propto \text{SFR}^{1.16 \pm 0.15}$ for LERGs and $f_{RL}^{HE,blue} \propto \text{SFR}^{1.24 \pm 0.27}$ for HERGs. In addition, the normalization of $f_{RL}^{y,blue}$ is fairly similar for both excitations. This similarity in slope and normalization is also found in the green galaxy population. In contrast to the blue galaxy population, the fraction of green galaxies that hosts either a HERG or a LERG hardly shows any SFR dependence. The red population does show a difference in its $f_{RL}^{y,red}(\text{SFR})$ when comparing HERG and LERG. The probability for a red galaxy to host a LERG is typically 1 to 1.5 orders of magnitude higher than it is to host a HERG. $f_{RL}^{y,red}$ generally does not depend strongly on SFR. However, if a trend had to be identified this would be increasing with SFR for the red HERG population and decreasing with SFR for the red LERG population. All these trends shown in Fig. 3.6 are largely independent of the radio-luminosity cut.

3.6 Discussion

The results presented in the previous sections generally support the ‘radio-mode’ vs ‘quasar-mode’ AGN paradigm in which RL AGN are preferentially hosted by old (red) elliptical galaxies and radio-loud quasars by younger, star forming systems [27, 28]. It is thought that the former are powered through the accretion of hot halo gas. Our results support this scenario, as LERGs of all colours show the $f_{RL}^{LE,x} \propto M_*^{2.5}$ power law, which is indicative of the accretion of hot halo gas [2]. However, additional processes must be occurring when cold gas is present inside the host galaxy. Our results indicate that the probability that one of the rare massive ($M_* > 10^{10.8} M_\odot$) blue galaxies is host to a luminous ($L_{1.4\text{GHz}} \gtrsim 10^{24.5} \text{ W Hz}^{-1}$) LERG is higher than for one of the many red galaxies with a similar mass. It is the scarceness of massive blue galaxies that results in the fact that red LERGs dominate the radio AGN population in the local Universe; this is a dominance, which can already be seen from the absolute numbers in Table 3.1. Red LERGs are ten times more numerous than either LERGs of other colours or HERGs, even at moderate radio luminosities ($L_{1.4\text{GHz}} \geq 10^{24.5} \text{ W Hz}^{-1}$). In addition, the absolute value of $f_{RL}^{LE,red}$ is generally higher than for other combination of (y, x) .

The strong SFR dependence of $f_{RL}^{LE,blue}$ found for the massive blue galaxies corroborates the idea that the enhanced probability and radio luminosity of blue LERG is the result of the presence of cold gas within the host galaxy. We speculate that this cold gas is the result of the higher cooling rates required to support the increased accretion rate needed for a more powerful AGN. This increased amount of cooling gas could result in a level of cold gas within the host that equates to a significant amount of star formation. Alternatively, the cold gas could be brought into the host galaxy through merging events or tidal interactions with nearby galaxies. This supply mechanism for cold gas is supported by a visual inspection of the SDSS images of all red, green and blue radio galaxies with a redshift $z \leq 0.1$. At least five of the 18 blue LERGs show morphological signs (such as tails) indicative of a merging event. Around 5% of the red LERGs show signs of a merging event as well. However, all these mergers are in a very early stage. This could be concluded from the fact that the two original nuclei could still be identified in all cases.

The most important result with respect to the HERGs is the completely different mass dependence compared to LERGs. The fraction of galaxies hosting a HERG follows a $f_{RL}^{HE} \propto M_*^{1.5}$ power law. This puts them, as expected, more in line with optically identified (‘quasar-mode’) AGN [7]. HERGs are thought to be accreting cold gas supplied through galaxy interactions, which is in line with the fact that $\sim 25\%$ of the HERGs at $z < 0.1$ show signs of a past merging event in their morphology. Galaxy interaction are less dependent on galaxy mass, hence the lower mass dependence of the hosting probability. However, the fact that HERGs still have some mass dependence and optically identified AGN do not, suggests a mass dependence of radio-loudness even in quasar-like states. In addition, it is worth noting that at the lowest masses consid-

ered, $10^{10.25} \leq M_*/M_\odot \leq 10^{10.5}$, the fraction of galaxies hosting a HERG and LERG is approximately equal. This is the mass range in which Tasse et al. [8] found a switch between HERG and LERG domination.

Green galaxies are generally considered to be the transitional stage when galaxies evolve from the blue cloud to the red sequence. Therefore their properties are generally expected to be at intermediate levels, smoothly connecting the properties of the blue and red galaxy population [29]. In this work we find this is not true with respect to green galaxies hosting radio galaxies of either excitation. The left-hand panels of figures 3.4 and 3.5 show that the probability of hosting a LERG of a fixed radio luminosity is lower for a green galaxy than for a red or blue galaxy of similar mass. In addition, the probability of finding a HERG in a given galaxy peaks within the green population. These results are also a clear indication that the green galaxy sample identified here is not just a mixture of poorly separated blue and red galaxies. In that case all trends would be in between those of red and blue, which is not the case. We speculate that the reduced probability of finding a LERG in a green galaxy is due AGN feedback [27]. The quasar winds and radio jets that are the result of the high-excitation AGN activity in massive blue and green galaxies will blow the remaining cold gas out of the galaxy, stopping star formation and cold gas accretion. Meanwhile, the radio jets also reheat the gas halo, which temporarily reduces the cooling flow of the halo gas to the SMBH. This effectively stops all AGN activity and allows the stellar population to age across the green valley. Only after the galaxy has reached the red sequence will the halo gas have cooled enough to re-establish the cooling flow and trigger a new episode of RL AGN activity through hot gas accretion.

3.7 Conclusion

We investigated the fraction of massive blue, green and red galaxies that are host to a RL AGN. In this we consider RL AGN that are classified as LERG separately from those classified as HERG. It is shown that:

1. RL AGN in the local Universe are dominated by LERGs. This is true even if the red, green and blue galaxy population are considered individually. The probability that a galaxy of any colour hosts a LERG follows a $f_{RL}^{LE,x} \propto M_*^{2.5}$ power law. This is much steeper than what is found for HERGs: $f_{RL}^{HE} \propto M_*^{1.5}$.
2. The probability that a red galaxy of a given mass hosts a LERG depends strongly on the applied radio luminosity cut. This radio power dependence is much weaker for HERGs of any colour and LERGs hosted by the blue galaxy population.
3. The probability that a green galaxy of a given mass is host to a LERG is lower compared to both the red and the blue galaxy population by a factor of 2–3 for

$L_{1.4\text{GHz}}^{\min} \approx 10^{24.5} \text{ W Hz}^{-1}$. The $f_{RL}^{LE,green}$ depends on $L_{1.4\text{GHz}}^{\min}$ in a similar way as $f_{RL}^{LE,red}$, but the slope is slightly weaker. However, the probability to host a HERG in a blue or green galaxy is significantly higher than it is in red galaxies. The maximum hosting probability for HERG is found for $M_* \approx 10^{11.5} M_{\odot}$ green galaxies with a typical $\text{SFR} = 3 M_{\odot}/\text{yr}$. The hosting probability of HERG decreases towards lower masses and SFR and the maximum shifts to bluer galaxies for more luminous radio sources.

4. Within the blue galaxy population the probability to host a RL AGN (both LERG and HERG) shows a $f_{RL}^{y,blue} \propto \text{SFR}$ dependence. This SFR dependence is weaker or absent in the red and green population. However, the absolute value of the hosting probability of blue galaxies is too low to have an effect on the AGN population as a whole.

These results suggest that the presence of cold gas in a galaxy enhances the probability that its SMBH becomes a luminous ($L_{1.4\text{GHz}} \geq 10^{24.5} \text{ W Hz}^{-1}$) RL AGN compared to the typical ‘model’ LERG in red elliptical galaxies. However, the presence of cold gas with the host galaxy does not automatically generate a high-excitation AGN. HERGs clearly prefer galaxies rich in cold gas and typically host luminous AGN. We speculate that feedback of this AGN activity is responsible for the reduced probability of green galaxies to host a LERG.

References

- [1] T. A. Matthews, W. W. Morgan, and M. Schmidt, *A Discussion of Galaxies Identified with Radio Sources.*, The Astrophysical Journal **140**, 35 (1964).
- [2] P. N. Best, C. R. Kaiser, T. M. Heckman, and G. Kauffmann, *AGN-controlled cooling in elliptical galaxies*, Monthly Notices of the Royal Astronomical Society **368**, L67 (2006).
- [3] R. A. Laing, C. R. Jenkins, J. V. Wall, and S. W. Unger, *Spectrophotometry of a Complete Sample of 3CR Radio Sources: Implications for Unified Models*, Astronomical Society of the Pacific Conference Series **54**, 201 (1994).
- [4] D. A. Evans, D. M. Worrall, M. J. Hardcastle, R. P. Kraft, and M. Birkinshaw, *Chandra and XMM-Newton Observations of a Sample of Low-Redshift FR I and FR II Radio Galaxy Nuclei*, The Astrophysical Journal **642**, 96 (2006).
- [5] D. Whysong and R. Antonucci, *Thermal Emission as a Test for Hidden Nuclei in Nearby Radio Galaxies*, The Astrophysical Journal **602**, 116 (2004).

- [6] C. Tadhunter, T. G. Robinson, R. M. González Delgado, K. Wills, and R. Morganti, *Starbursts and the triggering of the activity in nearby powerful radio galaxies*, Monthly Notices of the Royal Astronomical Society **356**, 480 (2005).
- [7] P. N. Best, G. Kauffmann, T. M. Heckman, J. Brinchmann, S. Charlot, et al., *The host galaxies of radio-loud active galactic nuclei: mass dependences, gas cooling and active galactic nuclei feedback*, Monthly Notices of the Royal Astronomical Society **362**, 25 (2005).
- [8] C. Tasse, P. N. Best, H. Röttgering, and D. Le Borgne, *Radio-loud AGN in the XMM-LSS field. II. A dichotomy in environment and accretion mode?*, Astronomy & Astrophysics **490**, 893 (2008).
- [9] R. C. Hickox, C. Jones, W. R. Forman, S. S. Murray, C. S. Kochanek, et al., *Host Galaxies, Clustering, Eddington Ratios, and Evolution of Radio, X-Ray, and Infrared-Selected AGNs*, The Astrophysical Journal **696**, 891 (2009).
- [10] P. N. Best and T. M. Heckman, *On the fundamental dichotomy in the local radio-AGN population: accretion, evolution and host galaxy properties*, Monthly Notices of the Royal Astronomical Society **421**, 1569 (2012).
- [11] D. G. York, J. Adelman, J. E. Anderson Jr., S. F. Anderson, J. Annis, et al., *The Sloan Digital Sky Survey: Technical Summary*, The Astronomical Journal **120**, 1579 (2000).
- [12] C. Stoughton, R. H. Lupton, M. Bernardi, M. R. Blanton, S. Burles, et al., *Sloan Digital Sky Survey: Early Data Release*, The Astronomical Journal **123**, 485 (2002).
- [13] I. Strateva, Ž. Ivezić, G. R. Knapp, V. K. Narayanan, M. A. Strauss, et al., *Color Separation of Galaxy Types in the Sloan Digital Sky Survey Imaging Data*, The Astronomical Journal **122**, 1861 (2001).
- [14] K. N. Abazajian, J. K. Adelman-McCarthy, M. A. Agüeros, S. S. Allam, C. Allende Prieto, et al., *The Seventh Data Release of the Sloan Digital Sky Survey*, The Astrophysical Journal Supplement Series **182**, 543 (2009).
- [15] J. J. Condon, W. D. Cotton, E. W. Greisen, Q. F. Yin, R. A. Perley, et al., *The NRAO VLA Sky Survey*, The Astronomical Journal **115**, 1693 (1998).
- [16] R. H. Becker, R. L. White, and D. J. Helfand, *The FIRST Survey: Faint Images of the Radio Sky at Twenty Centimeters*, The Astrophysical Journal **450**, 559 (1995).
- [17] J. Brinchmann, S. Charlot, S. D. M. White, C. Tremonti, G. Kauffmann, et al., *The physical properties of star-forming galaxies in the low-redshift Universe*, Monthly Notices of the Royal Astronomical Society **351**, 1151 (2004).

-
- [18] M. A. Strauss, D. H. Weinberg, R. H. Lupton, V. K. Narayanan, J. Annis, et al., *Spectroscopic Target Selection in the Sloan Digital Sky Survey: The Main Galaxy Sample*, The Astronomical Journal **124**, 1810 (2002).
- [19] G. Kauffmann, T. M. Heckman, S. D. M. White, S. Charlot, C. Tremonti, et al., *Stellar masses and star formation histories for 10^5 galaxies from the Sloan Digital Sky Survey*, Monthly Notices of the Royal Astronomical Society **341**, 33 (2003).
- [20] G. Kauffmann, T. M. Heckman, S. D. M. White, S. Charlot, C. Tremonti, et al., *The dependence of star formation history and internal structure on stellar mass for 10^5 low-redshift galaxies*, Monthly Notices of the Royal Astronomical Society **341**, 54 (2003).
- [21] P. N. Best, G. Kauffmann, T. M. Heckman, and Ž. Ivezić, *A sample of radio-loud active galactic nuclei in the Sloan Digital Sky Survey*, Monthly Notices of the Royal Astronomical Society **362**, 9 (2005).
- [22] J. A. Baldwin, M. M. Phillips, and R. Terlevich, *Classification parameters for the emission-line spectra of extragalactic objects*, Publications of the Astronomical Society of the Pacific **93**, 5 (1981).
- [23] G. Kauffmann, T. M. Heckman, and P. N. Best, *Radio jets in galaxies with actively accreting black holes: new insights from the SDSS*, Monthly Notices of the Royal Astronomical Society **384**, 953 (2008).
- [24] M. L. Balogh, S. L. Morris, H. K. C. Yee, R. G. Carlberg, and E. Ellingson, *Differential Galaxy Evolution in Cluster and Field Galaxies at $z \sim 0.3$* , The Astrophysical Journal **527**, 54 (1999).
- [25] M. Schmidt, *Space Distribution and Luminosity Functions of Quasi-Stellar Radio Sources*, The Astrophysical Journal **151**, 393 (1968).
- [26] J. V. Wall and C. R. Jenkins, *Practical Statistics for Astronomers*, Cambridge University Press, Cambridge, UK (2003).
- [27] D. J. Croton, V. Springel, S. D. M. White, G. De Lucia, C. S. Frenk, et al., *The many lives of active galactic nuclei: cooling flows, black holes and the luminosities and colours of galaxies*, Monthly Notices of the Royal Astronomical Society **365**, 11 (2006).
- [28] M. J. Hardcastle, D. A. Evans, and J. H. Croston, *Hot and cold gas accretion and feedback in radio-loud active galaxies*, Monthly Notices of the Royal Astronomical Society **376**, 1849 (2007).
- [29] D. C. Martin, T. K. Wyder, D. Schiminovich, T. A. Barlow, K. Forster, et al., *The UV-Optical Galaxy Color-Magnitude Diagram. III. Constraints on Evolution from the Blue to the Red Sequence*, The Astrophysical Journal Supplement Series **173**, 342 (2007).

Chapter 4

Morphology of radio-loud AGN hosted by massive blue galaxies

4.1 Introduction

Radio galaxies are hosted by massive red elliptical galaxies; this has been a classical paradigm in astronomy since at least Moffet’s ARA&A article in 1966 [1]. But to what extent is that an accurate assessment? We know that radio-luminous galaxies are typically massive [e.g. 2] and that spiral galaxies are much less common at high mass [e.g. 3]. Furthermore, there are some radio galaxies, Centaurus A being a particularly prominent example, which are disturbed but the overall structure is often elliptical in nature [4]. This raises the question if the classical picture is just a reflection of the dearth of massive spiral galaxies.

As first pointed out by Laing et al. [5], the radio galaxy population appears to fall into two fairly well-defined classes: high-excitation radio galaxies (HERGs) and low-excitation radio galaxies (LERGs). The former correspond to Active Galactic Nuclei (AGN) with a high accretion rate. HERGs are often referred to as ‘quasar-mode’ or ‘radiative-mode’ AGN and follow the orientation-based AGN unification scheme [6]. HERGs typically reside in blue star forming galaxies at the massive end of the main sequence of star formation, indicating that there is star formation associated with the radio activity [7]. HERGs dominate the radio-loud AGN population at high radio luminosities.

In contrast, the LERGs are predominantly located in massive red elliptical galaxies and dominate at low radio luminosities. They are thought to be triggered by the slow accretion of hot halo gas [e.g. 8]. Because this mode of accretion is radiatively inefficient, LERG lack the emission lines as well as the X-ray and infrared emission generally

Based upon the observation proposals W13AN019 and W14AN024 by R. M. J. Janssen, H. J. A. Röttgering, P. N. Best and J. Brinchmann, and the observational results of these proposals.

associated with AGN. As such, they only have a clear AGN signature in the form of a radio jet and as a result are often referred to as ‘radio-mode’ or ‘jet-mode’ AGN.

Until recently, samples of these classes of radio galaxies were small, limiting statistical studies. This has now changed; by combining all-sky optical (SDSS) and radio (NVSS and FIRST) surveys Best and Heckman [7] have been able to create a large sample of both HERGs and LERGs. Janssen et al. [9] used this sample to perform a statistical analysis on the hosting probability as a function of host galaxy stellar mass, star formation rate, radio luminosity and colour. Due to the large size of the sample Janssen et al. [9] were able to identify a population of blue galaxies hosting a jet-mode AGN. The fraction of blue galaxies hosting a radio-mode AGN depends on the host galaxy mass as $f_{\text{BLERG}} \propto M_*^{2.5}$. This mass dependence is the same for LERGs hosted by red galaxies. The power law is thought to be the result of the accretion of hot halo gas to power the AGN [8]. This suggests that the primary gas source of blue LERGs is hot halo gas. However, these blue LERGs also show an enhanced radio luminosity with respect to red LERGs at the same galaxy mass, which suggests an enhanced gas flow to the super-massive black hole. Janssen et al. [9] found that at least 10% of the blue galaxies hosting a LERG at $z < 0.1$ appears to have tails or other signs of recent interaction, which suggest that galaxy interactions are responsible for the enhanced gas flow. However, these conclusions were not very robust, because 90% of their sample of blue LERGs reside at higher redshift ($\langle z \rangle \sim 0.18$). Furthermore, the SDSS images are too shallow and with too poor seeing to accurately trace the light profile and classify the majority of galaxies in their sample into spirals or ellipticals on the basis of a Sersic index. This is particularly true, if there are strong point sources in the objects as there might be in the presence of an AGN.

We propose four hypotheses that explain the nature of these blue jet-mode AGN:

1. Blue LERGs are hosted by massive spiral galaxies where the (relatively) blue colours reflect the on-going star formation in their disks.
2. Blue LERGs are hosted by massive ellipticals with an enhanced halo cooling, which also increases their star formation with respect to their red counterparts.
3. Blue LERGs have undergone a recent merging event that has brought additional gas into these blue galaxies to trigger star formation and enhanced AGN activity.
4. Blue LERGs have young radio jets, which are still actively interacting with the gas inside the host galaxy. This positive feedback enhances the star formation in the host galaxy regardless of the host galaxy’s optical morphology.

Comparing the optical and radio morphology of jet-mode AGN in massive blue galaxies to those in massive red galaxies and radio-quiet blue galaxies will be the key to distinguishing between these scenarios. If we detect extended tails or a disturbed morphology in the majority of the blue radio galaxies, mergers are a likely source of gas,

while a smooth light profile with a high Sersic index would indicate that the galaxies are structurally ellipticals despite their blue colours.

In this Chapter we will present preliminary results that investigate the optical and radio morphology of blue radio galaxies. In Sect. 4.2 we present the overall sample of local radio galaxies and inactive galaxies. To get a better image of the contribution of merger signatures, we have a subsample of blue radio galaxies for which deep observations from SDSS Stripe 82 [10], NOAO Deep Wide Field Survey (NDWFS) [11], the Kilo Degree Survey (KiDS) [12] and the Canada-France-Hawaii Telescope Legacy Survey (CFHTLS)¹ [13] are available. While these surveys provide plenty of galaxies for our reference samples (red radio galaxies and blue inactive galaxies) they only contain 16 jet-mode AGN in a massive blue galaxies. Therefore we have taken additional deep optical images of blue LERGs using the Prime Focus Imaging Platform on the 4.2 m William Herschel Telescope. These deep observations are found in Sect. 4.3. In Sect. 4.4 we will investigate the optical morphology of both the entire sample and the deep observations. In Sect. 4.5 we will perform a preliminary investigation of the radio morphologies based on radio images from the Faint Images of the Radio Sky at Twenty centimetres survey (FIRST) [14]. We will discuss the current weaknesses of these initial results presented in this Chapter in Sect. 4.6 and suggest further work. We will draw some preliminary conclusions in Sect. 4.7 and compare these to our hypotheses.

Throughout this Chapter we assume the cosmological parameters $H_0 = 70 \text{ km s}^{-1} \text{ Mpc}^{-1}$, $\Omega_m = 0.3$, and $\Omega_\Lambda = 0.7$. The radio spectral index, α , is defined as $S_\nu \propto \nu^{-\alpha}$ and taken as $\alpha = 0.8$ where necessary.

4.2 Jet-mode AGN hosted by blue galaxies

Following Janssen et al. [9, J12 hereafter] we use the sample of radio-loud AGN defined by Best and Heckman [7, BH12 hereafter] as the basis for our investigation. The BH12 sample was constructed by cross-comparing the positions of galaxies in the seventh data release (DR7) [15] of the SDSS spectroscopic sample with data from the National Radio Astronomy Observatory (NRAO) Very Large Array (VLA) Sky Survey (NVSS) [16] and FIRST [14]. The optical parent sample consists of all galaxies in the value-added spectroscopic catalogues (VASC) created by the Max Planck Institute for Astrophysics and Johns Hopkins University group [17]. These objects are either targets from the SDSS main galaxy sample [18] with a usable spectrum, or QSOs with a spectrum that is clearly dominated by the emission of stars in the host galaxy. For each galaxy the VASC contains a number of derived quantities such as the stellar mass, M_* , and star formation rate, SFR [3, 19]. Within the 927522 galaxies of the VASC, Best and Heckman [7] identified over 10000 radio-loud AGN. Of these radio-loud AGN 9863 sources are

¹<http://www.cfht.hawaii.edu/Science/CFHLS/>

classified as LERGs and 481 as HERGs using emission line properties. In addition to these classifications, we define all galaxies from the VASC not classified as a radio-loud AGN as inactive or radio quiet.

In order to get a morphological classification for a large part of our sample we combine the VASC with the results of Galaxy Zoo 1 (GZ1) [20]. Galaxy Zoo is a citizen science project in which the general public is asked to assist in the classification of galaxies observed by SDSS. For every galaxy in SDSS DR6 votes were collected for either an elliptical morphology, various spiral morphologies or merger indications. We match the data in Table 2 of the GZ1 data release [21] to the VASC using the sky positions of the sources in both catalogues and a 5 arcsec matching radius. We find morphological information for 703065 galaxies. The main reason that ~ 200000 galaxies do not have a morphological classification from GZ1 is that the VASC uses SDSS DR7 whereas GZ1 is based upon DR6. We find 863 sources in the VASC with two potential matches in the GZ1 data. These are generally the result of duplicate observations by SDSS or multiple observations of very nearby galaxies. Given that both instances in GZ1 are classified using the same image their voting fractions are extremely similar. As such we take the nearest of the two instances.

We define our blue LERG sample as all spectroscopically classified LERGs, which are hosted by a blue galaxy at $0.03 < z < 0.3$ with a morphological entry in GZ1. Here we define a galaxy as blue if their 4000 Å break value [22] is $D_{n4000} < 1.45$ (see J12). Our total blue LERG sample contains 138 sources, all of which have a host galaxy mass in the range $10^{10.25} < M_* < 10^{12.0} M_\odot$.

We compare the morphology of these blue LERGs to a matched sample of red LERGs and inactive blue galaxies. Here red is defined as $D_{n4000} > 1.70$. Both samples are constrained to the same redshift and mass range as the blue LERG sample. We have GZ1 entries for 5464 and 109454 sources in the total red LERG and blue galaxy sample, respectively. There are many correlations between galaxy properties and their stellar mass. Furthermore, Best and Heckman [7] showed that the key parameter for radio-loud AGN is the Eddington-scaled accretion rate, which for LERGs scales with the radio luminosity per unit stellar mass. Therefore, we also define matched samples of red LERGs and blue galaxies. This enables a fair comparison between the blue LERG population and the comparison samples. Redshift is included as more distant objects will appear smaller and as such are more readily classified as elliptical galaxies or radio point sources. Following Pace and Salim [23] we select for every blue LERG the best matches in the inactive blue galaxy population using the metric

$$R = \sqrt{\left(\frac{\Delta z}{\sigma(z)}\right)^2 + \left(\frac{\Delta \log_{10}(M_*)}{\sigma(\log_{10}(M_*))}\right)^2 + \left(\frac{\Delta D_{n4000}}{\sigma(D_{n4000})}\right)^2} \quad (4.1)$$

Here Δ indicates the difference between the properties of the blue LERGs and the candidates from the control sample. σ is the standard deviation in the given quantity from the combined blue LERG and control sample. For each blue LERG the 10 candi-

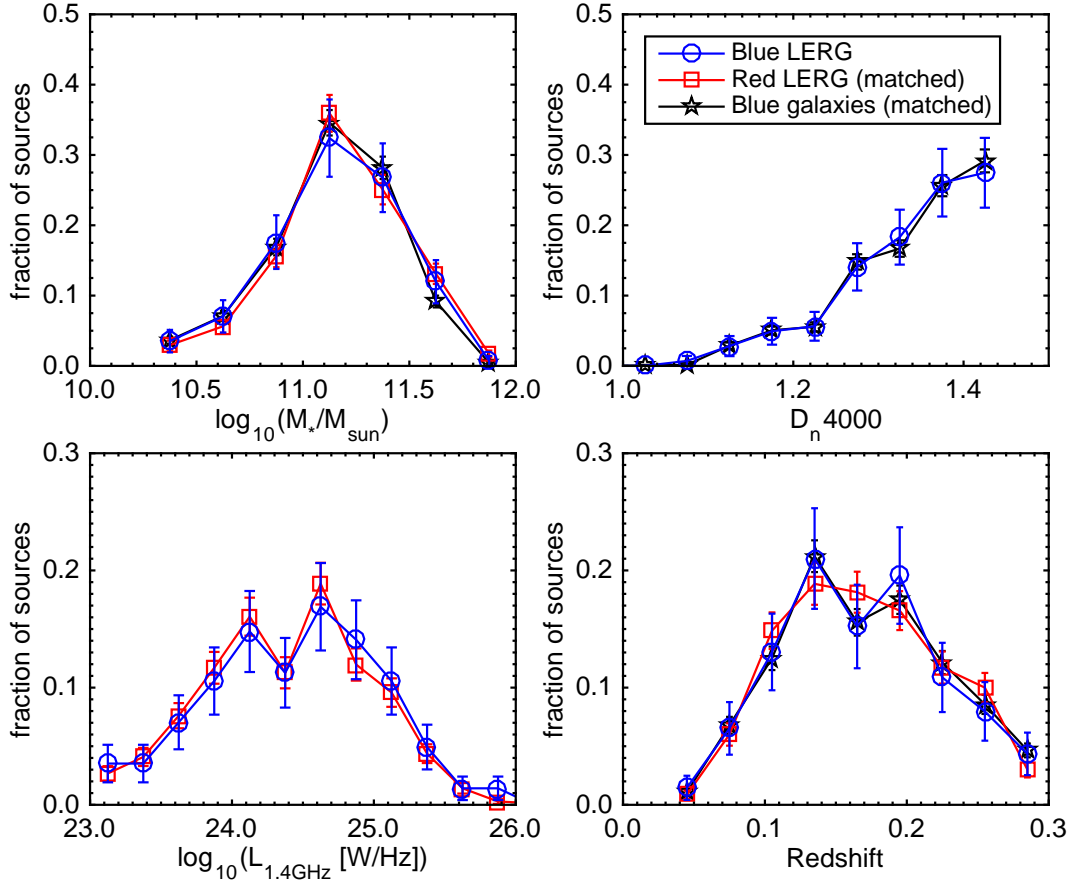


Figure 4.1: The fraction of blue LERGs (blue) as a function of host galaxy stellar mass, 4000 Å break value, radio luminosity and redshift. The same distribution is shown for the matched samples of red LERGs (red) and blue inactive galaxies (black). 1σ Poissonian errors are shown in all distributions. We observe that the distributions of the matched samples are identical (within the error bars) to that of the blue LERG for all parameters.

date blue inactive galaxies with the lowest R are selected for the matched sample. For every blue LERG 5 red LERGs are selected following the same procedure. However, $\log_{10}(L_{1.4\text{GHz}})$ is used instead of $D_n 4000$.

Fig. 4.1 shows the distribution of the blue LERGs and two matched samples in stellar mass, 4000 Å break value, radio luminosity and redshift. This figure clearly shows the success of the matching procedure. In all 4 parameters the distribution of the matched samples is within 1σ of distribution set by the blue LERGs.

4.3 Deep optical imaging

In order to properly identify the optical morphology of LERGs at a redshift $z > 0.1$ deeper observations are required than those available from the SDSS. This is especially

true for signatures of galaxy interactions. GZ1 does have an option to vote for mergers. However, in addition to the difficulty of seeing merger signatures in SDSS images, people are hesitant to vote for such an exclusive category. As a result, GZ1 underestimates the number of mergers. Genuine mergers are found in galaxies that have merger vote fractions as low as 20% [24, 25].

We have obtained deep optical imaging for 16 blue LERGs of the BH12 sample from four deep imaging surveys: SDSS Stripe 82 [10], NOAO Deep Wide Field Survey (NDWFS) [11], the Kilo Degree Survey (KiDS) [12] and the Canada-France-Hawaii Telescope Legacy Survey (CFHTLS)¹ [13]. Table 4.1 lists the number of blue and red LERGs identified in their respective survey area. For reference, the number of red and blue LERGs in the complete BH12 sample is given as well. The r-band image of the blue LERGs from these four surveys are shown in Fig. 4.2 to 4.4.

As can be seen in Table 4.1 the deep surveys provide plenty of galaxies for the two reference samples (red radio galaxies and blue inactive galaxies). However, they only contain 16 massive blue LERGs. To supplement the subsample of blue LERGs with deep imaging in public surveys we have obtained 6 dark nights of observation time on the William Herschel Telescope (WHT) in May 2013 (2 nights, proposal W13AN019) and March 2014 (4 nights, proposal W14AN024). Unfortunately, the second run was completely lost due to bad weather. In addition, the first run suffered from heavy cloud coverage, which severely limited our effective observation time. Nevertheless, usable data was obtained for 8 sources. Each of these sources was observed using the WHT Prime Focus Imaging Platform (PFIP) and the TAURUS T6273 r-band filter. This filter was chosen because it allowed the largest field of view and could achieve the deepest images in the shortest amount of time. This large field of view would also allow us to do photometric calibration with sources in the field of view while using SDSS as a

Table 4.1: The number of blue and red LERGs from the BH12 sample found in the 4 deep imaging surveys used in this work. The number of inactive blue galaxies (VASC) that are covered by these surveys is given as well. In the final row the number of blue LERGs for which usable data was obtained during the observation nights at the WHT is given. For reference the number of inactive blue galaxies (VASC), red LERGs and blue LERGs in the complete BH12 sample is given in the top row.

Survey	blue LERG	red LERG	inactive blue galaxies	reference
BH12 - SDSS	138	5464	109454	[7]
SDSS Stripe 82	4	140	3994	[10]
NDWFS	1	8	112	[11]
KiDS	6	106	2121	[12]
CFHTLS-Wide ¹	5	34	652	[13]
WHT observations	8	0	0	this work

reference. Our aim was to achieve a 1σ surface brightness of $26.7 \text{ mag/arcsec}^2$ in 30 minutes of observation time per source. This image depth is approximately two magnitudes deeper than the regular SDSS and comparable to the SDSS Stripe 82 co-added data [26]. The latter would enable us to use red LERGs and inactive blue galaxies from SDSS Stripe 82 as a reference sample without introducing a bias due to different image depths.

We have observed the 8 sources between 1000 and 2340 seconds depending on weather conditions. Sub-exposures of 3 or 6 minutes were used following a quincunx dither pattern of 1.5 arcmin on the side. All images were corrected using a master bias and master flat field. These were constructed using a series of 12 bias frames and 12 flat fields taken during dusk. The corrected sub-exposures were stacked using the Astromatic² software tools SExtractor [27], SWARP [28] and SCAMP [29]. R-band imaging data obtained from the regular SDSS DR7 was used as a reference in order to obtain a world coordinate system for our observations. For all deep imaging data (both WHT observations and survey data) a 1.5 arcmin square image was extracted and visualized using STIFF [30]. These images are shown in Fig. 4.2 to 4.5. For two of the SDSS Stripe 82 sources (Fig. 4.2(b,d)) an image with improved contrast was manually created using SAOimage³ DS9. This was done to compensate for a very bright source in the 1.5 arcmin field of view. The reason some cuts came out rectangular is unclear at this moment. The long edge is 1.5 arcmin and the short edge has been cut smaller by the software. It is confirmed that no image distortion has taken place.

4.4 Optical morphology

Following Bamford et al. [31] we interpret the debiased vote fractions of GZ1 as the probability, p_x , that a source has a spiral, $x = \text{S}$, or elliptical, $x = \text{E}$, morphology. Fig. 4.6 shows the mean probability, $P_x = \text{mean}(p_x)$, for blue LERGs, red LERGs and inactive blue galaxies to be a spiral or elliptical galaxy as a function of galaxy mass. The uncertainty on the mean is determined from the standard deviation in p_x divided by the square root of the number of sources in each mass bin. Each mass bin is 0.25 dex wide. The most massive bin is not shown, as it only contains a single blue LERG (in an elliptical host).

It is clear from Fig. 4.6 that the morphology of blue LERG differs from the matched comparison samples. At high masses ($M_* > 10^{11} M_\odot$) the fraction of blue LERGs in elliptical galaxies is at least 0.2 higher than an inactive blue galaxy. Both P_{spiral} and $P_{\text{elliptical}}$ of the blue and red LERGs are within 2σ of each other at these high masses. At lower masses the blue LERGs seem to be a mixed population with similar fractions

²<http://www.astromatic.net/>

³<http://ds9.si.edu/site/Home.html>

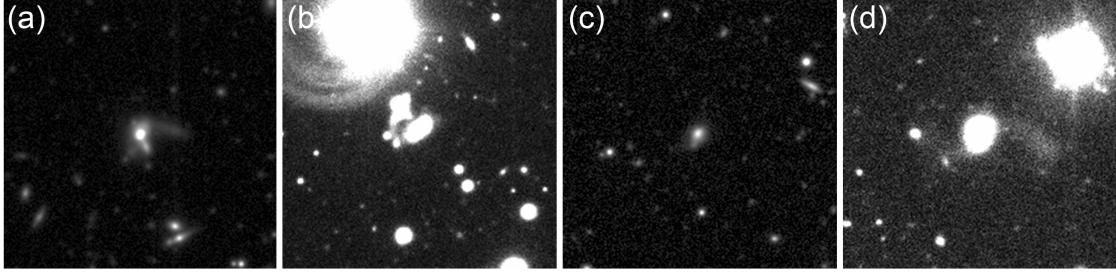


Figure 4.2: Deep r-band observations for 4 LERG obtained from SDSS Stripe 82. Each subfigure is a 1.5 arcmin on the side and centred on the blue host galaxy. The contrast in images (b) and (d) had to be manually adjusted due to presence of a bright source. Detailed information of each galaxy can be found in Table 4.2.

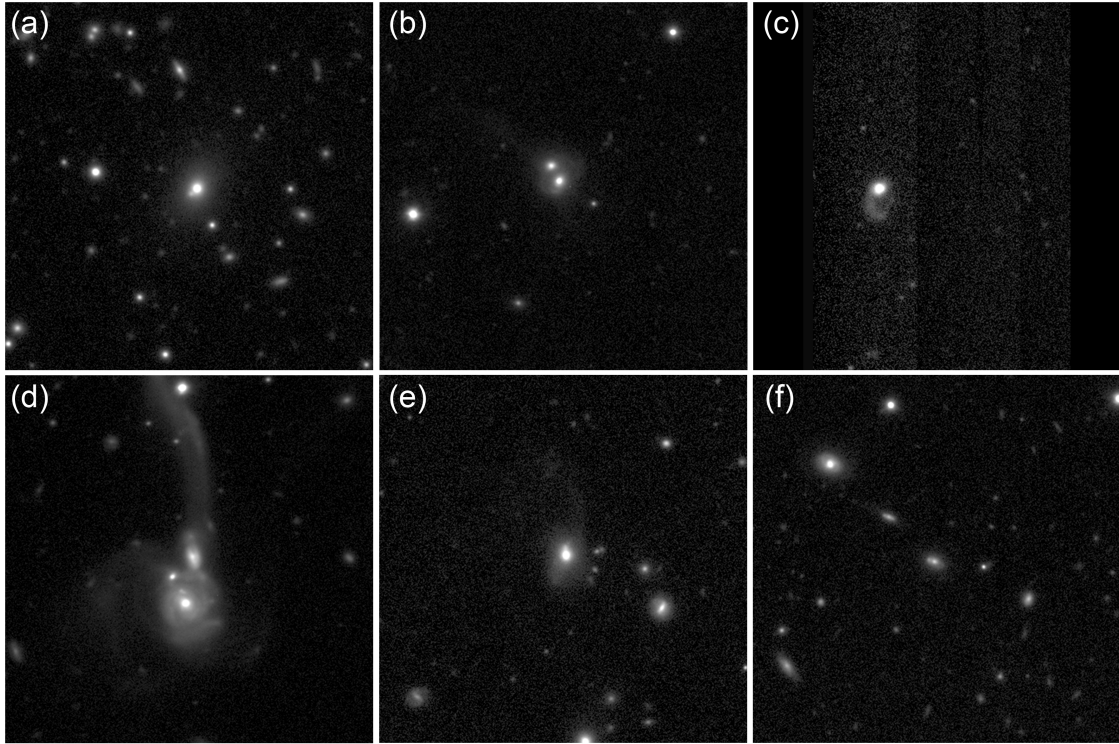


Figure 4.3: Deep r-band observations for 6 LERG obtained from the Kilo Degree Survey. Each subfigure is a 1.5 arcmin on the side and centred on the blue host galaxy. Detailed information of each galaxy can be found in Table 4.2.

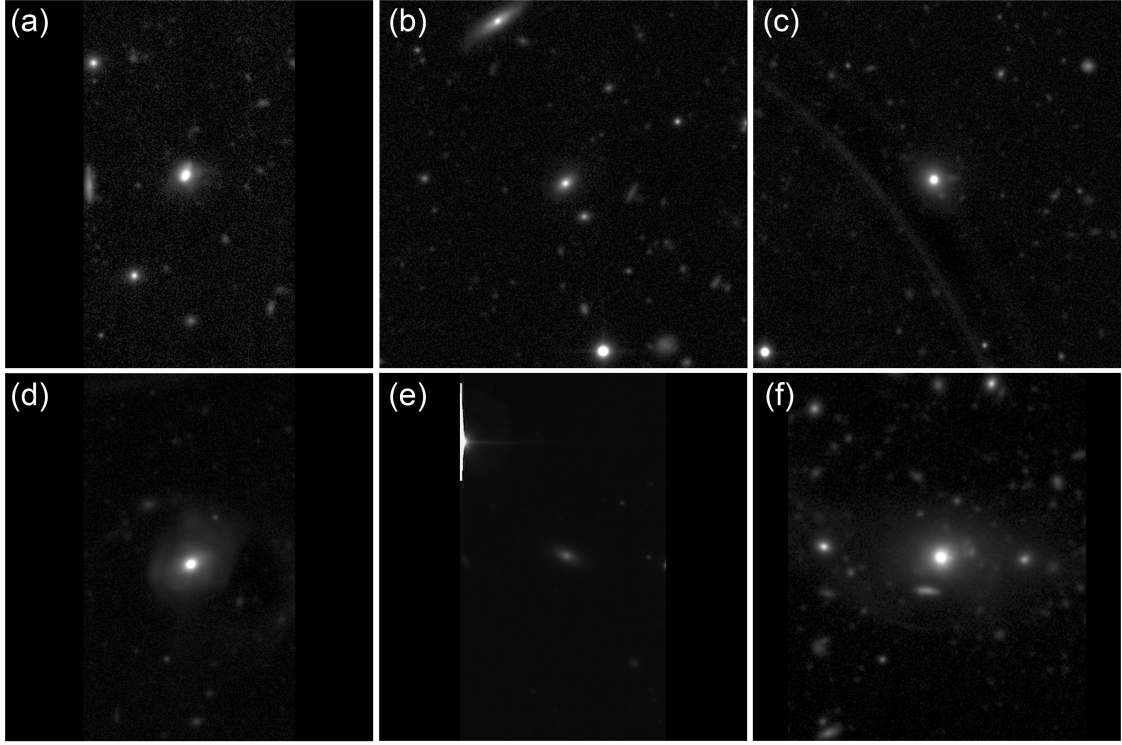


Figure 4.4: Deep r-band observations for 5 LERG obtained from the Wide CFHT Legacy Survey (a–e) as well as 1 LERG from the NOAO Deep Wide Field Survey (f). Each subfigure is a 1.5 arcmin on the side and centred on the blue host galaxy. Detailed information of each galaxy can be found in Table 4.2.

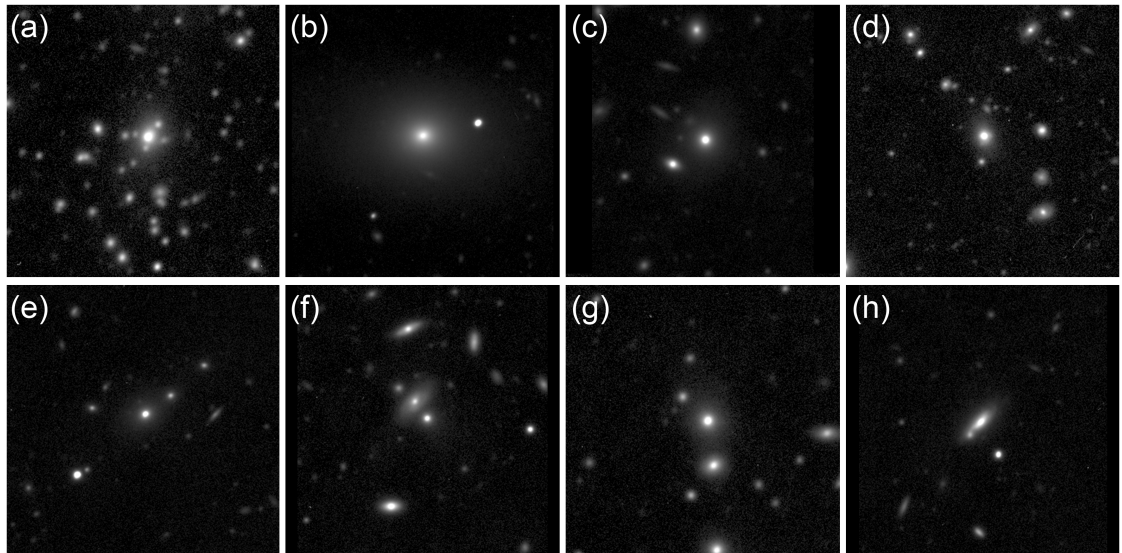


Figure 4.5: Deep r-band observations for 8 LERG obtained using the WHT PFIP. Each subfigure is a 1.5 arcmin on the side and centred on the blue host galaxy. Detailed information of each galaxy can be found in Table 4.2.

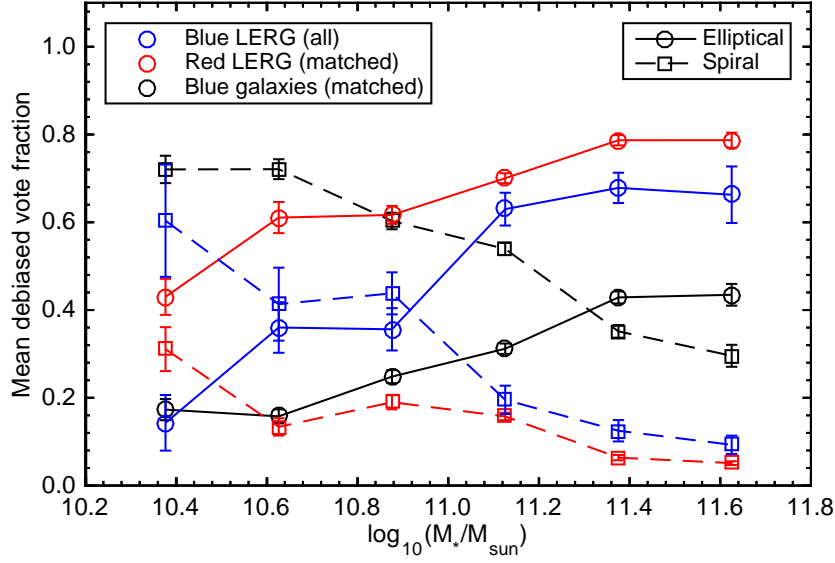


Figure 4.6: The fraction of blue LERGs (blue), red LERGs (red) and inactive blue galaxies (black) with an elliptical (circles, solid line) or spiral morphology (squares, dashed line) as a function of galaxy mass. Both the sample of inactive galaxies and red LERGs have been matched in mass, redshift and either colour or radio luminosity to the sample of blue LERGs. The 1σ statistical error is given for all data points.

(both $\sim 40\%$) of spirals and ellipticals. Red LERGs have a high ($> 60\%$) fraction of ellipticals and blue inactive galaxies a high ($> 60\%$) fraction of spirals at these masses. As an initial indication, we use the raw votes for GZ1 to determine the fraction of mergers for our three samples. Blue LERGs have a fraction of mergers $P_{\text{merger}} = 0.077 \pm 0.012$ with respect to the comparison samples: $P_{\text{merger}} = 0.063 \pm 0.005$ for red LERGs and $P_{\text{merger}} = 0.064 \pm 0.004$ for inactive blue galaxies. The fraction of mergers in blue LERGs is slightly higher compared to the matched samples, but the difference is not significant. However as stated earlier, GZ1 votes are for various reasons unreliable in the identification of mergers.

Inspection of the deep imaging of blue LERGs in Fig. 4.2 to 4.5 shows tails, bridges or a disturbed morphology in at least 10 out of the 24 sources. A summary of the visual morphological classification of these 24 sources can be found in Table 4.2. This table also lists the origin of their image, host galaxy mass, radio luminosity, redshift and the subfigure in which their image is shown. The sources are listed in order of decreasing host galaxy mass. Inspection of Table 4.2 supports our earlier finding that (especially at high masses, $M_* > 10^{11} M_{\odot}$) a large fraction of the blue LERGs is hosted by a galaxy, which is elliptical in nature. Merger signatures on the other hand, seem to be more common at $M_* \lesssim 10^{11.2} M_{\odot}$.

Table 4.2: An overview of the 24 blue LERGs for which deep imaging data has been collected. For each blue LERG the source of the deep image (as noted in the final column), host galaxy mass, M_* , radio luminosity, $L_{1.4\text{GHz}}$, redshift and r-band morphology are listed. The direction of tidal tails is indicated using the wind directions, where north is up in the shown image. The r-band morphology is split into overall galaxy morphology and signatures of galaxy interaction. The blue LERGs are organized in order of descending M_* .

Name	Survey	M_* [M_\odot]	$L_{1.4\text{GHz}}$ [W Hz^{-1}]	Redshift	Morphology	Interaction	Figure
BLERG210p3	WHT	$10^{11.70}$	$10^{24.85}$	0.252	Elliptical / Bulgy Spiral	No, brightest cluster galaxy	4.5(a)
BLERG182p22	WHT	$10^{11.59}$	$10^{24.95}$	0.065	Elliptical	No	4.5(b)
BLERG208p38	WHT	$10^{11.50}$	$10^{24.72}$	0.216	Elliptical	No	4.5(c)
BLERG134p2	KiDS	$10^{11.45}$	$10^{25.32}$	0.281	Elliptical	Second nucleus (?)	4.3(a)
BLERG140p1	KiDS	$10^{11.39}$	$10^{24.51}$	0.262	Elliptical	Double nucleus, tail to NW	4.3(b)
BLERG178p11	WHT	$10^{11.36}$	$10^{24.78}$	0.284	Elliptical	No	4.5(d)
BLERG175p15	WHT	$10^{11.34}$	$10^{25.08}$	0.244	Elliptical	No	4.5(e)
BLERG227p27	WHT	$10^{11.30}$	$10^{24.91}$	0.270	Elliptical	No, nearby spiral	4.5(f)
BLERG202p12	WHT	$10^{11.27}$	$10^{24.80}$	0.204	Elliptical	No	4.5(g)
BLERG170p28	WHT	$10^{11.26}$	$10^{24.72}$	0.113	Spiral	Tail to second core	4.5(h)
BLERG213p55	CFHTLS	$10^{11.17}$	$10^{25.48}$	0.282	Irregular	Various tails	4.4(a)
BLERG34m9	CFHTLS	$10^{11.09}$	$10^{24.57}$	0.217	Elliptical / Bulgy Spiral	No	4.4(b)
BLERG176p1	KiDS	$10^{11.03}$	$10^{24.53}$	0.245	Elliptical	Big tail to S	4.3(c)
BLERG32m1	S82	$10^{11.00}$	$10^{24.20}$	0.176	Irregular	Three tails	4.2(a)
BLERG219p35	NDWFS	$10^{10.98}$	$10^{23.92}$	0.129	Elliptical	No	4.4(f)
BLERG32m10	CFHTLS	$10^{10.91}$	$10^{24.20}$	0.166	Elliptical	Tail to E (?)	4.4(c)
BLERG321m0	S82	$10^{10.91}$	$10^{24.04}$	0.183	Bulgy Spiral	Bridge to second galaxy	4.2(b)
BLERG330m0	S82	$10^{10.76}$	$10^{23.81}$	0.205	Elliptical	Tail to SSW (?)	4.2(c)
BLERG212p55	CFHTLS	$10^{10.70}$	$10^{23.16}$	0.089	Elliptical	Distorted outer halo	4.4(d)
BLERG177m3	KiDS	$10^{10.68}$	$10^{23.68}$	0.123	Spiral	Multiple galaxies, big tails	4.3(d)
BLERG176p2	KiDS	$10^{10.60}$	$10^{25.24}$	0.132	Elliptical	Asymmetric, tail to N	4.3(e)
BLERG136p3	KiDS	$10^{10.54}$	$10^{25.01}$	0.277	Spiral	No	4.3(f)
BLERG7p1	S82	$10^{10.51}$	$10^{24.83}$	0.104	Elliptical	Two tails to E & W	4.2(d)
BLERG217p56	CFHTLS	$10^{10.35}$	$10^{23.35}$	0.081	Spiral	No	4.4(e)

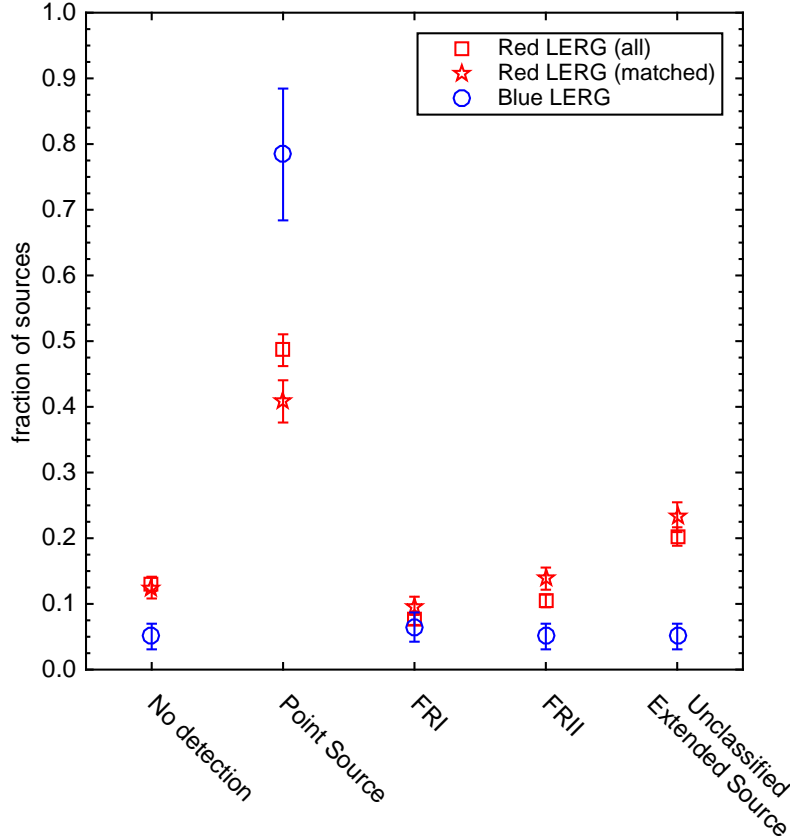


Figure 4.7: The fraction of LERG in blue host galaxies (blue) with a given radio morphology as classified using images from FIRST. For comparison the complete and matched sample of LERGs in red host galaxies (red) are shown. 1σ Poissonian errors are shown for all fractions. We observe a significant increase of point sources in the LERGs with blue hosts.

4.5 Radio morphology

To investigate the radio morphology of our LERG sample we have used the images provided by FIRST [14]. For all radio sources in the BH12 sample we retrieved an image of a $6.0' \times 6.0'$ region (200×200 pixels) around the position of the host galaxy from the FIRST Cutout Server⁴. Based on these images the radio galaxies are manually classified as point sources or extended sources. If possible, extended sources were classified as Fanaroff-Riley (FR) type 1 or 2 [32]. We have classified 139 blue LERGs and 1234 red LERGs. Following the methodology described in Sect. 4.2 we have constructed a new matched sample of red LERGs, which contains 4 candidate red LERGs with a classified radio morphology for each blue LERG. Due to the lower number of available red LERGs the matching quality is slightly worse than that shown in Fig. 4.1. In particular the blue LERGs have a slightly higher $L_{1.4\text{GHz}}$ and the red LERGs a slightly higher M_* . However, the differences remain within 2σ Poissonian errors.

⁴<http://third.ucllnl.org/cgi-bin/firstcutout>

Fig. 4.7 shows the fraction of blue and red LERGs classified as point source or extended source. The errors were calculated using Poissonian statistics. Blue LERG are twice more likely to be a point source compared to the matched red LERG sample. This reduces all types of extended sources to a $\sim 5\%$ level, with the exception of FRI. These results also hold when the fraction of point sources is considered as a function of host galaxy mass.

4.6 Discussion

In this Chapter we have investigated the optical and radio morphologies of blue LERGs with respect to red LERGs and blue inactive galaxies. We have used the debiased votes from GZ1 to investigate the fraction of galaxies with an elliptical or spiral morphology in our blue LERG and two matched comparison samples. Our main result from the GZ1 morphologies as shown in Fig. 4.6 is that at high masses $M_* \gtrsim 10^{11} M_\odot$ $65.4\% \pm 2.5\%$ of the blue LERGs has an elliptical morphology. This is significantly different from the matched sample of inactive blue galaxies, which have a probability of $37.4\% \pm 0.9\%$ to have an elliptical morphology. The morphology of blue LERGs is more in line with that of the matched sample of red LERGs, of which $75.0\% \pm 0.8\%$ have an elliptical morphology. The selection method of matched samples as presented in Sect. 4.2 means that 23% of the galaxies in the red LERG sample is present more than once. For the blue inactive galaxies this is 9%. We have confirmed that these duplicates have a minimal effect on the results presented in Fig 4.6.

To investigate the effect of mergers we have obtained deep r-band observations of 24 blue LERGs. A preliminary investigation of these sources shows that at least 10 have tidal features. These sources are predominantly found at $M_* \lesssim 10^{11.2} M_\odot$. However, these initial results should be viewed with skepticism until the deep r-band images have been subjected to a more quantitative analysis. Step one in this analysis would be determining the imaging depth of all surveys and the WHT PFIP data. The observations at the WHT were all aimed at high mass objects. As such these observations dominate masses $M_* > 10^{11.2} M_\odot$. At these masses nearly no mergers are observed, while below this break many mergers are observed in the images of the public deep surveys. While this could be a true difference, it could also be the result of shallow PFIP images in which merger signatures are not yet visible. Given the high cirrus clouds during the observations, this should be carefully checked.

Morphological classification of our deep images has now been done by eye. As a next step, this could be quantified using, for example, GalFit [33]. Furthermore, matching samples of red LERGs and inactive blue galaxies should be retrieved from the deep surveys. Only comparison to these samples can show if the observed merger rate in blue LERGs is exceptional at these image depths.

Finally, we have shown in Sect. 4.5 the radio emission of 80% of the blue LERGs is a

point source. This is in stark contrast with a matched sample of red LERGs of which only 40% has a radio point source. We believe this main result is robust due to the simple nature of classifying point sources and the well matched comparison samples. Nevertheless, there are quite a few improvements possible over the current classification method of the radio morphologies. We believe that classification using combined optical/radio images could be an improvement as it simultaneously checks the matching by Best et al. [34]. To remove classifier bias, the most favourable method would be to classify the entire BH12 sample, before making any distinctions between galaxies. However, this would be extremely time consuming. Especially, if more than one ‘vote’ per object is desired instead of classification by a single astronomer as done in this work. We expect these modifications to the classification procedure could very well affect the distribution of extended morphologies. However, we expect it will not affect the main result that blue LERGs are predominantly point sources. As such, the smart way of classification will probably be selecting all blue LERGs and the matched red LERG sample before classification. Automatic classification of point sources could be an alternative way to reduce the time required for classification.

In Sect. 4.1 we have proposed four hypothesis that could explain the increased presence and increased radio luminosity of jet-mode AGN in massive blue galaxies compared to their red counterparts.

1. Blue LERGs are hosted by massive spiral galaxies where the (relatively) blue colours reflect the on-going star formation in their disks.
2. Blue LERGs are hosted by massive ellipticals with an enhanced halo cooling, which also increases their star formation with respect to their red counterparts.
3. Blue LERGs have undergone a recent merging event that has brought additional gas into these blue galaxies to trigger star formation and enhanced AGN activity.
4. Blue LERGs have young radio jets, which are still actively interacting with the gas inside the host galaxy. This positive feedback enhances the star formation in the host galaxy regardless of the host galaxy’s optical morphology.

Based on the initial results presented in this Chapter we can reject our first hypothesis that blue LERGs are hosted by massive spiral galaxies. All other three hypotheses remain valid explanations. For high mass ($M_* > 10^{11} M_\odot$) LERGs, where merger signatures are less common, the results suggest blue and red LERGs are very similar in optical morphology. However, the blue LERGs have a much smaller radio jet. We speculate that this is the result of an enhanced halo cooling and positive feedback from the radio jets. The enhanced cooling flow increases the gas supply available for both AGN activity and star formation. However, an increased gas density also means that the radio jet is more easily contained within the galaxy. Hydrodynamical simulations have shown that the collision between the radio jet and interstellar medium

can induce shocks and turbulence, which enhances the formation of stars [35]. Our finding, that blue LERGs have predominantly small radio jets is consistent with the findings by Chandola and Saikia [36]. All compact LERGs in their sample have a WISE colour $[4.6 \mu\text{m}] - [12 \mu\text{m}] > 2$ and $> 70\%$ of them has a strong HI detection. These observations suggest that compact LERGs are predominantly found in gas and dust rich systems, i.e. blue LERGs. To confirm the hypothesis of positive feedback by the radio jet high resolution radio observations are unavoidable evidence. A point source in FIRST corresponds to a physical diameter of $10 - 30$ kpc for all sources in the BH12 sample. This diameter is equal to the typical size of a galaxy.

At low masses ($M_* < 10^{11} M_\odot$) our initial results suggest blue LERGs are triggered by a recent merger with a gas rich galaxy. This merger has triggered both star formation and a young (and therefore small) radio jet. The triggering of LERGs by minor mergers has been speculated upon in recent works [37]. It is also consistent with the initial findings of Janssen et al. [9] on the nature of blue LERGs. However, we do note that the triggering by mergers as well as masses $M_* \sim 10^{10.5} M_\odot$ are reminiscent of radiative-mode AGN [38]. Furthermore, we observe the potential beginning of a big blue bump in the SDSS spectra of 3 out of the 24 blue LERGs with deep imaging. On the other hand, none of these blue LERG have a strong [OIII] emission line (and as such they are classified as LERGs). Future work should investigate the possibility that blue LERGs are radiative-mode AGN caught at a time when the accretion rate is low. Signatures of such a weak radiative-mode AGN could be masked by the emission of the star forming galaxy in which they are hosted. This state might, for example, occur when the AGN first switches on, which would be consistent with our finding that blue LERGs are predominantly point-like radio sources. If blue LERGs are indeed AGN fuelled in the same manner as HERGs (e.g. by cold gas) observed during a period of low accretion rate, this would support the hypothesis by Best et al. [39] that the cosmic evolution of LERGs is driven by a contribution from ‘HERG-like’ sources at low accretion rate.

4.7 Conclusion

In this Chapter we have presented a preliminary investigation of the optical and radio morphology of LERGs hosted by blue galaxies. These preliminary results indicate that:

1. At $M_* \gtrsim 10^{11} M_\odot$ $65.4\% \pm 2.5\%$ of the blue LERGs have an elliptical morphology. This is significantly different from inactive blue galaxies which have a probability of $37.4\% \pm 0.9\%$ to have an elliptical morphology. The morphology of blue LERGs is more in line with that of red LERGs which have a probability of $75.0\% \pm 0.8\%$ to have an elliptical morphology.
2. At least 10 out of the 24 blue LERGs with deep r-band observations show signatures of recent galaxy-galaxy interactions. These mergers are predominantly

found at $M_* \lesssim 10^{11.2} M_\odot$, although observational effects could be affecting this break.

3. 80% of the blue LERGs are point sources at radio wavelengths compared to 40% of the red LERGs.

Based on these results we can reject our first hypothesis that blue LERGs are hosted by massive spiral galaxies. All other three hypotheses remain valid explanations. The evidence supports a scenario of a recent merger with a gas rich galaxy, which has triggered star formation and a young (and thereby small) radio jet. This is especially true at low masses. At higher masses ($M_* > 10^{11} M_\odot$), where merger signatures are less common, the results can be explained by enhanced halo cooling and positive feedback from the radio jets. However, higher resolution radio images will be required to confirm the latter.

References

- [1] A. T. Moffet, *The Structure of Radio Galaxies*, Annual Review of Astronomy and Astrophysics **4**, 145 (1966).
- [2] P. N. Best, G. Kauffmann, T. M. Heckman, J. Brinchmann, S. Charlot, et al., *The host galaxies of radio-loud active galactic nuclei: mass dependences, gas cooling and active galactic nuclei feedback*, Monthly Notices of the Royal Astronomical Society **362**, 25 (2005).
- [3] G. Kauffmann, T. M. Heckman, S. D. M. White, S. Charlot, C. Tremonti, et al., *The dependence of star formation history and internal structure on stellar mass for 10^5 low-redshift galaxies*, Monthly Notices of the Royal Astronomical Society **341**, 54 (2003).
- [4] H. Arp, *Atlas of Peculiar Galaxies*, The Astrophysical Journal Supplement Series **14**, 1 (1966).
- [5] R. A. Laing, C. R. Jenkins, J. V. Wall, and S. W. Unger, *Spectrophotometry of a Complete Sample of 3CR Radio Sources: Implications for Unified Models*, Astronomical Society of the Pacific Conference Series **54**, 201 (1994).
- [6] C. M. Urry and P. Padovani, *Unified Schemes for Radio-Loud Active Galactic Nuclei*, Publications of the Astronomical Society of the Pacific **107**, 803 (1995).
- [7] P. N. Best and T. M. Heckman, *On the fundamental dichotomy in the local radio-AGN population: accretion, evolution and host galaxy properties*, Monthly Notices of the Royal Astronomical Society **421**, 1569 (2012).
- [8] P. N. Best, C. R. Kaiser, T. M. Heckman, and G. Kauffmann, *AGN-controlled cooling in elliptical galaxies*, Monthly Notices of the Royal Astronomical Society **368**, L67 (2006).

- [9] R. M. J. Janssen, H. J. A. Röttgering, P. N. Best, and J. Brinchmann, *The triggering probability of radio-loud AGN. A comparison of high and low excitation radio galaxies in hosts of different colors*, *Astronomy & Astrophysics* **541**, A62 (2012).
- [10] L. Jiang, X. Fan, F. Bian, I. D. McGreer, M. A. Strauss, et al., *The Sloan Digital Sky Survey Stripe 82 Imaging Data: Depth-optimized Co-adds over 300 deg² in Five Filters*, *The Astrophysical Journal Supplement Series* **213**, 12 (2014).
- [11] B. T. Jannuzi and A. Dey, *The NOAO Deep Wide-Field Survey*, *Astronomical Society of the Pacific Conference Series* **191**, 111 (1999).
- [12] J. T. A. de Jong, G. A. Verdoes Kleijn, D. R. Boxhoorn, H. Buddelmeijer, M. Capaccioli, et al., *The first and second data releases of the Kilo-Degree Survey*, *Astronomy & Astrophysics* **582**, A62 (2015).
- [13] P. Hudelot, Y. Goranova, Y. Mellier, H. J. McCracken, F. Magnard, et al., *T0007: The Final CFHTLS Release*, (2012), <http://terapix.iap.fr/cplt/T0007/doc/T0007-doc.pdf>.
- [14] R. H. Becker, R. L. White, and D. J. Helfand, *The FIRST Survey: Faint Images of the Radio Sky at Twenty Centimeters*, *The Astrophysical Journal* **450**, 559 (1995).
- [15] K. N. Abazajian, J. K. Adelman-McCarthy, M. A. Agüeros, S. S. Allam, C. Allende Prieto, et al., *The Seventh Data Release of the Sloan Digital Sky Survey*, *The Astrophysical Journal Supplement Series* **182**, 543 (2009).
- [16] J. J. Condon, W. D. Cotton, E. W. Greisen, Q. F. Yin, R. A. Perley, et al., *The NRAO VLA Sky Survey*, *The Astronomical Journal* **115**, 1693 (1998).
- [17] J. Brinchmann, S. Charlot, S. D. M. White, C. Tremonti, G. Kauffmann, et al., *The physical properties of star-forming galaxies in the low-redshift Universe*, *Monthly Notices of the Royal Astronomical Society* **351**, 1151 (2004).
- [18] M. A. Strauss, D. H. Weinberg, R. H. Lupton, V. K. Narayanan, J. Annis, et al., *Spectroscopic Target Selection in the Sloan Digital Sky Survey: The Main Galaxy Sample*, *The Astronomical Journal* **124**, 1810 (2002).
- [19] G. Kauffmann, T. M. Heckman, S. D. M. White, S. Charlot, C. Tremonti, et al., *Stellar masses and star formation histories for 10⁵ galaxies from the Sloan Digital Sky Survey*, *Monthly Notices of the Royal Astronomical Society* **341**, 33 (2003).
- [20] C. Lintott, K. Schawinski, S. Bamford, A. Slosar, K. Land, et al., *Galaxy Zoo 1: data release of morphological classifications for nearly 900 000 galaxies*, *Monthly Notices of the Royal Astronomical Society* **410**, 166 (2011).
- [21] C. J. Lintott, K. Schawinski, A. Slosar, K. Land, S. Bamford, et al., *Galaxy Zoo: morphologies derived from visual inspection of galaxies from the Sloan Digital Sky Survey*, *Monthly Notices of the Royal Astronomical Society* **389**, 1179 (2008).

- [22] M. L. Balogh, S. L. Morris, H. K. C. Yee, R. G. Carlberg, and E. Ellingson, *Differential Galaxy Evolution in Cluster and Field Galaxies at $z \sim 0.3$* , The Astrophysical Journal **527**, 54 (1999).
- [23] C. Pace and S. Salim, *Suppression of Star Formation in the Hosts of Low-excitation Radio Galaxies*, The Astrophysical Journal **818**, 65 (2016).
- [24] D. W. Darg, S. Kaviraj, C. J. Lintott, K. Schawinski, M. Sarzi, et al., *Galaxy Zoo: the fraction of merging galaxies in the SDSS and their morphologies*, Monthly Notices of the Royal Astronomical Society **401**, 1043 (2010).
- [25] D. W. Darg, S. Kaviraj, C. J. Lintott, K. Schawinski, M. Sarzi, et al., *Galaxy Zoo: the properties of merging galaxies in the nearby Universe - local environments, colours, masses, star formation rates and AGN activity*, Monthly Notices of the Royal Astronomical Society **401**, 1552 (2010).
- [26] J. Bakos and I. Trujillo, *Deep Surface Brightness Profiles of Spiral Galaxies from SDSS Stripe82: Touching Stellar Halos*, ArXiv e-prints, 1204.3082 (2012).
- [27] E. Bertin and S. Arnouts, *SExtractor: Software for source extraction.*, Astronomy & Astrophysics Supplement Series **117**, 393 (1996).
- [28] E. Bertin, Y. Mellier, M. Radovich, G. Missonnier, P. Didelon, et al., *The TERAPIX Pipeline*, Astronomical Society of the Pacific Conference Series **281**, 228 (2002).
- [29] E. Bertin, *Automatic Astrometric and Photometric Calibration with SCAMP*, Astronomical Society of the Pacific Conference Series **351**, 112 (2006).
- [30] E. Bertin, *Displaying Digital Deep Sky Images*, Astronomical Society of the Pacific Conference Series **461**, 263 (2012).
- [31] S. P. Bamford, R. C. Nichol, I. K. Baldry, K. Land, C. J. Lintott, et al., *Galaxy Zoo: the dependence of morphology and colour on environment*, Monthly Notices of the Royal Astronomical Society **393**, 1324 (2009).
- [32] B. L. Fanaroff and J. M. Riley, *The morphology of extragalactic radio sources of high and low luminosity*, Monthly Notices of the Royal Astronomical Society **167**, 31P (1974).
- [33] C. Y. Peng, L. C. Ho, C. D. Impey, and H.-W. Rix, *Detailed Structural Decomposition of Galaxy Images*, The Astronomical Journal **124**, 266 (2002).
- [34] P. N. Best, G. Kauffmann, T. M. Heckman, and Ž. Ivezić, *A sample of radio-loud active galactic nuclei in the Sloan Digital Sky Survey*, Monthly Notices of the Royal Astronomical Society **362**, 9 (2005).
- [35] W. Ishibashi and A. C. Fabian, *Active galactic nucleus feedback and triggering of star formation in galaxies*, Monthly Notices of the Royal Astronomical Society **427**, 2998 (2012).

-
- [36] Y. Chandola and D. J. Saikia, *H i absorption towards low-luminosity radio-loud active galactic nuclei of different accretion modes and WISE colours*, Monthly Notices of the Royal Astronomical Society **465**, 997 (2017).
 - [37] S. L. Ellison, D. R. Patton, and R. C. Hickox, *Galaxy pairs in the Sloan Digital Sky Survey - XII. The fuelling mechanism of low-excitation radio-loud AGN*, Monthly Notices of the Royal Astronomical Society **451**, L35 (2015).
 - [38] T. M. Heckman and P. N. Best, *The Coevolution of Galaxies and Supermassive Black Holes: Insights from Surveys of the Contemporary Universe*, Annual Review of Astronomy and Astrophysics **52**, 589 (2014).
 - [39] P. N. Best, L. M. Ker, C. Simpson, E. E. Rigby, and J. Sabater, *The cosmic evolution of radio-AGN feedback to $z = 1$* , Monthly Notices of the Royal Astronomical Society **445**, 955 (2014).

Chapter 5

Classification of radio galaxies using broadband mid-infrared observations

Currently, the most reliable way to classify radio-loud AGN as high- and low-excitation radio galaxies (HERGs–LERGs) is using optical spectral lines. We investigate methods to perform this separation using broadband mid-infrared observations, where the presence or absence of a torus is anticipated to differentiate the two populations. We obtained near- and mid-infrared fluxes from the Wide-Field Infrared Survey Explorer (WISE) for 8263 LERGs and 272 HERGs identified in SDSS and classified using their optical spectra. We find that LERGs have the same mid-infrared luminosity distribution as inactive galaxies with similar mass, star formation rate and redshift. HERGs on the other hand typically have a mid-infrared luminosity comparable to or in excess of the 5% most luminous radio-quiet galaxies with matching properties. As a result of this, the mean $22\ \mu\text{m}$ luminosity of all HERGs in our sample is 0.5 dex higher than that of the LERG population. Despite these trends we have not identified a way to separate HERGs and LERGs with a $> 70\%$ completeness and reliability for both populations using only broadband observations. This is the result of: 1. The large spread in $22\ \mu\text{m}$ luminosity of both radio-loud AGN populations, which is (at least partially) due to the emission of dust heated by young stars. 2. The numerical dominance of LERGs within our sample. 3. A subpopulation of HERGs without an observed excess of $22\ \mu\text{m}$ emission. Based on their properties we speculate that this subpopulation of HERGs represent episodes of weak AGN activity during the later stages of an active period.

5.1 Introduction

Steep-spectrum radio sources are a class of active galactic nuclei (AGN), which play a key role in regulating galaxy formation processes through the interplay of their expanding radio jets with the intracluster and interstellar medium [e.g. 1–5]. The population of steep-spectrum radio sources can be further divided into two subclasses: high-excitation radio galaxies (HERGs) and low-excitation radio galaxies (LERGs). HERGs are ‘standard’ AGN, which accrete cold gas at rates close to the Eddington limit in a radiatively efficient manner. They are most likely merger driven. In addition to their radio emission HERGs also emit X-ray and infrared emission as well as optical emission lines typically associated with quasars. Therefore, they have been referred to as ‘cold-mode’ or ‘quasar-mode’ radio galaxies. LERGs on the other hand have been argued to accrete hot gas directly from their halo at sub-Eddington ($\lesssim 1\%$) rates. As this is a radiatively inefficient process LERGs only exhibit radio jets, which identifies them as AGN. Thus, they are referred to as ‘hot-mode’ or ‘radio-mode’ AGN. Cold-mode sources are typically the more powerful of the two classes. However, it should be noted that sources of both types exist at all powers. [c.f. 6, and references therein].

Studying the behaviour of the radio galaxy population across cosmic time is essential for understanding the timescales upon which their feedback processes occur. This evolution of the radio luminosity function has generally been measured for the population as a whole, and then only for luminosities $> 10^{24}$ W/Hz at 1.4 GHz [7, 8]. For a complete picture of these objects, LERGs and HERGs should be considered separately. However, this critically depends on accurate classification of the two AGN modes out to high redshifts and across large samples. By definition, classification using spectral lines is the most reliable method of HERG/LENG categorization. However, it is currently too observationally expensive to obtain spectra in the quantities needed to constrain the evolving radio luminosity functions (RLFs). A first attempt at this was made by Best et al. [9], who constructed a spectroscopically classified sample of 211 radio-loud AGN with $0.5 < z < 1.0$ and compared this to an equivalent large sample of local AGN from the Sloan Digital Sky Survey (SDSS) [10, 11]. Their results raised the intriguing possibility of a contribution to the hot-mode population by cold-mode sources at an early stage of their growth, but they were unable to investigate this fully due to the limitations of their sample.

It is clear that a simple method for HERG/LENG identification using easily obtainable datasets would be a valuable asset for RLF evolution studies. In this Chapter we investigate HERG/LENG separation using broadband observations, in particular focusing on mid-infrared (mid-IR) observations. Recent work [e.g. 12, 13] has shown that HERGs have a significantly higher mid-IR luminosity compared to LERGs. This excess emission is attributed to the dusty torus thought to be present in radiatively efficient accretion-mode AGN (i.e. HERGs). We will study the mid-IR properties of HERGs and LERGs using a large sample of low-redshift, low-luminosity radio-loud AGN [14].

The details of this sample are described in Section 5.2. In Sect. 5.3 we investigate the mid-IR of this sample as a function of host galaxy redshift, mass, star formation rate and colour. We formulate a break luminosity, $L_{22\mu\text{m},\text{break}}$, that provides the optimal separation between the two AGN populations. In Sect. 5.4 we compare the mid-IR luminosity of HERGs and LERGs to that of inactive galaxies with similar broadband optical properties. We will compare the different separation methods discussed in this Chapter in Sect. 5.5 and summarize our conclusions in Sect. 5.6.

In this Chapter values for the cosmological parameters of $H_0 = 70 \text{ km s}^{-1}\text{Mpc}^{-1}$, $\Omega_m = 0.3$ and $\Omega_\Lambda = 0.7$ are used. The radio spectral index, α is defined as $S_\nu \propto \nu^{-\alpha}$, and taken as $\alpha = 0.8$ where necessary. For clarity cold- and hot-mode sources will be referred to as HERGs and LERGs, respectively, in the remainder of this work.

5.2 Low-redshift sample of radio-loud AGN

Best and Heckman [14, hereafter BH12] constructed a large, local radio galaxy sample by combining spectroscopic data from SDSS [10, 11] with radio data from National Radio Astronomy Observatory Very Large Array Sky Survey (NVSS) [15] and the Faint Images of the Radio Sky at Twenty centimetres (FIRST) survey [16]. This resulted in a catalogue of over 10000 radio galaxies, which were classified as LERGs (9863 sources) or HERGs (481 sources) on the basis of their emission line flux measurements. These emission line measurements were taken from the value added spectroscopic catalogue (VASC) created by the Max Planck Institute for Astrophysics and Johns Hopkins University [cf. 17]. The VASC is the parent sample for the BH12 radio-loud AGN sample and we will use it as the reference sample of inactive galaxies. We classify a galaxy as inactive if it has not been identified as a radio-loud AGN by BH12. The VASC also provides derived quantities such as stellar masses, M_* , and star formation rates, SFR, used in this paper. These derived quantities are obtained by fitting a spectral energy distribution (SED) to the optical broadband measurements from SDSS.

The corresponding near- and mid-IR data for the galaxies in the VASC comes from the Wide-Field Infrared Survey Explorer (WISE) [18], which observed the sky in four bands (3.4, 4.6, 12 and 22 μm). We use the near- and mid-IR fluxes, in particular at 22 μm , from the SDSS–WISE catalogue of Chang et al. [19]. Chang et al. [19] cross-matched the SDSS spectroscopic galaxy sample as compiled in the New York University value-added galaxy catalogue (NYU-VAGC) [20] with the AllWISE source catalogue with a search radius of 6 arcsec. Thus, we obtain 8263 LERGs and 272 HERGs with a 22 μm flux from the AllWISE catalogue in the redshift range $0.03 < z < 0.4$. 91% of the LERG and 49% of the HERG with an entry in the AllWISE catalogue has a 2σ upper limit on the detected 22 μm flux instead of a $> 2\sigma$ detection. From the WISE fluxes, S_ν , the IR luminosity is calculated using $L_\nu = \nu \times S_\nu \times 4\pi D_{lum}^2$. Given the low redshift

of our sample we do not include a K-correction.

5.2.1 Volume-limited sample

The high fraction of upper limits on the WISE mid-IR luminosities can make interpretation of the results complex. Therefore, we define a pseudo-volume-limited sample by selecting all galaxies that satisfy the following criteria:

- $z \leq 0.15$
- $z_{max,radio} \geq 0.15$
- $z_{max,optical} \geq 0.15$
- a $> 2\sigma$ detection in $L_{22\mu m}$
- $L_{22\mu m} \geq 10^{36.0}$ W
- $M_*/M_\odot \geq 10^{10.5}$
- $0.5 \leq D_n4000 \leq 2.5$

The mass limit is not strictly necessary in this definition as it does not remove any radio-loud AGN from the sample. However, it does remove low-mass galaxies from the inactive galaxy population used as a comparison sample. As such, the mass limit creates a more representative comparison sample. The above criteria select a sample of 26275 galaxies, 159 of which are classified as radio-loud AGN. Due to the non-uniform depth of the WISE survey over the area of the SDSS there is a large number of galaxies (45862 of which 951 are radio-loud AGN) that satisfy the above criteria, but have a 2σ upper limit on $L_{22\mu m}$. This upper limit is equivalent to a mid-IR luminosity in the range $10^{36.0} \geq L_{22\mu m} [W] \geq 10^{36.4}$. We nevertheless decide to keep the luminosity cut at $L_{22\mu m} \geq 10^{36.0}$ W, which corresponds to the detection limit for the deepest WISE areas, as it enables us to study the behaviour of galaxies and AGN well below the apparent HERG/LERG cross-over at $L_{22\mu m} = 10^{36.6}$ W (see further Fig. 5.1).

Throughout this paper we will refer to the pseudo-volume-limited sample as the volume-limited sample (VLS) and present only the results from the sources with mid-IR detections. All galaxies with an upper limit on $L_{22\mu m}$ follow the trends set by the detected counterparts of their subpopulation, if we assume that $L_{22\mu m}$ is equal to the value set by the 2σ upper limit. Any significant or notable deviations induced by the inclusion of the upper limit population will be mentioned explicitly.

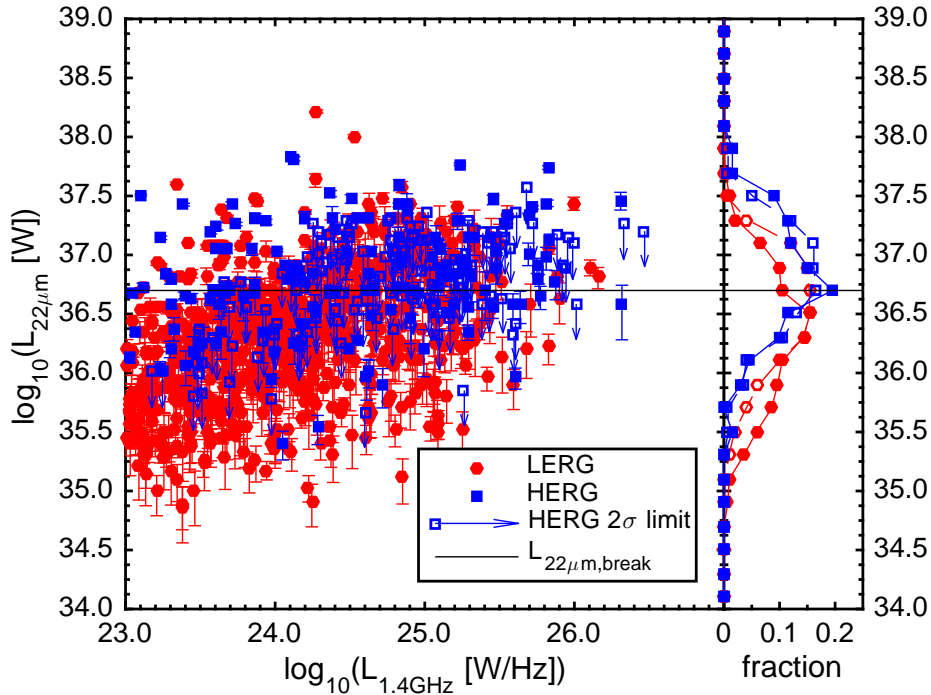


Figure 5.1: (left) $22\ \mu\text{m}$ luminosity vs. $1.4\ \text{GHz}$ radio luminosity for the LERGs (red circles) and HERGs (blue squares) from the BH12 sample investigated in this paper. The solid black line indicates the optimal separation between HERGs and LERGs $L_{22\mu\text{m},\text{break}} = 10^{36.6}\ \text{W}$. Upper limits on the $L_{22\mu\text{m}}$ of HERGs are indicated by open squares with arrows. Upper limits for LERG are not shown for clarity. However, the 2σ values span the same parameter space as the LERG detections shown in the figure. (right) A histogram showing the distribution of $L_{22\mu\text{m}}$ for HERGs (blue squares) and LERGs (red circles). The solid lines include only $> 2\sigma$ detections, while the open symbols connected by dashed lines also include upper limits.

5.3 The mid-IR luminosity of radio-loud AGN

Fig. 5.1 shows $L_{22\mu\text{m}}$ as a function of $L_{1.4\text{GHz}}$ for the HERGs (blue squares) and LERGs (red circles) in the BH12 sample. Upper limits on the $L_{22\mu\text{m}}$ of HERGs are shown by blue arrows. Upper limits for LERGs are not shown for clarity, but span the same parameter space as the LERGs with a $22\ \mu\text{m}$ detection. The HERG population does appear to be offset with respect to the LERGs in $L_{22\mu\text{m}}$. This is confirmed by the right-hand side panel of Fig. 5.1. This panel shows the $L_{22\mu\text{m}}$ distribution of HERGs (blue squares) and LERGs (red circles). The solid lines include only $> 2\sigma$ detections, while the open symbols connected by dashed lines also include upper limits. Both populations can be described by a Gaussian distribution with $\langle \log_{10}(L_{22\mu\text{m}}) \rangle = 36.83 \pm 0.48$ for HERGs and $\langle \log_{10}(L_{22\mu\text{m}}) \rangle = 36.34 \pm 0.58$ for LERGs. A log-rank test that takes into account censored data [21] confirms that HERGs and LERGs are a statistically different population in $L_{22\mu\text{m}}$.

Following Gürkan et al. [12] we define a break luminosity, $L_{22\mu\text{m},\text{break}}$, that separates

the two populations as

$$\log_{10}(L_{22\mu\text{m},\text{break}} [\text{W}]) = L_0 \quad (5.1)$$

We determine L_0 by minimizing the fraction of sources that is misidentified, f_{misid} .

$$f_{\text{misid}}^2 = \left(\frac{I_{\text{HERG}}}{N_{\text{HERG}}} \right)^2 + \left(\frac{I_{\text{LERG}}}{N_{\text{LERG}}} \right)^2 \quad (5.2)$$

Here I_x is the number of incorrectly classified HERGs or LERGs and N_x the total number of these AGN. Considering only the radio-loud AGN with a detection at $22 \mu\text{m}$ we find $L_0 = 36.57$ at $f_{\text{misid}} = 0.41$. If the AGN with an upper limit on $L_{22\mu\text{m}}$ are included L_0 increases slightly to 36.64 at $f_{\text{misid}} = 0.56$. Fig. 5.1 shows $L_{22\mu\text{m},\text{break}} = 10^{36.6} \text{ W}$ as a solid black line. It is obvious from Fig. 5.1 as well as the values of f_{misid} that this method of separation suffers from a strong cross-contamination. 31% of the LERG with a $22 \mu\text{m}$ detection are located above the empirical separation line. In addition, 30% of the HERG with a detection at $22 \mu\text{m}$ and 35% of the HERG with an upper limit on $L_{22\mu\text{m}}$ are located below $L_{22\mu\text{m},\text{break}} = 10^{36.6} \text{ W}$.

5.3.1 Influence of star formation

Figure 5.2 shows the $22 \mu\text{m}$ luminosity distribution of the VLS as a function of galaxy colour: Red ($1.7 \leq D_n4000 \leq 2.5$), Green ($1.45 \leq D_n4000 \leq 1.7$), Blue ($0.5 \leq D_n4000 \leq 1.45$) and All ($0.5 \leq D_n4000 \leq 2.5$) [22]. The error bars are determined using Poissonian statistics. We observe that LERGs have $L_{22\mu\text{m}}$ comparable to the population of inactive galaxies, while HERGs have a clear excess of $22 \mu\text{m}$ emission. $L_{22\mu\text{m},\text{break}} = 10^{36.6} \text{ W}$ is included in Fig. 5.2 as a visual aid in the form of a vertical dashed line. This reveals the origin of the poor performance of $L_{22\mu\text{m},\text{break}} = 10^{36.6} \text{ W}$ as a separator between HERGs and LERGs. Blue star forming galaxies have an inherently higher $L_{22\mu\text{m}}$. This gives LERGs hosted by blue (and to a lesser degree green) galaxies a mid-IR luminosity that is typically associated with HERGs. In turn, there appears to be a population of green HERGs with an untypical low mid-IR luminosity. Inclusion of the upper limit sources from the VLS shows a similar population in the red galaxy population.

These two phenomena are again observed in Fig. 5.3. Fig. 5.3 shows the $L_{22\mu\text{m}} - \text{SFR}$ -plane. The grey contours show the distribution of inactive galaxies from the VLS. The blue cloud (at high SFR) and the top end of the red sequence (at low SFR) are clearly recognizable. With the exception of a few outliers, the LERG population (red symbols) follows the distribution of the inactive galaxy population. As a result, a number of LERGs with a high SFR have a mid-IR luminosity which is unusually high compared to the LERG hosted by red galaxies (the numerically dominant part of the LERG population). HERGs (blue) generally have excess mid-IR emission in comparison

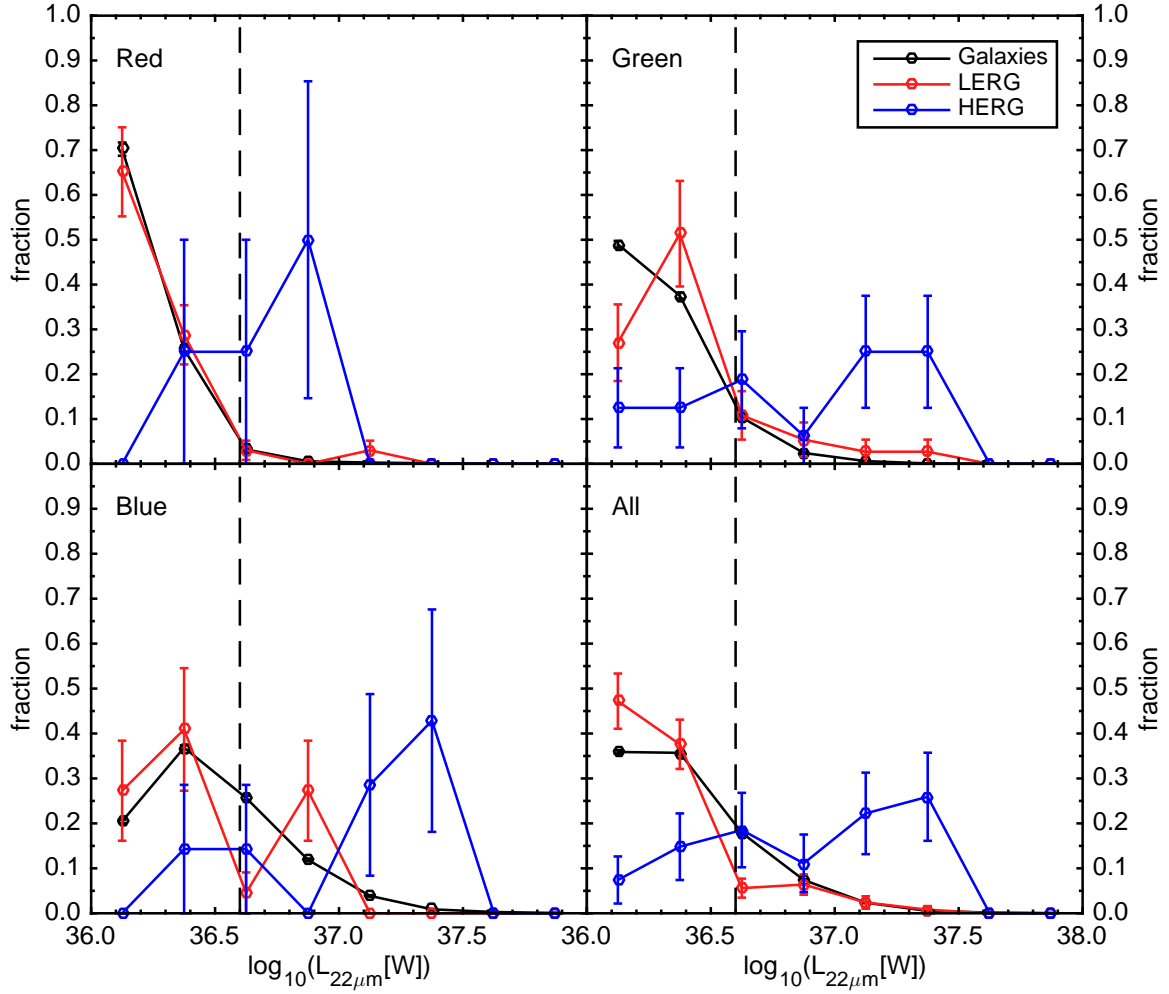


Figure 5.2: The luminosity distribution of LERGs (red), HERGs (blue) and regular galaxies (black) as a function of galaxy colour for the volume limited sample defined in Section 5.2.1. The error bars are based upon Poissonian statistics. The vertical dashed line is $L_{22\mu\text{m},\text{break}} = 10^{36.6} \text{ W}$.

with inactive hosts. Taking into account the presence of the blue cloud we can refine the $L_{22\mu\text{m},\text{break}}$ criteria to separate HERGs and LERGs. We redefine $L_{22\mu\text{m},\text{break}}$ as

$$\log_{10}(L_{22\mu\text{m},\text{break}}[\text{W}]) = \min(L_0, L_1 + \Delta L_1 \times \log_{10}(SFR[\text{M}_{\odot}/\text{yr}])) \quad (5.3)$$

We determine L_0 , L_1 and ΔL_1 by minimizing f_{misid} . For the VLS we obtain a minimum $f_{\text{misid}} = 0.18$ with the parameters $L_0 = 36.41$, $L_1 = 36.46$ and $\Delta L_1 = 0.41$. This gives a completeness of 90% and 88% for LERGs and HERGs, respectively. The reliability for the separation is 97% for LERGs and 66% for HERGs. The inclusion of the upper limit population in Fig. 5.3 accentuates the location of the red sequence as well as the dominance of LERGs in this region. The distribution of these sources suggests a slight increase of L_0 to the range $36.5 < L_0 < 36.7$. However, the most notable difference is the presence of another 4 HERGs with low mid-IR luminosity.

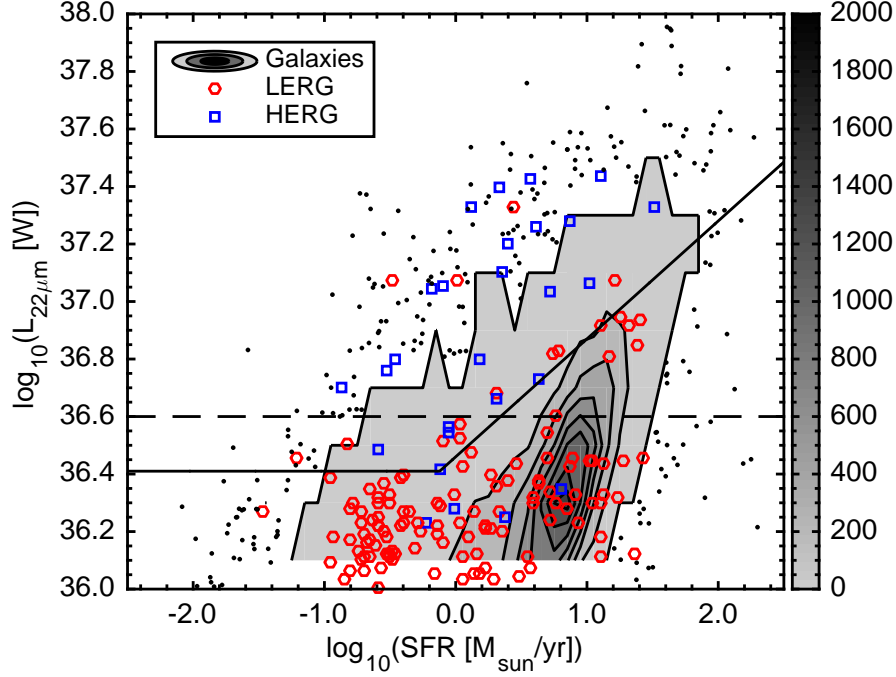


Figure 5.3: $L_{22\mu\text{m}}$ as a function of the host galaxies star formation rate for LERGs (red circles) and HERGs (blue squares) in the volume limited sample defined in Sect. 5.3.1. The background contours shows the distribution of the regular galaxies from the same sample in the $L_{22\mu\text{m}} - \text{SFR}$ -plane. The greyscale on the right indicates the number of galaxies per bin of size $(\delta \text{SFR}, \delta \log_{10}(L_{22\mu\text{m}})) = (0.1, 0.2)$. If the number of galaxies is less than 5, the galaxies are shown as black dots instead. The black dashed line indicates the $L_{22\mu\text{m},\text{break}} = 10^{36.6}$ W separation line, while the black solid line indicates the more advanced separation given in Section 5.3.1.

5.3.2 Influence of redshift and host galaxy mass

Closer inspection of the VLS shows that it is effectively equivalent to a redshift cut $0.10 < z < 0.15$. In addition, host galaxy mass is known to be a dominant factor in the properties of both the AGN and its host [6]. To investigate how robust our advanced separation criterion is against these two parameters, we investigate the mid-IR luminosity of radio-loud AGN as a function of redshift and host galaxy mass. Starting from the complete flux limited population we select all galaxies in two redshift bins: $0.03 < z < 0.15$ and $0.15 < z < 0.30$. Within each redshift bin we split the galaxies in three stellar mass bins: $10.5 \leq \log_{10}(M_*/M_\odot) < 11.0$, $11.0 \leq \log_{10}(M_*/M_\odot) < 11.5$ and $\log_{10}(M_*/M_\odot) \geq 11.5$. Fig. 5.4 shows the distribution of inactive galaxies (grey contours), HERGs (blue squares) and LERGs (red circles) with a detection in $L_{22\mu\text{m}}$ in the $L_{22\mu\text{m}} - \text{SFR}$ -plane for these six (z, M_*) -bins. The number of inactive galaxies (black), HERGs (blue) and LERGs (red) with a $L_{22\mu\text{m}}$ detection in each redshift bin is listed in the bottom right of each figure. In brackets the number of sources with a 2σ upper limit on their $22\mu\text{m}$ emission is listed for each population. 97.5% and 2.5%

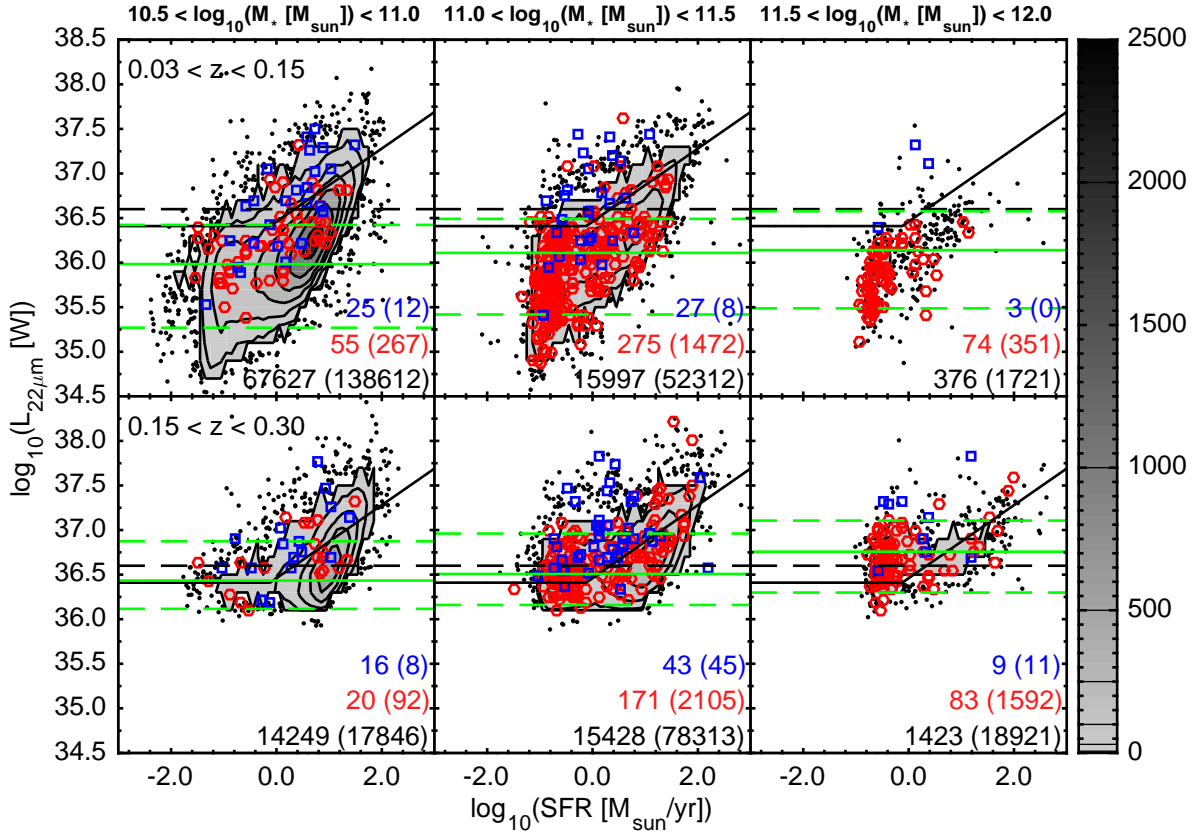


Figure 5.4: $L_{22\mu\text{m}}$ as a function of the host galaxies star formation rate for LERGs (red circles) and HERG (blue squares) for two redshift (rows) and three mass bins (columns). The background contours shows the distribution of the inactive galaxies from the same bin in the $L_{22\mu\text{m}} - \text{SFR}$ -plane. The greyscale on the far right indicates the number of galaxies per bin of size $(\delta\text{SFR}, \delta\log_{10}(L_{22\mu\text{m}})) = (0.1, 0.2)$. Contour levels are located at 5, 30, 100, 250 500, 1000 and 2000 sources, which is indicated by the black lines in the greyscale on the right. If the number of galaxies is less than 5, the galaxies are shown as black dots instead. The dashed black line indicates the $L_{22\mu\text{m},\text{break}} = 10^{36.6}$ W separation line. The solid black line shows it's SFR-dependent counterpart identified in Section 5.3.1. The green lines indicates $L_{22\mu\text{m}}$ below which 97.5%, 50% and 2.5% of all upper-limits in that bin are located. The numbers in the bottom right of each figure indicate the number of HERGs (blue), LERGs (red) and inactive galaxies (black) from the complete sample presented in Sect. 5.2 that satisfy the redshift and mass requirements and have a $L_{22\mu\text{m}}$ detection or upper limit (in brackets).

of these upper limits on $L_{22\mu\text{m}}$ are located below the upper and lower dashed green line, respectively. The median $L_{22\mu\text{m}}$ of of all galaxies with an upper limits on this in each (z, M_*) -bin is indicated by the solid green line. Between the dashed green lines the luminosities equivalent to the upper limits follow the distribution of their detected counterparts. It is worth noting that the HERGs with upper limits on $L_{22\mu\text{m}}$ are predominantly located at the top of the red sequence; $\text{SFR} \leq 3 \text{ M}_{\odot}/\text{yr}$ and $\text{SFR} \leq 1 \text{ M}_{\odot}/\text{yr}$ for the middle and low mass bins, respectively.

These six bins all show the trends set by the VLS: LERGs follow the distribution of the inactive galaxy population. At the highest masses there appear to be almost exclusively LERGs. However, the few HERGs that are present in these massive galaxies, are also clearly the most luminous sources in the mid-IR. The offset in $L_{22\mu\text{m}}$ between the HERGs and LERGs decreases for a decrease in host galaxy mass. In the lowest mass bin, the HERG population overlaps with the top of LERGs and inactive galaxy population. For increasing redshift the opposite appears to happen as an increased amount of LERGs crosses $L_{22\mu\text{m},\text{break}}$. It is clear from Fig. 5.4 that $L_{22\mu\text{m},\text{break}} = 10^{36.6}$ W (black dashed line) as well as its SFR-dependent counterpart identified in Sect. 5.3.1 (solid black line) both fail to consistently separate the two populations with a high completeness and reliability.

5.4 Comparison between radio-loud AGN and inactive galaxies

Fig. 5.4 shows that $L_{22\mu\text{m},\text{break}}$ would have to be re-optimized for every redshift and mass in order to achieve an effective separation between HERGs and LERGs. This would result in a separation criterion which is dependent on at least three derived quantities. Obtaining these is an additional step in the separation of the two radio-loud AGN populations. In addition, it would require significant knowledge about the sample under investigation to define $L_{22\mu\text{m},\text{break}}$ at all. In order to avoid this we also investigate a different separation method.

Pace and Salim [13] have shown that HERGs, LERGs and inactive galaxies have very similar optical magnitudes for a given set of host galaxies properties. For every HERG and LERG in the BH12 sample with a detection in $L_{22\mu\text{m}}$ we identify a luminosity matched comparison sample of inactive galaxies. The comparison sample of a radio-loud AGN contains all similar inactive galaxies from the VASC. Here similar is defined as: the inactive galaxies have a property X within dX of the radio-loud AGN under investigation. Here X is allowed to be any absolute optical magnitude as observed by SDSS, the absolute IR magnitude as observed at 3.4 and 4.6 μm , or any colour between these broadband observations. Furthermore, the redshift is allowed to be constrained. After identifying the comparison sample for a radio-loud AGN the fraction of inactive galaxies that are more luminous at 22 μm is determined. A minimum, f_{min} , and maximum, f_{max} , fraction is determined to take into account the inactive galaxies that have only upper limits on $L_{22\mu\text{m}}$.

$$f_{\text{min}} = N_{>L_{22\mu\text{m},\text{det}}}/N_{\text{inactive}} \quad (5.4a)$$

$$f_{\text{max}} = (N_{>L_{22\mu\text{m},\text{det}}} + N_{>L_{22\mu\text{m},\text{ul}}})/N_{\text{inactive}} \quad (5.4b)$$

$$f_{\text{mean}} = 0.5 * (f_{\text{min}} + f_{\text{max}}) \quad (5.4c)$$

Here $N_{>L_{22\mu\text{m}}}$ is the number of inactive galaxies in the comparison sample that are more luminous at $22\ \mu\text{m}$ than the radio-loud AGN. $L_{22\mu\text{m}}$ is determined either from a detection by WISE (det) or by assuming that the 2σ upper limit represents the actual luminosity (ul). N_{inactive} is the total number of inactive galaxies in the comparison sample. Fig. 5.5(a) shows the range $[f_{\min}, f_{\max}]$ for all radio-loud AGN with a $22\ \mu\text{m}$ detection in our AGN sample. The constraints imposed on the reference sample of each AGN are

- redshift $[z_{\text{AGN}} - dz, z_{\text{AGN}} + dz]$ with $dz = 0.06$
- optical magnitude $[M_{\text{AGN}} - dM, M_{\text{AGN}} + dM]$ with $dM = 0.5$ for U, R, and I band.
- optical color $[C_{\text{AGN}} - dC, C_{\text{AGN}} + dC]$ with $dC = 0.3$ for $U - R$ and $R - I$ optical colors.

HERGs typically are in the top 5% of mid-IR luminosity distribution set by the reference sample. They have a small range spanned by f_{\min} and f_{\max} as their detected mid-IR luminosity is higher than the luminosity set by upper limits. LERGs typically have a large range between f_{\min} and f_{\max} . Only a few of the inactive galaxies need to have an actual luminosity close to the upper limit, to set the mid-IR luminosity of the LERG in the bottom 95% of the $L_{22\mu\text{m}}$ distribution set by the reference sample.

Fig. 5.5(b) shows this even more clearly. Fig. 5.5(b) shows the distribution of f_{mean} for HERGs (blue) and LERGs (red) using 1% wide bins. Negative values are radio-loud AGN that don't have at least 100 inactive galaxies within the constraints set above. HERGs show a clear peak at $f_{\text{mean}} = 0.005$ with a rapid decline to the 3% level at $f_{\text{mean}} = 0.035$. LERGs have a uniform distribution over the range $0.02 \leq f_{\text{mean}} \leq 0.6$. The distribution of both HERGs and LERGs becomes 0 at values $f_{\text{mean}} > 0.6$, because of the large number inactive galaxies with only an upper limit on their $22\ \mu\text{m}$ luminosity. This means $[f_{\min}, f_{\max}]$ regularly spans a large part of its maximum range, i.e. $[0, 1]$, especially for LERGs (as also shown in Fig. 5.5(a)). The peak at $f_{\text{mean}} = 0.005$ of the LERGs is most likely the consequence of an Eddington bias. Our analysis only uses radio-loud AGN with a mid-IR detection, which favours the selection of the most luminous galaxies in each population. When compared to the luminosity distribution set by the total population of comparable galaxies these will naturally cluster towards the high luminosities. The peak at $f_{\text{mean}} = 0.005$ of the LERGs disappears when a comparison is made using only galaxies with a mid-IR detection or when using the VLS. In both cases the distribution of HERGs is not altered compared to that shown in Fig. 5.5(b). It should also be noted that f_{\min} , f_{mean} and f_{\max} show a decreasing trend with redshift for LERGs at $z < 0.1$. This is the result of the imbalance in the redshift of comparison galaxies. The higher redshift comparison galaxies generally have a higher (equivalent) $22\ \mu\text{m}$ luminosity. At $z < 0.09$ the AGN under investigation have an increasing fraction of luminous high redshift sources for a decreasing redshift. This means the nominator of f_{\min} and f_{\max} increases with decreasing redshift. HERGs are

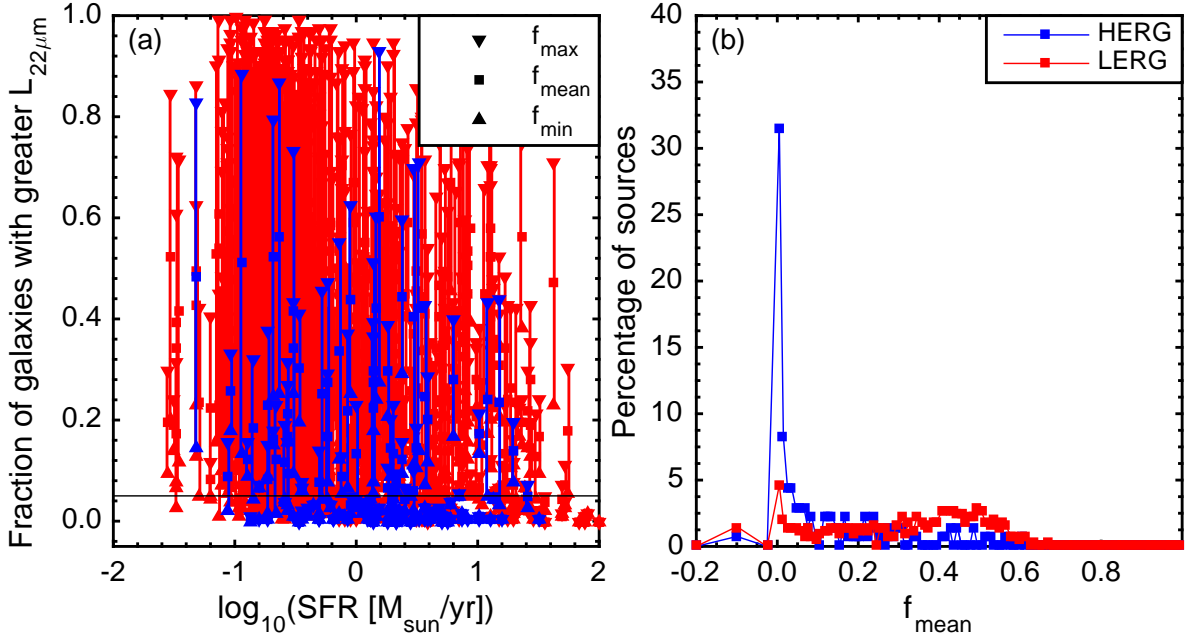


Figure 5.5: (a) Fraction of comparable inactive galaxies that have a $L_{22\mu\text{m}}$ greater than the HERG (blue) or LERG (red) under investigation. Most radio-loud AGN have a range of potential fractions, as defined in Equation 5.4, due to the large number of upper limits on the WISE detections. The solid black line at 5% indicates the proposed separation between HERG and LERG. (b) Distribution of f_{mean} for HERGs (blue) and LERGs (red) for the constraints on the reference sample given in Sect. 5.4. Bins of 0.01 are used along the x-axis. The absolute values on the y-axis will depend on this bin width. Negative values of f_{mean} indicate that there are less than 100 galaxies in the reference sample of inactive galaxies.

less susceptible to this effect due to their (on average) higher $L_{22\mu\text{m}}$. Considering this redshift effect $dz = 0.06$ is quite large. However, the large redshift range is required to obtain at least 100 comparison galaxies for each radio-loud AGN.

Based on the clear difference in the distribution of f_{mean} we can define a separation criterion between HERGs and LERGs. The magnitude constraints given above and the requirement that $f_{\text{mean}} < 0.05$ give the highest completeness and reliability for this separation method. We achieve a completeness of 87% and 52% for LERGs and HERGs, respectively. The reliability for the separation is 91% for LERGs and 46% for HERGs. These numbers are primarily driven by the redshift constraints and the numerical difference of the two populations. While the fraction of HERGs and LERGs at $f_{\text{mean}} = 0.005$ is significantly different, in absolute number they are about equal. In addition, we find that the specifications above do not constrain the similarity of galaxies as well as derived quantities such as SFR and M_* . In particular, despite the colour constraints the match in SFR is poor to negligible.

5.5 Discussion

We have investigated the mid-IR properties of HERGs and LERGs using a sample of low-redshift radio-loud AGN. Our results are generally consistent with the current view on these two populations of radio-loud AGN as presented by Heckman and Best [6]. HERGs show an increased mid-IR emission with respect to inactive galaxies similar to the host galaxy of the HERG. This excess emission is attributed to the presence of a torus. LERGs follow the mid-IR luminosity distribution set by the inactive galaxy population. In this Section we will first discuss the effects of different mid-IR luminosity calculations on the results. After this we will compare our detailed findings for HERGs and LERGs as well as the potential of separating the two using mid-IR observations with results found in recent literature.

5.5.1 K-correction

Motivated by the low redshift of our sample we have chosen not to include a K-correction in the calculation of $L_{22\mu\text{m}}$. Other authors, such as Gürkan et al. [12, hereafter G14], included a K-correction by assuming the mid-IR spectrum can be described by a power law given by $S_\nu \propto \nu^{-\alpha_{34}}$. Fig. 5.6 shows the value of α_{34} as a function of the 4000 Å break [23] for HERGs (blue squares) and LERGs (red circles) in the BH12 sample as well as the regular galaxies from the VASC (grey contours) with detections in both the 12 and 22 μm WISE bands. We observe that LERGs follow the distribution of spectral slopes found by the regular galaxy population. HERGs on the other hand show $\alpha_{34} = 1.69 \pm 0.55$ (yellow lines) independent of host galaxy colour. This value is lower than $\alpha_{34} = 2.45 \pm 0.88$ (Fig. 5.6, green lines) found by G14 using only narrow-line radio galaxies in the 3CRR population.

Based on Fig. 5.6 one can argue that HERGs and LERGs have a different K-correction. To check the effect of this $L_{22\mu\text{m}}$ is recalculated using the following scheme to determine α_{34} : 1) if the source has a 2σ detection in both the 12 and 22 μm bands of WISE, α_{34} is derived directly from these fluxes. If either W3 or W4 is an upper limit then 2a) a HERG uses $\alpha_{34} = 1.69$, 2b) a LERG or inactive galaxy uses the median value of α_{34} found for all galaxies with similar mass and 4000 Å break. Here similar is defined as a maximum difference of 0.15 and 0.3 in $D_{\text{n}4000}$ and $\log_{10}(M_*/M_\odot)$, respectively. This method of calculating $L_{22\mu\text{m}}$ introduces negligible differences in our results. A comparison between the corrected (using the above scheme or $\alpha_{34} = 2.45$) and uncorrected luminosities shows we underestimate $L_{22\mu\text{m}}$ by up to 50%.

The low redshift of our sample allows us to ignore the K-correction and avoid introducing an a-priori bias through a different α_{34} . However, at higher redshifts a K-correction will be crucial, but this will require a well constrained SED. As shown by Fig. 5.6 there is a large spread in the slope of the SED between 12 and 22 μm for both LERGs and

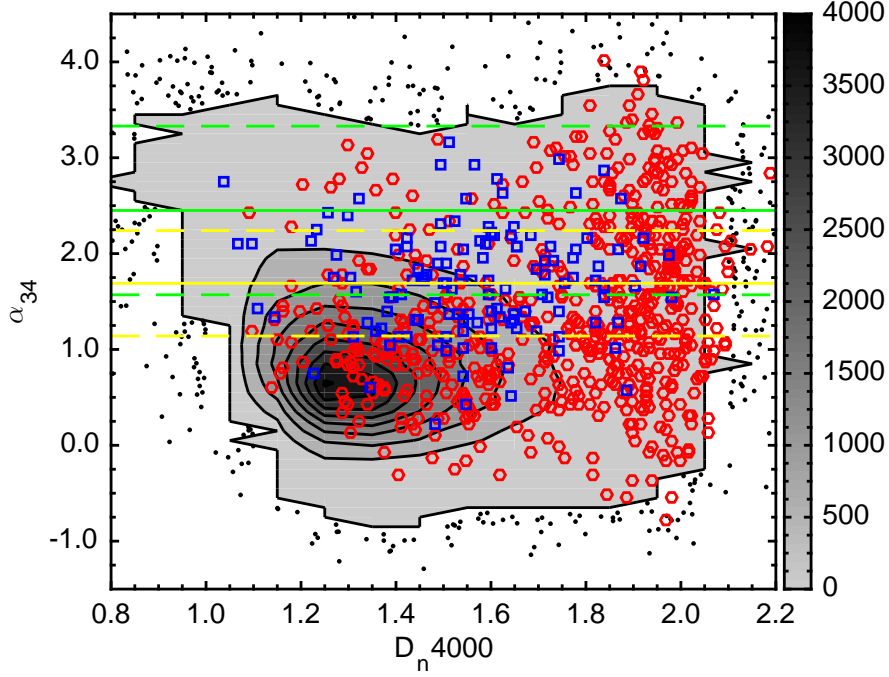


Figure 5.6: α_{34} as a function of the host galaxies 4000 Å break for the LERG (red circles) and HERG (blue squares) from the BH12 sample investigated in this paper. The background contours show the distribution of the regular galaxies from the VASC in the $\alpha_{34} - D_{n4000}$ -plane. The greyscale on the right indicates the number of galaxies per bin of size $(\delta D_{n4000}, \delta \alpha_{34}) = (0.1, 0.1)$. If the number of galaxies is less than 5, the galaxies are shown as black dots instead. The green lines indicate the mean (solid) and $\pm 1\sigma$ (dashed) values of $\alpha_{34} = 2.45 \pm 0.88$ found by G14. The yellow lines show $\alpha_{34} = 1.69 \pm 0.55$ found for the HERG in the BH12 sample.

HERGs. Large differences in the SED of various AGN have also been identified in higher redshift AGN [e.g. 24]. Extrapolation using a single value of α_{34} therefore appears a precarious exercise. Alternatively, one could consider using a lower base wavelength, for example 12 μm . This would allow for a more secure K-correction as the use of α_{34} would be an interpolation. However, at 12 μm the trends presented in this paper are present, but significantly less pronounced.

5.5.2 High-excitation radio galaxies

At least 50% of the HERGs in the BH12 sample show a clear excess of mid-IR emission with respect to comparable inactive galaxies. The additional emission is assumed to be associated with the AGN torus present in these radiatively-efficient accretors. However, there is a subpopulation of HERGs that deviates from this trend. Throughout our analysis we observe a population of HERGs with a very low mid-IR luminosity. For

all these sources the HERG classification was confirmed by visual inspection of their optical spectra from SDSS. A closer inspection of this population of low $L_{22\mu\text{m}}$ HERGs shows:

- They are predominantly hosted by galaxies in the green valley or red sequence that have low SFRs ($SFR < 1.0 M_{\odot}/\text{yr}$).
- We have performed a visual inspection of the radio morphologies of the HERG population as observed by FIRST. Sources were classified as extended (FRI / FRII if possible), point source and unclassifiable. Approximately 65% of the mid-IR weak HERGs are point sources compared to $\sim 50\%$ of the HERGs with excess mid-IR emission. The additional fraction of point sources is predominantly due to a decrease in the fraction of FRII sources.
- The HERGs with an excess $L_{22\mu\text{m}}$ luminosity have more OIII emission than their counterparts without the excess $L_{22\mu\text{m}}$ emission. The median equivalent width (EW) of the OIII emission line is 7 \AA for the HERGs with a low $L_{22\mu\text{m}}$ while the population with a high $L_{22\mu\text{m}}$ has $\text{EW}[\text{OIII}] \sim 13 \text{ \AA}$.
- The fundamental difference between HERGs and LERGs has been suggested to be the Eddington scale accretion rate, $\lambda = \frac{L_{\text{rad}} + L_{\text{mech}}}{L_{\text{Edd}}}$. Fig. 5.7 shows $L_{22\mu\text{m}}$ as a function of λ for all radio-loud AGN in the BH12 sample with a $z < 0.1$. λ was calculated following the method outlined in Best and Heckman [14]. For a secure λ value the redshift of the sources shown is limited to $z < 0.1$. No trends are visible within the limited number of HERGs shown in Fig. 5.7. This is confirmed by a partial correlation analysis that takes into account censored data [25] as shown in Table 5.1. However, when a larger number of (higher redshift, $z < 0.3$) sources are included a significant positive partial correlation is present.

Based on this evidence we hypothesize that the HERGs with low mid-IR luminosities are weak HERGs that have only a small gas supply available to them. This results in an AGN with a lower power and a shorter lifetime. Therefore the host galaxy will dominate the observed mid-IR emission [26] instead of the weaker torus emission. The jet will not have the strength or duration to grow large, thereby explaining the increased number of radio point sources.

Based on the location of composite, Seyfert 2 and LINER galaxies from the SDSS in the $SFR - M_{\star}$ -plane Leslie et al. [27] presented a scenario in which galaxies have episodes of increasingly weaker AGN activity during their evolution from the main sequence of star formation to the red sequence. Analogous to this we speculate that the high power HERGs are the radio-loud equivalent of quasars and are responsible for the initial quenching of its host galaxy and its departure from the main sequence of star formation. During the subsequent evolution to the red sequence further episodes

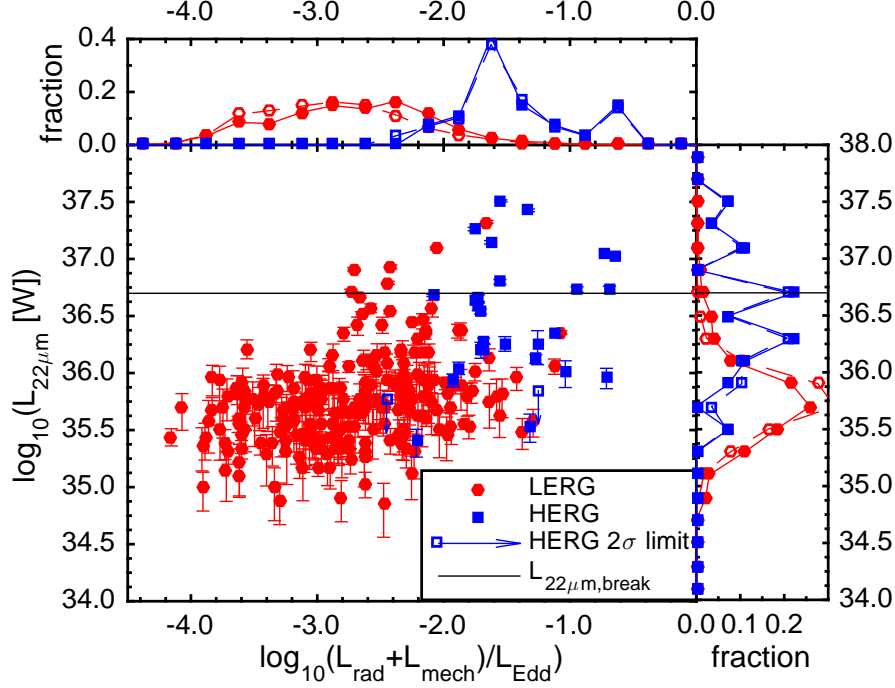


Figure 5.7: $22\ \mu\text{m}$ luminosity as a function of the Eddington-scaled accretion rate, λ , for all LERGs (red circles) and HERGs (blue squares) with a $z < 0.1$. The black line indicates the empirical separation between HERGs and LERGs at $L_{22\mu\text{m},\text{break}} = 10^{36.6}\ \text{W}$ found in Sect. 5.3. Upper limits on the $L_{22\mu\text{m}}$ of HERGs are indicated by open squares. Upper limits for LERG are not shown for clarity. However, the 2σ values span the same parameter space as the LERG detections shown in the figure. (right) A histogram showing the distribution of $L_{22\mu\text{m}}$ for HERGs (blue squares) and LERGs (red circles). (top) A histogram showing the distribution of λ for HERGs (blue squares) and LERGs (red circles). In both histograms the solid lines include only sources with $> 2\sigma$ detections in $L_{22\mu\text{m}}$, while the open symbols connected by dashed lines also include upper limits.

of radio-loud AGN activity will be observable as the low power (mid-IR weak) HERGs. Alternatively, the low mid-IR luminosity could be attributed to the orientation of the HERGs. Podigachoski et al. [28] found that powerful radio galaxies seen on-axis have higher mid-IR luminosities with respect to their edge-on counterparts. These results are supported by radiative transfer models of AGN torii [e.g. 29]. However, a larger fraction of extended radio sources is expected for the less luminous edge-on HERGs. This is the opposite of our observations. Furthermore, the VASC (and by extension the BH12 sample) is inherently biased against quasars and broad-line radio galaxies as their spectra do not allow a reliable derivation of secondary quantities. Based on these arguments we deem this a less likely explanation.

5.5.3 Low-excitation radio galaxies

Our results support the view that LERGs lack an obscuring structure and thus lack the additional mid-IR emission associated with it. Throughout this paper LERGs have followed the mid-IR luminosity distribution set by the inactive galaxy population, suggesting that their mid-IR luminosity is dominated by their host galaxy. This finding is in line with the work of Pace and Salim [13], but in contrast with the findings of G14, which showed a correlation between the luminosity of the radio core and mid-IR luminosity. The latter suggests that there is a jet contribution to the mid-IR luminosity. A partial correlation analysis [25] shows no correlation between the radio and mid-IR luminosity of LERGs. It should be noted, however, that the BH12 sample predominantly contains much weaker radio sources ($S_{1.4\text{GHz}} \geq 5$ mJy or 29.7 mJy at 151 MHz; ~ 16 times fainter than the faintest sample in G14), which might be too weak to provide a measurable contribution to the mid-IR luminosity.

The subpopulation of LERG with high mid-IR luminosities in the BH12 sample is the result of radio-loud AGN being hosted by a population of blue, actively star forming galaxies. These LERGs hosted by the most massive blue galaxies were previously identified by Janssen et al. [22]. The IR-luminous LERGs all have Eddington-scaled accretion rates at the high end of the LERG distribution, as seen in Fig. 5.7. It is also worth noting that LERGs have a weak, but significant, correlation between λ and $L_{22\mu\text{m}}$ (Table 5.1).

5.5.4 Broadband separation methods

As described above, the HERGs and LERGS follow clear trends with respect to their mid-IR luminosity. Despite these trends we have not been able to identify a criterion that separates the two AGN populations with both a high ($> 70\%$) completeness and reliability. Table 5.2 lists for each of the three methods discussed in this paper the completeness and reliability achieved. Besides the obvious issue with the low $L_{22\mu\text{m}}$ HERGs, we have shown that a reliable separation criterion takes into account star formation, redshift and galaxy mass. This would require a lot of additional derived quantities and a-priori calibration using a known dataset before classification is possible. The main weakness of using exclusively optical through mid-IR broadband magnitudes and colours as presented in Sect. 5.4 is the poor constraint on SFR. If this can be remedied with additional observations, this might appear to be a very promising approach.

The poor separation performance is in stark contrast to the findings of G14, who concluded that there exists an empirical cut-off between LERGs and HERGs of $L_{22\mu\text{m}} = 5 \times 10^{43}$ erg/s = $10^{36.7}$ W. This break is remarkably similar to $L_{22\mu\text{m},\text{break}} = 10^{36.6}$ W found in this work. However, were G14 find this cut to be very clean for their sample of radio-loud AGN from the 3CRR, 2Jy, 6CE and 7CE catalogues Fig. 5.1 shows

Table 5.1: Results of the partial correlation analysis following Akritas and Siebert [25]. The significance of the Kendall τ (column 5) indicates the strength of the partial correlation between the variables listed in columns 1 and 2 whilst taking into account the presence of redshift. λ is the Eddington-scale accretion rate of the AGN as described in Section 5.5. The analysis takes into account upper limits. The analysis has been performed on three samples: 1) BH12; the complete sample studied in this paper and described in Section 5.2. 2) Eq.S.; the sample of radio-loud AGN selected in Appendix A to mimic the original sample of G14. 3) $z < 0.1$; all sources in the BH12 sample with $z < 0.1$ to allow a reliable determination of λ as described in Section 5.5.

Abscissa	Ordinate	Sample	No. Sources	τ/σ
$L_{1.4\text{GHz}}$	$L_{22\mu\text{m}}$	LERG (BH12)	1000 ^a	0.79
		HERG (BH12)	272	1.56
$L_{1.4\text{GHz}}$	$L_{22\mu\text{m}}$	LERG (Eq.S.)	70	1.63
		HERG (Eq.S.)	151	1.76
λ	$L_{22\mu\text{m}}$	LERG ($z < 0.1$)	950	7.10
		HERG ($z < 0.1$)	29	0.73

^a 1000 LERGs are randomly selected from the complete BH12 sample containing 8263 sources to limit the required computation time.

it performs very poorly for the lower luminosity BH12 sample. Using mock samples drawn from the BH12 catalogue to mimic the G14 samples we show that the observed differences are the result of the differences in sample size, flux limit and relative number of HERGs and LERGs between the G14 and BH12 samples (See Appendix A). When looking at a low number of BH12 sources with a relatively high HERG fraction and high radio luminosities the empirical cut-off by G14 also appears as a clean separator. This clearly shows that the numerical dominance of LERGs within the BH12 sample has a

Table 5.2: The completeness and reliability of the three separation criteria discussed in this paper: single valued break in $L_{22\mu\text{m}}$ (Section 5.3); advanced SFR-dependent $L_{22\mu\text{m}}$ -break (Section 5.3.1); comparison with inactive galaxies (Section 5.4). For each criteria the completeness and reliability is listed if only $> 2\sigma$ detections in $L_{22\mu\text{m}}$ are taken into account. In addition, for the first two criteria the best and worst case values are listed (in brackets) when the upper limits on $L_{22\mu\text{m}}$ are taken into account.

		G14 $L_{22\mu\text{m}}$ -break	Advanced $L_{22\mu\text{m}}$ -break	$f_{\text{mean}} < 0.05$
Completeness	LERG	73% (97% - 58%)	67% (97% - 43%)	87%
	HERG	68% (65% - 22%)	75% (74% - 25%)	52%
Reliability	LERG	93% (98% - 94%)	94% (99% - 92%)	91%
	HERG	31% (94% - 2%)	29% (55% - 2%)	46%

strong impact on the performance of any separation criterion. The number of LERGs in the BH12 sample as a whole is so great that their completeness and reliability are not significantly affected by the exact separation criterion. In turn, a few misidentified LERGs have a dramatic effect on the performance of the HERG population.

5.6 Conclusion

We examined the mid-IR properties of a sample of HERGs and LERGs identified within the SDSS using WISE observations. Using these measurements we have investigated the potential to separate the two populations of radio-loud AGN based exclusively on broadband observations. We conclude, that:

1. LERGs have the same mid-IR luminosity distribution as inactive galaxies with the same mass, star formation rate and redshift as the LERG's host.
2. HERGs, generally, have a mid-IR luminosity comparable to or in excess of the top 5% most luminous inactive galaxies similar to the AGN host.
3. There is a subpopulation of HERGs that have a $L_{22\mu\text{m}}$ in line with inactive galaxies. These are predominantly found in the red sequence and green valley.
4. As a result of the above the HERG population has 0.5 dex higher $L_{22\mu\text{m}}$ than the LERG population.

Despite these trends we have not been able to identify a clear criterion using exclusively broadband observations based on which HERGs and LERGs can be separated without significant cross-contamination. This is not only the result of the low-luminosity HERGs, but also due to:

- The large inherent spread in the mid-IR luminosity of radio-loud AGN and inactive galaxies. This intrinsic spread is (at least partially) due to dust heated by young star, which dominates $L_{22\mu\text{m}}$ in LERGs and a fraction of the HERGs [26].
- The poor constraint on active star formation provided by using only optical through mid-IR observations.
- The numerical dominance of LERGs within the BH12 sample.

Comparing $L_{22\mu\text{m}}$ of a radio-loud AGN to that of similar inactive counterparts has shown to be a powerful way to identify HERGs. This is especially true, if host galaxy mass, star formation rate and redshift can all be properly constrained. However, additional multiwavelength observations (other than SDSS and WISE) will be required to achieve this. Far-IR and UV observations would be first additions to enable a rigid

estimation the star formation contamination. The next step in HERGs and LERGs separation will be using SED decomposition which measures the stellar, dust and AGN components by fitting them to UV through far-IR broadband data. [30, 31].

References

- [1] A. C. Fabian, J. S. Sanders, G. B. Taylor, S. W. Allen, C. S. Crawford, et al., *A very deep Chandra observation of the Perseus cluster: shocks, ripples and conduction*, Monthly Notices of the Royal Astronomical Society **366**, 417 (2006).
- [2] P. N. Best, C. R. Kaiser, T. M. Heckman, and G. Kauffmann, *AGN-controlled cooling in elliptical galaxies*, Monthly Notices of the Royal Astronomical Society **368**, L67 (2006).
- [3] P. N. Best, A. von der Linden, G. Kauffmann, T. M. Heckman, and C. R. Kaiser, *On the prevalence of radio-loud active galactic nuclei in brightest cluster galaxies: implications for AGN heating of cooling flows*, Monthly Notices of the Royal Astronomical Society **379**, 894 (2007).
- [4] D. J. Croton, V. Springel, S. D. M. White, G. De Lucia, C. S. Frenk, et al., *The many lives of active galactic nuclei: cooling flows, black holes and the luminosities and colours of galaxies*, Monthly Notices of the Royal Astronomical Society **365**, 11 (2006).
- [5] R. G. Bower, A. J. Benson, R. Malbon, J. C. Helly, C. S. Frenk, et al., *Breaking the hierarchy of galaxy formation*, Monthly Notices of the Royal Astronomical Society **370**, 645 (2006).
- [6] T. M. Heckman and P. N. Best, *The Coevolution of Galaxies and Supermassive Black Holes: Insights from Surveys of the Contemporary Universe*, Annual Review of Astronomy and Astrophysics **52**, 589 (2014).
- [7] E. E. Rigby, P. N. Best, M. H. Brookes, J. A. Peacock, J. S. Dunlop, et al., *The luminosity-dependent high-redshift turnover in the steep spectrum radio luminosity function: clear evidence for downsizing in the radio-AGN population*, Monthly Notices of the Royal Astronomical Society **416**, 1900 (2011).
- [8] E. E. Rigby, J. Argyle, P. N. Best, D. Rosario, and H. J. A. Röttgering, *Cosmic downsizing of powerful radio galaxies to low radio luminosities*, Astronomy & Astrophysics **581**, A96 (2015).
- [9] P. N. Best, L. M. Ker, C. Simpson, E. E. Rigby, and J. Sabater, *The cosmic evolution of radio-AGN feedback to $z = 1$* , Monthly Notices of the Royal Astronomical Society **445**, 955 (2014).

-
- [10] D. G. York, J. Adelman, J. E. Anderson Jr., S. F. Anderson, J. Annis, et al., *The Sloan Digital Sky Survey: Technical Summary*, The Astronomical Journal **120**, 1579 (2000).
- [11] C. Stoughton, R. H. Lupton, M. Bernardi, M. R. Blanton, S. Burles, et al., *Sloan Digital Sky Survey: Early Data Release*, The Astronomical Journal **123**, 485 (2002).
- [12] G. Gürkan, M. J. Hardcastle, and M. J. Jarvis, *The Wide-field Infrared Survey Explorer properties of complete samples of radio-loud active galactic nucleus*, Monthly Notices of the Royal Astronomical Society **438**, 1149 (2014).
- [13] C. Pace and S. Salim, *Suppression of Star Formation in the Hosts of Low-excitation Radio Galaxies*, The Astrophysical Journal **818**, 65 (2016).
- [14] P. N. Best and T. M. Heckman, *On the fundamental dichotomy in the local radio-AGN population: accretion, evolution and host galaxy properties*, Monthly Notices of the Royal Astronomical Society **421**, 1569 (2012).
- [15] J. J. Condon, W. D. Cotton, E. W. Greisen, Q. F. Yin, R. A. Perley, et al., *The NRAO VLA Sky Survey*, The Astronomical Journal **115**, 1693 (1998).
- [16] R. H. Becker, R. L. White, and D. J. Helfand, *The FIRST Survey: Faint Images of the Radio Sky at Twenty Centimeters*, The Astrophysical Journal **450**, 559 (1995).
- [17] J. Brinchmann, S. Charlot, S. D. M. White, C. Tremonti, G. Kauffmann, et al., *The physical properties of star-forming galaxies in the low-redshift Universe*, Monthly Notices of the Royal Astronomical Society **351**, 1151 (2004).
- [18] E. L. Wright, P. R. M. Eisenhardt, A. K. Mainzer, M. E. Ressler, R. M. Cutri, et al., *The Wide-field Infrared Survey Explorer (WISE): Mission Description and Initial On-orbit Performance*, The Astronomical Journal **140**, 1868 (2010).
- [19] Y.-Y. Chang, A. van der Wel, E. da Cunha, and H.-W. Rix, *Stellar Masses and Star Formation Rates for 1M Galaxies from SDSS+WISE*, The Astrophysical Journal Supplement Series **219**, 8 (2015).
- [20] M. R. Blanton, D. J. Schlegel, M. A. Strauss, J. Brinkmann, D. Finkbeiner, et al., *New York University Value-Added Galaxy Catalog: A Galaxy Catalog Based on New Public Surveys*, The Astronomical Journal **129**, 2562 (2005).
- [21] E. D. Feigelson and P. I. Nelson, *Statistical methods for astronomical data with upper limits. I - Univariate distributions*, The Astrophysical Journal **293**, 192 (1985).
- [22] R. M. J. Janssen, H. J. A. Röttgering, P. N. Best, and J. Brinchmann, *The triggering probability of radio-loud AGN. A comparison of high and low excitation radio galaxies in hosts of different colors*, Astronomy & Astrophysics **541**, A62 (2012).

- [23] M. L. Balogh, S. L. Morris, H. K. C. Yee, R. G. Carlberg, and E. Ellingson, *Differential Galaxy Evolution in Cluster and Field Galaxies at $z \sim 0.3$* , The Astrophysical Journal **527**, 54 (1999).
- [24] K. I. Caputi, *A Generalized Power-law Diagnostic for Infrared Galaxies at $z > 1$: Active Galactic Nuclei and Hot Interstellar Dust*, The Astrophysical Journal **768**, 103 (2013).
- [25] M. G. Akritas and J. Siebert, *A test for partial correlation with censored astronomical data*, Monthly Notices of the Royal Astronomical Society **278**, 919 (1996).
- [26] G. Gürkan, M. J. Hardcastle, M. J. Jarvis, D. J. B. Smith, N. Bourne, et al., *Herschel-ATLAS: the connection between star formation and AGN activity in radio-loud and radio-quiet active galaxies*, Monthly Notices of the Royal Astronomical Society **452**, 3776 (2015).
- [27] S. K. Leslie, L. J. Kewley, D. B. Sanders, and N. Lee, *Quenching star formation: insights from the local main sequence*, Monthly Notices of the Royal Astronomical Society **455**, L82 (2016).
- [28] P. Podigachoski, P. Barthel, M. Haas, C. Leipski, and B. Wilkes, *The Unification of Powerful Quasars and Radio Galaxies and Their Relation to Other Massive Galaxies*, The Astrophysical Journal Letters **806**, L11 (2015).
- [29] M. Schartmann, K. Meisenheimer, M. Camenzind, S. Wolf, K. R. W. Tristram, et al., *Three-dimensional radiative transfer models of clumpy tori in Seyfert galaxies*, Astronomy & Astrophysics **482**, 67 (2008).
- [30] S. Berta, D. Lutz, P. Santini, S. Wuyts, D. Rosario, et al., *Panchromatic spectral energy distributions of Herschel sources*, Astronomy & Astrophysics **551**, A100 (2013).
- [31] G. Calistro Rivera, E. Lusso, J. F. Hennawi, and D. W. Hogg, *AGNfitter: A Bayesian MCMC Approach to Fitting Spectral Energy Distributions of AGNs*, The Astrophysical Journal **833**, 98 (2016).

Chapter 6

Controlled illumination of microwave kinetic inductance detectors

6.1 Microwave kinetic inductance detectors

Microwave Kinetic Inductance Detectors (MKIDs) [1] are microwave resonators made from a superconducting material and optimized to absorb radiation of a desired frequency. Inside a superconductor the electrons form Cooper pairs, which can carry current without resistance. However, in an alternating electric field the inertia of the Cooper pairs can be expressed as a kinetic inductance. Hence, the inductance and resistance in a superconducting resonator depends on the number of Cooper pairs and unpaired electrons (or quasiparticles). When electromagnetic (EM) radiation is absorbed with an energy larger than the binding energy of the Cooper pairs ($h\nu > 2\Delta$), the Cooper pairs are broken and quasiparticles are created (Fig. 6.1(a)). This changes the resistance and inductance of the superconductor. These changes can be observed by creating a resonant circuit out of the superconducting material. Superconducting microwave resonators upon which MKIDs are based may be represented by the RLC-circuit shown in Fig. 6.1(b). The variable resistance and inductance are the result of the superconductor's sensitivity to radiation. This resonant circuit is coupled either capacitively or inductively to a feedline. The forward transmission of the feedline will show a dip at the resonance frequency of the resonator as shown in Fig. 6.1(c). For increased illumination the increased resistance decreases the depth and increases the width of the resonance feature. In addition, the change in kinetic inductance decreases the resonance frequency. This is also shown in Fig. 6.1(c).

Two incarnations of MKIDs are currently actively investigated for application in astronomy: Lumped Element KIDs (LEKIDs) and antenna-coupled KIDs. LEKIDs are based on a lumped capacitor and inductor [2]. An example is shown in Fig. 6.2(a). LEKIDs are generally simple planar structures making fabrication easier. Radiation is directly absorbed in the inductor, which enables LEKIDs to detect throughout the EM spectrum. However, the direct absorption in the resonator couples the absorption

properties of the LEKID to the resonator properties, which determines their sensitivity. This makes the design of LEKIDs more challenging [3].

An example of an antenna-coupled MKID is shown in Fig. 6.2(b). Antenna-coupled MKIDs use a distributed resonator into which radiation is coupled using a planar antenna. The advantage of this implementation is that the radiation coupling and detector performance are decoupled and can be individually optimised. However, their application is limited to frequencies below 10 THz due to the fabrication limits on the antenna dimensions.

In this Chapter we will review the operational principle of antenna-coupled MKIDs. Sect. 6.2 discusses the conductivity of metals, insulators and semiconductors using the semi-classical Drude-Sommerfeld model. In addition, it describes the microscopic process responsible for superconductivity and the complex conductivity that results from the formation of Cooper pairs. Sect. 6.3 uses this complex conductivity to review the response to temperature and radiation of distributed superconducting microwave resonators, which are at the heart of antenna-coupled MKIDs. A summary of known noise sources is given as well. Sect. 6.4 presents the cryogenic (optical) setup used in Chapters 7 and 8 to perform a controlled optical measurement of MKIDs. We will focus on the optical aspects and mathematically define the emission seen by MKIDs mounted in the setup. Sect. 6.5 discusses the coupling of radiation into an MKID. After a discussion of the general formalism, we will apply this to determine the optical throughput in the setup discussed in Sect. 6.4. Sect. 6.6 discusses some considerations in MKID design to achieve photon noise limited performance. It summarizes how a measurement of the photon noise can be used to experimentally determine the detector efficiency of MKIDs. Finally, Sect. 6.7 will give in detail the fabrication procedure used to manufacture the hybrid NbTiN-Al MKIDs used in Chapters 7 and 8.

6.2 Electrical conductivity

6.2.1 Metals, insulators and semiconductors

The (crystalline) solids observed in the world around us can be divided into three categories based on their electrical conductivity at room temperature: metals, semiconductors and insulators. Metals (both elemental and alloys) have a high conductivity, $\sigma > 10^3 \Omega^{-1}\text{cm}^{-1}$. Plastics and ceramics, which typically are insulators, have a conductivity $\sigma < 10^{-8} \Omega^{-1}\text{cm}^{-1}$. Semiconductors have a room temperature conductivity in-between these values. This difference in electrical resistance is the result of the number of electrons that are free to move through the material, n_e , and their mobility, μ_e . In a single atom, electrons occupy the quantized energy levels of the orbitals. However, when multiple atoms together form the lattice of a solid, these orbitals broaden and together form a quasi-continuous energy band: a region in energy in which many

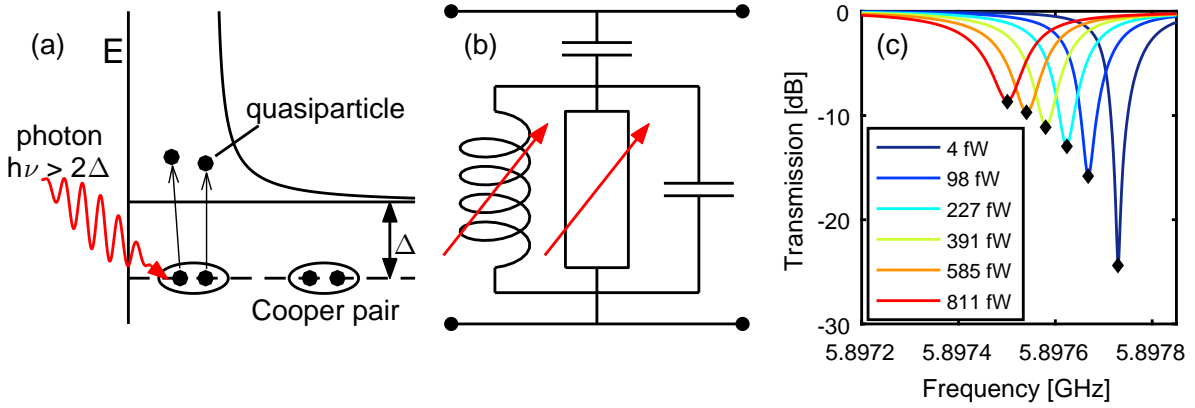


Figure 6.1: Operational principle of MKIDs. (a) Inside a superconductor electrons form (Cooper) pairs, which can carry current without resistance. However, these Cooper pairs act as a (kinetic) inductance when an alternating electric field is applied. When EM radiation with a energy larger than the binding energy of the pairs ($h\nu > 2\Delta$) is absorbed in a superconductor the Cooper pairs are broken. This changes the resistance and (kinetic) inductance of the superconductor and makes the resistance and inductance of the resonator luminosity dependent. (b) The circuit diagram for an electrical RLC resonator, which is capacitively coupled to the feedline. In the case of an MKID R and L are determined by the superconductor and therefore depend on the intensity of the pair-breaking radiation. (c) The RLC resonator shown in (b) creates a dip in the forward transmission of the feedline at its resonance frequency. For increased illumination the increased resistance decreases the depth of the resonance feature. In addition, the change in kinetic inductance decreases the resonance frequency.

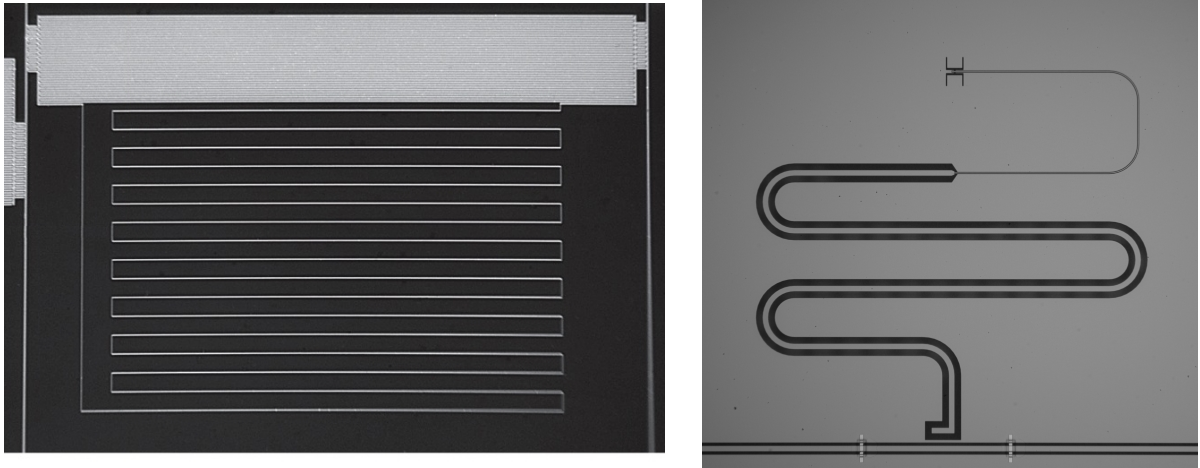


Figure 6.2: Examples of a lumped element KID (left) and an antenna-coupled MKID, which uses a distributed resonator (right). The lumped element KID consists of a meandering inductor in the bottom of the image and a capacitor at the top. This KID is capacitively coupled to the feedlines on both sides of the resonator. The distributed resonator is capacitively coupled to the feedline at the bottom of the image. A microlens focusses the light on the sensitive part of each resonator. Image of the lumped element KID is taken from McCarrick et al. [4].

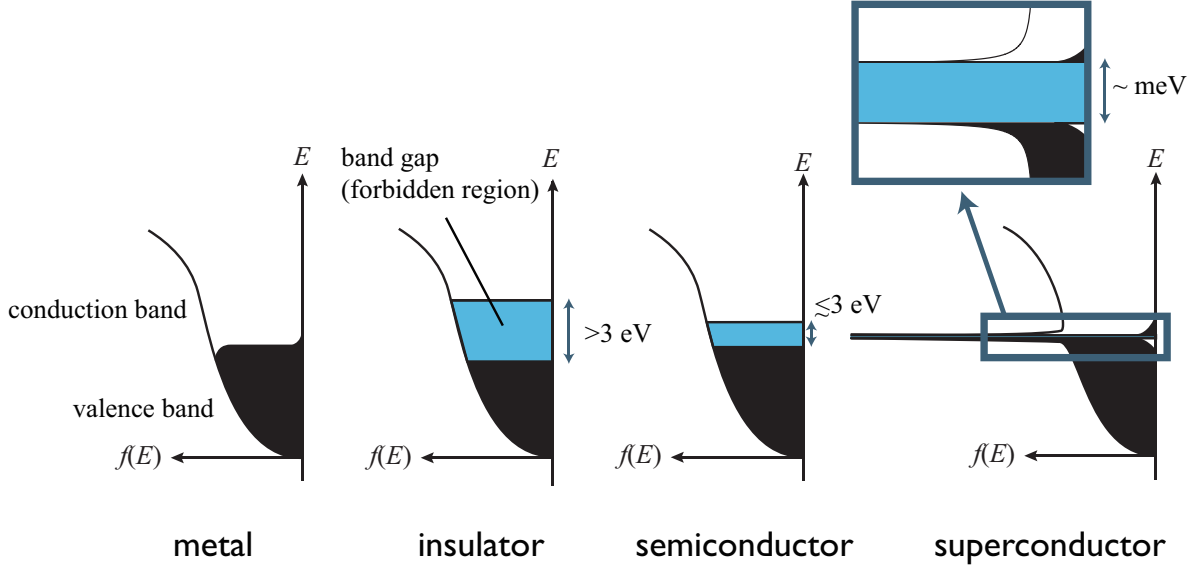


Figure 6.3: The density of electronic states for metals, insulators, semiconductors and superconductors. In black the occupation of states at a low temperature is shown. The horizontal edge of this region is located at the Fermi energy. The Fermi-Dirac distribution at low temperatures creates free electrons in the metal and superconductor, but not in the semiconductor and insulator, both of which have a larger gap. Image courtesy of Endo [5]

states are available for electrons to occupy. Each of these states is associated with an energy, E . Due to the Pauli exclusion principle only a single electron can occupy a state. As such, the lowest energy available to the system is when all states up to an energy E_F , the Fermi energy, are filled. In the case of insulators or semiconductors the Fermi level is located in the energy gap between two bands, as shown in Fig. 6.3. For metals E_F is located inside a band.

This difference in their density of states, $g(E)dE$, which describes the number of states in an energy range dE around energy E , plays a key role in the conductivity of a material. The ability of electrons to act as charge carriers depends on the availability of vacant electronic states. This allows the electrons to increase their energy (i.e., accelerate) when an electric field is applied. In metals these vacant states are readily available as the Fermi energy is located inside an energy band and the typical energy change of $\sim \mu\text{eV}$ can be accommodated for many electrons. As a result metals have a high number of electrons ($n_e \sim 10^{11} \mu\text{m}^{-3}$ [6]) which can participate in the electrical conduction.

In semiconductors and insulators no vacant states are available in the lower energy band or ‘valence’ band. For conduction to occur, external energy needs to be supplied to generate electrons in the higher energy conduction band where vacant states are present (as well as creating a limited amount of free states in the valence band) [7]. The two most common mechanisms to excite electrons are thermal fluctuations or the

absorption of photons. The latter is readily used in digital cameras, which use semiconducting detectors. The energy gap of semiconductors is ~ 1 eV (Si $E_{\text{gap}} = 1.09$ eV, Ge $E_{\text{gap}} = 0.72$ eV), which enables near-infrared and optical photons to create conduction electrons. Hence the conductivity of the semiconductor depends on the flux of optical photons. Thermal fluctuations redistribute the electrons by providing energy during collisions between the electrons and the lattice vibrations (phonons). The energy distribution function of fermions $f(E, T)$ in thermal equilibrium at temperature T is given by the Fermi-Dirac distribution

$$f_{\text{FD}}(E, T) = \frac{1}{1 + \exp(E - E_{\text{F}}/k_{\text{B}}T)} \quad (6.1)$$

where k_{B} is Boltzmann's constant. It can be seen from this equation that the number of conduction electrons in an insulator which has an $E_{\text{gap}} \gtrsim 10$ eV, will be negligible. In addition, UV or X-ray photons will be required for photo-excitation. This means that the flow of electrons from the valence to the conduction band in insulators is negligible under normal conditions.

The density of conduction electrons may be estimated by [6]

$$n_{\text{e}}(T) = \int_{E_{\text{c}}}^{\infty} g(E) f(E) dE \quad (6.2)$$

Here E_{c} is the lowest energy available in the conduction band.

An intuitive model to understand the conduction of metals and semiconductors in the presence of a charge carrier density, n_{c} , is the classical Drude model [7]. This model describes the motion of conducting particles in a lattice as competition between the acceleration by the electric field, \vec{E} , and relaxation by scattering events.

$$m \frac{\partial \vec{v}}{\partial t} = e\vec{E} - \frac{m\vec{v}}{\tau} \quad (6.3)$$

Here m , e and v are the mass, charge and average velocity of the charge carriers. τ is the relaxation time, or equivalently the mean time between two scattering events. In the presence of an alternating electric field $\vec{E}(t) = \text{Re}(\vec{E}(\omega)e^{-i\omega t})$ and considering Ohm's law

$$\vec{j}(\omega) = n_{\text{c}}e\vec{v} = \sigma(\omega)\vec{E}(\omega) \quad (6.4)$$

we can obtain the complex conductivity σ of the material [6]

$$\sigma(\omega) = \frac{n_{\text{c}}e^2\tau/m_{\text{eff}}}{1 - i\omega\tau} = \frac{n_{\text{c}}e^2\tau}{m_{\text{eff}}(1 + (\omega\tau)^2)} + i\omega \frac{n_{\text{c}}e^2\tau^2}{m_{\text{eff}}(1 + (\omega\tau)^2)} = \sigma_1 + i\sigma_2 \quad (6.5)$$

In the crystal lattice of a metal the collisions are either with thermally excited phonons or impurities in the lattice. Following Matthiessen's rule $1/\tau(T) = 1/\tau_{\text{ph}}(T) + 1/\tau_0$. τ_{ph} describes the temperature dependent electron-phonon interactions. τ_{ph} is in the

order of 10^{-14} s at room temperature and decreases with temperature as the number of thermally excited phonons decreases. Near room temperature $\tau_{\text{ph}} \propto T^{-1}$ for most metals. τ_0 describes the temperature independent impurity scattering. For metals, where $\partial n_c / \partial T \approx 0$, this results in a linear decrease of the resistivity at high temperatures (> 50 K). However, at low temperatures (< 15 K) impurity scattering dominates and a residual resistance remains. This residual resistance is determined by the purity of the metal as can be seen in the left-hand side panel of Fig. 6.4, which shows the resistivity of copper as a function of temperature [8]. While conduction electrons inside a semiconductors also experience scattering, they have a strong increase in conductivity with temperature. This is driven by the increase in n_c with increasing T . Around room temperature the changes in n_c and τ_{ph} become comparable and the conductivity becomes a weak function of temperature [7].

In Eq. 6.5 both the resistive (real) part of the conductivity and inductive (imaginary) part can be recognized. The imaginary part is the result of the inertia of the charge carriers and is often called the kinetic inductance. Because of the short scattering times in normal metals (even at low temperatures), both the inductive term of the complex conductivity and the $\omega^2 \tau^2$ term are negligible.

The classical Drude model discussed above disregards the Coulomb interactions between the electrons and ions and between different electrons. A quantum mechanical description of these effects would consider the collective behaviour of all particles. However, due to screening effects, this collective behaviour can be described in terms of ‘electron-like’ quasiparticles. The Landau quasiparticles in a normal metal have only subtle differences with the free electrons of the Drude-Sommerfeld model, which can be captured using an effective mass, m_{eff} , or an effective density of states [9].

6.2.2 Superconductivity

When researching the low temperature electrical properties of pure metals [11], Kamerlingh Onnes [12] discovered in 1911 that the electrical resistance of mercury disappeared at temperatures below a critical temperature, T_c . He later found the same behaviour for lead and tin [13]. This fourth category of electrical conduction is superconductivity. Superconductivity has two characteristic macroscopic effects: absence of DC resistance and the exclusion of a magnetic field from the interior of the superconductor, i.e. the Meissner effect [14]. The latter is true both when a superconductor enters a magnetic field and when the sample is cooled through T_c while in a magnetic field.

A microscopic description of these phenomena was given in 1957 by the BCS theory [15]. Inside a superconductor the conduction electrons form Cooper pairs. Cooper pairs are pairs of electrons with opposite momentum and spin, which are weakly bound through electron-phonon interaction. A simplified description of this process is the following. As an electron passes it attracts the nearby lattice ions through Coulomb interaction.

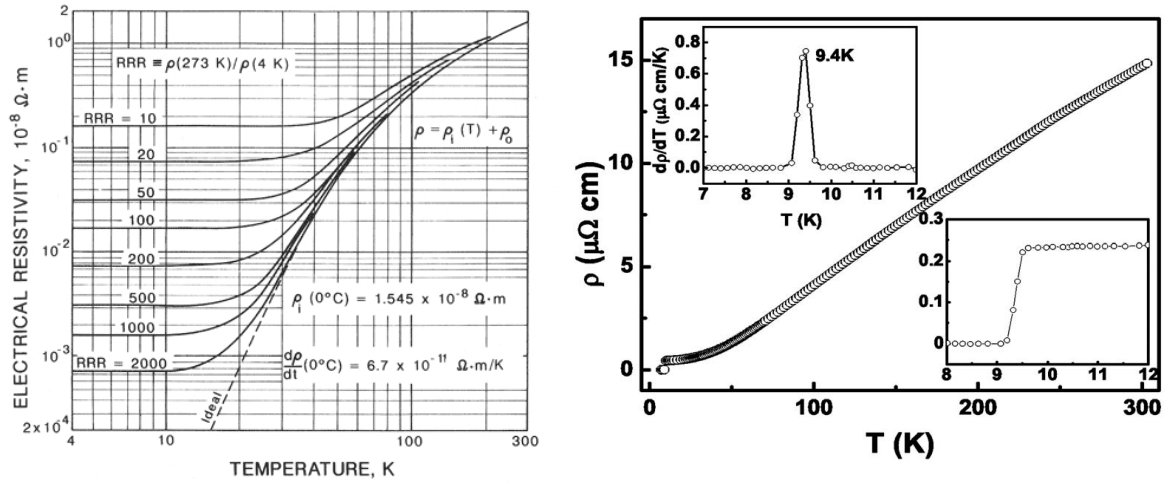


Figure 6.4: The resistivity of copper (left) and niobium (right) as a function of temperature. At temperatures above ~ 50 K the resistivity increases linearly with temperature. Below ~ 50 K the resistivity saturates at a limiting value ρ_0 . ρ_0 decreases for increasing purity of the material. This effect can be seen for copper in the left panel. The insets of the right panel shows the transition of Niobium into the superconducting state at a temperature of $T_c = 9.4$ K. Below this temperature the resistivity is negligible. Images reproduced from Powell and Fickett [8] and Soni and Okram [10].

However, as the ions are much more massive their displacement will remain after the electron has moved on. This leaves a positively charged wake behind the electron. The positively charged region attracts further electrons, thereby coupling their presence to that of the first electrons. The sphere of influence of this first electron or the size of the Cooper pair is called the coherence length, $\xi_0 = \hbar v_F / \pi \Delta_0$, with v_F the Fermi velocity and \hbar the reduced Planck constant and Δ_0 the energy gap at $T = 0$.

As a result of the weak attractive interaction, the electrons condense into a collective superconducting state. This state can be described by a single wavefunction $|\Delta|e^{i\phi}$ with a well-defined phase ϕ . The Cooper-pair density $n_s \propto |\Delta|^2$. Δ is half the size of the energy gap created in the superconducting density of states as a result of the attractive electron-phonon interaction. The superconducting bandgap is illustrated in Fig. 6.3 and is typically in the order of a few meV. The temperature dependence of Δ can be obtained numerically by inversion of

$$\frac{1}{N_0 V_{sc}} = \int_{\Delta(T)}^{k_B T_D} \frac{1 - 2f(E)}{\sqrt{E^2 - \Delta^2(T)}} dE \quad (6.6)$$

Here N_0 is the single spin density of states at the Fermi energy, V_{sc} is the potential energy describing the attractive electron-phonon interaction and T_D the Debye temperature which represents the highest energy state available to phonons in the system. In thermal equilibrium, $f(E)$ is the Fermi-Dirac distribution given by Eq. 6.1, with the Fermi

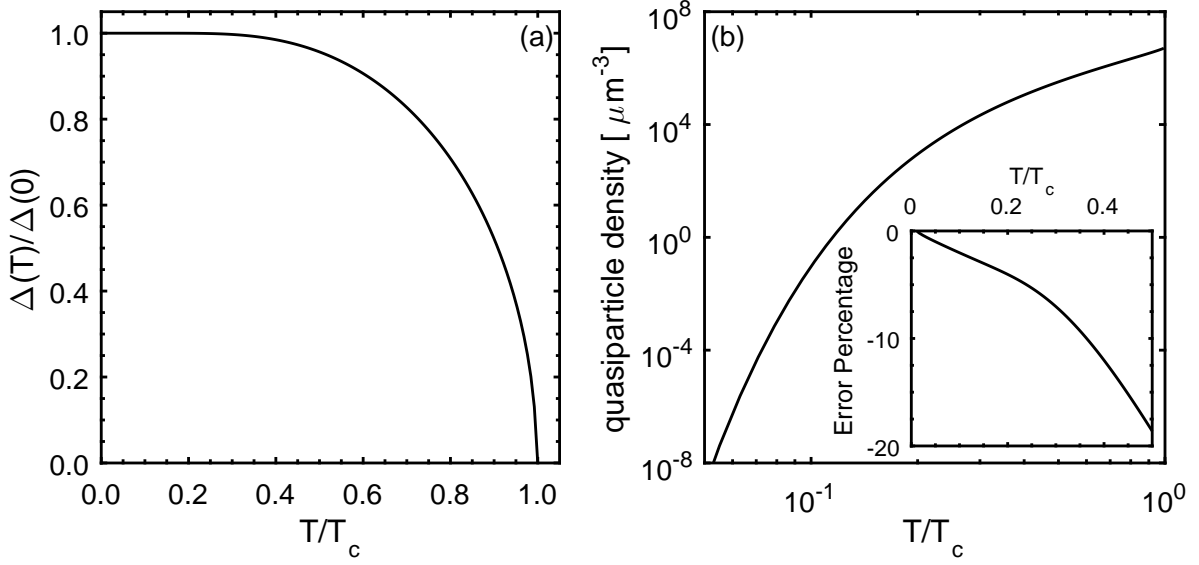


Figure 6.5: (a) The superconducting gap, Δ as a function of temperature. Δ is normalized to the value at $T = 0$ and the temperature is scaled to T_c . (b) The quasiparticle density, n_{qp} , in Al as a function of the normalized temperature T/T_c . At $T < 0.1T_c$ n_{qp} decreases exponentially. The inset in panel (b) shows the error in n_{qp}^0 calculated by Eq. 6.10. This error $(n_{qp}^0 - n_{qp})/n_{qp}$ is determined by comparing n_{qp}^0 to n_{qp} determined using the full integrals of Eq. 6.8 and a temperature dependent gap. Images inspired by de Visser [16] and Vardoulakis [17].

energy taken as the zero level, i.e. $E_F = 0$. The resulting temperature dependence of Δ is shown in Fig. 6.5(a). At $T = 0$ Δ is given by the BCS value Δ_0 [15].

$$2\Delta_0 = 3.52k_B T_c \quad (6.7)$$

Quasiparticle generation

Due to the absence of states around the Fermi energy, the superconducting electrons cannot be scattered unless an energy $> 2\Delta$ is invested to break the Cooper pair and bridge the superconducting energy gap. The breaking of Cooper pairs creates excitations inside the superconductor, which are generally referred to as (Bogoliobov) quasiparticles. The quasiparticles describe the collective behavior of all filled states above the Fermi energy and all empty state below it. However, they can be treated as a single fermionic particle.

Three main processes have been identified inside MKIDs, which are responsible for the generation of quasiparticles: temperature, absorption of pair breaking photons ($h\nu > 2\Delta$) [18, 19] and the absorption of microwave photons from the readout system ($h\nu < 2\Delta$) [16, 20, 21]. Each of these processes changes the quasiparticle energy distribution $f(E) = f(E, T, P_{\text{opt}}, P_{\mu\text{w}})$, which in turn changes the density of quasipar-

ticles, n_{qp} , inside the superconductor.

$$n_{\text{qp}}(T) = 4N_0 \int_0^\infty N_s(E, T) f(E) dE \quad (6.8)$$

Here N_s is the normalized BCS quasiparticle density of states [15].

$$N_s(E, T) = \text{Re} \left(\frac{E}{\sqrt{(E)^2 - \Delta^2(T)}} \right) \quad (6.9)$$

In thermal equilibrium $f(E)$ is given by the Fermi-Dirac distribution presented in Eq. 6.1. The quasiparticle density in Al ($\Delta_0 = 193 \mu\text{eV}$, $N_0 = 1.74 \times 10^{10} \text{ eV}^{-1} \mu\text{m}^{-3}$ [17]) as a function of T/T_c is shown in Fig. 6.5(b). At low temperatures the density of thermally excited quasiparticles may be approximated using

$$n_{\text{qp}}^0 = 2N_0 \sqrt{2\pi k_B T \Delta_0} \exp \left(\frac{-\Delta_0}{k_B T} \right) \quad (6.10)$$

This approximation is correct within 5% for $T < 0.2T_c$ as shown by the inset of Fig. 6.5(b). However, instead of a ‘random’ error it is a systematic underestimation which can influence the response analysis of MKIDs as shown in Ch. 8.

When photons with an energy $h\nu > 2\Delta$ are absorbed in a superconductor, these can directly break Cooper pairs. If the photon arrival rate is high with respect to the quasiparticle recombination time, τ_{qp} (discussed below), the superconductor will experience a continuous influx of absorbed power, P_{abs} . The number of additional quasiparticles, N_{qp} generated by P_{abs} in a steady state can be estimated using [22]

$$\eta_{\text{pb}} P_{\text{abs}} = \frac{N_{\text{qp}} \Delta}{\tau_{\text{qp}}} \quad (6.11)$$

η_{pb} is the pair breaking efficiency which reflects the fact that the complex conductivity discussed in Sect. 6.2.2 is most sensitive to quasiparticles at $E = \Delta$. High energy (X-ray) photons will create a photo-electron, which through electron-electron and electron-phonon interactions will cascade down in energy to create many quasiparticles with an average energy of 1.7Δ or equivalently $\eta_{\text{pb}} = 0.57$ [23, 24]. Most of this energy is lost in the slower, final stage of electron-phonon interactions. In this stage energy is carried away by the lattice in the form of phonons with an energy $< 2\Delta$, which can no longer break Cooper pairs. Recent simulations by Guruswamy et al. [19] for photons with energy $2 < E_{\text{ph}}/\Delta < 10$ have shown that pair breaking photons actually create a non-equilibrium distribution, $f(E)$. The effective η_{pb} experienced by MKIDs depends on the electron-phonon interaction time, the phonon escape time and the photon energy. $\eta_{\text{pb}} = 1$ for $E_{\text{ph}} \approx 2\Delta$ and decreases to $\eta_{\text{pb}} \approx 0.6$ for $E_{\text{ph}} > 4\Delta$. This was experimentally verified by de Visser et al. [25].

The absorption of microwave photons by already existing quasiparticles also creates

a non-thermal $f(E)$ that shows an increased occupation of states at multiples of $h\nu$ above the energy gap [20, 26]. Through sequential absorption of multiple microwave photons quasiparticles can reach energies $> 4\Delta$. When these quasiparticles decay to a state near the gap they release a phonon with an energy $> 2\Delta$, which can in turn break a Cooper pair. This method of quasiparticle generation through the absorption of microwave power is extensively discussed by de Visser [16]. Through the redistribution of quasiparticles the microwave photons effectively ‘cool’ the superconductor at high temperatures [21]. Ground-based MKID cameras can benefit from this effect as it effectively increases the internal quality factor of the resonator by a factor of a few. In turn this increases the resonator response by the same factor (see also Sect. 6.3.3).

Quasiparticle recombination

Both phonons and photons can generate quasiparticles in a superconductor. However, even in thermal equilibrium or under a continuous illumination the quasiparticle density will vary in time. This is a result of the continuous competition between quasiparticle creation and recombination. The superconductor will tend towards the lowest energy state by recombining pairs of quasiparticles into Cooper pairs. At temperatures $T \ll T_c$ and for quasiparticles near the gap, $E \approx \Delta$, the quasiparticle lifetime in thermal equilibrium can be approximated by [27]

$$\tau_{qp} = \frac{\tau_0}{\sqrt{\pi}} \left(\frac{k_B T_c}{2\Delta} \right)^{5/2} \sqrt{\frac{T_c}{T}} \exp(\Delta/k_B T) = \frac{\tau_0}{n_{qp}} \frac{N_0(k_B T_c)^3}{2\Delta^2} \quad (6.12)$$

τ_0 is the characteristic electron-phonon interaction time, which is $\tau_0 \approx 450$ ns for Al [28]. The proportionality between the quasiparticle lifetime and density, $\tau_{qp} \propto 1/n_{qp}$ has only been proven mathematically for a thermal quasiparticle distribution. de Visser et al. [21] found that this proportionality also holds for non-equilibrium distributions due to the microwave readout power of the MKIDs. However, the full range of non-equilibrium distributions for which $\tau_{qp} \propto 1/n_{qp}$ remains applicable is unknown.

Complex conductivity

Under normal conditions a superconductor will contain two charge carriers: quasiparticles and Cooper pairs. To describe the complex conductivity of a superconductor London and London [29] added to the Drude model a kinetic term describing the superconducting electrons. In this two fluid model part of the current is carried by the quasiparticles and part by the Cooper pairs.

$$\sigma(\omega) = \frac{n_{qp} e^2 \tau}{m} - i \frac{n_s e^2}{\omega m} = \sigma_1 - i\sigma_2 \quad (6.13)$$

Here n_s is the density of electrons bound into Cooper pairs. The first term is the resistance due to the scattering of quasiparticles. The second term can be identified as

an inductive term due to the inertia of the superconducting electrons. It can also be derived by equating the energy stored in an inductor, $\frac{1}{2}LI^2$, to the kinetic energy of the superconducting electrons, $\frac{1}{2}n_s ev^2$.

In addition to the complex conductance London and London [29] derived the magnetic penetration depth

$$\lambda_L = \sqrt{\frac{m}{\mu_0 n_s e^2}} \quad (6.14)$$

Here μ_0 is the magnetic permeability of vacuum. λ is the length scale over which a magnetic field decays inside a superconductor. A magnetic field will induce a screening current near the surface of a superconductor, which creates an equal and opposite field. As a result, the interior of the superconductor will be free of magnetic fields. Because the screening current experiences no resistance, it can be maintained even if the magnetic field is static.

However, the first measurements of λ found values larger than those predicted by the London expression. This is the result of a non-local response of the superfluid. In a normal metal the current at a given location depends on the electric field in a volume around it. The size of this volume is given by the mean free path, $l = v_F \tau$, which is related to the mean scattering time through the Fermi velocity. In a superconductor the size of the response volume is given by the effective coherence length [30]: $1/\xi = 1/l + 1/\xi_0$.

MKIDs generally use thin film superconductors in which the mean free path is limited by the thickness of the film $t < l$ and the motion of the superconducting electrons is governed by diffusion. In this so-called dirty limit the effective magnetic penetration depth can be generalised to $\lambda_{\text{eff}} = 0.615\lambda_L \sqrt{\xi_0/l}$ [31]. When a perpendicular magnetic field is applied to a thin film, the magnetic penetration depth is given by the Pearl length, $\lambda_{\perp} \approx \lambda^2/t$, due to the interaction of magnetic vortices created by the field [32]. As a result of the above, the electromagnetic response of a thin film superconductor is generally that of a superconductor in the dirty ($t = l \ll \xi_0$) local ($\lambda > l = t$) limit. In this limit the magnetic penetration depth can be rewritten into the experimentally convenient form [33, 34]

$$\lambda \approx 105 \text{ [nm]} \times \sqrt{\frac{\rho \text{ [\mu}\Omega\text{cm}]}{T_c \text{ [K]}}} \quad (6.15)$$

Expressions for the complex conductivity $\sigma = \sigma_1 - i\sigma_2$ in the dirty and extreme anomalous limit ($\xi \gg \lambda, l \gg \xi_0$) were derived by Mattis and Bardeen [35].

$$\begin{aligned} \frac{\sigma_1}{\sigma_N} &= \frac{2}{h\nu} \int_{\Delta}^{\infty} [f(E) - f(E + h\nu)] g_1(E) dE \\ &+ \frac{1}{h\nu} \int_{\min(\Delta - h\nu, -\Delta)}^{-\Delta} [1 - 2f(E + h\nu)] g_1(E) dE \end{aligned} \quad (6.16)$$

$$\frac{\sigma_2}{\sigma_N} = \frac{1}{\hbar\omega} \int_{\max(\Delta - h\nu, -\Delta)}^{\Delta} [1 - 2f(E + h\nu)] g_2(E) dE \quad (6.17)$$

where σ_N is the normal state conductivity and

$$\begin{aligned} g_1(E) &= \frac{E^2 + \Delta^2 + h\nu E}{(E^2 - \Delta^2)^{1/2} [(E + h\nu)^2 - \Delta^2]^{1/2}} \\ &= \left(1 + \frac{\Delta^2}{E(E + h\nu)} \right) N_s(E) N_s(E + h\nu) \end{aligned} \quad (6.18)$$

$$\begin{aligned} g_2(E) &= \frac{E^2 + \Delta^2 + h\nu E}{(\Delta^2 - E^2)^{1/2} [(E + h\nu)^2 - \Delta^2]^{1/2}} \\ g_2(E) &= -i \times g_1(E) \end{aligned} \quad (6.19)$$

The integration limits assume a density of states with no available states at $|E| < \Delta$ (a hard gap). When a broadened density of states or subgap states are introduced, these boundaries have to be reconsidered [36]. Fig. 6.6(a) shows the imaginary and real parts of the complex conductivity as a function of temperature for the material parameters of Al. σ_1 increases and σ_2 decreases with temperature. This may be directly understood from Eq. 6.13 due to a decreasing number of Cooper pairs and increasing number of quasiparticles. Fig. 6.6(b) shows σ_1 and σ_2 as a function of frequency, also using Al as an example. At frequencies below the gap, ~ 90 GHz, photons can only be absorbed by the existing quasiparticles and the first integral in Eq. 6.16 dominates. As soon as the photons become pair breaking the second integral in Eq. 6.16 starts to dominate and the superconductor obtains a resistivity as if it were a normal metal, $\sigma_1 = \sigma_n$. Note that even pair-breaking photons experience a significant inductive response, σ_2 , as a result of the Cooper pairs.

For a thermal quasiparticle distribution, $f_{FD}(E, T)$ and $k_B T, h\nu < 2\Delta$ Eqs. 6.16 and 6.17 reduce to [37]:

$$\frac{\sigma_1}{\sigma_N} = \frac{4\Delta}{h\nu} \exp(-\Delta/k_B T) \sinh\left(\frac{h\nu}{2k_B T}\right) K_0\left(\frac{h\nu}{2k_B T}\right) \quad (6.20)$$

$$\frac{\sigma_2}{\sigma_N} = \frac{\pi\Delta}{h\nu} \left[1 - 2 \exp(-\Delta/k_B T) \exp\left(\frac{-h\nu}{2k_B T}\right) I_0\left(\frac{h\nu}{2k_B T}\right) \right] \quad (6.21)$$

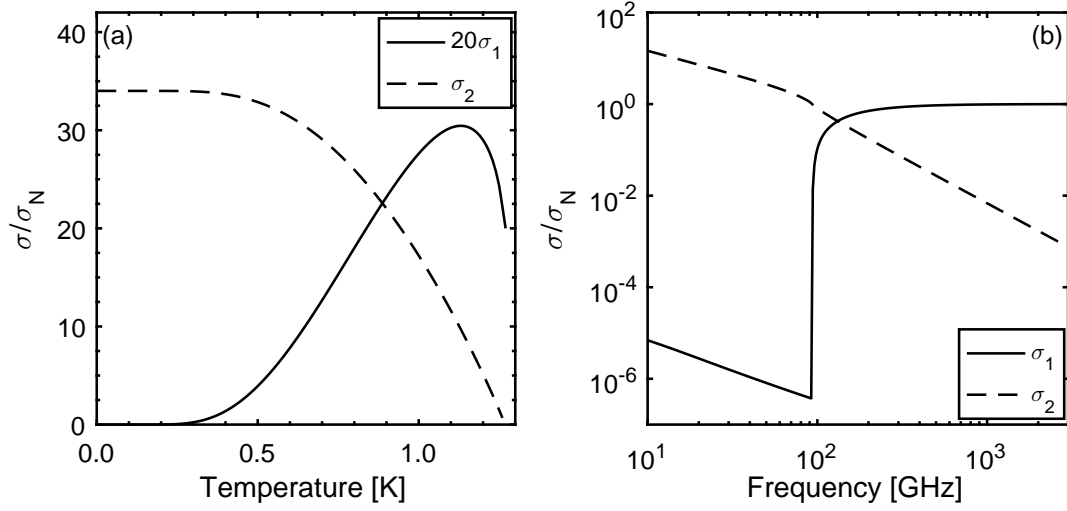


Figure 6.6: The real (solid line) and imaginary (dashed line) part of the superconducting complex conductivity as a function of temperature (a) and frequency (b). These relations are calculated using the integral equations given by Eq. 6.16–6.17 and a temperature dependent gap given by Eq. 6.6. A constant frequency $h\nu = \Delta/10$ and a constant temperature $T = T_c/8$ are assumed in panels (a) and (b), respectively. These parameters correspond to the typical MKID operating temperature and readout frequency for the material parameters of Al which has a $T_c \approx 1.27$ K and $2\Delta_0/h \approx 90$ GHz. Note that σ_1 is scaled by a factor 20 in panel (a). Image inspired by de Visser [16].

Here I_0 and K_0 are the modified Bessel functions of the first and second kind, respectively. Combining the above equations with Eq. 6.10 $d\sigma/dn_{qp}$ may be obtained [38]

$$\frac{d\sigma_1}{dn_{qp}} \simeq \sigma_N \frac{1}{N_0 h\nu} \sqrt{\frac{2\Delta_0}{\pi k_B T}} \sinh\left(\frac{h\nu}{2k_B T}\right) K_0\left(\frac{h\nu}{2k_B T}\right) \quad (6.22)$$

$$\frac{d\sigma_2}{dn_{qp}} \simeq \sigma_N \frac{-\pi}{2N_0 h\nu} \left[1 + 2\sqrt{\frac{2\Delta_0}{\pi k_B T}} \exp\left(\frac{-h\nu}{2k_B T}\right) I_0\left(\frac{h\nu}{2k_B T}\right) \right] \quad (6.23)$$

Fig. 6.7 shows $d\sigma/dn_{qp}$ as a function of temperature (a) and frequency (b) for Al [16]. A constant frequency $h\nu = \Delta/10$ and a constant temperature $T = T_c/8$ are assumed in panels (a) and (b), respectively. These values correspond to typical operational conditions of MKIDs for the material parameters of Al. In panel (a) we observe that $d\sigma/dn_{qp}$ changes slowly with temperature. Thus for not too large changes in n_{qp} the complex conductivity changes approximately linearly with n_{qp} . Panel (b) shows that the inductive response to a changing quasiparticle number is stronger at lower frequencies. Hence a lower readout frequency is desirable to maximize the phase response of MKIDs as given in Eq. 6.51 [34].

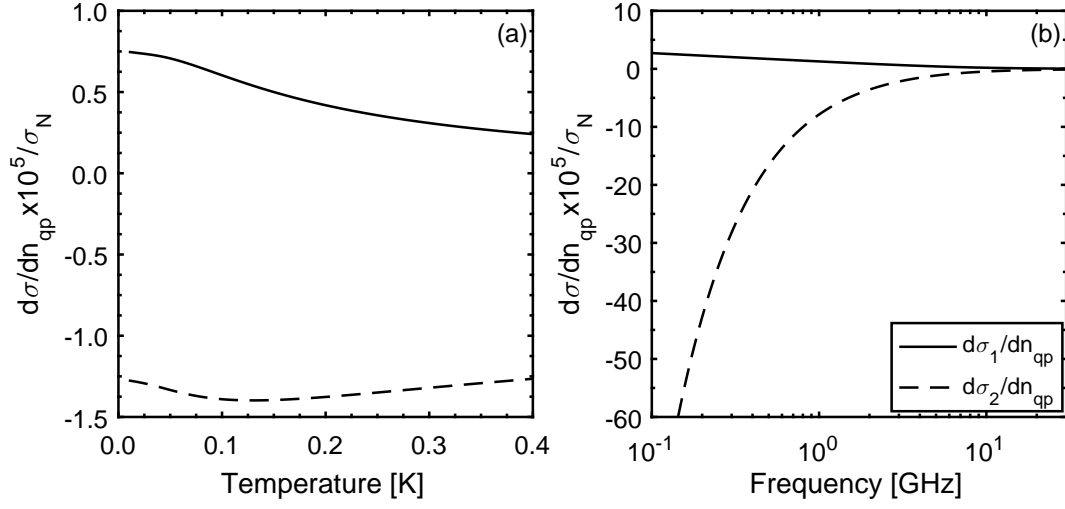


Figure 6.7: The response of the real (solid line) and imaginary (dashed line) part of the superconducting complex conductivity to a change in quasiparticle density as a function of temperature (a) and frequency (b). A constant frequency $h\nu = \Delta/10$ and a constant temperature $T = T_c/8$ are assumed in panels (a) and (b), respectively. These parameters correspond to the typical MKID operating temperature and readout frequency for the material parameters of Al which has a $T_c \approx 1.27$ K and $2\Delta_0/h \approx 90$ GHz. Image inspired by de Visser [16].

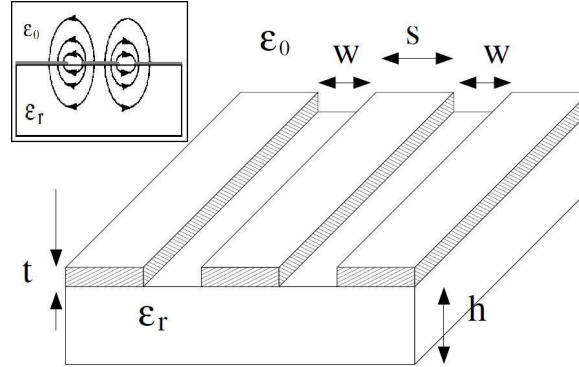


Figure 6.8: The geometry of a coplanar waveguide. A film of thickness t is present on top of a substrate. The metallic film consist of a central conductor of width S , which is separated from two ground planes by slots of width W . The inset shows the electric field lines present in the TEM mode transmission of this line. Figure and inset were taken from Vardoulakis [17] and Collins [39], respectively.

6.3 Superconducting microwave resonator

6.3.1 Superconducting transmission line

The MKIDs studied in this thesis are transmission line resonators based on a superconducting coplanar waveguide (CPW). A CPW is the planar version of a coaxial cable and consists of a central conductor of width S , which is separated from the ground plane by a slot of width W on either side. This is illustrated in Fig. 6.8. The characteristic impedance, Z_0 , and complex propagation constant, γ , of a CPW transmission line are given by [40]:

$$Z_0 = \sqrt{\frac{R + i\omega L}{G + i\omega C}} \quad (6.24)$$

$$\gamma = \alpha + i\beta = \sqrt{(R + i\omega L)(G + i\omega C)} \quad (6.25)$$

- R is the resistance per unit length in Ω/m for current travelling along the line. In the case of our superconducting resonators $R = g_c R_{s,c} + g_g R_{s,g}$, where $R_{s,c}$ and $R_{s,g}$ are the sheet resistance of the central line and ground plane, respectively. g_c and g_g are geometry factors and are discussed below.
- L is the inductance per unit length in H/m experienced by the current travelling along the line. In case of a superconducting line this is the sum of the kinetic inductance $L_{\text{kin}} = g_c L_{s,c} + g_g L_{s,g}$ and the geometric inductance $L_g = \frac{\mu_0}{4} \frac{K(k')}{K(k)}$ [39].
- C is the capacitance per unit length in F/m between the central line and ground planes. Analogous to the geometric inductance, this is given by the geometry of the CPW: $C_g = 4\epsilon_0\epsilon_{\text{eff}} \frac{K(k)}{K(k')}$, where ϵ_{eff} is the effective dielectric constant. Because roughly half the electric field lines are in the substrate $\epsilon_{\text{eff}} \approx (1 + \epsilon_{\text{substrate}})/2$ [39].
- G is the shunt conductance per unit length in $\text{S}/\text{m} = 1/(\Omega\text{m})$. By using highly resistive substrates, this is assumed to be negligible, $G = 0$, for most practical MKID applications. However, the losses as a result of two-level systems also may be included here.

In the above, $K(x)$ is the complete elliptic integral, $k = S/(S + 2W)$ and $k^2 + k'^2 = 1$. The geometric factors g_c and g_g for a CPW are given by [39]

$$g_c = \frac{1}{4S(1 - k^2)K^2(k)} \left[\pi + \ln \left(\frac{4\pi S}{t} \right) - k \ln \left(\frac{1 + k}{1 - k} \right) \right] \quad (6.26)$$

$$g_g = \frac{k}{4S(1 - k^2)K^2(k)} \left[\pi + \ln \left(\frac{4\pi(S + 2W)}{t} \right) - \frac{1}{k} \ln \left(\frac{1 + k}{1 - k} \right) \right] \quad (6.27)$$

where t is the film thickness. These equations are valid for $t < S/20$ and $k < 0.8$. The latter is practically always satisfied to get a transmission line impedance close to $Z \sim 50 \Omega$. For MKIDs the first condition is barely satisfied or broken as typical values

for t and S are $50 < t < 300$ nm and $S \gtrsim 1$ μ m. The limit on S is driven by the use of optical lithography. Even though sub-micron CPW resonators have been made using electron beam lithography by Janssen et al. [41], optical lithography is still the most reliable and reproducible way to fabricate kilopixel MKID arrays. Eqs. 6.26 and 6.27 have been experimentally verified for superconducting resonators with $t \geq S/3$ by Gao et al. [42]. They showed that at $S/t = 7.5$ the above equations incur an error of $\sim 15\%$ [43]. The equations derived [44] and tested by Booth and Holloway [45] are essentially equivalent to Eqs. 6.26 and 6.27.

Using the above information and $g = g_c + g_g$ we can rewrite the characteristic impedance of a superconducting CPW as

$$Z_0 = \sqrt{\frac{gR_s + i\omega(gL_s + L_g)}{i\omega C_g}} = \sqrt{\frac{gZ_s + i\omega L_g}{i\omega C_g}} \quad (6.28)$$

This assumes a single superconducting material with surface impedance, Z_s , for both the ground plane and central line. In the local dirty limit the surface impedance of a superconductor is given by [46]

$$Z_s = R_s + i\omega L_s = \sqrt{\frac{i\mu_0\omega}{\sigma_1 - i\sigma_2}} \coth\left(\frac{t}{\lambda} \sqrt{1 + i\frac{\sigma_1}{\sigma_2}}\right) \quad (6.29)$$

Here λ is the penetration depth of the bulk material. At low temperatures and microwave readout frequencies $\sigma_2 \gg \sigma_1$, as can be seen in Fig. 6.6(a). This makes it possible to split Z_s into R_s and L_s [37].

$$R_s = \sqrt{\frac{\mu_0\omega}{\sigma_2}} \frac{\sigma_1}{2\sigma_2} \zeta \coth\left(\frac{t}{\lambda}\right) \quad (6.30)$$

$$L_s = \sqrt{\frac{\mu_0}{\omega\sigma_2}} \coth\left(\frac{t}{\lambda}\right) \quad (6.31)$$

where ζ takes into account the thickness of the film with respect to the bulk magnetic penetration depth. ζ varies between 1 (thick films) and 2 (thin films).

$$\zeta = 1 + \frac{2t/\lambda}{\sinh(2t/\lambda)} \quad (6.32)$$

The relation between the magnetic penetration depth and σ is given by [47]

$$\lambda(\omega, T) = \sqrt{\frac{1}{\mu_0\omega\sigma_2(\omega, T)}} \quad (6.33)$$

This relation can be easily derived using the London equations (Eqs. 6.13 and 6.14) and the assumption $\sigma \approx -i\sigma_2$. The effective magnetic penetration depth for perpendicular magnetic fields is $\lambda_{\text{eff}} = \lambda \coth(t/\lambda)$ [48].

At pair breaking frequencies, $h\nu > 2\Delta$, the approximation $\sigma \approx -i\sigma_2$ is no longer valid

as σ_1 becomes comparable to σ_2 . For $h\nu \gg 2\Delta$ a superconductor behaves as if it were a normal metal and the surface impedance is dominated by R_s . The attenuation constant α for pair breaking radiation is given by [40]

$$\alpha = \frac{g_c R_{s,c} + g_g R_{s,g}}{2Z_0} \quad (6.34)$$

The fraction of the power absorbed in a superconducting CPW of length l is given by

$$\eta_{\text{abs}} = 1 - e^{-2\alpha l} \quad (6.35)$$

Here the factor 2 in the exponent is the result of measuring the attenuation to power instead of current or voltage.

6.3.2 Superconducting $\lambda/4$ resonator

Antenna-coupled MKIDs, such as shown in Fig. 6.2, use a quarterwave ($l = \lambda/4$) transmission line resonator, which consists of a transmission line with an open end near the feedline and a shorted end near the antenna. Their resonance frequency, $\omega_0 = 2\pi f_0$, is determined by their length, l , and the phase velocity, $v_p = \omega/\beta \approx 1/\sqrt{LC}$, inside the superconducting transmission line [37].

$$\omega_0 = \frac{2\pi}{4l\sqrt{(L_g + L_{\text{kin}})C_g}} \quad (6.36)$$

The input impedance, Z_{STL} , of a shorted transmission line of length l is given by [40]

$$Z_{\text{STL}} = Z_0 \tanh(\gamma l) = Z_0 \frac{1 - i \tanh(\alpha l) \cot(\beta l)}{\tanh(\alpha l) - i \cot(\beta l)} \quad (6.37)$$

For a low loss ($\tanh(\alpha l) \approx \alpha l$) superconducting microwave resonator near resonance ($\omega = \omega_0 + \delta\omega_0$) this may be approximated by [40]

$$Z_{1/4} = Z_0 \frac{1}{\alpha l + i(\pi/2)(\delta\omega_0/\omega_0)} \quad (6.38)$$

This equation is identical to the impedance of a lumped element parallel RLC circuit as shown in Fig. 6.1(b). The lumped element equivalent values are [43]

$$\tilde{R} = \frac{Z_0}{\alpha l} = \frac{2}{l} \frac{L_g + L_{\text{kin}}}{g R_s C_g} \quad (6.39)$$

$$\tilde{L} = \frac{4Z_0}{\pi\omega_0} = \frac{8l}{\pi^2} (L_g + L_{\text{kin}}) \quad (6.40)$$

$$\tilde{C} = \frac{\pi}{4\omega_0 Z_0} = \frac{l}{2} C_g \quad (6.41)$$

The quality factor of a resonator is defined as the energy inside the resonator divided by the energy lost per cycle. The quality factor of a superconducting quarterwave resonator is given by

$$Q_i = \omega_0 \tilde{R} \tilde{C} = \frac{\omega L_s}{\alpha_{\text{kin}} R_s} \quad (6.42)$$

Here $\alpha_{\text{kin}} = L_{\text{kin}}/(L_g + L_{\text{kin}})$ is the kinetic inductance fraction. Due to the low losses in a superconducting resonator the internal quality factor Q_i can easily be $> 10^5$.

Coupled resonator

The presence of the coupling capacitance C_c changes the impedance, resonance frequency, ω_{res} , and total or loaded quality factor, Q_1 , of the resonator.

$$Z_{\text{res}} = Z_{1/4} + \frac{-i}{\omega C_c} \quad (6.43)$$

$$\frac{\delta\omega_{\text{res}}}{\omega_{\text{res}}} = \frac{\delta\omega_0}{\omega_0} - \sqrt{\frac{2}{\pi Q_c}} \quad (6.44)$$

$$Q_1 = \frac{Q_c Q_i}{Q_c + Q_i} \quad (6.45)$$

Here the coupling quality factor is given by $Q_c = \frac{\pi}{2Z_{\text{feedline}}Z_{\text{res}}\omega^2 C_c^2}$ and determines the fraction of the power entering or leaving the resonator each cycle. C_c is determined by the length of the resonator's transmission line that is parallel to the feedline and the distance between the two. This section of the resonator is generally referred to as the coupler and is located in 6.2(b) at the bottom of the image. However, instead of designing C_c explicitly, the Q_c of a resonator is designed instead by simulation the transmission from a feedline into the coupler of resonator using software such as Sonnet [17, 22].

6.3.3 Response

A quarterwave resonator creates a parallel-type (anti)resonance in the feedline transmission, S_{21} , which near resonance, $\omega = \omega_{\text{res}} + \delta\omega_{\text{res}}$, can be described with

$$S_{21} = \frac{2}{2 + Z_{\text{feedline}}/Z_{\text{res}}} \approx \frac{Q_1/Q_i + i2Q_1 \frac{\delta\omega_{\text{res}}}{\omega_{\text{res}}}}{1 + i2Q_1 \frac{\delta\omega_{\text{res}}}{\omega_{\text{res}}}} \quad (6.46)$$

This transmission can be represented as $|S_{21}|$ as a function of frequency, $f = \frac{\omega}{2\pi}$, as shown in Fig. 6.1(c). The Lorentzian resonance feature has a minimum transmission $S_{21}^{\text{min}} = Q_1/Q_i$ at the resonance frequency of the resonator. The full width half maximum of the resonance feature is given by $\text{FWHM}(f) = f_{\text{res}}/Q_1$. For increasing optical loading the resonance feature shifts to lower frequencies and becomes shallower, i.e. S_{21}^{min} increases. Generally, the FWHM of the resonance feature is (nearly) independent

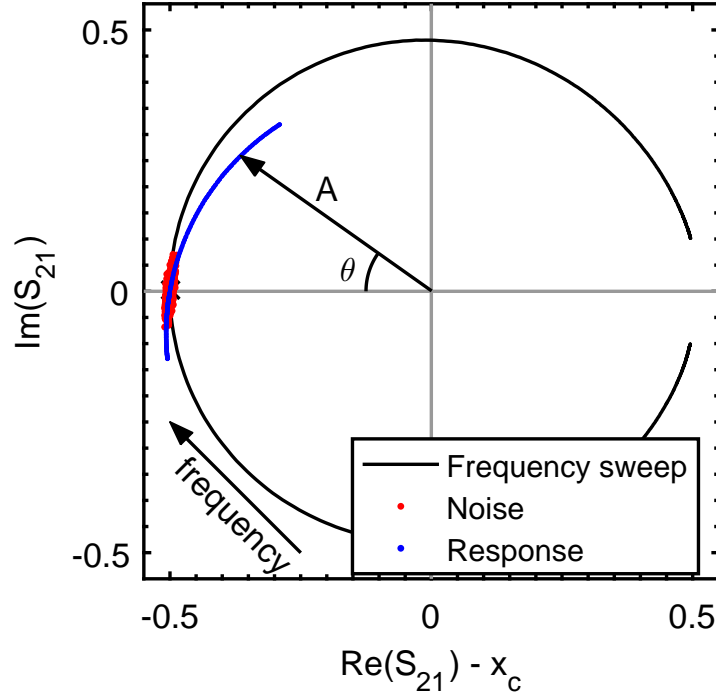


Figure 6.9: The microwave transmission S_{21} around the resonance frequency of an MKID represented in the imaginary plane. The solid black line shows a measured frequency sweep, which traces a circle in the complex plane. This circle has been translated by $x_c = \frac{1}{2} + \frac{1}{2}S_{21}^{\min}$ such that the circle is centred on the origin and the resonance frequency located at $(-0.5, 0)$ in case of $S_{21}^{\min} = 0$. Frequency increases in a clockwise direction. The blue dots show the response to optical power at constant frequency. This response can be described as a change in phase, θ , and amplitude, A . The temporal fluctuation at constant optical power (noise) are shown in red. For illustrative purposes the scatter in the noise with respect to their mean value has been increased by a factor of four.

of P_{opt} as Q_1 is limited by Q_c . Distortion of the resonance feature with respect to the Lorentzian shape given by Eq. 6.46 may be the result of heating by readout power [49] or an impedance mismatch between the on-chip feedline and the $50 \, \Omega$ microwave cables in the setup [50]. Estimating the impedance of the on-chip feedline is particularly difficult for disordered superconductors such as TiN [51].

Alternatively the forward transmission of the feedline can be represented in the complex plane as shown in Fig. 6.9. The frequency trace translates into a clockwise circle in the complex plane. To calculate the changes in phase, θ , and amplitude, A , with respect to this KID circle, it is translated from its original location at $(x_c, 0)$ to the origin such that f_{res} is located at $((S_{21}^{\min} - 1)/2, 0)$. Fig. 6.9 shows two changes in $S_{21}(f_{\text{res}})$: the response to a changing optical power (blue) and the temporal changes (noise) at constant loading (red).

Based on the above we can identify four observables that measure the response of MKIDs to a change in optical power, P_{opt} , or equivalently a change in the quasiparticle

density, n_{qp} ,

$$\frac{dx}{dP_{\text{opt}}} = \frac{dN_{\text{qp}}}{dP_{\text{opt}}} \frac{dx}{dN_{\text{qp}}} \approx \frac{\eta_{\text{pb}} \tau_{\text{qp}}}{\Delta} \frac{dx}{dN_{\text{qp}}} \quad (6.47)$$

The four observables, x , are resonance frequency, internal quality factor, amplitude and phase. Their responsivities are given by [16, 22]

$$\frac{df_{\text{res}}}{dN_{\text{qp}}} = \frac{\alpha_{\text{kin}} \zeta f_{\text{res}}}{4|\sigma|V} \frac{d\sigma_2}{dn_{\text{qp}}} \quad (6.48)$$

$$\frac{d(1/Q_i)}{dN_{\text{qp}}} = \frac{\alpha_{\text{kin}} \zeta}{2|\sigma|V} \frac{d\sigma_1}{dn_{\text{qp}}} \quad (6.49)$$

$$\frac{dA}{dN_{\text{qp}}} = -\frac{\alpha_{\text{kin}} \zeta Q_1}{|\sigma|V} \frac{d\sigma_1}{dn_{\text{qp}}} \quad (6.50)$$

$$\frac{d\theta}{dN_{\text{qp}}} = -\frac{\alpha_{\text{kin}} \zeta Q_1}{|\sigma|V} \frac{d\sigma_2}{dn_{\text{qp}}} \quad (6.51)$$

Here V is the volume of the superconductor in which n_{qp} is changed and ζ depends on the thickness of the superconductor as given by Eq. 6.32. In these equations Q_1 is assumed constant i.e. not limited by quasiparticle losses. In addition, the effective temperature is assumed to be $T \ll T_c$. At these temperatures, $\delta\sigma_2 \sim 3\delta\sigma_1$ and $|\sigma| \approx \sigma_2$. Note that changes in A and Q_i represent changes in σ_1 , whereas frequency and phase are sensitive to changes in σ_2 . In practical applications, phase [52] or frequency [53, 54] readout are preferred to amplitude readout, because of the higher response in σ_2 . The response of an MKID to radiation of a given frequency may be increased by a higher kinetic induction fraction, smaller volume, higher quasiparticle lifetime, smaller superconducting gap and higher Q .

6.3.4 Noise

Three main sources of noise have been identified that can limit the performance of MKIDs designed for the detection of sub-mm radiation. For these three noise sources we will discuss their origin and their noise spectra. Experimentally, noise spectra are obtained by taking a time trace of $\text{Re}(S_{21})$ and $\text{Im}(S_{21})$ at constant operation conditions. The results of such a time trace are shown by the red dots in Fig. 6.9. From the time trace an autocorrelation of θ and A can be obtained, which can be transformed into a power spectral density (PSD) using a Fourier transform.

In addition to the three noises below, MKIDs detecting near-infrared photons or more energetic particles also suffer from Fano noise [55].

Generation-recombination noise

Generation-recombination (GR) noise is the result of the dynamic equilibrium between Cooper pairs and quasiparticles inside a superconductor [28, 56]. Both generation by

phonons and recombination are Poissonian processes in which the variance is determined by the number of quasiparticle, N_{qp} , in the superconductor. As such it is driven primarily by temperature and the microwave readout power [57]. The PSD of GR noise in both amplitude, $x = A$, and phase, $x = \theta$, is given by [16]

$$S_{\text{GR},x} = \frac{4N_{\text{qp}}\tau_{\text{qp}}}{1 + \omega^2\tau_{\text{qp}}^2} \left(\frac{(dx/dN_{\text{qp}})}{1 + \omega^2\tau_{\text{res}}^2} \right)^2 \quad (6.52)$$

Note that the GR noise level at low temperatures $T < T_c/4$ will be effectively constant with N_{qp} . This is due to the proportionality $n_{\text{qp}} \propto 1/\tau_{\text{qp}}$ found in Sect. 6.2.2 and the fact that the responsivity is only very weakly dependent on T . The latter can be quickly seen from Eqs. 6.50 and 6.51 and Figs. 6.6(a) and 6.7(b). At low temperatures $|\sigma| = \sigma_2$, which is nearly temperature independent. This is also true for the quality factor if $Q_1 = Q_c$. In addition $d\sigma/dn_{\text{qp}}$ varies only weakly with temperature. As a result, only a change in the roll off will be observed as a result of a temperature change, given that $\tau_{\text{qp}} \ll \tau_{\text{res}}$. This signature behaviour of GR noise has experimentally verified by de Visser et al. [57].

Two-level system noise

The dominant noise source in phase readout intrinsic to MKIDs is the so-called two-level systems (TLS) noise. This noise has been extensively studied [e.g. 37, 43] and is the result of fluctuations by TLS with a dipole moment. The fluctuations of these TLS change ϵ_{eff} , which in turn results in fluctuations of C_g and increased microwave losses, G . The TLS noise spectrum has a characteristic $S_{\text{TLS},\theta} \propto \omega^{-0.5}$ slope and rolls off with the resonator ring time. Key TLS noise properties, which can be used to minimize their effect, are:

- The effects of TLS decrease in bigger structures [58–60]. It is therefore advantageous to use a wide CPW near the open end of a CPW resonator or a large capacitor in the case of a LEKID. In these regions the TLS have the strongest effect due to the high electric fields.
- TLS are predominantly located in the oxides located at the metal-air, metal-substrate and substrate-air interfaces [61]. Oxides in the metal-air interface can be reduced by using materials that do not oxidise, such as NbTiN and TiN [59, 62]. The metal-substrate interface can be chemically cleaned of oxides before metal deposition. The lowest TLS is found for high-resistivity crystalline silicon that has been dipped into hydrofluoric acid [59]. The effect of TLS on the substrate-air interface can be reduced by etching trenches in the substrate [63–65].
- Both the TLS noise and losses are decreased by increasing the microwave readout power, P_{read} . The noise level $S_{\text{TLS}} \propto P_{\text{int}}^{-1/2}$, where P_{int} is the power inside the

resonator [58, 59, 66]. Hence, one of the simplest ways to limit the effects of TLS is to use a higher readout power. This simultaneously decreases the amplifier noise as discussed in the next paragraph. However, in practice P_{read} is limited by the resonators, which show non-linear behaviour and hysteretic switching when overdriven [e.g. 67].

Amplifier noise

Although not a noise source inherent to the MKID, the system noise often limits the amplitude noise [1] and at high modulation frequencies in both quadratures. The noise PSD of the system is white and given by [16]

$$S_{\text{system}} = \frac{k_B T_N}{P_{\text{read}}} \left(\frac{2}{1 - S_{21}^{\text{min}}} \right)^2 \quad (6.53)$$

Here P_{read} is the readout power used in the feedline near the MKIDs. This is typically $P_{\text{read}} \sim -80$ dBm. The first term in the above equation is the noise of the impedance matched amplifier. For most realistic readout systems the system noise temperature is limited by the low-noise cryogenic amplifier. In case of the system discussed in Sect. 6.4 this is the HEMT with a noise temperature $T_N \approx 5$ K.

The second term in Eq. 6.53 corrects for the MKID dip depth. Using the definition of S_{21}^{min} we can write

$$S_{\text{system}} = \frac{4k_B T_N}{P_{\text{read}}} \left(1 + \frac{Q_c}{Q_i} \right)^2 \quad (6.54)$$

To reduce the effect of the amplifier noise a high readout power and a low Q_c/Q_i ratio are favourable. However, reducing Q_c to make S_{21}^{min} smaller also reduces the responsivity of the resonator. Hence, typically the ideal case is $Q_c = Q_i$, which corresponds to $S_{21}^{\text{min}} = -6$ dB.

6.4 Experimental setup

Fig. 6.10(a) shows a schematic representation of the experimental cryogenic setup [16, 68] used in this thesis to measure the performance of hybrid NbTiN-Al MKIDs. The cryogenic system is based on a dual-stage adiabatic demagnetization refrigerator (ADR), which is pre-cooled using a pulse tube. The pulse tube has an intermediate stage at 50K and reaches a base temperature of 3.5 K. On this ‘4K-stage’ the ADR is mounted which provides both a 500 mK stage for thermal anchoring and the 100 mK experimental stage. The experimental stage can reach temperatures as low as 30 mK, but operation at 100 mK increases the hold time to 36 hours. 100 mK is low enough that the number of thermally generated quasiparticles in Al is much lower than those generated by either the sub-mm or readout signal [16].

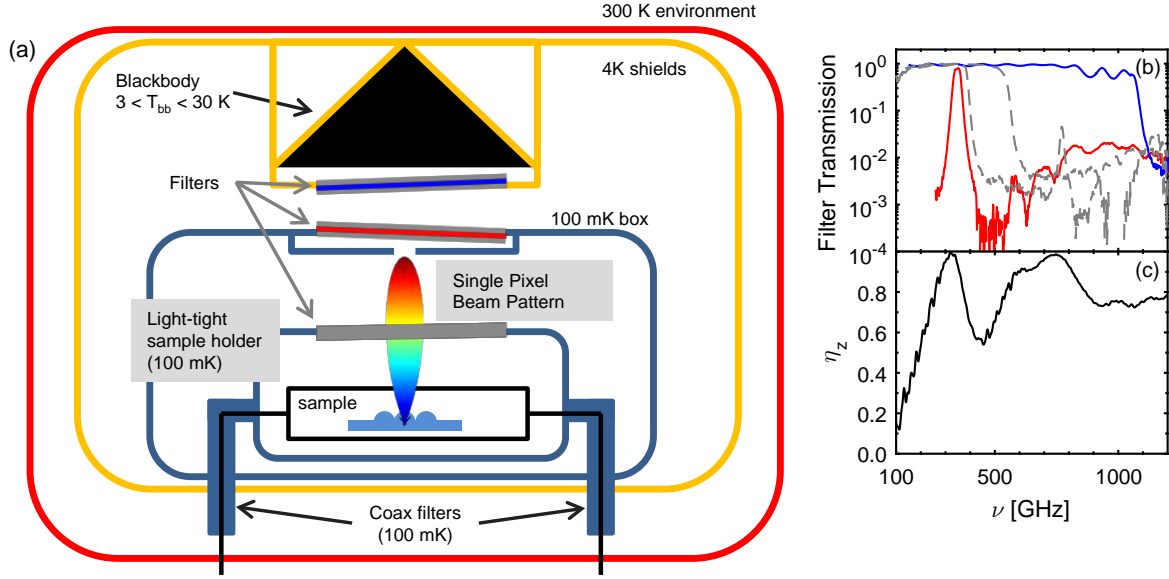


Figure 6.10: (a) A schematic representation of the cryogenic layout used for the controlled illumination of MKIDs [68]. The sample is located inside two 100 mK boxes, which have been coated in carbon-loaded epoxy [69] to minimize stray light. Home-made coax filter [70] suppress EM radiation of the 4K-stage entering through the microwave read out. Light from a blackbody located at the 4K-stage reaches the sample through 2 filters: a 1.1 THz low-pass filter located near the blackbody and a 350 GHz band-pass filter located on the outer 100 mK box. The transmission of both these filters is shown in (b). A third filter position is available on the inner sample box. A 2 mm diameter aperture at a height of 15 mm above the sample further constrains the radiation. These dimensions are shown on scale. This is also true for the relative angular dimensions of the main beam and aperture opening angle. The beam pattern of a single lens antenna is a simulation obtained using CST MWS. The matching efficiency, η_z , as given by CST MWS [71] is shown in (c).

On the experimental stage a ‘box-in-a-box’ design contains the MKIDs. This geometry is designed to minimize stray light from the 4K-stage onto the MKIDs. The chip with MKIDs is mounted in a gold-plated copper sample holder, which is surrounded by an outer box of the same material. The lid of both boxes is coated in 3 mm thick carbon-loaded epoxy mixed with 1 mm SiC grains. The carbon-loaded epoxy consist of 3% by weight lamp black (pure carbon powder) in Epotek-920 epoxy [72, 73]. The absorber layer needs to be thick enough to absorb the radiation of the lowest frequency that is able to break Cooper pairs. In the case of Al this is $\nu \sim 80$ GHz or $\lambda \sim 3.7$ mm. Furthermore, both lids are equipped with labyrinths that are filled with carbon-loaded epoxy. A separate labyrinth with carbon-loaded epoxy is used to shield two 2 mm holes that are used to evacuate the outer box. These holes do not have direct line of sight to the inner box.

To eliminate stray light entering through the coaxial cables used for the microwave measurement, home-made feedthrough filters [70] are used to connect the wires at the

4K-stage and the inside of the outer box. The filters contain a dielectric of epoxy and bronze powder, which creates a low-pass filter. The filter transmission can be described by a single exponential roll-off with a characteristic frequency of 10.4 GHz. This functional form would imply an attenuation of -45 dB at 80 GHz.

The performance of the box-in-a-box design in combination with the filters has been verified by a measurement of the quasiparticle lifetime in Al MKIDs. A lifetime of 2 ms was measured independent of the temperature of the 4K-stage. An upper limit of 0.06 fW of absorbed stray light per MKID has been experimentally determined [68].

An outer shield of cryoperm and an inner shield coated with superconducting lead-tin surround the entire box-in-a-box design as well as a blackbody radiator. These shields are used to shield the sample from magnetic fields, especially those needed for the operation of the ADR.

6.4.1 Illumination source

The MKIDs are illuminated using a cryogenic blackbody radiator that is made from a 40 mm diameter copper cone, coated with 2 layers of carbon-loaded epoxy containing 1 mm grains of SiC. The cone is connected to the 4K-stage using a 18 mm long, 0.3 mm thick phosphor-bronze wire. The blackbody radiator can be heated by three resistors placed around the cone to ensure a uniform temperature profile. The temperature of the blackbody, T_{BB} , can be varied between the temperature of the 4K-stage and 30 K. The blackbody radiation reaches the MKIDs through up to three filter stacks located at the blackbody, on the lid of the outer 100 mK box and on the lid of the sample holder. In the experiments presented in Chapters 7 and 8 a 1.1 THz low-pass filter is placed at the blackbody and a 50 GHz wide band-pass filter centred at 345 GHz is located at the outer box. The transmission of these filters can be seen in Fig. 6.10(b). Note the $> 1\%$ filter transmission at $\nu > 780$ GHz. Approximately 10% of the total power emitted into the 100 mK environment is at $\nu > 425$ GHz for $T_{\text{BB}} = 9$ K. This percentage increases to $\sim 35\%$ for the highest T_{BB} . More recent experiments [74] have alleviated this problem by moving the 345 GHz band-pass filter to the sample box and placing two additional low-pass filters on the outer 100 mK box. These filters have cut-off frequencies at 400 and 600 GHz as shown by the dashed dark grey lines in Fig. 6.10(b). The addition of these filters reduces the out-of-band radiation by 4 orders of magnitude. These additional filters also reduce the out-of-band infrared radiation that can be absorbed by the final filter. Absorption of infrared radiation heats the metal mesh filters used in this setup and creates additional loading on the MKIDs [75]. This additional loading can be reduced to negligible levels by using enough filters.

For the experiments presented in the next Chapters an $R_{\text{ap}} = 1$ mm radius aperture is placed on the lid of the outer 100 mK box. The centre of the aperture is located at $(x, y, z) = (0, 0, H)$. Here $H = 15.05$ mm is the height of the aperture above the

MKIDs. Because the rest of the MKIDs environment both minimizes stray light and is made from the same black material as the blackbody radiator, it can be considered to be $T_0 = 100$ mK blackbody. Therefore we can define the source distribution, $S_\nu(\theta, \phi)$, seen by the MKIDs as:

$$S_\nu(\theta, \phi) = \begin{cases} \frac{1}{2}(F_\nu B_\nu(T_{\text{BB}}) + (1 - F_\nu)\epsilon_{\text{F}}B_\nu(T_{\text{F}})) & \text{if } x^2 + y^2 \leq R_{\text{ap}}^2 \text{ and } z = H \\ \frac{1}{2}B_\nu(T_0) & \text{otherwise} \end{cases} \quad (6.55)$$

Here (θ, ϕ) are the angles in a spherical coordinate system, F_ν is the combined transmission of all filters and $B_\nu(T)$ the blackbody spectrum. ϵ_{F} is the emissivity of the filters. The factor $\frac{1}{2}$ is due to the fact that basic LEKIDs and most antenna-coupled MKIDs are sensitive to a single polarization, while blackbody radiation is unpolarised. Because the flux of $\nu > 80$ GHz photons decreases exponentially below 4K, we can assume that the contribution of $B_\nu(T_0)$ to the load on the MKIDs is negligible. If enough filters are used, such that also the filter temperature, T_{F} , is low and the filter emission is negligible, then S_ν reduces to

$$S_\nu(\theta, \phi) = \begin{cases} \frac{1}{2}F_\nu B_\nu(T_{\text{BB}}) & \text{if } x^2 + y^2 \leq R_{\text{ap}}^2 \text{ and } z = H \\ 0 & \text{otherwise} \end{cases} \quad (6.56)$$

6.4.2 Lens-antenna system

Fig. 6.11 shows the design of the Si microlens (a) and the antenna (b) used to couple radiation into the MKIDs presented in the next Chapters. The microlens has an elliptical design [76] in which the eccentricity is matched to the index of refraction of Si ($n_{\text{Si}} = 3.42$). This ensures that the optical focus is located at the geometric focus of the ellipse. A twin-slot antenna designed to receive radiation at 350 GHz is located in the second focus of the ellipse as indicated by the blue line in Fig. 6.11(a). The detailed design of the planar antenna is shown in Fig. 6.11(b). In red the central line of the CPW MKID is shown. The blue outline encompassed all areas in which the ground plane is removed. All dimensions are given in μm . Yates et al. [18] used the sample planar antenna and lens design. However, the lenses used in Yates et al. [18] were smaller: $a = 586.56 \mu\text{m}$, $b = 613.35 \mu\text{m}$, $R_{\text{lens}} = 0.5 \text{ mm}$ and $\phi_0 = 45^\circ$.

The beam pattern of these lens-antenna systems have been simulated using CST Microwave Studio (MWS) [71]. The shape of the gain, $G(\theta, \phi)$, for the larger lenses is shown in Fig. 6.10(a). Even though Fig. 6.10(a) is (in general) not to scale, the relative dimensions of H and R_{ap} are correct in this image. This is also true for the angular size of the main beam. Fig. 6.10(c) shows $\eta_z(\nu) = 1 - S_{11}^2$ as obtained from CST MWS. S_{11} is the scattering matrix element of the electrical system describing the reflections back to port 1 which is feeding the antenna at the end of the short piece of CPW shown in Fig. 6.11.

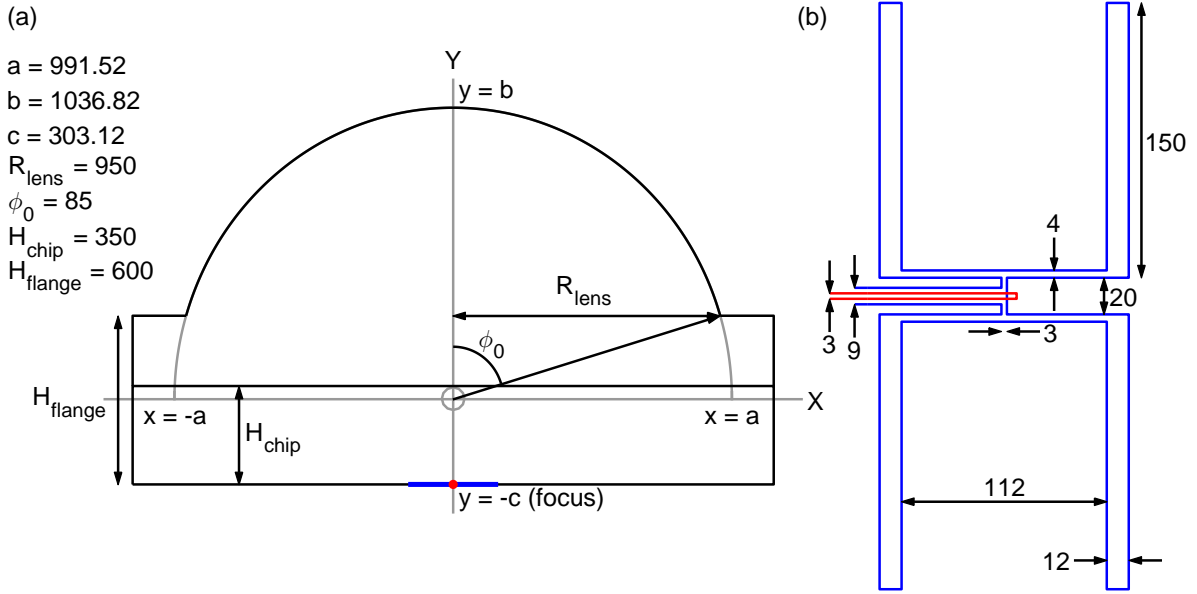


Figure 6.11: Design of the Si lens (a) and planar antenna (b) attached to the resonators for which experiments are presented in Ch. 7 and 8. The lens is a true ellipse [76] with a semi-major axis $b = 1036.82 \mu\text{m}$ and a semi-minor axis $a = 991.52 \mu\text{m}$. The antenna is located in the second focus of the ellipse as shown by the blue line in (a). The opening angle $\phi_0 = 58^\circ$ results in an effective lens radius of $R_{\text{lens}} = 0.95 \text{ mm}$. Further dimensions in both panels are given in μm . Yates et al. [18] used the sample planar antenna and lens design. However, the lenses used in Yates et al. [18] were smaller: $a = 586.56 \mu\text{m}$, $b = 613.35 \mu\text{m}$, $R_{\text{lens}} = 0.5 \text{ mm}$ and $\phi_0 = 45^\circ$.

6.4.3 Microwave setup

Fig. 6.12 shows the microwave setup used to measure the properties of the MKIDs presented in Ch. 7 and 8. The system consists of room temperature electronics as well as cryogenic components. The microwave signal from the signal generator (Agilent E8257D) is split in two. One part of the signal is fed into the cryogenic system using steel coax cables (down to the 4K-stage) and NbTi SMA cables (at lower temperatures). Because NbTi is a superconductor, these cables have negligible microwave losses and a low thermal conductance. This minimizes the thermal loading and maximizes the signal transmission. Single and double DC blocks interrupt the galvanic connection of the microwave lines at each thermal stage, which reduces the thermal conductivity. Furthermore, the signal is attenuated at each thermal stage to reduce the Johnson-Nyquist (thermal) noise. The microwave signal enters and leaves the light-tight box-in-a-box setup at 100 mK through the home-made coax filters discussed in the beginning of

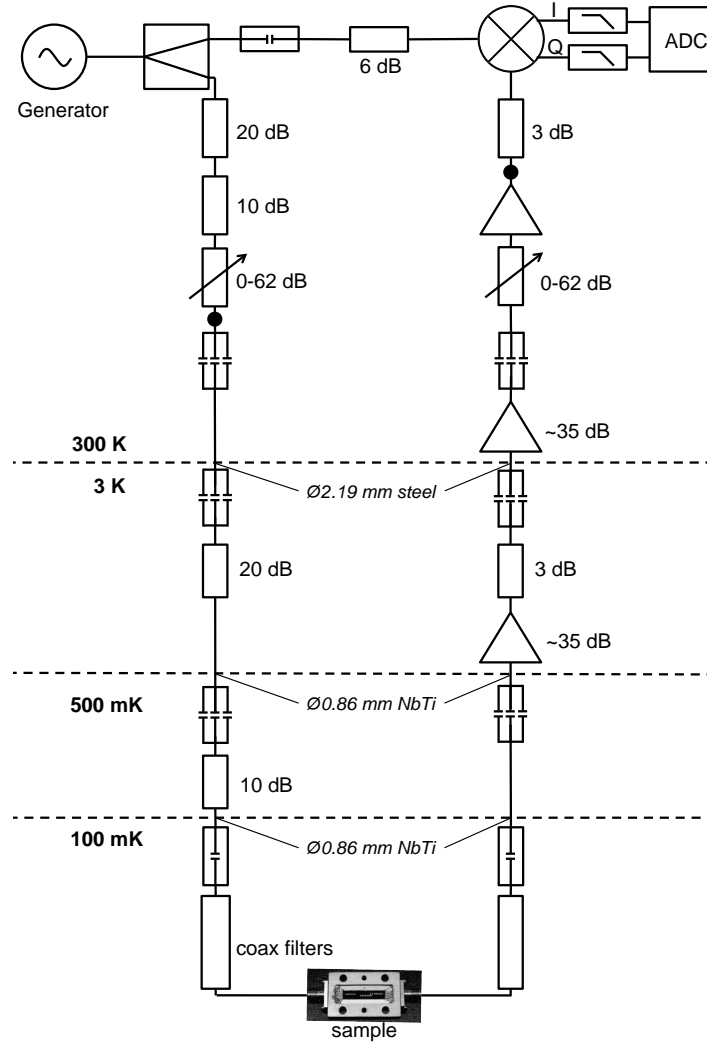


Figure 6.12: Detailed layout of the microwave components used to read out the MKIDs in Chapters 7 and 8. This signal from the generator is split. One part is fed into the cryogenic system using flexible SMA cables made from either steel or NbTi. At each temperature stage the signal is attenuated to minimize the Johnson-Nyquist (thermal) noise from higher temperature stages. The signal line is interrupted by DC blocks to reduce the thermal conductivity between each stage. The signal enters the 100 mK stage through home-made coax filters aimed to minimize the transmission of pair breaking radiation ($\nu > 80$ GHz). The signal leaves the sample box through a similar filter and it subsequently amplified by a low-noise HEMT amplifier located on the 4K-stage. Further amplification occurs at room temperature. The two variable attenuators in this chain are used to maintain a constant signal power at the IQ-mixer, while varying the read power at the sample. The two parts of the microwave signal (the original and the signal that travelled through the cryogenic system) are combined in an IQ-mixer. Alternatively, the signal generator and IQ-mixer can be replaced by a vector network analyser (VNA). The VNA is primarily used for rapid characterisation and of the microwave transmission and replaces everything above the black dots. Figure from de Visser [16].

this section. Cu cables are used to connect the filters and the sample box in which the MKIDs are coupled to feed line that carries the microwave signal between the two connectors. The returning signal is amplified at the 4K-stage using a low-noise high-electron-mobility transistor (HEMT) amplifier (CITCRYO4-12A Wadefalk/Weinreb) which is similar to the amplifiers used in modern radio telescopes [77]. Two additional amplifiers which are located at room temperature, further amplify the signal before it is combined with the original signal in the IQ-mixer (Miteq IRM0218LC1Q). Two variable attenuators (Aeroflex/Weinschel 8310) are used to maintain a constant signal power at the entrance of the IQ-mixer, while varying the signal power used to read the MKIDs. A 2-channel ADC (National Instruments PXI-5922) digitizes the output of the IQ-mixer with a maximum rate of 2 MHz. The entire system is calibrated for phase imbalance, gain imbalance and DC offset using the calibration procedure presented by Barends [37]. I and Q directly correspond to the real and imaginary part of S_{21} . For a rapid characterisation of S_{21} over a wide frequency range, the signal generator and IQ-mixer can be replaced by a vector network analyser (Agilent PNA-L N5230A).

6.5 Coupling radiation into an MKIDs

The two incarnations of MKIDs presented in Sect. 6.1 use different methods to couple radiation into the superconductor. The meandered inductor of a LEKID can be considered as a resistive sheet which absorbs light which has its electric field parallel to the strips. The absorbed power can be calculated using the geometric throughput of the light. The lens-antenna systems used to couple radiation into distributed resonators are more sensitive to the direction of the light source. This directivity can be described by their beam pattern. In the following subsections we will formulate the power absorbed by an MKID from a source distribution, $S_\nu(\theta, \phi)$, using both geometrical arguments and information from beam pattern simulations.

6.5.1 Geometrical throughput

The power received by an absorber from sources around it can be determined using

$$P = \int_{\nu} \int_{4\pi} S_\nu(\theta, \phi) \eta_\nu^{\text{abs}} d\nu d^2\mathcal{E} \quad (6.57)$$

Here η_ν^{abs} is the frequency dependent absorption efficiency of the resistive sheet. η_ν^{abs} is generally dominated by the impedance mismatch between the absorber and the surrounding medium. Rösch [78] reviews a number of common scenarios for LEKIDs. $d^2\mathcal{E}$ is the so-called throughput, or etendue. The geometrical definition of the etendue for

light crossing an infinitesimal surface element, dS , at an angle θ with respect to the vector, \vec{n}_S , which is perpendicular to dS , is

$$d^2\mathcal{E} = n dS \cos(\theta) d\theta \quad (6.58)$$

$$d^2\mathcal{E} = n^2 dS \cos(\theta) d\Omega \quad (6.59)$$

in 2D and 3D, respectively. Here n is the refractive index of the medium in which dS is immersed and $d\Omega$ is the solid angle in which the light crossing the surface dS is confined. The product $dS \cos \theta$ is the area of dS projected in the direction of the light propagation. Because angles, solid angles, and refractive indices are dimensionless quantities, etendue has units of area (given by dS).

In the cryogenic setup presented in Sect. 6.4 the radiation will travel through vacuum which has $n = 1$ at all frequencies. This means $d^2\mathcal{E}$ is frequency independent. Using the source distribution given by Eq. 6.56 we can rewrite Eq. 6.57.

$$P = \int_{\nu} \frac{1}{2} F_{\nu} B_{\nu}(T_{\text{BB}}) \eta_{\nu}^{\text{abs}} d\nu \int_{\text{aperture}} dS \cos(\theta) d\Omega \quad (6.60)$$

The second integral is often called the total throughput, \mathcal{E} , from the aperture to the MKID.

$$\mathcal{E} = \int d^2\mathcal{E} = \int dS \cos(\theta) d\Omega \quad (6.61)$$

For a circular absorber with radius R_{abs} and centred on $(x, y, z) = (0, 0, 0)$ in combination with a circular aperture with radius R_{ap} centred on $(x, y, z) = (0, 0, H)$, \mathcal{E} can be evaluated to be

$$\mathcal{E} = \frac{\pi^2 R_{\text{ap}}^2 R_{\text{abs}}^2}{R_{\text{ap}}^2 + R_{\text{abs}}^2 + H^2} \quad (6.62)$$

if $H^2 \gg R_{\text{ap}}^2 + R_{\text{abs}}^2$. Or equivalently

$$\mathcal{E} = \pi^2 R_{\text{abs}}^2 (1 - \cos^2(\gamma)) \quad (6.63)$$

Here $\gamma = \arctan(R_{\text{ap}}/H)$ is the aperture opening angle. A circular absorber might seem weird for MKIDs, which typically have a rectangular absorber. However, to minimize the volume of the inductor (and increase the responsivity) many LEKIDs use a lens to increase the filling factor of the array. The inductor of the LEKID is placed in the focus of a lens with radius R_{lens} . In this situation we can assume $R_{\text{lens}} = R_{\text{abs}}$. For an aperture of radius $R_{\text{ap}} = 1$ mm, at a height $H = 15.05$ mm the etendue of a 1 or 1.9 mm diameter lens is $\mathcal{E} = 1.08 \times 10^{-8}$ and $\mathcal{E} = 3.92 \times 10^{-8}$, respectively, using Eq. 6.63. Eq. 6.62 gives values, which are 0.1% and 0.4% lower for the smaller and larger lens, respectively. This is well below any experimental errors.

Note that in both Eq. 6.62 and Eq. 6.63 the area of the absorber can be recognized as πR_{abs}^2 . Hence, we can write

$$\mathcal{E} = \pi A_{\text{abs}} (1 - \cos^2(\gamma)) \quad (6.64)$$

This equation is valid regardless of the shape of the absorber, if the maximum linear dimension of the absorber is smaller than H .

6.5.2 Lens-antenna coupling

Alternatively, the sub-mm radiation can be launched into a superconducting resonator using the combination of a lens and a planar antenna. In this case the power received by the MKID can be calculated using the beam pattern of the lens-antenna system. The power received by any antenna is given by [79]

$$P = \int_{\nu} \int_{4\pi} S_{\nu}(\theta, \phi) A_{\text{eff}}(\theta, \phi) d\Omega d\nu \quad (6.65)$$

Here A_{eff} is the effective area of the antenna, which is equal to the area that would absorb an equivalent amount of radiation as the antenna. For any lossless antenna this value is normalised to λ^2 , which is the throughput of a single mode.

$$\int_{4\pi} A_{\text{eff}}(\theta, \phi) d\Omega = \lambda^2 = \frac{c^2}{\nu^2} \quad (6.66)$$

Here λ is the wavelength of the radiation and c the speed of light. The *weak reciprocity* theorem of antennas states [79]: *The power pattern of an antenna is the same for transmitting and receiving.* Therefore, we can relate $A_{\text{eff}}(\theta, \phi)$ to the directivity, $D(\theta, \phi)$, or beam pattern using

$$\frac{\lambda^2}{4\pi} D(\theta, \phi) = A_{\text{eff}}(\theta, \phi) \quad (6.67)$$

Like the effective area of a lossless antenna, the total directivity is normalized

$$\int_{4\pi} D(\theta, \phi) d\Omega = 4\pi \quad (6.68)$$

This normalization follows directly from the conservation of energy. Power delivered to a point in space will, in principle, radiate to all directions equally, $D = 1$. An antenna can only focus this radiation towards certain directions, $D > 1$, if in other direction the emitted power is reduced $D < 1$. An antenna can never emit more power than it receives at its feed. Combining Eqs. 6.65 and 6.67 allows us to calculate the power received by an antenna once the beam pattern is known.

$$P = \frac{\lambda^2}{4\pi} \int_{\nu} \int_{4\pi} S_{\nu}(\theta, \phi) D(\theta, \phi) d\Omega d\nu \quad (6.69)$$

Comparison with Eq. 6.57 shows that the etendue is equivalent to

$$d^2\mathcal{E} = \frac{\lambda^2}{4\pi} D(\theta, \phi) d\Omega \quad (6.70)$$

This assumes perfect absorption by the absorber i.e. $\eta_{\nu}^{\text{abs}} = 1$ and a lossless antenna. However, just like absorbers are not perfect, a lens-antenna system will also not launch all the received radiation into the MKID. We can define the antenna gain $G(\theta, \phi) = \eta_{\text{feed}} D(\theta, \phi)$. Here η_{feed} is the lens-antenna feed efficiency which is given by the fraction of the power sent to the port of an antenna that ends in the far-field beam pattern. Four loss components can be identified in the emission process:

- the impedance mismatch between the antenna and the port (waveguide) that feeds it. This is given by the matching efficiency, η_z .
- ohmic or resistive losses by the metal structure of the antenna. Because the antennas in this work are made from superconducting material with a gap, 2Δ , which is larger than the energy of the received EM radiation, we expect no ohmic losses. Hence, this efficiency is expected to be unity, $\eta_R = 1$
- Reflection losses at the interface between the lens dielectric and the air/vacuum. These reflection losses are captured by the reflection efficiency, η_{ref} .
- A fraction of the power emitted by the antenna will be emitted into the Si wafer or the flange of the lens array as shown in Fig. 6.11(a). Any power emitted with an angle $\phi > \phi_0$ will not reach the emitting surface of the lens and as such is lost to the emission process. The fraction of the power lost this way is captured by the lens spill-over efficiency, $\eta_{\text{so}}^{\text{lens}}$.

The total lens antenna feed efficiency is given by:

$$\eta_{\text{feed}} = \eta_z \eta_R \eta_{\text{ref}} \eta_{\text{so}}^{\text{lens}} \quad (6.71)$$

In addition to losses in the lens-antenna system, there are also losses in the MKID detector. These are given by the detector efficiency, η_{det} , which describes the fraction of power launched into the superconducting transmission line that is seen by the detector. η_{det} will include η_{abs} as given by Eq. 6.35, but may for example also include losses due to the creation of quasiparticles in the ground plane of the transmission line. The combination of the feed efficiency and detector efficiency is called the radiation efficiency

$$\eta_{\text{rad}} = \eta_{\text{feed}} \eta_{\text{det}} \quad (6.72)$$

The formalism presented above enables us to calculate the power detected by MKIDs in our cryogenic system. Eq. 6.69 can be specified using the description of our source

as given by Eq. 6.56 and the simulated beam patterns, $G(\theta, \phi)$, shown in Sect. 6.4.2.

$$P = \frac{\lambda^2}{4\pi} \eta_{\text{det}} \int_{\nu} \frac{1}{2} \eta_{\text{feed}}(\nu) F_{\nu} B_{\nu}(T_{\text{BB}}) d\nu \int_{\text{ap}} D(\theta, \phi) d\Omega \quad (6.73)$$

Splitting the frequency integral and the spatial integral is allowed, if the directivity of the beam does not change significantly over the frequency in which radiation is received. For the narrow-band twin-slot antenna used in this work, for which the directivity at 350 GHz is known, this is a valid assumption if F_{ν} restricts the out-of-band radiation. The directivity is obtained by normalizing the gain pattern

$$P = \lambda^2 \int_{\nu} \frac{1}{2} \eta_{\text{rad}}(\nu) F_{\nu} B_{\nu}(T_{\text{BB}}) d\nu \frac{\int_{\text{ap}} G(\theta, \phi) d\Omega}{\int_{4\pi} G(\theta, \phi) d\Omega} \quad (6.74)$$

Within this equation we recognize the spill-over efficiency of the far-field beam pattern with respect to the source.

$$\eta_{\text{so}}^{\Omega_{\text{S}}} = \frac{\int_{\text{ap}} G(\theta, \phi) d\Omega}{\int_{4\pi} G(\theta, \phi) d\Omega} \quad (6.75)$$

The use of $\eta_{\text{so}}^{\Omega_{\text{S}}}$ is preferred with respect to the direct use of the simulated gain, because it leaves all the efficiency terms in the frequency integral. This enables us to take any known frequency dependency into account. Furthermore, $\eta_{\text{so}}^{\Omega_{\text{S}}}$ allows a direct comparison to the values of \mathcal{E} found in Sect. 6.5.1.

$$\mathcal{E}_{\text{BP}} = \lambda^2 \eta_{\text{so}}^{\Omega_{\text{S}}} = \lambda^2 \frac{\int_{\text{ap}} G(\theta, \phi) d\Omega}{\int_{4\pi} G(\theta, \phi) d\Omega} \quad (6.76)$$

Fig. 6.13 compares the geometric etendue as given by Eq. 6.63 (dashed lines) and the throughput determined from a simulated beam pattern (Eq. 6.76, solid lines) as a function of the aperture opening angle γ . In general the geometric etendue will overestimate the actual throughput, especially at large γ . For the 2 mm lenses used in this thesis (see Sect. 6.4.2) the geometric etendue is an overestimation even at small opening angles. This is the result of the highly directive beam created by the 2 mm lenses. As shown in Fig. 6.10(a) the gain varies within the solid angle spanned by the aperture. This decreases the total radiation received. The geometric throughput assumes equal response to radiation from all directions. For the wider beam of the 1 mm lenses the assumption of constant gain is valid for $\gamma \leq 9^\circ$.

Off-axis aperture

A co-alignment of aperture and the lens-antenna is a convenient situation to evaluate the performance of a detector. However, in reality this situation will not often be the case if a small aperture is used. In the case of a small aperture not all pixels in an

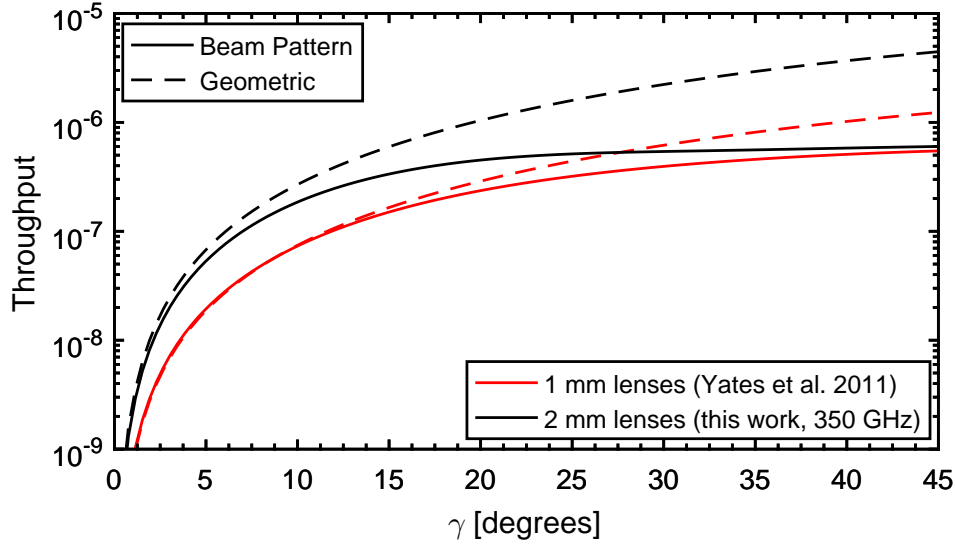


Figure 6.13: The etendue \mathcal{E} as a function of the opening angle, γ of the aperture. Both the geometric etendue (dashed) as given by Eq. 6.63 and the beam pattern throughput (solid) as given by Eq. 6.76 are shown. The black lines are for the lens-antenna system used in this work, whereas the blue lines show the results for Yates et al. [18] who used smaller lenses.

array will view the aperture at broadside. Furthermore, the alignment of a single pixel also incurs tolerances. To investigate the effect of a non-coaxial setup, $S_\nu(\theta, \phi)$ needs to be determined for an aperture located at $(x, y, z) = (x_{\text{ap}}, y_{\text{ap}}, H)$. The focal point of the lens-antenna system is assumed to be located at the origin of this Cartesian coordinate system. In this case the surface integral in (θ, ϕ) -space over the aperture present in Eq. 6.74 is significantly more complex due to interdependence of the integration boundaries.

Using the dummy parameter α the outside of the pinhole can be parametrized in Cartesian

$$x = R_{\text{ap}} \cos(\alpha) + x_{\text{ap}} \quad (6.77)$$

$$y = R_{\text{ap}} \sin(\alpha) + y_{\text{ap}} \quad (6.78)$$

$$z = H \quad (6.79)$$

and ISO80000 spherical coordinates (see App. B).

$$r^2 = R_{\text{ap}}^2 + x_{\text{ap}}^2 + y_{\text{ap}}^2 + H^2 + 2R_{\text{ap}}(x_{\text{ap}} \cos(\alpha) + y_{\text{ap}} \sin(\alpha)) \quad (6.80)$$

$$\cos(\theta) = H/r \quad (6.81)$$

$$\tan(\phi) = \frac{R_{\text{ap}} \sin(\alpha) + y_{\text{ap}}}{R_{\text{ap}} \cos(\alpha) + x_{\text{ap}}} \quad (6.82)$$

We would like to know for a given θ , which values of ϕ are inside the aperture, or vice versa. Note that α is in this respect a convenient intermediate parameter. The above

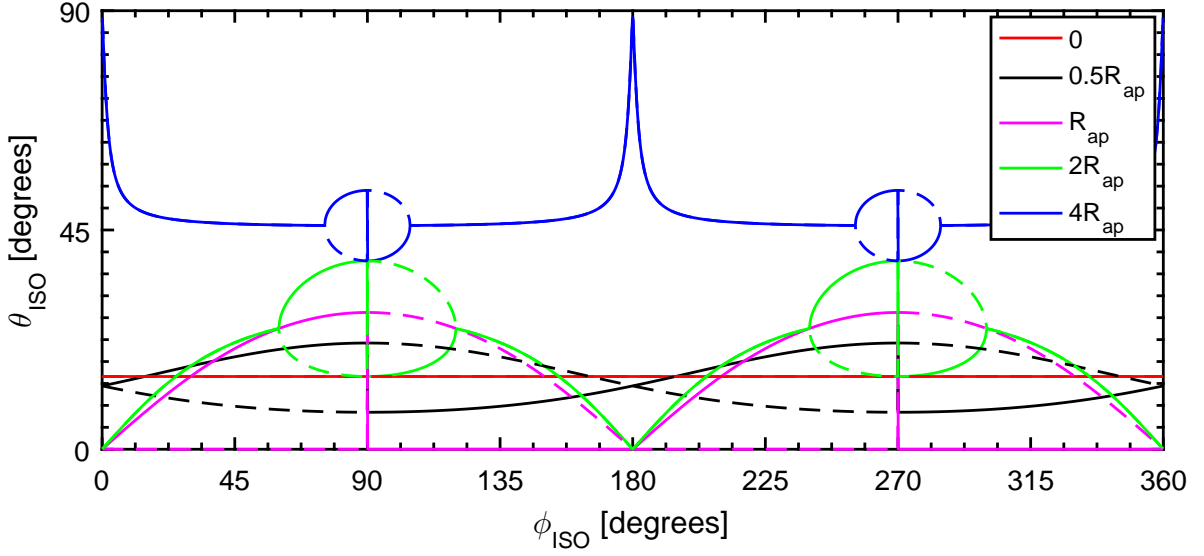


Figure 6.14: The location of an off-axis aperture in ISO80000 spherical coordinates. In Cartesian coordinates the aperture is located a $(0, y_{\text{ap}}, H)$, where $H = 15$ mm, y_{ap} is indicated by the legend and $R_{\text{ap}} = 4$ mm. The limiting values of $\theta(\alpha_-)$ (solid line) and $\theta(\alpha_+)$ (dashed line) surrounding the apertures as a function of ϕ are shown. Note the mirror image of the aperture at $\phi_c + \pi$ and the switch between the role as upper and lower limit at $\phi = 0.5\pi$ and $\phi = 1.5\pi$.

equation for $\tan(\phi)$ is solved for α .

$$\alpha_{\pm} = -i \ln \left(\frac{-1}{2R_{\text{ap}}} \left(x_{\text{ap}}(1 - e^{2i\phi}) + i y_{\text{ap}}(1 + e^{2i\phi}) \pm \sqrt{B(\phi)} \right) \right) \quad (6.83)$$

$$B(\phi) = (x_{\text{ap}}(1 - e^{2i\phi}) + i y_{\text{ap}}(1 + e^{2i\phi}) - 2i R_{\text{ap}} e^{i\phi}) \times (x_{\text{ap}}(1 - e^{2i\phi}) + i y_{\text{ap}}(1 + e^{2i\phi}) + 2i R_{\text{ap}} e^{i\phi}) \quad (6.84)$$

For every value of ϕ the two limiting values of θ can be determined by substituting the two values of α into Eqs. 6.80 and 6.81. Fig. 6.14 shows the solutions θ as a function of ϕ for five different offsets in the positive y direction (colours). Solutions for both α_- (solid line) and α_+ (dashed line) are shown. In these examples $H = 15$ mm and $R_{\text{ap}} = 4$ mm. It is clear from Fig. 6.14 that the solution of an aperture centred at $\phi = \phi_c$ is mirrored at $\phi = \phi_c \pm \pi$. Furthermore, the role of minimum and maximum boundary of $\theta(\phi)$ switches between the two solutions. This switch always occurs at $\phi = 0.5\pi$ and $\phi = 1.5\pi$ and is independent of ϕ_c . Both these effects have to be accounted for in order to select the right angles that together span the aperture.

6.6 Photon noise limited performance by MKIDs

The most precious commodity during any astronomical observation is observation time. To achieve the deepest images in the shortest observation time possible photon noise limited detectors are required that, ideally, detect every single photon within the observational bandwidth. These two requirements can be expressed as two key performance measures for a single MKID pixel: the sensitivity and the radiation efficiency, η_{rad} .

6.6.1 Sensitivity

The sensitivity of any detector may be expressed in terms of the noise equivalent power (NEP). The NEP is defined as the signal power that yields a signal-to-noise of unity in a 1 Hz bandwidth. For MKIDs using phase, $x = \theta$, or amplitude, $x = A$, readout the NEP it is given by

$$NEP_x(\omega) = \sqrt{S_x(\omega)} \left(\frac{dx}{dP} \right)^{-1} \sqrt{1 + \omega^2 \tau_{\text{qp}}} \sqrt{1 + \omega^2 \tau_{\text{res}}} \quad (6.85)$$

Here $\tau_{\text{res}} = Q_1/(\pi f_{\text{res}})$ is the resonator ring time and ω the modulation frequency. The goal for MKIDs is to achieve photon noise limited performance at the loading levels relevant for the envisioned application. Photon noise is the noise in a detector due to the random arrival rate of photon. Photon noise limited performance is achieved if $NEP_x(\omega)$ is identical to the photon noise limited NEP, which implies that the detector does not add any noise of its own. The NEP of a photon noise limited MKID is given by [80]

$$NEP^{\text{ph}}(P_{\text{abs}}) = \sqrt{2P_{\text{abs}} (h\nu(1 + \eta_{\text{co}}^{\Omega_s}(\nu)B) + \Delta/\eta_{\text{pb}})} \quad (6.86)$$

Here P_{abs} is the power absorbed in the MKID and B the photon occupation number of the (single) mode received by the detector. $\eta_{\text{co}}^{\Omega_s}$ is the optical coupling efficiency between the radiation source and the detector, which is given by

$$\eta_{\text{co}}^{\Omega_s}(\nu) = \eta_{\text{rad}}(\nu) F_{\nu} \eta_{\text{so}}^{\Omega_s} \quad (6.87)$$

The first term in the square root of Eq. 6.86 describes the random photon arrival rate. In this term $1 + \eta_{\text{co}}^{\Omega_s} B$ is the correction to Poisson statistics due to wave bunching. The second term describes the recombination of the optically excited quasiparticles. The photon noise limited NEP is independent of the response and as such will be equal in phase and amplitude. The photon noise limited noise PSD can be obtain by multiplying Eq. 6.86 by the relevant response and squaring the result. Note that following the same reasoning as for the GR noise, the photon noise level is independent of the absorbed power. Photon noise limited performance at loading levels expected on ground based

sub-mm telescopes was first achieved by Yates et al. [18] using MKIDs in amplitude readout. However, to achieve this performance trade-offs have to be made in the choice of superconducting materials and geometry.

Superconducting resonators made from aluminium have a long quasiparticle lifetime ($\tau_{\text{qp}} \sim 1$ ms) and can achieve internal quality factors $Q_i \sim 10^7$ [81]. Aluminium resonators have shown GR noise limited performance [28], which is ultimate performance limit of MKIDs. The NEP limited set by the GR noise is given by [26, 82]

$$NEP^{GR} = \frac{2\Delta}{\eta_{\text{pb}}} \sqrt{\frac{N_{\text{qp}}}{\tau_{\text{qp}}}} \quad (6.88)$$

GR noise limited aluminium MKIDs have shown photon noise limited performance down to 0.1 fW of 1.5 THz radiation, which is equal to $NEP_A = 4 \times 10^{-19}$ W/ $\sqrt{\text{Hz}}$. This sensitivity would be sufficient for a far-infrared camera on a cold 3 meter class space telescope [83]. However, the use of amplitude readout limits the extension into large format arrays. Furthermore, aluminium has a very low sheet resistance, which makes direct absorption as used by LEKIDs challenging. Other elemental superconductors, such as tantalum and niobium, can be used to fabricate high-Q resonators. However, they have a lower quasiparticle lifetime, which reduces the sensitivities that can be achieved by these materials.

Leduc et al. [84] proposed TiN as an alternative to aluminium. TiN has a high Q_i , low TLS noise and $\lambda_{\text{TiN}} > \lambda_{\text{Al}}$. The latter means TiN can achieve a higher kinetic induction fraction than aluminium for the same geometry and can reach the same resonance frequency using a smaller volume. In addition, TiN has a high normal-state surface resistance, which makes direct absorption of radiation from free space easier. Furthermore, the T_c of TiN can be changed by varying the nitrogen fraction. Photon noise limited performance has been shown for TiN LEKIDs [85] at powers > 1 pW. This ‘poor’ performance of such a promising material is attributed to the anomalous response of TiN [86, 87]. The hypothesis is that the high normal-state resistivity of TiN is the result of an extremely short mean free path, which means localisation effects affect the superconducting state [88]. This means that the response of high resistivity (disordered) superconductors cannot be described by Mattis-Bardeen theory [36]. Nevertheless, disordered superconductors are an attractive material for LEKIDs and research into different superconducting compounds is ongoing [e.g. 89].

Besides a choice of material, a choice in geometry has to be made. In this not only the choice of LEKID or distributed resonator is important, but also the dimensions of their structures. For example, the suppression of TLS noise would favour large structures. However, this is in conflict with the small volume required to maximize responsivity. In LEKIDs this can be accommodated by using a large interdigitated capacitor to suppress the TLS noise and a small inductor to increase the response. However, in distributed resonators this is more difficult, because the electric and magnetic fields are present throughout the resonator.

Another geometrical design is that of C_c . Generally, the optimum value of Q_c is a value equal to Q_i at the expected optical loading. Minimization of Q_c decreases the system noise as shown in Eq. 6.53, because more readout power enters the resonator. However, as soon as $Q_c < Q_i$ it also reduces the MKIDs response. Furthermore it increases the width of the resonator, which decreases the number of resonators (pixels) per unit readout bandwidth.

6.6.2 Radiation efficiency

The efficiency of a detector in detecting incoming photons is often expressed in terms of the optical efficiency: The fraction of photons from a given source detected by the detector. The disadvantage of this definition is that it depends on the definition of the optical system: the optical efficiency depends on the coupling between the source and detector. To alleviate this problem the optical performance of an MKID may be separated into a system independent aperture efficiency, η_A , and a radiation efficiency $\eta_{\text{rad}} = \eta_{\text{feed}}\eta_{\text{det}}$, which describes the losses inside the entire MKID detector.

$$\eta_A = \eta_{\text{feed}}\eta_{\text{det}} \frac{\lambda^2 D(\theta_{\text{BS}}, \phi_{\text{BS}})}{4\pi A} \quad (6.89)$$

Here $(\theta_{\text{BS}}, \phi_{\text{BS}})$ is the direction of maximum gain of the detector and A its physical area. As can be seen it requires knowledge about the beam pattern, which may be obtained using simulation software such as CST microwave studio [71]. This software can also give an accurate measure of η_{feed} for the intended device geometry.

η_{rad} will capture any losses in the detector. For example, we will find a reduction of η_{rad} through η_{det} , if the CPW is not sufficiently long to absorb all the incoming radiation, i.e. $\eta_{\text{abs}} < 1$. To determine η_{rad} experimentally we follow the procedure presented in Chapter 7. The power absorbed by MKIDs in a given experimental setup can be calculated using Eq. 6.74. Based on this calculated power, P_{calc} , we can determine an expected photon noise limited NEP, $NEP_{\text{calc}}^{\text{ph}}(P_{\text{calc}})$ using Eq. 6.86. However, the true power absorbed by the MKID, i.e. the power to which it responds, is ϵP_{calc} . Differences may be the result of minor difference between the simulated and real geometry or an improper description of loss mechanisms within the resonator. The measured photon noise limited NEP will be given by $NEP_{\text{meas}}^{\text{ph}}(\epsilon P_{\text{calc}})$. The ratio between the expected and the measured photon noise limited NEP is

$$\frac{NEP_{\text{calc}}^{\text{ph}}(P_{\text{calc}})}{NEP_{\text{meas}}^{\text{ph}}(\epsilon P_{\text{calc}})} \propto \frac{\sqrt{P_{\text{calc}}}}{\sqrt{\epsilon P_{\text{calc}}}} \propto \sqrt{\frac{1}{\epsilon}} \quad (6.90)$$

This assumes that the NEP as a result of detector related noise is negligible or corrected for. More importantly, it assumes that either the photon bunching is negligible or the coupling efficiency between the radiation source and the detector is well known and as a result ϵ is close to 1. If photon bunching is significant and ϵ deviates significantly

from 1 this implies that $\eta_{\text{co}}^{\Omega_s}$ is poorly understood and the photon bunching term is not correctly estimated.

Note that for a correct determination of both η_A and η_{rad} an experimental verification of the shape of the beam pattern is required. If the shape of the pattern is verified, the maximum directivity obtained from normalizing the gain can be used to determine η_A . Furthermore, the complete shape of the gain is used in Eq. 6.74 to calculate the coupling efficiency, $\eta_{\text{co}}^{\Omega_s}$, between the MKID and the radiation source in the given setup.

6.7 Fabrication of hybrid MKIDs

The hybrid NbTiN-Al MKIDs for which results are presented in the next Chapters were fabricated [90] in the cleanrooms at the Kavli Nanolab at Delft and SRON at Utrecht in June 2011.

The MKIDs are produced on a 4 inch diameter wafer of high resistivity ($\rho > 10 \text{ k}\Omega\text{cm}$ at room temperature) undoped Si. The $350 \text{ }\mu\text{m}$ thick wafer is cleaned using a O_2 descum in a TePla 300. The substrate's native oxide is removed by a 1 minute dip in a buffered hydrogen fluoride (HF) solution. This process also passivates the surface. Immediately after the HF dip, the wafer is loaded in the Nordiko 2000 system at the Kavli Nanolab and 200 nm NbTiN is deposited using DC reactive magnetron sputtering. This system achieves a base pressure of 2×10^{-7} Torr using an 11 K cryopump. An operational pressure of 6 mTorr is created using an inflow of 100 sccm Ar and 8.4 sccm N_2 . A power-biased plasma is maintained with 300 W of forward power at $\sim 320 \text{ V}$. A deposition rate of 25 nm/min is achieved using these parameters, as such taking 8 min for the complete deposition process. NbTiN with a $T_c > 15 \text{ K}$ and a resistivity $\rho < 100 \text{ }\mu\Omega\text{cm}$ was achieved under these conditions. Bos et al. [91] and Thoen et al. [92] describe a recent re-optimization of both the Nordiko 2000 and the Evatec LLS801 (described below) to reliably achieve NbTiN with these properties in both the Kavli and SRON cleanroom.

After deposition the wafer is spin-coated with hexamethyldisilazane (HMDS), which improves the adhesion of a photoresist. Subsequently, the photoresist AZ5214 is spun onto the wafer. Both fluids are spun at 4000 rpm for 65 s which includes a 5 s ramp at both the beginning and the end. The resist is baked at $90 \text{ }^\circ\text{C}$ for 60 s on a hot plate to allow use in positive mode. The feedline, ground planes and MKIDs are defined with UV contact lithography in which the mask is pressed to the wafer using hard contact and a vacuum. An illumination time of 10 s is used, which is equivalent to a dose of 200 mJ/cm^2 . The resist is developed by submerging the wafer in MF321 for 60 s and pure H_2O for 30 s.

The photoresist pattern is transferred to the NbTiN using reactive ion etching. The etch is performed inside the Leybold reactive ion etcher and uses a gas mixture of SF_6

(13.5 sccm) and O₂ (20 sccm). At a pressure of 8 μ bar a plasma is maintained with ~ 345 V and 50 W of forward power. This process creates a sloped edge in the NbTiN, which helps the step coverage during the deposition of Al. The etch is monitored with a camera to determine the termination point. A typical overetch of 15 s is used to ensure all NbTiN is removed where required.

When a complete etch is achieved the resist is removed using acetone. The wafer is then rinsed with isopropanol and blown dry. New resist is spun onto the wafer following the above procedure to protect the wafer during shipment to Utrecht.

After arrival in Utrecht the protective resist is removed using acetone and isopropanol. The Si wafer with patterned NbTiN layer is then dipped in a solution containing 5% (volume) HF for 10 seconds to remove any oxides formed on the exposed Si. A 48 nm thick layer of Al is sputter-deposited over the patterned NbTiN layer in an Evatec LLS801 system which is an extensively customized version of an industrial Balzers LLS801. The LLS801 is equipped with a cryopump and a load-lock and is able to achieve a background pressure below 2×10^{-7} mbar. The Al is grown at a rate of 0.4 nm/s by DC magnetron sputtering, at a power of 800 W and a pressure of 5 mTorr (Ar).

The wafer is spin-coated with HMDS and a 1.2 μ m thick layer of AZ6612 photoresist. The wafer is then baked on a hot plate for 60 s at 100 °C. The aluminium central lines are patterned using contact UV lithography. The resist is exposed for 5 s, which equals a dose of 100 mJ/cm², and developed by suspending it in AZ Developer 111 for 25 s. After development the alignment between the patterned NbTiN and photoresist is checked using an optical microscope. If the alignment is found to be acceptable, any unwanted leftovers of the resist are removed by reactive ion etching using an oxygen plasma for 15 s. If the patterns are misaligned the HMDS and AZ6612 are stripped from the wafer and the lithography process is repeated.

The pattern in the photoresist is transferred onto the Al using wet etching. The wafer is submerged for 105 s in a mixture of phosphoric acid, acetic acid, water and nitric acid (also known as PAWN or Transene A). Acetone is spun onto the wafer to remove the remaining resist pattern.

AZ6612 resist is spun onto the wafer and baked for 30 s at 110 °C on a hot plate. The resist protects the wafer during dicing and is removed before mounting by soaking the chips in acetone and rinsing them with isopropanol. The chip is placed in the sample holder with the MKIDs facing down and fixed using 4 small flat phosphor-bronze springs. A microlens array is then mounted onto the chip. The microlens array is produced by Veldlaser¹ using commercial laser ablation of high resistivity Si ($\rho > 5$ k Ω cm) and receives an anti-reflection coating of Parylene with a $\lambda/4$ thickness after production. The following procedure is used to accurately align the lens centres with the planar antennas on the chip. The sample holder is placed on an x-y-rotation

¹www.veldlaser.nl

stage of a microscope and aligned for rotation. Using the absolute calibration of the microscope, the distance between a chip corner and antenna centre is measured. A second alignment stage holds the microlens array and presses it to the backside of the wafer whilst still allowing movement. The microlenses are aligned for rotation and subsequently in the x-y-direction. The x-y-alignment is done using the absolute distance calibration and the previous distance measure between a chip corner and antenna centre. Once the lens and antenna centres are aligned, the lens array is glued to the chip using two droplets of cyanoacrylate glue at the sides of the lenses. The glue will flow under the lensarray due to capillary action and hardens in 10 min. This procedure achieves a typical alignment accuracy of 10 μm , but only works for small chips. Large arrays on Si require alignment markers on the back to align the lens array accurately. Alternatively, sapphire wafers are transparent, which makes lens alignment easier.

References

- [1] P. K. Day, H. G. LeDuc, B. A. Mazin, A. Vayonakis, and J. Zmuidzinas, *A broadband superconducting detector suitable for use in large arrays*, Nature **425**, 817 (2003).
- [2] S. Doyle, P. Mauskopf, J. Naylor, A. Porch, and C. Duncombe, *Lumped Element Kinetic Inductance Detectors*, Journal of Low Temperature Physics **151**, 530 (2008).
- [3] J. J. A. Baselmans, *Kinetic Inductance Detectors*, Journal of Low Temperature Physics **167**, 292 (2012).
- [4] H. McCarrick, D. Flanigan, G. Jones, B. R. Johnson, P. Ade, et al., *Horn-coupled, commercially-fabricated aluminum lumped-element kinetic inductance detectors for millimeter wavelengths*, Review of Scientific Instruments **85**, 123117 (2014).
- [5] A. Endo, *Aln tunnel barriers for submillimeter wave sis mixers*, University of Tokyo, Tokyo, Japan (2008).
- [6] N. W. Ashcroft and N. D. Mermin, *Solid State Physics*, Harcourt College Publishers, Orlando, Florida (1976).
- [7] J. R. Hook and H. E. Hall, *Solid State Physics*, John Wiley & Sons, Inc., Chichester, UK (2005).
- [8] R. L. Powell and F. R. Fickett, *Cryogenic properties of copper*, International Copper Research Association (1979).
- [9] D. Pines and P. Nozières, *The theory of quantum liquids: volume 1*, W. A. Benjamin, Inc. (1966).
- [10] A. Soni and G. S. Okram, *Resistivity and thermopower measurement setups in the temperature range of 5-325 K*, Review of Scientific Instruments **79**, 125103 (2008).

- [11] D. van Delft and P. Kes, *The discovery of superconductivity*, Physics Today **63**, 38 (2010).
- [12] H. Kamerlingh Onnes, *Further experiments with liquid helium. G. On the electrical resistance of pure metals, etc. VI. On the sudden change in the rate at which the resistance of mercury disappears.*, Communications from the Physical Laboratory of the University of Leiden, 124c (1911).
- [13] H. Kamerlingh Onnes, *Further experiments with liquid helium. G. On the electrical resistance of pure metals, etc. VI. On the sudden change in the rate at which the resistance of mercury disappears.*, Communications from the Physical Laboratory of the University of Leiden, 133b (1913).
- [14] W. Meissner and R. Ochsenfeld, *Ein neuer Effekt bei Eintritt der Supraleitfähigkeit*, Naturwissenschaften **21**, 787 (1933).
- [15] J. Bardeen, L. N. Cooper, and J. R. Schrieffer, *Theory of Superconductivity*, Physical Review **108**, 1175 (1957).
- [16] P. J. de Visser, *Quasiparticle dynamics in aluminium superconducting microwave resonators*, Delft University of Technology, Delft, The Netherlands (2014).
- [17] G. Vardoulakis, *Superconducting kinetic inductance detectors: theory, simulations and experiments*, University of Cambridge, Cambridge, UK (2007).
- [18] S. J. C Yates, J. J. A Baselmans, A. Endo, R. M. J. Janssen, L. Ferrari, et al., *Photon noise limited radiation detection with lens-antenna coupled microwave kinetic inductance detectors*, Applied Physics Letters **99**, 073505 (2011).
- [19] T. Guruswamy, D. J. Goldie, and S. Withington, *Quasiparticle generation efficiency in superconducting thin films*, Superconductor Science Technology **27**, 055012 (2014).
- [20] D. J. Goldie and S. Withington, *Non-equilibrium superconductivity in quantum-sensing superconducting resonators*, Superconductor Science Technology **26**, 015004 (2013).
- [21] P. J. de Visser, D. J. Goldie, P. Diener, S. Withington, J. J. A. Baselmans, et al., *Evidence of a Nonequilibrium Distribution of Quasiparticles in the Microwave Response of a Superconducting Aluminum Resonator*, Physical Review Letters **112**, 047004 (2014).
- [22] B. A. Mazin, *Microwave kinetic inductance detectors*, California Institute of Technology, Pasadena, California (2004).
- [23] A. Kozorezov, A. Volkov, J. Wigmore, A. Peacock, A. Poelaert, et al., *Quasiparticle-phonon downconversion in nonequilibrium superconductors*, Physical Review B **61**, 11807 (2000).

- [24] M. Kurakado, *Possibility of high resolution detectors using superconducting tunnel junctions*, Nuclear Instruments and Methods **196**, 275 (1982).
- [25] P. J. de Visser, S. J. C. Yates, T. Guruswamy, D. J. Goldie, S. Withington, et al., *The non-equilibrium response of a superconductor to pair-breaking radiation measured over a broad frequency band*, Applied Physics Letters **106**, 252602 (2015).
- [26] P. J. de Visser, J. J. A. Baselmans, J. Bueno, N. Llombart, and T. M. Klapwijk, *Fluctuations in the electron system of a superconductor exposed to a photon flux*, Nature Communications **5**, 3130 (2014).
- [27] S. B. Kaplan, C. C. Chi, D. N. Langenberg, J. J. Chang, S. Jafarey, et al., *Quasi-particle and phonon lifetimes in superconductors*, Physical Review B **14**, 4854 (1976).
- [28] P. J. de Visser, J. J. A. Baselmans, P. Diener, S. J. C. Yates, A. Endo, et al., *Number Fluctuations of Sparse Quasiparticles in a Superconductor*, Physical Review Letters **106**, 167004 (2011).
- [29] F. London and H. London, *The Electromagnetic Equations of the Supraconductor*, Proceedings of the Royal Society of London Series A **149**, 71 (1935).
- [30] A. B. Pippard, *An Experimental and Theoretical Study of the Relation between Magnetic Field and Current in a Superconductor*, Proceedings of the Royal Society of London Series A **216**, 547 (1953).
- [31] D. Saint-James, G. Sarma, and E. J. Thomas, *Type II superconductors*, First, Pergamon Press, Oxford, UK (1969).
- [32] J. Pearl, *Current Distribution in Superconducting Films Carrying Quantized Fluxoids*, Applied Physics Letters **5**, 65 (1964).
- [33] J. A. Stern, B. Bumble, H. G. Leduc, J. W. Kooi, and J. Zmuidzinas, *Fabrication and DC-Characterization of NbTiN Based SIS Mixers for Use Between 600 and 1200 GHz*, International Symposium on Space Terahertz Technology **9**, 305 (1998).
- [34] J. Zmuidzinas, *Superconducting microresonators: physics and applications*, Annual Reviews of Condensed Matter Physics **3**, 169 (2012).
- [35] D. Mattis and J. Bardeen, *Theory of the anomalous skin effect in normal and superconducting metals*, Physical Review **111**, 412 (1958).
- [36] E. F. C. Driessen, P. C. J. J. Coumou, R. R. Tromp, P. J. de Visser, and T. M. Klapwijk, *Strongly Disordered TiN and NbTiN s-Wave Superconductors Probed by Microwave Electrodynamics*, Physical Review Letters **109**, 107003 (2012).
- [37] R. Barends, *Photon-detecting superconducting resonators*, Delft University of Technology, Delft, The Netherlands (2009).

- [38] J. Gao, J. Zmuidzinis, A. Vayonakis, P. Day, B. Mazin, et al., *Equivalence of the Effects on the Complex Conductivity of Superconductor due to Temperature Change and External Pair Breaking*, Journal of Low Temperature Physics **151**, 557 (2008).
- [39] R. E. Collins, *Foundations for microwave engineering*, second, McGraw-Hill, New York (2001).
- [40] D. M. Pozar, *Microwave Engineering*, John Wiley & Sons, Inc., Hoboken, New Jersey (2012).
- [41] R. M. J. Janssen, A. Endo, J. J. A. Baselmans, P. J. Visser, R. Barends, et al., *Power Handling and Responsivity of Submicron Wide Superconducting Coplanar Waveguide Resonators*, Journal of Low Temperature Physics **167**, 354 (2012).
- [42] J. Gao, J. Zmuidzinis, B. A. Mazin, P. K. Day, and H. G. Leduc, *Experimental study of the kinetic inductance fraction of superconducting coplanar waveguide*, Nuclear Instruments and Methods in Physics Research A **559**, 585 (2006).
- [43] J. Gao, *The physics of superconducting microwave resonators*, California Institute of Technology, Pasadena, California (2008).
- [44] C. L. Holloway and E. F. Kuester, *Closed-form expressions for the current density on the ground plane of a microstrip line, with application to ground plane loss*, IEEE Transactions on Microwave Theory Techniques **43**, 1204 (1995).
- [45] J. C. Booth and C. L. Holloway, *Conductor loss in superconducting planar structures: calculations and measurements*, IEEE Transactions on Microwave Theory Techniques **47**, 769 (1999).
- [46] R. L. Kautz, *Picosecond pulses on superconducting striplines*, Journal of Applied Physics **49**, 308 (1978).
- [47] R. F. Broom and P. Wolf, *Q factor and resonance amplitude of Josephson tunnel junctions*, Physical Review B **16**, 3100 (1977).
- [48] W. Henkels and C. Kircher, *Penetration depth measurements on type II superconducting films*, IEEE Transactions on Magnetics **13**, 63 (1977).
- [49] P. J. de Visser, S. Withington, and D. J. Goldie, *Readout-power heating and hysteretic switching between thermal quasiparticle states in kinetic inductance detectors*, Journal of Applied Physics **108**, 114504 (2010).
- [50] M. S. Khalil, M. J. A. Stoutimore, F. C. Wellstood, and K. D. Osborn, *An analysis method for asymmetric resonator transmission applied to superconducting devices*, Journal of Applied Physics **111**, 054510 (2012).
- [51] P. C. J. J. Coumou, E. F. C. Driessen, J. Bueno, C. Chapelier, and T. M. Klapwijk, *Electrodynamic response and local tunneling spectroscopy of strongly disordered superconducting TiN films*, Physical Review B **88**, 180505 (2013).

- [52] J. van Rantwijk, M. Grim, D. van Loon, S. Yates, A. Baryshev, et al., *Multiplexed readout for 1000-pixel arrays of microwave kinetic inductance detectors*, IEEE Transactions on Microwave Theory and Techniques **64**, 1876 (2016).
- [53] A. D’Addabbo, R. Adam, A. Adane, P. Ade, P. André, et al., *The NIKA instrument: results and perspectives towards a permanent KID based camera for the Pico Veleta observatory*, ArXiv e-prints, 1312.4801 (2013).
- [54] L. Bisigello, S. J. C. Yates, V. Murugesan, J. J. A. Baselmans, and A. M. Baryshev, *Calibration Scheme for Large Kinetic Inductance Detector Arrays Based on Readout Frequency Response*, Journal of Low Temperature Physics **184**, 161 (2016).
- [55] U. Fano, *Ionization Yield of Radiations. II. The Fluctuations of the Number of Ions*, Physical Review **72**, 26 (1947).
- [56] P. J. Visser, J. J. A. Baselmans, P. Diener, S. J. C. Yates, A. Endo, et al., *Generation-Recombination Noise: The Fundamental Sensitivity Limit for Kinetic Inductance Detectors*, Journal of Low Temperature Physics **167**, 335 (2012).
- [57] P. J. de Visser, J. J. A. Baselmans, S. J. C. Yates, P. Diener, A. Endo, et al., *Microwave-induced excess quasiparticles in superconducting resonators measured through correlated conductivity fluctuations*, Applied Physics Letters **100**, 162601 (2012).
- [58] J. Gao, M. Daal, J. M. Martinis, A. Vayonakis, J. Zmuidzinas, et al., *A semiempirical model for two-level system noise in superconducting microresonators*, Applied Physics Letters **92**, 212504 (2008).
- [59] R. Barends, H. L. Hortensius, T. Zijlstra, J. J. A. Baselmans, S. J. C. Yates, et al., *Noise in NbTiN, Al, and Ta Superconducting Resonators on Silicon and Sapphire Substrates*, IEEE Transactions on Applied Superconductivity **19**, 936 (2009).
- [60] O. Noroozian, J. Gao, J. Zmuidzinas, H. G. LeDuc, and B. A. Mazin, *Two-level system noise reduction for Microwave Kinetic Inductance Detectors*, American Institute of Physics Conference Series **1185**, 148 (2009).
- [61] J. Wenner, R. Barends, R. C. Bialczak, Y. Chen, J. Kelly, et al., *Surface loss simulations of superconducting coplanar waveguide resonators*, Applied Physics Letters **99**, 113513 (2011).
- [62] M. R. Vissers, J. Gao, D. S. Wisbey, D. A. Hite, C. C. Tsuei, et al., *Low loss superconducting titanium nitride coplanar waveguide resonators*, Applied Physics Letters **97**, 232509 (2010).
- [63] R. Barends, N. Vercruyssen, A. Endo, P. J. de Visser, T. Zijlstra, et al., *Minimal resonator loss for circuit quantum electrodynamics*, Applied Physics Letters **97**, 023508 (2010).

- [64] R. Barends, N. Vercruyssen, A. Endo, P. J. de Visser, T. Zijlstra, et al., *Reduced frequency noise in superconducting resonators*, Applied Physics Letters **97**, 033507 (2010).
- [65] A. Bruno, G. de Lange, S. Asaad, K. L. van der Enden, N. K. Langford, et al., *Reducing intrinsic loss in superconducting resonators by surface treatment and deep etching of silicon substrates*, Applied Physics Letters **106**, 182601 (2015).
- [66] J. Gao, J. Zmuidzinas, B. A. Mazin, H. G. Leduc, and P. K. Day, *Noise properties of superconducting coplanar waveguide microwave resonators*, Applied Physics Letters **90**, 102507 (2007).
- [67] L. J. Swenson, P. K. Day, B. H. Eom, H. G. Leduc, N. Llombart, et al., *Operation of a titanium nitride superconducting microresonator detector in the nonlinear regime*, Journal of Applied Physics **113**, 104501 (2013).
- [68] J. J. A. Baselmans, S. J. C. Yates, P. Diener, and P. J. de Visser, *Ultra Low Background Cryogenic Test Facility for Far-Infrared Radiation Detectors*, Journal of Low Temperature Physics **167**, 360 (2012).
- [69] T. O. Klaassen, M. C. Diez, C. Smorenburg, K. J. Wildeman, J. H. Blok, et al., *Optical Characterization of Absorbing Coatings for Sub-millimeter Radiation*, International Symposium on Space Terahertz Technology **12**, 400 (2001).
- [70] F. P. Milliken, J. R. Rozen, G. A. Keefe, and R. H. Koch, *50 Ω characteristic impedance low-pass metal powder filters*, Review of Scientific Instruments **78**, 024701 (2007).
- [71] *CST Microwave Studio*, Computer Simulation Technology, Darmstadt, Germany (2013), <http://www.cst.com>.
- [72] M. C. Diez, T. O. Klaassen, K. Smorenburg, V. Kirschner, and K. J. Wildeman, *Reflectance measurements on submillimeter absorbing coatings for HIFI*, Proceedings of the SPIE **4013**, 129 (2000).
- [73] P. C. Hargrave, B. Maffei, R. Hermoso, G. Gannaway, M. J. Griffin, et al., *A low-background ^3He bolometer array test facility and its use in evaluating prototype arrays for FIRST-SPIRE*, Nuclear Instruments and Methods in Physics Research A **444**, 427 (2000).
- [74] L. Ferrari, O. Yurduseven, N. Llombart, S. J. C. Yates, A. M. Baryshev, et al., *Performance verification of a double-slot antenna with an elliptical lens for large format KID arrays*, Proceedings of the SPIE **9914**, 99142G (2012).
- [75] J. Bueno, P. J. de Visser, S. Doyle, and J. J. A. Baselmans, *Study on Optical Filter Heating in Background Limited Detector Experiments*, Journal of Low Temperature Physics **176**, 1089 (2014).

- [76] D. F. Filipovic, S. S. Gearhart, and G. M. Rebeiz, *Double-slot antennas on extended hemispherical and elliptical silicon dielectric lenses*, IEEE Transactions on Microwave Theory and Techniques **41**, 1738 (1993).
- [77] S. Weinreb, M. W. Pospieszalski, and R. Norrod, *Cryogenic, HEMT, Low-Noise Receivers for 1.3 to 43 GHz Range*, IEEE MTT-S International Microwave Symposium Digest (1988).
- [78] M. J. Rösch, *Development of lumped element kinetic inductance detectors for mm-wave astronomy at the iram 30 m telescope*, KIT Scientific Publishing, Karlsruhe, Germany (2014).
- [79] T. L. Wilson, K. Rohlf, and S. Hüttemeister, *Tools of radio astronomy*, Springer, Heidelberg, Germany (2013).
- [80] R. Boyd, *Photon bunching and the photon-noise-limited performance of infrared detectors*, Infrared Physics **22**, 157 (1982).
- [81] A. Megrant, C. Neill, R. Barends, B. Chiaro, Y. Chen, et al., *Planar superconducting resonators with internal quality factors above one million*, Applied Physics Letters **100**, 113510 (2012).
- [82] A. V. Sergeev, V. V. Mitin, and B. S. Karasik, *Ultrasensitive hot-electron kinetic-inductance detectors operating well below the superconducting transition*, Applied Physics Letters **80**, 817 (2002).
- [83] J. J. A. Baselmans, J. Bueno, S. J. C. Yates, O. Yurduseven, N. Llombard, et al., *A kilo-pixel imaging system for future space based far-infrared observatories using microwave kinetic inductance detectors*, submitted.
- [84] H. G. Leduc, B. Bumble, P. K. Day, B. H. Eom, J. Gao, et al., *Titanium nitride films for ultrasensitive microresonator detectors*, Applied Physics Letters **97**, 102509 (2010).
- [85] J. Hubmayr, J. Beall, D. Becker, H.-M. Cho, M. Devlin, et al., *Photon-noise limited sensitivity in titanium nitride kinetic inductance detectors*, Applied Physics Letters **106**, 073505 (2015).
- [86] J. Gao, M. R. Vissers, M. O. Sandberg, F. C. S. da Silva, S. W. Nam, et al., *A titanium-nitride near-infrared kinetic inductance photon-counting detector and its anomalous electrodynamics*, Applied Physics Letters **101**, 142602 (2012).
- [87] J. Bueno, P. C. J. J. Coumou, G. Zheng, P. J. de Visser, T. M. Klapwijk, et al., *Anomalous response of superconducting titanium nitride resonators to terahertz radiation*, Applied Physics Letters **105**, 192601 (2014).
- [88] P. C. J. J. Coumou, *Electrodynamics of strongly disordered superconductors*, Delft University of Technology, Delft, The Netherlands (2015).

-
- [89] P. Szypryt, B. A. Mazin, G. Ulbricht, B. Bumble, S. R. Meeker, et al., *High quality factor platinum silicide microwave kinetic inductance detectors*, Applied Physics Letters **109**, 151102 (2016).
 - [90] Y. J. Y. Lankwarden, A. Endo, J. J. A. Baselmans, and M. P. Bruijn, *Development of NbTiN-Al Direct Antenna Coupled Kinetic Inductance Detectors*, Journal of Low Temperature Physics **167**, 367 (2012).
 - [91] B. G. C. Bos, D. J. Thoen, E. A. F. Haalebos, P. M. L. Gimbel, T. M. Klapwijk, et al., *Reactive magnetron sputter deposition of superconducting niobium titanium nitride thin films with different target sizes*, IEEE Transactions on Applied Superconductivity **27**, 1 (2016).
 - [92] D. J. Thoen, B. G. C. Bos, E. A. F. Haalebos, T. M. Klapwijk, J. J. A. Baselmans, et al., *Superconducting NbTiN Thin Films with Highly Uniform Properties over a 100 mm diameter Wafer*, IEEE Transactions on Applied Superconductivity **27**, 1 (2016).

Chapter 7

High optical efficiency and photon noise limited sensitivity of microwave kinetic inductance detectors using phase readout

We demonstrate photon noise limited performance in both phase and amplitude readout in microwave kinetic inductance detectors (MKIDs) consisting of NbTiN and Al, down to 100 fW of optical power. We simulate the far-field beam pattern of the lens-antenna system used to couple radiation into the MKID and derive an aperture efficiency of 75%. This is close to the theoretical maximum of 80% for a single-moded detector. The beam patterns are verified by a detailed analysis of the optical coupling within our measurement setup.

This chapter is based upon R. M. J. Janssen, J. J. A. Baselmans, A. Endo, L. Ferrari, S. J. C. Yates, A. M. Baryshev, T. M. Klapwijk, *Applied Physics Letters* **103**, 203503 (2013).

7.1 Introduction

In the next decades millimetre (mm) and sub-mm astronomy require [1] large format imaging arrays to complement the high spatial resolution of the Atacama Large Millimetre/sub-millimetre Array [2]. The desired sensors should have a background limited sensitivity and a high optical efficiency and enable arrays of up to megapixels in size. The most promising candidate to fulfil these requirements are microwave kinetic inductance detectors (MKIDs) [3] due to their inherent potential for frequency domain multiplexing. MKIDs are superconducting resonators, thousands of which can be coupled to a single feedline. Each resonator is sensitive to changes in the Cooper pair density induced by absorption of sub-mm radiation. By monitoring the change in either phase or amplitude of the complex feedline transmission at the MKID resonance one can measure the absorbed photon power. Using amplitude readout photon noise limited performance has been shown [4]. However, for practical applications two key properties need to be demonstrated: (1) Photon noise limited operation in phase readout. (2) A measurement of the aperture efficiency [5], which describes the absolute optical coupling of a MKID imaging array to a plane wave.

In this letter we present antenna-coupled hybrid NbTiN-Al MKIDs designed for ground-based sub-mm astronomy. We show that these devices achieve photon noise limited performance in both amplitude and phase readout. Through a detailed analysis of the optical coupling within our setup we validate the simulation of the lens-antenna far-field beam pattern. From this we derive an aperture efficiency of 75%. This is close to the theoretical maximum of 80% for a single-moded detector.

7.2 Device design

The device design, shown in Fig. 7.1, aims to simultaneously maximize the phase response and minimize the two-level system (TLS) noise contribution [6]. The device is a $L \approx 5$ mm long quarter-wavelength coplanar-waveguide (CPW) resonator consisting of two sections. The first section (~ 4 mm), at the open end of the resonator, is a wide CPW made entirely from 200 nm thick NbTiN. NbTiN has 10 dB lower TLS noise than conventional superconductors such as Al [7]. The TLS noise is further reduced by the width of the CPW [7], $23.7 \mu\text{m}$ and $5.4 \mu\text{m}$ for the CPW gap and central line, respectively.

The second section (1 mm), at the shorted end of the resonator, is a narrow CPW with NbTiN ground planes and a 48 nm thick Al central line. The Al is galvanically connected to the NbTiN central line (Fig. 7.1 inset) and the NbTiN ground plane at the resonator short. The NbTiN is lossless for frequencies up to the gap $2\Delta_0/h = 1.1$ THz ($T_c \approx 14$ K). Any radiation with a frequency $0.09 < \nu < 1.1$ THz is therefore absorbed in the Al ($T_c = 1.28$ K) central line of the second section. The optically excited quasiparticles are trapped in the Al, because it is connected to a high gap

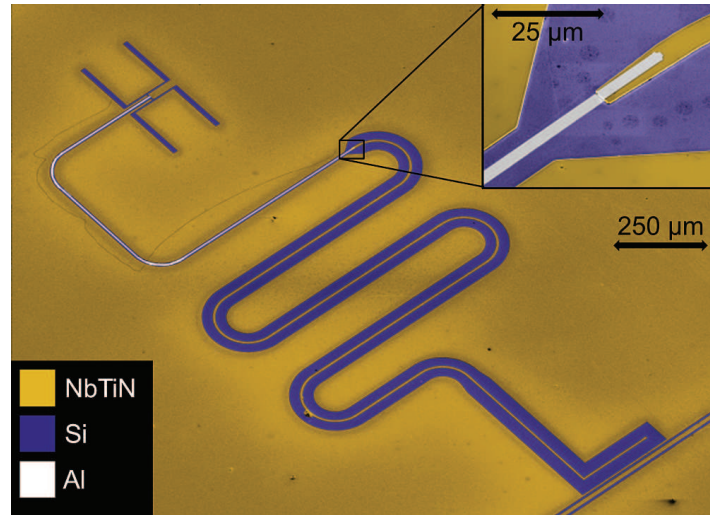


Figure 7.1: Scanning electron micrograph of the antenna-coupled hybrid NbTiN-Al MKIDs used. A wide NbTiN CPW resonator is used to minimize the two-level system noise contribution. At the shorted end, where the planar antenna is located, one millilitre of CPW is reduced in width and the central line is made from thin Al. The Al is galvanically connected to the NbTiN at both ends (inset).

superconductor. This quantum well structure confines the quasiparticles in the most responsive part of the MKID and allows us to maximize the response by minimizing this active volume. Therefore, we use a narrow CPW in section two, $2.3\ \mu\text{m}$ and $3.7\ \mu\text{m}$ for the central line and slots, respectively. Using a narrow Al line at the shorted end of the MKID does not increase the TLS noise significantly, because of the negligible electric field strength in this part of the detector.

At the shorted end of the resonator light is coupled into the device through a single-polarization twin-slot antenna, which is optimized for $\nu = 350\ \text{GHz}$. The advantage of using antenna-coupling is that it can be designed independently from the distributed CPW resonator. The disadvantage is that the antenna occupies only $\sim 1\%$ of the total pixel footprint. To achieve a high filling fraction we use elliptical lenses to focus the light on the antennas.

The design presented here is an improvement on that by Yates et al. [4]. Our design has a wider body in section one, which provides $\sim 7\ \text{dB}$ reduction of the TLS noise. In addition we have thinner Al, 48nm instead of $80\ \text{nm}$. This increases the kinetic inductance fraction by 45% to $\alpha = 0.09$ and reduces the volume by 40% . Both give a linear increase in the phase response. An array of 24 pixels has been fabricated¹ [8] on a high-resistivity ($> 10\ \text{k}\Omega\ \text{cm}$) $\langle 100 \rangle$ -oriented Si substrate. All pixels are capacitively coupled to a single feedline with a coupling $Q_c \sim 58\text{k}$, which is matched to the Q_i

¹Measurements have shown that the amount of direct absorption by the resonator is negligible when lenses are used. Therefore, we do not use air bridges to connect the ground planes of the CPW resonator.

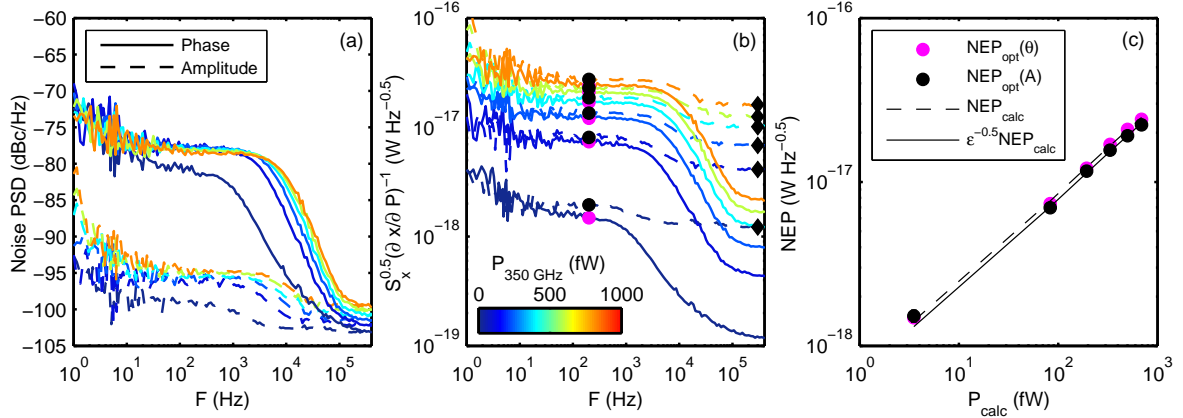


Figure 7.2: (a) The power spectral density of the amplitude (dashed) and phase (solid) noise measured under various optical loading. A white noise spectrum is observed, the level of which is constant with loading power, for $P_{350\text{GHz}} > 100$ fW. The roll-off above 1 kHz is due to the quasiparticle lifetime, which is reduced by an increasing optical load. Note that the photon noise level is 16 dB higher in phase readout. Nevertheless, at a given loading the NEP is the same for phase and amplitude readout as shown in (b). (b) The optical NEP² [10] for amplitude (dashed) and phase (solid) readout as a function of optical loading. (c) The optical NEP measured at a modulation frequency of 200 Hz, NEP_{opt} , as a function of the estimated optical loading, P_{calc} . For every optical loading the NEP in phase (magenta dots) and amplitude (black dots) readout is equal, if for the latter the amplifier contribution (black diamonds) is subtracted. This contribution is insignificant in phase readout. The error bars on the NEP measurement are of the order of the symbol size. The measured NEP follows the same slope as $NEP_{\text{calc}} \propto \sqrt{P_{\text{calc}}}$ (dashed black line). By fitting the relation between measured amplitude NEP and NEP_{calc} (solid black line) $\epsilon = 1.06 \pm 0.06$ is determined.

expected for an optical loading of ~ 10 pW. After mounting an array of 16 laser machined Si lenses with a diameter of 2 mm on the central pixels, the array is evaluated using a pulse tube pre-cooled adiabatic demagnetization refrigerator with a box-in-a-box cold stage design [9]. In this design the array is fully enclosed in a 100 mK environment with the exception of a 2 mm aperture, which is located 15.05 mm above the approximate centre of the MKID array. This aperture is isotropically illuminated by a large temperature-controlled blackbody [10]. Two metal mesh filters provide a minimum rejection of 20 dB at all wavelengths outside the 50 GHz bandpass centred on $\nu = 350$ GHz. This allows us to create a variable unpolarised illumination over a wide range of powers.

²For clarity the factor $\sqrt{(1 + (2\pi F)^2 \tau_{qp}^2)(1 + (2\pi F)^2 \tau_{res}^2)}$ is not included.

7.3 Photon noise limited performance

Fig. 7.2(a) shows the amplitude and phase noise spectra measured for a typical device as a function of the optical power absorbed in the Al, P_{350GHz} . In this figure we observe two characteristics that prove our device is photon noise limited:

1. The noise spectra in both phase and amplitude are white with a roll-off given by the quasiparticle lifetime, τ_{qp} , or resonator ring time, τ_{res} . For our devices we observe a white noise spectrum for $P_{350GHz} \geq 100$ fW, which has a roll-off due to τ_{qp} , because $\tau_{qp} > \tau_{res}$.
2. When reducing the optical loading from the photon noise limited situation one should observe at negligible power levels the transition to a noise spectrum that is limited by intrinsic noise sources of the detector. At a negligible optical loading ($P_{350GHz} = 4$ fW) the phase noise spectrum is no longer white and the noise level in both phase and amplitude readout is lower with respect to $P_{350GHz} > 4$ fW.

Fig. 7.2 shows three more features, which may be present in a photon noise limited MKID.

The photon noise level of the spectra observed in Fig. 7.2(a) is independent of the optical loading, because the product of quasiparticle number and quasiparticle lifetime is constant [10, 11] and the loaded Q did not change.

By fitting a Lorentzian roll-off [10] to the spectra presented in Fig. 7.2(a) we derive the quasiparticle lifetime as a function of the optical loading. Fig. 7.3 shows that the quasiparticle lifetime obtained from phase and amplitude readout is equal for all loading levels. For $P_{350GHz} > 100$ fW the quasiparticle lifetimes show a $\tau_{qp} \propto P_{350GHz}^{-0.50 \pm 0.02}$ relation, which matches the expected $\tau_{qp} \propto 1/\sqrt{P_{350GHz}}$ relation [11–13] for a homogeneously illuminated superconductor. At $P_{350GHz} = 4$ fW we observe $\tau_{qp} = 150 \mu s$, which deviates from the trend set by the photon noise limited regime and is significantly lower than the $\tau_{qp} \approx 2$ ms observed by de Visser et al. [14] in similar Al. Measurements on hybrid NbTiN-Al MKIDs with a varying length of the Al section show that the quasiparticle lifetime increases with the Al length. Based on this we tentatively conclude that the reduced lifetime we observe is due to poisoning by quasiparticles entering from the NbTiN.

Fig. 7.2(b) and 7.2(c) show the observed Noise Equivalent Power (NEP)² [10], the level of which only depends on the optical loading and is thus equal in amplitude and phase readout. The NEP follows the $NEP \propto \sqrt{P_{350GHz}}$ relation expected for photon noise limited MKIDs³ [4, 11].

³The $NEP \propto \sqrt{P_{350GHz}}$ expected for photon noise limited MKIDs would also be observed for amplifier limited MKIDs, due to the $\tau_{qp} \propto 1/\sqrt{P_{350GHz}}$ relation. However, in this situation the roll-off in the spectra of Fig. 7.2(a) would not be observed.

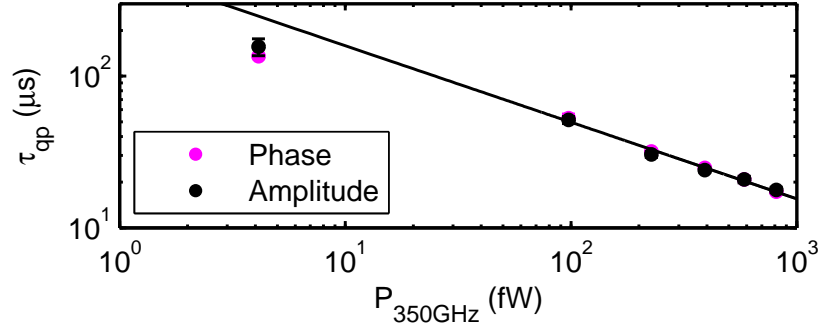


Figure 7.3: The quasiparticle lifetime, determined from the phase (magenta) and amplitude (black) noise roll-off, as a function of optical power absorbed by the MKID, P_{350GHz} . The Lorentzian fit gives a typically error of 5% in the estimated lifetime. As a result, error bars are usually smaller than the symbol size. A fit to the measured lifetimes for $P_{350GHz} > 100$ fW shows that $\tau_{qp} \propto P_{350GHz}^{-0.50 \pm 0.02}$.

7.4 Readout

Once photon noise limited performance is achieved the NEP in both phase and amplitude readout is equal as it is determined by the loading. However, as shown in Fig. 7.2(a), the photon noise level in phase readout is significantly higher than that in amplitude readout. Fig. 7.4(a) shows the measured amplitude (blue) and phase (red) noise spectra for an optical loading of 550 fW. The photon noise level in phase readout is 16 dB higher than that in amplitude readout, thereby relaxing the dynamic range requirements of the readout electronics. Fig. 7.4(b) shows the expected noise contribution (black dashed line) by a state-of-the-art readout system based upon the E2V EV10AQ190 analogue-to-digital converter (ADC) [15] for a given number of tones. We used an effective number of bits (ENOB) of 8 for this calculation and a ADC bandwidth of 1.25 GHz. If we allow for a 10% of observation time or ~ 1 dB of added noise by the ADC alone, we estimate [16, 17] that we can simultaneously read out approximately 1800 of the presented NbTiN-Al MKIDs in phase readout. Using the same electronics amplitude readout would only allow 30 pixels.

7.5 Aperture efficiency

In the photon noise limited regime it is favourable to have a high optical or aperture efficiency [5], η_A , because the observation time required to achieve a given signal-to-noise follows $t_\sigma \propto \eta_A^{-1}$. The most reliable way to determine the aperture efficiency of a MKID is through the measurement of the photon noise. Yates et al. [4] used this approach and determined the aperture efficiency by comparing the measured NEP to

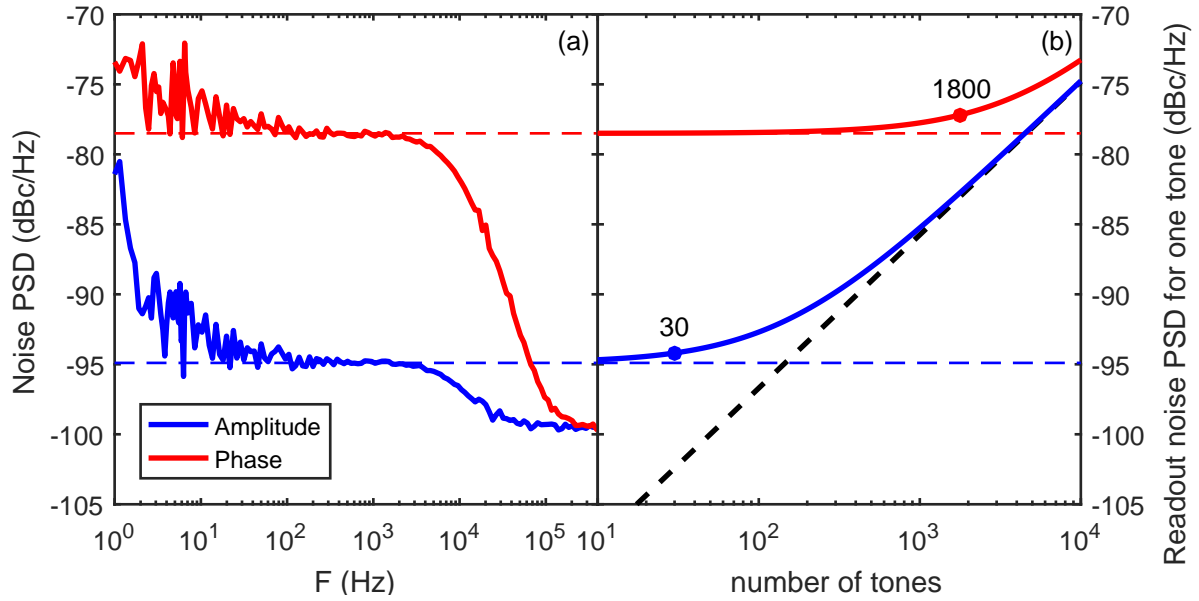


Figure 7.4: (a) The measured amplitude (blue) and phase (red) noise spectra for an optical loading of 550 fW. We observe photon noise limited white noise spectra at a -78.5 dBc/Hz and -94.9 dBc/Hz level for phase and amplitude, respectively. (b) The noise contribution (black dashed line) by a state-of-the-art readout system based upon the E2V EV10AQ190 ADC [15] for a given number of readout tones. The solid lines indicate the sum of the photon and readout noise for phase (red) and amplitude (blue). If we allow for a 10% degradation of observation time due to the noise added by the ADC alone, we can simultaneously operate 30 or 1800 tones in amplitude and phase readout, respectively. Figure inspired by Janssen et al. [18]

the NEP expected for a perfect absorber with the same area as a single pixel. The latter was determined using the geometrical throughput between the detector and the illuminating aperture. However, this approach is only valid if the gain of the antenna is equal to its maximum value within the entire angle spanned by the aperture.

We determine the aperture efficiency from the full far-field beam pattern, which is obtained from a simulation of the complete lens-antenna system using CST Microwave Studio. This gives us the freedom to adjust the design as required and allows a calculation of η_A independent of the measurement setup. However, the simulated beam pattern does require experimental verification. We will first show how we verify the coupling efficiency, C_ν , which describes the reflection losses due to mismatches between the antenna and the resonator CPW, and the gain pattern⁴, $G_\nu(\Omega)$, as a function of the angular direction, Ω , from the microlens focus. The gain pattern of our lens-antenna system is shown in Fig. 7.5(b). After the verification we will use C_ν and $G_\nu(\Omega)$, which we obtain from CST Microwave Studio, to calculate η_A .

We verify C_ν and $G_\nu(\Omega)$ using the photon noise limited optical NEP, NEP_{opt} , as the experimental observable. We compare NEP_{opt} to the photon noise limited NEP we

⁴We manually normalize the simulated beam pattern to obtain G_ν .

expect, NEP_{calc} , from the resonator. To calculate NEP_{calc} we need to know the power coupled to the lens-antenna system, P_{calc} , which is given by

$$P_{calc} = \frac{c^2}{4\pi} \int_{\nu} \int_{\Omega \in A_{ap}} \frac{F_{\nu} B_{\nu}(T_{BB})}{2\nu^2} C_{\nu} G_{\nu}(\Omega) d\Omega d\nu \quad (7.1)$$

Here c is the speed of light, F_{ν} the filter transmission and $B_{\nu}(T_{BB})$ Planck's law for a blackbody temperature T_{BB} . The factor $1/2$ takes into account that we receive only a single polarization. The second integral evaluates the solid angle Ω over the aperture area, A_{ap} . The rest of the detector enclosure is a 100 mK absorber that has a negligible emission at 350 GHz. Included in this calculation is the experimentally measured lateral shift between each pixel and the aperture. The effect of lateral deviations from co-alignment are shown in Fig. 7.5(a). The contours in this figure show the predicted reduction in received power as a function of the lateral translation between the lenses' optical axis and aperture center. The contours are normalized to a co-aligned system. The circles in Fig. 7.5 indicate the positions of the 16 lensed pixels. The colour indicates the relative frequency change between 5 and 90 fW of optical loading, which roughly approximates the relative absorbed power for all 16 pixels. The qualitative match is striking and assures us of the shape of $G_{\nu}(\Omega)$.

We can now define the power error ratio ϵ as the discrepancy between the calculated and measured photon noise limited NEP.

$$\begin{aligned} \epsilon &= \frac{NEP_{calc}^2}{NEP_{opt}^2} \\ &= \frac{2P_{calc}(h\nu(1+mB) + \Delta/\eta_{pb})}{NEP_{200Hz}^2 - NEP_{det}^2} \end{aligned} \quad (7.2)$$

Here $h\nu$ is the photon energy of the incoming radiation, $(1+mB)$ the correction to Poisson statistics due to wave bunching [10], Δ the superconducting energy gap of the absorbing material and $\eta_{pb} = 0.57$ the pair breaking efficiency inside this material. NEP_{opt} is equal to the measured NEP at a modulation frequency of 200 Hz, NEP_{200Hz} , after correction for any detector noise contribution to the NEP, NEP_{det} . In amplitude readout this is the amplifier noise contribution, which we estimate from the NEP value at a modulation frequency of 300 kHz (black diamonds in Fig. 7.2(b)). In phase readout $NEP_{det} = 0$ as both the frequency independent amplifier noise contribution, observed above the roll-off frequency, and the $1/\sqrt{F}$ TLS noise contribution, observed below 10 Hz, are insignificant at 200 Hz. We expect $\epsilon = 1$, if the description of the optical power flow is complete and the simulated beam patterns are correct. Fig. 7.2(c) shows the measured optical NEP, NEP_{opt} , as a function of P_{calc} for phase (magenta dots) and amplitude (black dots) readout. The measured photon noise NEPs from phase and amplitude are within 2σ of each other at all loading levels. The solid black line shows the best fit for the expected linear relation, $NEP_{opt} = NEP_{calc}/\sqrt{\epsilon}$. For the presented MKID, numbered 16, $\epsilon = 1.06 \pm 0.06$, if we disregard the lowest loading. For a different

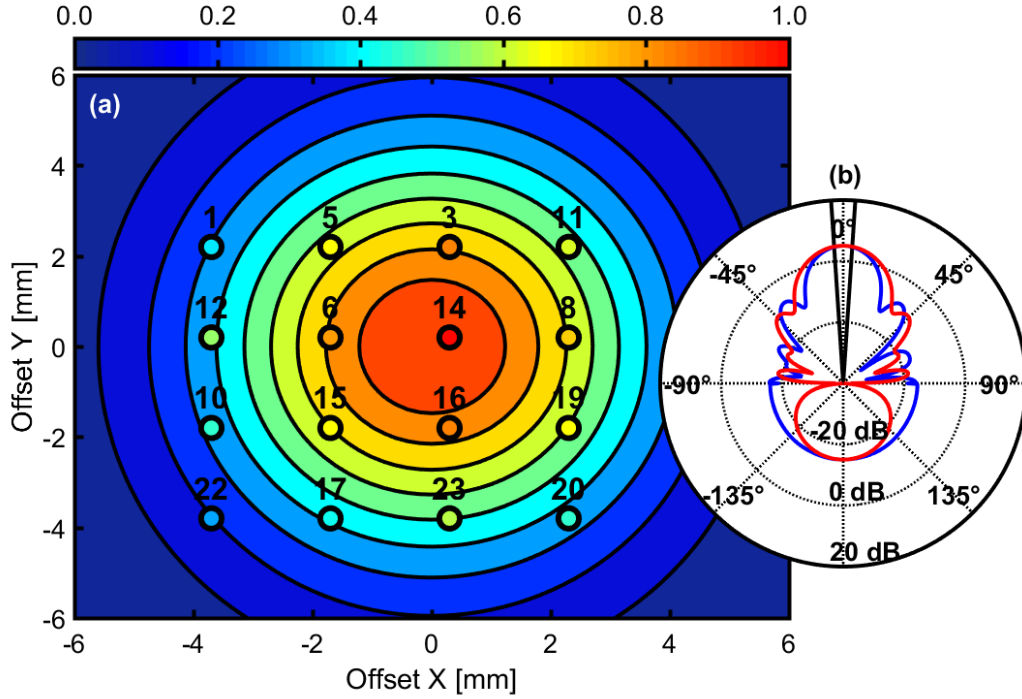


Figure 7.5: (a) This contour plot shows the power received by the hybrid MKIDs as a function of the offset between the lens and aperture centre. The scale is normalized to the power received at co-alignment. Overlaid in black circles are the positions of the 16 MKIDs with lenses. The colour inside each circle indicates the relative change in resonance frequency between 5 and 90 fW of optical loading, which is a proxy for the relative absorbed power. (b) The gain (in dB) of the complete lens-antenna system as a function of angle (in degrees) as obtained from CST. The red and blue line are the two orthogonal cross-sections. The black solid lines show the opening angle of the aperture used in this experiment.

MKID, numbered 3, the above analysis yields $\epsilon = 1.09 \pm 0.13$.

From the verified far-field beam pattern we can determine η_A , which is mathematically defined as

$$\eta_A = \frac{A_e}{A} = \frac{\lambda^2 G_\nu(\Omega_0) C_\nu}{4\pi A} \quad (7.3)$$

Here A is the physical area covered by the pixel; λ and ν are the wavelength and frequency of the observed radiation, respectively; and Ω_0 is the direction of the maximum gain. Using the circular area of the lenses $A = \pi \text{ mm}^2$, $C_{350\text{GHz}} = 0.98$ and the gain of the CST beam pattern at broadside, $G_\nu(\Omega_0) = 5.0 \text{ dB}$, an aperture efficiency of 75% is determined for a single pixel. The maximum achievable aperture efficiency of a circular antenna illuminated by a single-moded Gaussian beam is $\eta_A = 0.80$ [19]. For the measured array the filling fraction of the square packing means we have a total array aperture efficiency of 57%. Using an array with hexagonal packing the total array aperture efficiency can be increased to 66%.

7.6 Conclusion

In conclusion, we present hybrid NbTiN-Al MKIDs, which are photon noise limited in both phase and amplitude readout for loading levels $P_{350GHz} \geq 100$ fW with an aperture efficiency of 75%. The photon noise level will allow us to simultaneously read out approximately 1800 pixels using state-of-the-art electronics to monitor the phase. Given these specifications, hybrid NbTiN-Al MKIDs should enable astronomically usable kilopixel arrays for sub-mm imaging and moderate resolution spectroscopy.

References

- [1] D. Scott, P. Barnby, P. Bastien, J. Cami, E. Chapin, et al., *The Submillimetre Universe*, ArXiv e-prints, 1008.4159 (2010), <http://www.casa.ca/lrp2010>.
- [2] R. L. Brown, W. Wild, and C. Cunningham, *ALMA - the Atacama large millimeter array*, Advances in Space Research **34**, 555 (2004).
- [3] P. K. Day, H. G. LeDuc, B. A. Mazin, A. Vayonakis, and J. Zmuidzinas, *A broadband superconducting detector suitable for use in large arrays*, Nature **425**, 817 (2003).
- [4] S. J. C Yates, J. J. A. Baselmans, A. Endo, R. M. J. Janssen, L. Ferrari, et al., *Photon noise limited radiation detection with lens-antenna coupled microwave kinetic inductance detectors*, Applied Physics Letters **99**, 073505 (2011).
- [5] T. L. Wilson, K. Rohlf, and S. Hüttemeister, *Tools of radio astronomy*, Springer, Heidelberg, Germany (2013).
- [6] J. Gao, J. Zmuidzinas, B. A. Mazin, H. G. Leduc, and P. K. Day, *Noise properties of superconducting coplanar waveguide microwave resonators*, Applied Physics Letters **90**, 102507 (2007).
- [7] R. Barends, H. L. Hortensius, T. Zijlstra, J. J. A. Baselmans, S. J. C. Yates, et al., *Noise in NbTiN, Al, and Ta Superconducting Resonators on Silicon and Sapphire Substrates*, IEEE Transactions on Applied Superconductivity **19**, 936 (2009).
- [8] Y. J. Y. Lankwarden, A. Endo, J. J. A. Baselmans, and M. P. Bruijn, *Development of NbTiN-Al Direct Antenna Coupled Kinetic Inductance Detectors*, Journal of Low Temperature Physics **167**, 367 (2012).
- [9] J. J. A. Baselmans, S. J. C. Yates, P. Diener, and P. J. de Visser, *Ultra Low Background Cryogenic Test Facility for Far-Infrared Radiation Detectors*, Journal of Low Temperature Physics **167**, 360 (2012).

-
- [10] P. J. de Visser, J. J. A. Baselmans, J. Bueno, N. Llombart, and T. M. Klapwijk, *Fluctuations in the electron system of a superconductor exposed to a photon flux*, Nature Communications **5**, 3130 (2014).
 - [11] J. J. A. Baselmans, *Kinetic Inductance Detectors*, Journal of Low Temperature Physics **167**, 292 (2012).
 - [12] J. Bardeen, L. N. Cooper, and J. R. Schrieffer, *Theory of Superconductivity*, Physical Review **108**, 1175 (1957).
 - [13] S. B. Kaplan, C. C. Chi, D. N. Langenberg, J. J. Chang, S. Jafarey, et al., *Quasiparticle and phonon lifetimes in superconductors*, Physical Review B **14**, 4854 (1976).
 - [14] P. J. de Visser, J. J. A. Baselmans, P. Diener, S. J. C. Yates, A. Endo, et al., *Number Fluctuations of Sparse Quasiparticles in a Superconductor*, Physical Review Letters **106**, 167004 (2011).
 - [15] J. van Rantwijk, M. Grim, D. van Loon, S. Yates, A. Baryshev, et al., *Multiplexed readout for 1000-pixel arrays of microwave kinetic inductance detectors*, IEEE Transactions on Microwave Theory and Techniques **64**, 1876 (2016).
 - [16] W. Kester, *The Data Conversion Handbook*, Elsevier/Newnes, Oxford, UK (2005).
 - [17] S. Boyd, *Multitone Signals with Low Crest Factor*, IEEE Transactions on circuits and systems **33**, 1018 (1986).
 - [18] R. M. J. Janssen, J. J. A. Baselmans, A. Endo, L. Ferrari, S. J. C. Yates, et al., *Performance of hybrid NbTiN-Al microwave kinetic inductance detectors as direct detectors for sub-millimeter astronomy*, Proceedings of the SPIE **9153**, 91530T (2014).
 - [19] P. F. Goldsmith, *Quasioptical systems : Gaussian beam quasioptical propagation and applications*, Wiley - IEEE Press, New York, New York (1998).

Chapter 8

Equivalence of optical and electrical noise equivalent power of hybrid NbTiN-Al microwave kinetic inductance detectors

We have measured and compared the response of hybrid NbTiN-Al Microwave Kinetic Inductance Detectors (MKIDs) to changes in bath temperature and illumination by sub-mm radiation. We show that these two stimulants have an equivalent effect on the resonance feature of hybrid MKIDs. We determine an electrical NEP from the measured temperature responsivity, quasiparticle recombination time, superconducting transition temperature and noise spectrum, all of which can be measured in a dark environment. For the two hybrid NbTiN-Al MKIDs studied in detail the electrical NEP is within a factor of two of the optical NEP, which is measured directly using a blackbody source.

This chapter was published as R. M. J. Janssen, A. Endo, P. J. de Visser, T. M. Klapwijk, J. J. A. Baselmans, *Applied Physics Letters* **105**, 193504 (2013).

8.1 Introduction

In the development of megapixel sub-millimetre cameras for ground-based astronomy two different implementations of the Microwave Kinetic Inductance Detector (MKID) [1] are currently being pursued. One implementation is the Lumped Element MKID (LEKID) [2] made from TiN [3]. The high normal state resistance of TiN allows direct photon absorption and a lower readout frequency without a dramatic increase in pixel size [4]. A lower readout frequency reduces the cost of readout electronics. However, LEKIDs made from this high resistivity material have shown an anomalous optical response [5, 6]. An alternative MKID implementation is the lens-antenna-coupled hybrid NbTiN-Al MKID [7], which integrates an Al absorber in a NbTiN resonator. Sub-mm radiation creates quasiparticles in the Al, which will be trapped there, because the superconducting gap of NbTiN is much larger than that of Al. The lens-antenna-coupled hybrid MKIDs have shown the expected photon noise limited performance in both phase and amplitude readout down to 100 fW of optical loading as well as a high optical efficiency [7, 8].

A Noise Equivalent Power (NEP) in the 10^{-19} W/ $\sqrt{\text{Hz}}$ range has been measured electrically for MKIDs [3, 9]. The electrical NEP is determined from the MKIDs temperature responsivity, quasiparticle recombination time, superconducting energy gap and noise spectrum, all of which can be measured in a dark environment. Based on a simplified model-analysis Gao et al. [10] have argued that the change in complex conductivity due to thermally and optically excited quasiparticles is equivalent. This would imply that the electrical NEP is a convenient alternative to a full optical evaluation, which requires a time-consuming measurement and a dedicated setup with a controlled illumination source [8]. However, the relationship presented by Gao et al. [10] is not universally applicable to MKIDs, as illustrated in Fig. 8.1(b). Fig. 8.1(b) compares the response to thermal and optical excitations of well-studied Al coplanar waveguide (CPW) MKIDs[11]. Clearly, the temperature response deviates significantly from the optical response.

In this Letter we report a thorough analysis of the optical and electrical NEP of lens-antenna-coupled hybrid NbTiN-Al MKIDs. In Fig. 8.1(a) we show that, unlike the fully Al CPW MKIDs, hybrid MKIDs have an identical response to optical illumination and a change in bath temperature. We define a conversion between temperature and optical power based on energy arguments and show that for these hybrids the electrical NEP, which is determined from the temperature response, quasiparticle recombination time, superconducting energy gap and noise spectrum, is within a factor of two of the directly measured optical NEP.

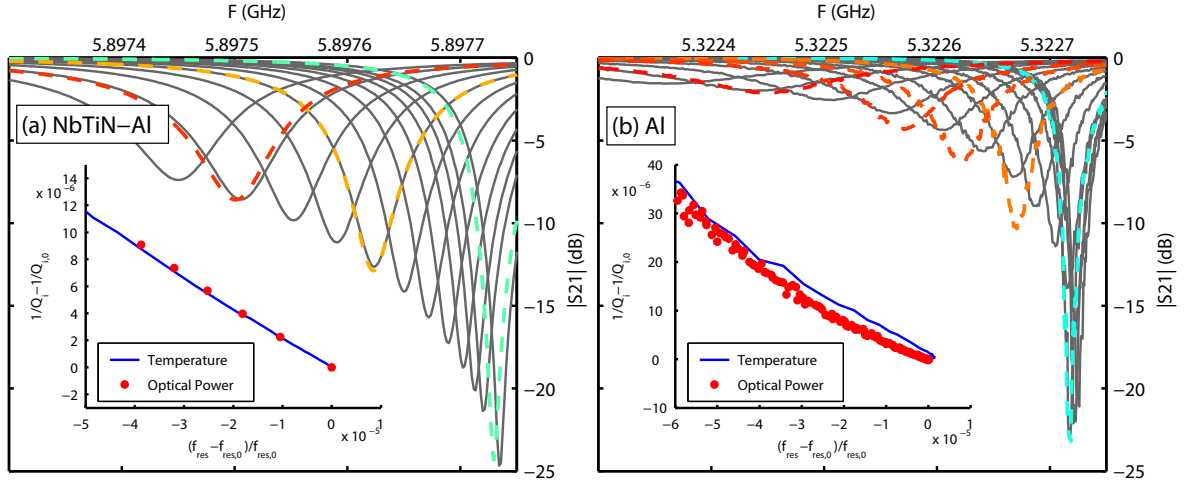


Figure 8.1: (a) The evolution of the resonance curve as a function of increasing temperature (grey) and increasing optical loading (colour) of a hybrid NbTiN-Al MKID. We see that this evolution is identical, as can be seen from the relative change in resonator losses, $(1/Q_i - 1/Q_{i,0})$, as a function of the change in resonance frequency, $(f_{\text{res}} - f_{\text{res},0})/f_{\text{res},0}$ (inset). (b) As (a), but for a fully Al CPW MKID [11]. Here a difference in the effect temperature and sub-millimetre radiation have on the complex conductivity is observed.

8.2 Measurement setup

The hybrid NbTiN-Al MKIDs [8] we study are quarter-wavelength CPW resonators (length ~ 5 mm), which consist of two sections. In the first section, at the open end of the resonator, the CPW is wide and made from NbTiN. In the second section, which is approximately 1 mm in length and located at the shorted end of the resonator, the NbTiN CPW is narrow and the central line is made from Al instead of NbTiN. This hybrid MKID design simultaneously maximizes the responsivity and minimizes the two-level system (TLS) noise [12] contribution.

We measure the properties of two representative devices (numbered No. 1 and No. 2) using a pulse tube pre-cooled adiabatic demagnetization refrigerator with a box-in-a-box cold stage design [13]. In this design the 4-by-4 array of MKIDs is fully enclosed in a 100 mK environment with the exception of a 2 mm aperture, which is located 15 mm above the approximate centre of the MKID array. The aperture is isotropically illuminated by a large blackbody [11]. Metal mesh filters define a 50 GHz bandpass around a central frequency of 350 GHz. The passband is matched to the antenna design [8]. This allows us to create an unpolarised illumination over a wide range of powers. From the blackbody temperature, T_{bb} , the filters and the optical coupling between the blackbody and the MKIDs we can determine the absorbed photon power, P_{opt} , to within 6% [8]. The magnetic field strength of the ADR is used to control the temperature, T , of the sample. Magnetic shielding prevents these fields from entering our sample stage. In our experiment we use a bath temperature $T_0 = 100$ mK and a blackbody temperature

$T_{\text{bb},0} = 4.2$ K as our initial condition for both our optical and thermal measurement. Quantities measured at these initial conditions will be denoted with subscript zero. Starting from $(T_{\text{bb},0}, T_0)$ we change either T_{bb} or T in the optical and thermal measurements, respectively. All measurements are made at a fixed readout power $P_{\text{read}} = -80$ dBm. In general the effect of microwave power on a quasiparticle distribution, which is modified from our baseline by an elevated temperature or optical illumination, is different [14, 15]. However, we expect that for the same number of quasiparticles, generated either thermally or optically, the effect of readout power is comparable.

8.3 Optical noise equivalent power

In order to determine the optical NEP of our detectors we first determine the base temperature resonance frequency of the MKID, $f_{\text{res},0}$, and we measure at $f_{\text{res},0}$ the noise spectrum in phase readout, $S_{\theta,0}$, and amplitude readout, $S_{A,0}$. Second, we measure the optical responsivity of the device, $\delta x / \delta P_{\text{opt}}$, by monitoring $x = \theta, A$ at $f_{\text{res},0}$, while increasing P_{opt} . Fig. 8.2(a) shows the measured phase (blue dots) and amplitude (red dots) response as a function of P_{opt} . We determine the optical responsivity directly from this measurement by a linear fit to the measured response at $P_{\text{bb}} \leq 1.1P_{\text{bb},0}$. These fits are shown in Fig. 8.2(a) for phase readout (blue line) and amplitude readout (red line) and their slopes give the optical responsivity values presented in Table 8.1. Table 8.1 also lists the uncertainty of the measured optical responsivity. The uncertainty is 5 – 10% and the result of uncertainty in the fit ($\sim 4\%$) and the uncertainty in P_{opt} ($\sim 6\%$).

Table 8.1: The optical and electrical phase and amplitude responsivity as well as their uncertainty for the two MKIDs.

MKID No. 1	Optical	Electrical
$d\theta/dP$	$(47.5 \pm 2.0) \times 10^{12}$	$(35.5 \pm 6.3) \times 10^{12}$
dA/dP	$(-4.59 \pm 0.29) \times 10^{12}$	$(-4.29 \pm 0.70) \times 10^{12}$
MKID No. 2	Optical	Electrical
$d\theta/dP$	$(32.7 \pm 3.5) \times 10^{12}$	$(20.3 \pm 3.6) \times 10^{12}$
dA/dP	$(-3.39 \pm 0.37) \times 10^{12}$	$(-2.41 \pm 0.43) \times 10^{12}$

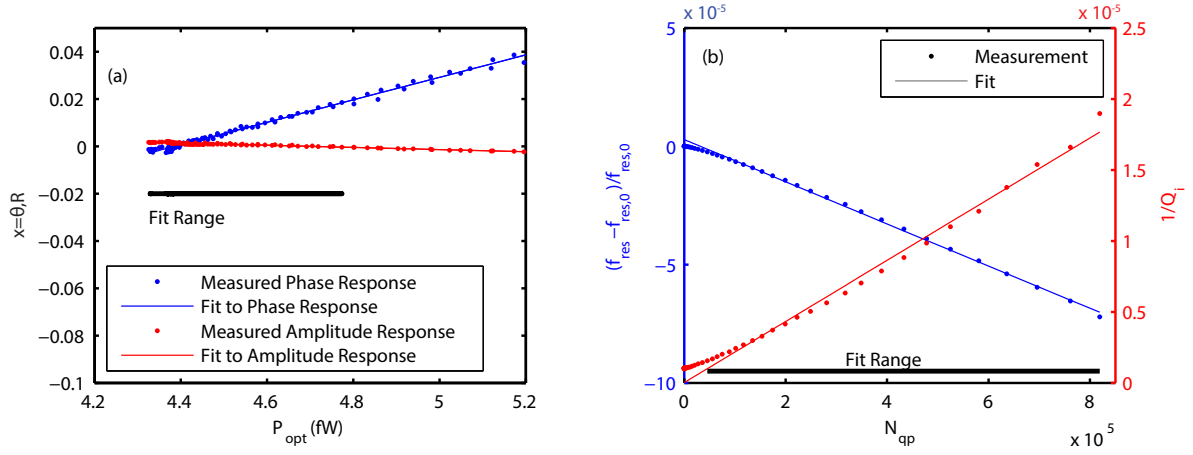


Figure 8.2: (a) The measured change in phase (blue dots) and amplitude (red dots) as a function of the absorbed sub-millimetre radiation. From this measurement the phase (blue line) and amplitude (red line) responsivity is determined using a linear fit. (b) The measured (dots) change in resonance frequency (blue) and resonator loss (red) as a function of the number of thermally generated quasiparticles as given by Eq. 8.2. A linear fit (lines) to this data gives us a quantity, which is proportional to the temperature responsivity (see Eq. 8.4).

8.4 Electrical noise equivalent power

An electrical NEP can only be used as a proxy for the optical NEP, if the response to temperature and sub-mm radiation is equivalent. Fig. 8.1(a) shows the evolution of the resonance curve of a hybrid NbTiN-Al MKID as a function of increasing temperature (solid black lines) and increasing optical loading (dashed coloured lines). For every optical loading a temperature can be found, which shows an identical resonance feature. This shows that, in case of the hybrid MKIDs, temperature generates an identical response in the MKIDs as sub-mm radiation. This shows sub-mm radiation and thermal excitation modifies the quasiparticle energy distribution in the Al in a comparable way and corroborates our expectation that alterations due to P_{read} are a second order effect, which is below the measurement accuracy. This is further illustrated by the inset of Fig. 8.1(a), which shows the change in internal quality factor, Q_i , as a function of the change in resonance frequency, f_{res} , for changing T (solid blue line) and P_{opt} (red dots). In contrast to hybrid MKIDs, radiation induces less losses for the same frequency shift in fully Al CPW MKID [11] as shown in Fig. 8.1(b).

We determine the electrical (dark) responsivity [16], $\delta x / \delta P_{\text{dark}}$, which based on energy arguments we expect to be equivalent to the optical responsivity, by

$$\frac{\delta x}{\delta P_{\text{dark}}} = \frac{\eta_{\text{pb}} \tau_{\text{qp}}(T)}{\Delta(0)} \frac{\delta x}{\delta N_{\text{qp}}(T)} \quad (8.1)$$

Here $\delta x/\delta N_{\text{qp}}(T)$ is the temperature responsivity, τ_{qp} is the quasiparticle recombination time, $\Delta(0)$ is the BCS superconducting energy gap and η_{pb} is the pair breaking efficiency. Table 8.1 gives the measured electrical responsivity and their uncertainty for our MKIDs. In the paragraphs below we detail how each of the parameters required for the calculation of $\delta x/\delta P_{\text{dark}}$ as well as their individual measurement uncertainty is obtained.

At temperatures $T \ll T_c$ Mattis-Bardeen theory [17] predicts a linear relation between the number of thermal quasiparticles and the real and complex part of the conductivity [10] or equivalently the internal losses and MKID resonance frequency. Fig 8.2(b) shows the measured (dots) linear relation between the number of quasiparticles, $N_{\text{qp}}(T)$, and the resonance frequency (blue) or the resonator losses (red). We determine $N_{\text{qp}}(T)$ from the bath temperature, T , using

$$N_{\text{qp}}(T) = V \times 4N_0 \int_0^\infty N_s(E, T) f_{FD}(E, T) dE \quad (8.2)$$

Here $V \approx 135 \mu\text{m}^3$ is the volume of the Al in the MKID, $N_0 = 1.7 \times 10^{10} \mu\text{m}^{-3} \text{ eV}^{-1}$ the single spin density of states of Al at the Fermi energy [18], $f_{FD}(E, T)$ is the Fermi-Dirac energy distribution and $N_s(E, T)$ the normalised BCS quasiparticle density

$$N_s(E) = \text{Re} \left(\frac{E}{\sqrt{E^2 - \Delta^2(T)}} \right) \quad (8.3)$$

From a linear fit to temperatures $0.18T_c < T < 0.25T_c$ we obtain the temperature responsivity, $\delta y/\delta N_{\text{qp}}$, of the resonance frequency, $y = (f_{\text{res}}(T) - f_{\text{res},0})/f_{\text{res},0}$, and internal quality factor, $y = 1/Q_i$. The fit range and resulting function are shown in Fig 8.2(b). From $\delta y/\delta N_{\text{qp}}$ we obtain the temperature responsivity, $\delta x/\delta N_{\text{qp}}$, for phase, $x = \theta$, and amplitude, $x = A$.

$$\frac{\delta \theta}{\delta N_{\text{qp}}} = \frac{-4Q}{f_{\text{res},0}} \frac{\delta(f_{\text{res}} - f_{\text{res},0})}{\delta N_{\text{qp}}}, \quad (8.4a)$$

$$\frac{\delta A}{\delta N_{\text{qp}}} = -2Q \frac{\delta(1/Q_i)}{\delta N_{\text{qp}}}, \quad (8.4b)$$

Here Q is the measured (total) resonator quality factor.

By selecting $T > 0.18T_c$ as a fit range for the temperature response we avoid the region below $N_{\text{qp}} \approx 0.4 \times 10^5$ where the non-linear TLS response dominates over the quasiparticle response, as shown by the measurements in Fig 8.2(b). At $T > 0.18T_c$ our minimum blackbody temperature, $T_{\text{bb},0} = 4.2 \text{ K}$, which corresponds to $P_{\text{opt},0} = 4.5 \text{ fW}$, generates a negligible amount of quasiparticles compared to those generated thermally. The commonly used approximation for Eq. 8.2 given by Eq. 6.10 systematically underestimates $N_{\text{qp}}(T)$ by up to 5% at $T = 0.25T_c$ as shown by the inset of Fig. 6.5(b). As a result we would overestimate $\delta x/\delta N_{\text{qp}}$ by 5.6%. To eliminate this error we use the

full BCS integral.

A quasiparticle recombination time $\tau_{qp,0} = 138 \pm 20 \mu s$ is determined from the roll-off in the noise spectrum [8]. This method is ideal, because one observes the MKID in an equilibrium situation. However, this can only be done if photon noise [7] or generation-recombination noise is observed [19]. Alternatively, the recombination time can be obtained by measuring the MKID's response to short high energy pulses¹ [19].

We determine the superconducting energy gap using $\Delta(0) = 1.76k_bT_c$. We find a $T_c = 1.283 \pm 0.019$ K for the Al used in the hybrid MKIDs. This T_c is the mid-point value from four-point DC measurements of the film resistance, $R(T)$, as a function of temperature. The DC measurement uses Al Hall bars of 3 and 100 μm wide, fabricated simultaneously with the MKIDs. We observe a change in T_c between the two Hall bars. Inspection of a 4" wafer excludes any effects due to changes in Al thickness, but shows a variation of 0.5 μm in the width of lines with the same design, due to the wet etch of the Al. We infer a 1.5% uncertainty in T_c due to these lithographic variations. We do not understand the physical mechanism responsible for the observed T_c variation. Nevertheless, the uncertainty in T_c is important, because it introduces an exponential uncertainty in the temperature responsivity through Eq. 8.2. A change of 1.5% in T_c introduces a 10% change in $\delta x / \delta N_{qp}$.

The pair-breaking efficiency is usually taken to be [20, 21] $\eta_{pb} = 0.57$. Recent simulations by Guruswamy et al. [15] of the absorption of sub-millimetre radiation by superconductors has corroborated this value for thick films of a BCS superconductor. However, they have also shown that η_{pb} depends on the device materials, geometry and the photon energy. For the hybrid NbTiN-Al MKIDs in this experiment, which uses 48 nm thick Al [8] and receives photons with an energy $h\nu \approx 7.5\Delta(0)$, the simulations show an $\eta_{pb} \approx 0.4$. Accordingly, we have used $\eta_{pb} = 0.4$ in our analysis.

8.5 Optical versus electrical noise equivalent power

Fig. 8.3 shows the optical (solid) and electrical (dashed) NEP for phase (blue) and amplitude (red) readout for KID No. 1. The NEPs are determined from the measured noise spectra and responsivities. The spectral shape of the optical and electrical NEP is identical, because they are both based on the noise spectrum measured at the base temperatures. Therefore, the difference between the optical and electrical NEP level is entirely due to the difference in the optical and electrical responsivity. The measured responsivities are given in Table 8.1. It is clear from Fig. 8.3 that the electrical NEP coincides with the optical NEP to within 37% for phase readout and within 7% for amplitude readout. For MKID No. 2 the optical and electrical NEP are within 62% and 41%, respectively.

¹While the pulse method is easier to implement in a dark environment, it is prone to introducing additional errors due to the non-equilibrium nature of the measurement.

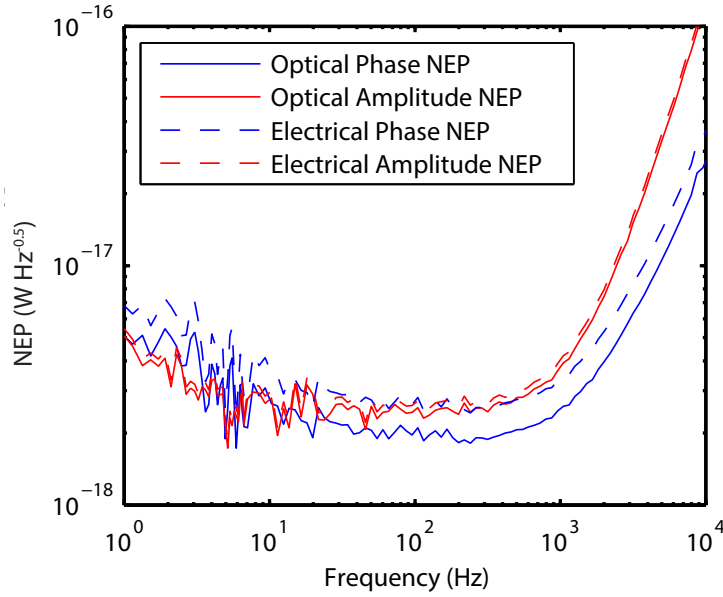


Figure 8.3: The optical NEP (solid line) compared to the electrical NEP (dashed line) for phase (blue) and amplitude (red) readout. The spectral shape of the electrical and optical NEP is identical, because they are both based on the noise spectrum measured at the base temperatures $T_{\text{bb},0} = 4$ K and $T_0 = 100$ mK.

8.6 Discussion

With the exception of the amplitude responsivity of MKID No. 1, the difference between the measured optical and electrical NEP is larger than the measurement uncertainties. $\Delta(0)$ and η_{pb} are the most likely candidates causing this discrepancy. We anticipate that the responsivity discrepancy is the result of not knowing the exact value of $\Delta(0)$, which we obtain from the mean-field T_c . However, the BCS factor of 1.76 used in this conversion is a theoretical quantity obtained in the limit of weak electron-phonon coupling. It is known to increase for a more realistic electron-phonon coupling, although for aluminium we do not expect a large deviation. A factor of 1.85 would bring all responsivities to within 1.1σ . Only, a direct measurement of $\Delta(0)$ would resolve this uncertainty. η_{pb} can resolve the discrepancy to a similar degree. This would require a phonon lifetime to phonon trapping time ratio four times larger than literature values [15, 22, 23].

The sensitivity to the exact value of Δ_0 and η_{pb} as well as the already large ($\sim 20\%$) uncertainties in the electrical NEP makes clear that it is impossible to determine the optical efficiency by the comparison between the optical and electrical NEP. A very

reliable way to determine the optical efficiency is to use the photon noise limited NEP as described in detail by Janssen et al. [8].

A possible equivalence between the optical and electrical NEP, and therefore responsivity, is based on the assumption that illumination by sub-millimetre radiation and providing an elevated temperature creates the same change in the weighted spatial average of the complex conductivity measured by the resonator. As shown in Fig. 8.1 for a hybrid MKID the evolution of the resonance feature is identical for temperature and optical loading. However, in a full Al MKID radiation induces less losses for the same frequency shift [11]. We interpret this difference as a result of the hybrid MKID geometry in which only the short aluminium section acts as the absorber. The 1 mm Al section is long enough to absorb the incoming radiation, but is shorter than the quasiparticle diffusion length. In addition, the electric field is roughly constant over this section of the MKID, which means that over the whole length of the aluminium the quasiparticle density has an identical contribution to the responsivity, regardless of its position.

Consequently, we show that for the specific case of hybrid MKIDs it is justified to assume the electrical NEP to be identical to the optical NEP. The geometrical advantage of hybrid NbTiN-Al CPW MKIDs is also present in fully Al LEKIDs [24], where both the radiation absorption and current are uniform within the inductive end of the resonator. This advantage is absent in Al CPW MKIDs. For fully TiN MKIDs, as mentioned in the introduction, it appears to be impossible to rely on an electrical NEP, as defined in this Letter, as a measure for the optical performance, because the response to radiation is in many aspects anomalous and possibly related to the inhomogeneous nature of the superconducting state [6].

8.7 Conclusion

In conclusion, we have shown for hybrid NbTiN-Al MKIDs that

1. the weighted spatial average of the complex conductivity measured by hybrid MKIDs is the same for thermal and optical excitation.
2. the electrical NEP, which is determined from the temperature responsivity, quasiparticle recombination time, superconducting transition temperature and noise spectrum, is within a factor of two of the optical NEP, which is measured directly using sub-millimetre radiation.

We argue that this is the result of the specific implementation of the hybrid NbTiN-Al MKID, and that in different MKID embodiments the equivalence between optical and electrical response is not a priori justified.

References

- [1] P. K. Day, H. G. LeDuc, B. A. Mazin, A. Vayonakis, and J. Zmuidzinas, *A broadband superconducting detector suitable for use in large arrays*, Nature **425**, 817 (2003).
- [2] S. Doyle, P. Mauskopf, J. Naylor, A. Porch, and C. Duncombe, *Lumped Element Kinetic Inductance Detectors*, Journal of Low Temperature Physics **151**, 530 (2008).
- [3] H. G. Leduc, B. Bumble, P. K. Day, B. H. Eom, J. Gao, et al., *Titanium nitride films for ultrasensitive microresonator detectors*, Applied Physics Letters **97**, 102509 (2010).
- [4] C. M. McKenney, H. G. Leduc, L. J. Swenson, P. K. Day, B. H. Eom, et al., *Design considerations for a background limited 350 micron pixel array using lumped element superconducting microresonators*, Proceedings of the SPIE **8452**, 84520S (2012).
- [5] J. Gao, M. R. Vissers, M. O. Sandberg, F. C. S. da Silva, S. W. Nam, et al., *A titanium-nitride near-infrared kinetic inductance photon-counting detector and its anomalous electrodynamics*, Applied Physics Letters **101**, 142602 (2012).
- [6] J. Bueno, P. C. J. J. Coumou, G. Zheng, P. J. de Visser, T. M. Klapwijk, et al., *Anomalous response of superconducting titanium nitride resonators to terahertz radiation*, Applied Physics Letters **105**, 192601 (2014).
- [7] S. J. C. Yates, J. J. A. Baselmans, A. Endo, R. M. J. Janssen, L. Ferrari, et al., *Photon noise limited radiation detection with lens-antenna coupled microwave kinetic inductance detectors*, Applied Physics Letters **99**, 073505 (2011).
- [8] R. M. J. Janssen, J. J. A. Baselmans, A. Endo, L. Ferrari, S. J. C. Yates, et al., *High optical efficiency and photon noise limited sensitivity of microwave kinetic inductance detectors using phase readout*, Applied Physics Letters **103**, 203503 (2013).
- [9] P. J. de Visser, J. J. A. Baselmans, S. J. C. Yates, P. Diener, A. Endo, et al., *Microwave-induced excess quasiparticles in superconducting resonators measured through correlated conductivity fluctuations*, Applied Physics Letters **100**, 162601 (2012).
- [10] J. Gao, J. Zmuidzinas, A. Vayonakis, P. Day, B. Mazin, et al., *Equivalence of the Effects on the Complex Conductivity of Superconductor due to Temperature Change and External Pair Breaking*, Journal of Low Temperature Physics **151**, 557 (2008).

- [11] P. J. de Visser, J. J. A. Baselmans, J. Bueno, N. Llombart, and T. M. Klapwijk, *Fluctuations in the electron system of a superconductor exposed to a photon flux*, Nature Communications **5**, 3130 (2014).
- [12] J. Gao, J. Zmuidzinas, B. A. Mazin, H. G. Leduc, and P. K. Day, *Noise properties of superconducting coplanar waveguide microwave resonators*, Applied Physics Letters **90**, 102507 (2007).
- [13] J. J. A. Baselmans, S. J. C. Yates, P. Diener, and P. J. de Visser, *Ultra Low Background Cryogenic Test Facility for Far-Infrared Radiation Detectors*, Journal of Low Temperature Physics **167**, 360 (2012).
- [14] D. J. Goldie and S. Withington, *Non-equilibrium superconductivity in quantum-sensing superconducting resonators*, Superconductor Science Technology **26**, 015004 (2013).
- [15] T. Guruswamy, D. J. Goldie, and S. Withington, *Quasiparticle generation efficiency in superconducting thin films*, Superconductor Science Technology **27**, 055012 (2014).
- [16] J. Baselmans, S. J. C. Yates, R. Barends, Y. J. Y. Lankwarden, J. R. Gao, et al., *Noise and Sensitivity of Aluminum Kinetic Inductance Detectors for Sub-mm Astronomy*, Journal of Low Temperature Physics **151**, 524 (2008).
- [17] D. Mattis and J. Bardeen, *Theory of the anomalous skin effect in normal and superconducting metals*, Physical Review **111**, 412 (1958).
- [18] R. D. Parks, *Superconductivity*, Vol. 2, Marcel Dekker Inc., New York, New York (1969).
- [19] P. J. de Visser, J. J. A. Baselmans, P. Diener, S. J. C. Yates, A. Endo, et al., *Number Fluctuations of Sparse Quasiparticles in a Superconductor*, Physical Review Letters **106**, 167004 (2011).
- [20] A. Kozorezov, A. Volkov, J. Wigmore, A. Peacock, A. Poelaert, et al., *Quasiparticle-phonon downconversion in nonequilibrium superconductors*, Physical Review B **61**, 11807 (2000).
- [21] M. Kurakado, *Possibility of high resolution detectors using superconducting tunnel junctions*, Nuclear Instruments and Methods **196**, 275 (1982).
- [22] S. B. Kaplan, C. C. Chi, D. N. Langenberg, J. J. Chang, S. Jafarey, et al., *Quasiparticle and phonon lifetimes in superconductors*, Physical Review B **14**, 4854 (1976).
- [23] S. B. Kaplan, *Acoustic matching of superconducting films to substrates*, Journal of Low Temperature Physics **37**, 343 (1979).

- [24] P. D. Mauskopf, S. Doyle, P. Barry, S. Rowe, A. Bidead, et al., *Photon-Noise Limited Performance in Aluminum LEKIDs*, Journal of Low Temperature Physics **176**, 545 (2014).

Chapter 9

Conclusions and future perspectives

9.1 Conclusions

This thesis presents a multiwavelength approach to study active galactic nuclei (AGN) and their role in galaxy evolution. In the first part, radio-loud AGN and their host galaxies in the local universe are studied using existing large area surveys (Chapters 2–5) and dedicated observations on the William Herschel Telescope. This large collection of optical, mid-infrared (mid-IR) and radio observations has enabled us to answer the question: “*Which galaxies host radio-loud AGN in the local universe?*” The second part of this thesis focusses on the performance of microwave kinetic inductance detectors (MKIDs). The MKID is a novel detector technology based on superconducting resonators (Chapters 6–8). Due to their inherent potential for frequency domain multiplexing MKIDs are expected to enable a new generation of large format (far-IR) cameras and spectrometers for astronomy. These instruments are expected to make key contributions in tracing the complete evolution of galaxies and their super massive black holes through cosmic time by observing the dust obscured universe.

9.1.1 Radio-loud AGN in the local universe

In the local universe radio-loud AGN can be divided into two populations: radiative-mode and jet-mode AGN. Radiative-mode AGN are thought to accrete matter at a high rate in a radiatively efficient way. These AGN are thought to follow the orientation-based unification model of AGN. Jet-mode AGN accrete matter at a low rate in a radiatively inefficient way. As a result they lack the broadband X-ray and IR emission and optical emission lines generally associated with AGN (*Chapter 2*).

We have performed a detailed analysis of these two AGN populations in the local universe using a combination of optical (SDSS) [1, 2], IR (WISE) [3] and radio (FIRST, NVSS) surveys [4, 5]. *Chapter 3* shows that more than 95% of the jet-mode AGN are hosted by red galaxies. The fraction of galaxies with a jet-mode AGN is proportional

to $f_{\text{jet-mode}} \propto M_*^{2.5}$ regardless of host galaxy colour or star formation rate (SFR). This proportionality is thought to be the result of the accretion of hot halo gas [6]. Radiative-mode AGN are primarily found in blue and green galaxies. These results are consistent with literature (*Chapter 2*), but our large sample enables us to look at more details. We show that the fraction of galaxies hosting a radio-loud radiative-mode AGN increases with host galaxy mass as $f_{\text{radiative-mode}} \propto M_*^{1.5}$. This is in contrast with radio-quiet radiative-mode AGN, for which the hosting probability shows no dependence on host galaxy mass [7]. In addition, we have identified 171 jet-mode AGN in massive blue galaxies. Given a red and a blue galaxy of the same mass, the probability of finding a jet-mode AGN in a blue galaxy is higher. These blue jet-mode AGN are generally also more powerful than their red counterparts.

The nature of these jet-mode AGN in blue host galaxies is investigated in *Chapter 4* using optical and radio images. Public data from the Galaxy Zoo project shows that a significantly higher fraction of blue galaxies have an elliptical morphology, if they have a jet-mode AGN. This brings them at $M_* \gtrsim 10^{11.2} M_\odot$ in line with the morphological classification of red galaxies which are the classical hosts of jet-mode AGN. At $M_* \lesssim 10^{11.2} M_\odot$ more than half of the blue galaxies hosting a jet-mode AGN show signs of mergers. Furthermore, the radio jets in blue galaxies (of all masses) appear to be small: more than 80% of them are point sources in the FIRST radio survey, whereas only 40% of the radio sources in a matched sample of red host galaxies are point sources. Based on this evidence we speculate that in the case of the low mass sources the AGN is just turning on and has been initiated by the recent galaxy interaction. In the high mass sources confinement of the radio jet inside the galaxy and/or positive feedback could also be the case.

To extend the above analysis to higher redshifts a method is required to classify radio-loud AGN as radiative-mode or jet-mode. At low redshifts this is done using optical spectra, but obtaining these spectra in large numbers is observationally expensive. In *Chapter 5* we investigate the mid-IR properties of radiative-mode and jet-mode AGN in the local universe. We show that jet-mode AGN have a mid-IR luminosity comparable to the general galaxy population, while at least 50% of the radiative-mode AGN has an excess emission. We attribute this excess mid-IR emission to the presence of a torus. Despite the above trends, we found that it is impossible to classify the two AGN populations with a high completeness and reliability. The key to achieving this will be a reliable constraint on the mid-IR emission by dust which has been heated by stars.

9.1.2 Performance of hybrid NbTiN-Al MKIDs

In the second part of this thesis we present performance measurements of Microwave Kinetic Inductance Detectors (MKIDs) made from a combination of NbTiN and Al (*Chapter 7*). Optical measurements show that hybrid NbTiN-Al MKIDs are photon

noise limited down to 100 fW of sub-mm radiation. This performance is achieved both in amplitude and phase readout. As a result of the high phase response, the photon noise level in phase readout is high enough to allow over 1000 pixels to be read simultaneously using state-of-the-art electronics. Owing to the combination of NbTiN and Al hybrid MKIDs can be used as detectors in the frequency range $0.1 < \nu < 1.1$ THz. Within these limits, the observation frequency of hybrid MKIDs can be easily adjusted by changing the planar antenna [8]. This can be done without affecting the performance of the distributed resonator which is used to sense the radiation. In this work we have used a twin-slot antenna at 350 GHz. With this antenna we have achieved an aperture efficiency of 75% which is close to the theoretical maximum of 80%.

Furthermore, *Chapter 8* shows that hybrid MKIDs have an equivalent response to temperature and sub-mm radiation. This is the result of the specific implementation of the hybrid MKIDs and not a priori true for any MKID. The optical and electrical noise equivalent power (NEP) of hybrid MKIDs is within a factor of two of each other. However, the error on the optical NEP determined using the methods described in *Chapters 6* and *7* is smaller than the error on the electrical NEP.

9.2 Future perspectives: tracing the co-evolution of galaxies and black holes

Over the last decades detailed knowledge about AGN in the local universe has been gained using large area surveys (see review by Heckman and Best [9]). These surveys have resulted in a detailed demographic of the radiative-mode AGN and jet-mode AGN population and their host galaxies. A new generation of large area surveys will enable us to extend the statistical analysis performed in the local universe out to redshift two and beyond. This analysis will answer the key question: “*Which galaxies host radiative- or jet-mode AGN in the high-redshift universe?*” If we answer this question in as great a detail as has been done for the local universe and compare the answer to our knowledge of AGN in the local universe, we can trace the evolution of jet-mode and radiative-mode AGN and determine the effect these AGN have on the star formation in their host galaxies.

9.2.1 AGN in the visible high-redshift universe

It is only in the last few years that representative populations of AGN have been studied [10, 11] out to redshift $z \sim 2$. These samples of X-ray selected radiative-mode AGN seem to follow the picture that radiative-mode AGN are hosted by normal galaxies with a SFR typical for the star forming galaxies at that redshift. However, radiative-mode and jet-mode AGN appear to evolve in a different way. Using a small sample of ~ 200

radio-loud AGN in optically visible hosts Best et al. [12] have shown that the activity of radio-loud radiative-mode AGN increases by a factor ~ 7 between the local universe and $z \approx 1$. This is very similar to what is found for radio-quiet AGN in optically visible galaxies [13] as well as the total increase in SFR (see Fig. 1.1). Therefore, the increased activity of radiative-mode AGN is thought to be the result of the increased abundance of gas and dust. In contrast to that, jet-mode AGN only show an increased number of the most powerful sources. The evolution of elliptical galaxies and their halo of hot gas is not sufficient to explain this evolution of jet-mode AGN. One possible explanation is a contribution of jet-mode AGN accreting cold gas at low rates. The population of powerful jet-mode AGN in blue star forming galaxies found in *Chapter 3* is very interesting in the light of this hypothesis.

In the near future large optical surveys such as the Dark Energy Survey [14] and Kilo-Degree Survey [15] will increase our samples of high redshift galaxies. These surveys will perform photometric observations of 100 million galaxies with a median redshift just below 1. In the more distant future EUCLID [16] and LSST [17] will provide for galaxies out to $z \sim 1$ both the data quality and data quantity currently only available for the local universe through SDSS. LOFAR [18] and the SKA [19] will complement these surveys with the radio observations required to trace the radio-loud AGN population out to high redshift [20]. For example, the EMU survey [21] will be an all-sky radio survey of the southern sky similar to NVSS used in this work. However, EMU will be 40 times more sensitive and be able to detect radio emission as a result of star formation in typical star forming galaxies out to redshift $z \sim 1$. By combining these radio and optical surveys the mass, morphology, colour and environment of galaxies hosting either a radio-mode and jet-mode AGN can be investigated. Furthermore, the effect of mergers on the triggering of both AGN modes can be revealed.

9.2.2 AGN in the dust-obscured high-redshift universe

The dust-obscured sub-mm galaxies (SMGs) present at $1 < z < 5$ would be strong candidates to have an AGN, based on the strong connection between star formation and AGN activity. Recent research confirms this as at least 10% of the hundreds of SMGs known today have been identified as hosting an AGN using either X-ray observations [22], mid-IR spectroscopy [23] or deep radio observations [24]. A major hurdle in the study of SMGs and the AGN therein is the faintness of these galaxies at optical wavelengths. This hampers the identification of optical counterparts, redshift determination, as well as the use of AGN diagnostics available at these wavelengths. Furthermore, these host galaxies will be largely missed by the large optical surveys described above. Hence, to obtain a complete view of the evolution of both radiative-mode and jet-mode AGN through cosmic time large area far-IR and sub-mm surveys are indispensable. However, currently no large area surveys are planned at these wavelengths due to a lack of

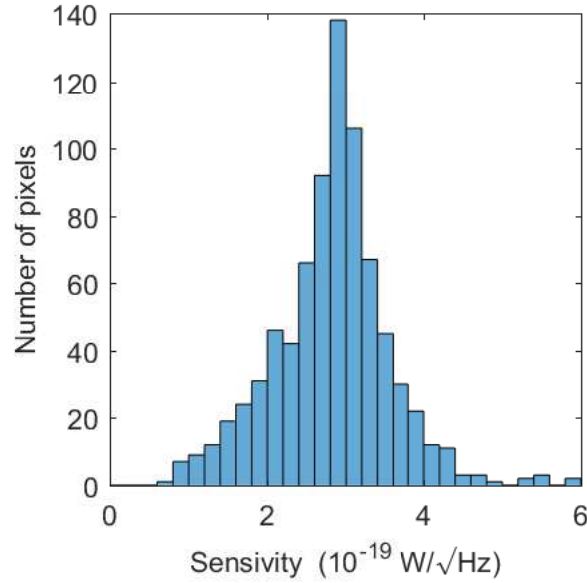


Figure 9.1: Histogram of the sensitivity of all 971 pixels in the imaging system based on hybrid MKIDs presented by Baselmans et al. [32]. The sensitivity is the electrical noise equivalent power as defined in *Chapter 8* whilst using phase readout.

suitable instrumentation. ALMA is not suited for blind large area surveys due to its narrow field of view.

A new generation of instruments based on MKID technology is on the horizon to enable these large area sub-mm surveys. The NIKA camera [25] has been installed on the IRAM 30 meter telescope [26] in 2013 and is now taking science data [e.g. 27]. It is expected to be replaced in the next few years by the larger NIKA2 camera [28], which will fill the entire field of view of the IRAM 30 meter. A-MKID, a sub-mm camera containing 25,000 MKID pixels, is currently being deployed at APEX [29]. A-MKID uses the hybrid NbTiN-Al MKIDs presented in this thesis. The results presented in *Chapter 7* have been key in showing these detectors could achieve the sensitivity requirements set during the development of the A-MKID instrument. Furthermore, the methodology to determine the radiative efficiency of MKIDs presented in this thesis is now a standard within the research field [30, 31]. Recent work by Baselmans et al. [32] has presented a kilopixel imaging system based on hybrid MKIDs. These hybrid MKIDs are a continued development of the work presented in this thesis. The main differences are a higher sensitivity and the use of a TiN backing layer [33] to reduce optical cross-talk and the effect of cosmic ray hits. Fig. 9.1 shows a histogram of the noise equivalent power (or sensitivity) of all 1000 pixels in the imaging system of Baselmans et al. [32]. The performance of this next-generation MKID imaging system satisfies the requirements for a far-IR imaging instrument on an actively cooled space telescope such as SPICA [34] and CALISTO [35]. This next generation of far-IR instruments will be able to extend the Herschel surveys and observe enough SMGs to achieve the number

statistics required for detailed AGN research.

The 2D maps of sub-mm cameras need to be complemented by far-IR spectroscopy to obtain the redshift of all SMGs discovered. The next generation far-IR spectrometers, such as DESHIMA [e.g. 36], will combine the hybrid MKIDs with NbTiN transmission lines and filters to achieve photon noise limited performance and a $\lambda/\Delta\lambda \sim 1000$ spectral resolution. These on-chip spectrometers are expected to arrive on telescopes in a few years. They will provide us with redshift measurements of SMG and AGN diagnostics in the far-IR [37]. In addition, they will provide us the information required to efficiently follow up the most interesting sources using facilities like NOEMA and ALMA [38].

References

- [1] D. G. York, J. Adelman, J. E. Anderson Jr., S. F. Anderson, J. Annis, et al., *The Sloan Digital Sky Survey: Technical Summary*, The Astronomical Journal **120**, 1579 (2000).
- [2] C. Stoughton, R. H. Lupton, M. Bernardi, M. R. Blanton, S. Burles, et al., *Sloan Digital Sky Survey: Early Data Release*, The Astronomical Journal **123**, 485 (2002).
- [3] E. L. Wright, P. R. M. Eisenhardt, A. K. Mainzer, M. E. Ressler, R. M. Cutri, et al., *The Wide-field Infrared Survey Explorer (WISE): Mission Description and Initial On-orbit Performance*, The Astronomical Journal **140**, 1868 (2010).
- [4] R. H. Becker, R. L. White, and D. J. Helfand, *The FIRST Survey: Faint Images of the Radio Sky at Twenty Centimeters*, The Astrophysical Journal **450**, 559 (1995).
- [5] J. J. Condon, W. D. Cotton, E. W. Greisen, Q. F. Yin, R. A. Perley, et al., *The NRAO VLA Sky Survey*, The Astronomical Journal **115**, 1693 (1998).
- [6] P. N. Best, C. R. Kaiser, T. M. Heckman, and G. Kauffmann, *AGN-controlled cooling in elliptical galaxies*, Monthly Notices of the Royal Astronomical Society **368**, L67 (2006).
- [7] P. N. Best, G. Kauffmann, T. M. Heckman, J. Brinchmann, S. Charlot, et al., *The host galaxies of radio-loud active galactic nuclei: mass dependences, gas cooling and active galactic nuclei feedback*, Monthly Notices of the Royal Astronomical Society **362**, 25 (2005).
- [8] R. M. J. Janssen, J. J. A. Baselmans, A. Endo, L. Ferrari, S. J. C. Yates, et al., *Performance of hybrid NbTiN-Al microwave kinetic inductance detectors as direct detectors for sub-millimeter astronomy*, Proceedings of the SPIE **9153**, 91530T (2014).

- [9] T. M. Heckman and P. N. Best, *The Coevolution of Galaxies and Supermassive Black Holes: Insights from Surveys of the Contemporary Universe*, Annual Review of Astronomy and Astrophysics **52**, 589 (2014).
- [10] J. Aird, A. L. Coil, J. Moustakas, M. R. Blanton, S. M. Burles, et al., *PRIMUS: The Dependence of AGN Accretion on Host Stellar Mass and Color*, The Astrophysical Journal **746**, 90 (2012).
- [11] K. Schawinski, B. D. Simmons, C. M. Urry, E. Treister, and E. Glikman, *Heavily obscured quasar host galaxies at $z \sim 2$ are discs, not major mergers*, Monthly Notices of the Royal Astronomical Society **425**, L61 (2012).
- [12] P. N. Best, L. M. Ker, C. Simpson, E. E. Rigby, and J. Sabater, *The cosmic evolution of radio-AGN feedback to $z = 1$* , Monthly Notices of the Royal Astronomical Society **445**, 955 (2014).
- [13] P. Madau and M. Dickinson, *Cosmic Star-Formation History*, Annual Review of Astronomy and Astrophysics **52**, 415 (2014).
- [14] B. Flaugher, *The Dark Energy Survey*, International Journal of Modern Physics A **20**, 3121 (2005).
- [15] J. T. A. de Jong, G. A. Verdoes Kleijn, D. R. Boxhoorn, H. Buddelmeijer, M. Capaccioli, et al., *The first and second data releases of the Kilo-Degree Survey*, Astronomy & Astrophysics **582**, A62 (2015).
- [16] R. J. Laureijs, L. Duvet, I. Escudero Sanz, P. Gondoin, D. H. Lumb, et al., *The Euclid Mission*, Proceedings of the SPIE **7731**, 77311H (2010).
- [17] J. A. Tyson, *Large Synoptic Survey Telescope: Overview*, Proceedings of the SPIE **4836**, 10 (2002).
- [18] M. P. van Haarlem, M. W. Wise, A. W. Gunst, G. Heald, J. P. McKean, et al., *LOFAR: The LOw-Frequency ARray*, Astronomy & Astrophysics **556**, A2 (2013).
- [19] R. T. Schilizzi, *The Square Kilometre Array*, EAS Publications Series **15**, 445 (2005).
- [20] A. D. Kapinska, M. Hardcastle, C. Jackson, T. An, W. Baan, et al., *Unravelling lifecycles and physics of radio-loud AGN in the SKA Era*, Advancing Astrophysics with the Square Kilometre Array (AASKA14), 173 (2015).
- [21] R. P. Norris, A. M. Hopkins, J. Afonso, S. Brown, J. J. Condon, et al., *EMU: Evolutionary Map of the Universe*, Publications of the Astronomical Society of Australia **28**, 215 (2011).
- [22] S. X. Wang, W. N. Brandt, B. Luo, I. Smail, D. M. Alexander, et al., *An ALMA Survey of Submillimeter Galaxies in the Extended Chandra Deep Field-South: The AGN Fraction and X-Ray Properties of Submillimeter Galaxies*, The Astrophysical Journal **778**, 179 (2013).

- [23] K. Coppin, A. Pope, K. Menéndez-Delmestre, D. M. Alexander, J. S. Dunlop, et al., *Mid-infrared Spectroscopy of Candidate Active Galactic Nuclei-dominated Submillimeter Galaxies*, The Astrophysical Journal **713**, 503 (2010).
- [24] M. Magliocchetti, D. Lutz, P. Santini, M. Salvato, P. Popesso, et al., *The PEP survey: evidence for intense star-forming activity in the majority of radio-selected AGN at $z \gtrsim 1$* , Monthly Notices of the Royal Astronomical Society **456**, 431 (2016).
- [25] A. Monfardini, L. J. Swenson, A. Bideaud, F. X. Désert, S. J. C. Yates, et al., *NIKA: A millimeter-wave kinetic inductance camera*, Astronomy & Astrophysics **521**, A29 (2010).
- [26] J. W. M. Baars, B. G. Hooghoudt, P. G. Mezger, and M. J. de Jonge, *The IRAM 30-m millimeter radio telescope on Pico Veleta, Spain*, Astronomy & Astrophysics **175**, 319 (1987).
- [27] R. Adam, B. Comis, J.-F. Macías-Pérez, A. Adane, P. Ade, et al., *Pressure distribution of the high-redshift cluster of galaxies CL J1226.9+3332 with NIKA*, Astronomy & Astrophysics **576**, A12 (2015).
- [28] A. Monfardini, R. Adam, A. Adane, P. Ade, P. André, et al., *Latest NIKA Results and the NIKA-2 Project*, Journal of Low Temperature Physics **176**, 787 (2014).
- [29] R. Güsten, R. S. Booth, C. Cesarsky, K. M. Menten, C. Agurto, et al., *APEX: the Atacama Pathfinder EXperiment*, Proceedings of the SPIE **6267**, 626714 (2006).
- [30] J. Hubmayr, J. Beall, D. Becker, H.-M. Cho, M. Devlin, et al., *Photon-noise limited sensitivity in titanium nitride kinetic inductance detectors*, Applied Physics Letters **106**, 073505 (2015).
- [31] D. Flanigan, H. McCarrick, G. Jones, B. R. Johnson, M. H. Abitbol, et al., *Photon noise from chaotic and coherent millimeter-wave sources measured with horn-coupled, aluminum lumped-element kinetic inductance detectors*, Applied Physics Letters **108**, 083504 (2016).
- [32] J. J. A. Baselmans, J. Bueno, S. J. C. Yates, O. Yurduseven, N. Llombard, et al., *A kilo-pixel imaging system for future space based far-infrared observatories using microwave kinetic inductance detectors*, submitted.
- [33] H. McCarrick, D. Flanigan, G. Jones, B. R. Johnson, P. A. R. Ade, et al., *A Titanium Nitride Absorber for Controlling Optical Crosstalk in Horn-Coupled Aluminum LEKID Arrays for Millimeter Wavelengths*, Journal of Low Temperature Physics **184**, 154 (2016).
- [34] L. J. Swenson, P. K. Day, C. D. Dowell, B. H. Eom, M. I. Hollister, et al., *MAKO: a pathfinder instrument for on-sky demonstration of low-cost 350 micron imaging arrays*, Proceedings of the SPIE **8452**, 84520P (2012).

-
- [35] C. M. Bradford, P. F. Goldsmith, A. Bolatto, L. Armus, J. Bauer, et al., *A Cryogenic Space Telescope for Far-Infrared Astrophysics: A Vision for NASA in the 2020 Decade*, ArXiv e-prints, 1505.05551 (2015).
 - [36] A. Endo, P. Werf, R. M. J. Janssen, P. J. Visser, T. M. Klapwijk, et al., *Design of an Integrated Filterbank for DESHIMA: On-Chip Submillimeter Imaging Spectrograph Based on Superconducting Resonators*, Journal of Low Temperature Physics **167**, 341 (2012).
 - [37] P. P. van der Werf, K. G. Isaak, R. Meijerink, M. Spaans, A. Rykala, et al., *Black hole accretion and star formation as drivers of gas excitation and chemistry in Markarian 231*, Astronomy & Astrophysics **518**, L42 (2010).
 - [38] R. L. Brown, W. Wild, and C. Cunningham, *ALMA - the Atacama large millimeter array*, Advances in Space Research **34**, 555 (2004).

Appendix A

Mid-IR classification of radio-loud AGN: A comparison between high and low radio power samples.

The poor separation performance between high-excitation radio galaxies (HERG) and low-excitation radio galaxies (LERGs) using mid-IR measurements found in Chapter 5 is in stark contrast to the findings of Gürkan et al. [1, hereafter G14]. Gürkan et al. [1] concluded that there exists an empirical cut-off between LERGs and HERGs of $L_{22\mu\text{m}} = 5 \times 10^{43} \text{ erg/s} = 10^{36.7} \text{ W}$, as illustrated in Fig. A.1 (a reproduction of Fig. 8 in G14). This break is remarkably similar to $L_{22\mu\text{m},\text{break}} = 10^{36.6} \text{ W}$ found in Chapter 5. However, comparing Fig. A.1 and Fig. 5.1 shows two distinct differences between the G14 and BH12 radio-loud AGN samples. First, the strong correlation between the $22 \mu\text{m}$ and radio luminosity observed by G14 is not obvious in Fig. 5.1. Second, there is a large cross-contamination across the empirical separation value for the BH12 sample. It is clear from Fig. 5.1 that there is no alternative value at which $L_{22\mu\text{m}}$ separates HERGs and LERGs with both a high completeness and high reliability. In this Appendix we present evidence to show that the observed differences are the result of the differences in sample size, flux limits and the fractions of HERGs and LERGs between the G14 and BH12 samples.

G14 analysed the mid-infrared properties of four complete radio samples spanning $0.003 < z < 3.395$, with flux density limits ranging from 0.5 Jy to 20 Jy at 151 MHz. The sample contained a total of 352 sources, of which 70 are classified as LERGs and 280 as HERGs using optical emission lines available in the literature. Full details of the flux density limits and redshift ranges for the samples are given in Table A.1. Mid-IR fluxes were obtained by matching the sources to the all-sky WISE catalogue using a $10''$ match radius. We exclude this as an origin of the difference by matching the BH12 sample directly with the WISE all-sky source catalogue. Using a $5''$ match radius we obtain counterparts for 99% of sources at $22 \mu\text{m}$. Using the directly matched sources does not affect our results.

Using the information in Table A.1 we select from the BH12 sample an equivalent

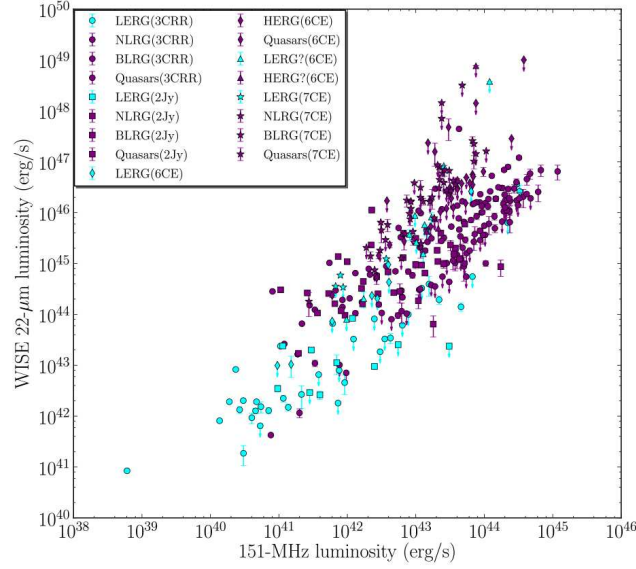


Figure A.1: 22 μm luminosity vs. 151 MHz radio luminosity reproduced from G14 [1, Figure 8] showing their observed separation between HERGs (purple filled symbols) and LERGs (cyan filled symbols).

sample for each of the four G14 subsamples. An equivalent sample is selected by first applying scaled flux limits at $S_{1.4\text{GHz}}$. These flux limits are exactly 10 times lower than the flux limits applied by G14. The exact values are listed in Table A.1. Note that an artificial upper limit was introduced in the 7CE sample to mimic the implicit upper flux limit apparent in G14 Fig. 1. After flux limits are applied the exact same number of HERGs and LERGs as in the G14 subsamples are randomly selected from the candidate sources. Sources selected for other subsamples are excluded from selection. No a-priori

Table A.1: Details of the radio samples used in G14, together with the equivalent flux density limits for the mock samples drawn from BH12 and described in Section 5.3.

Sample	Limit Jy	Redshift range	HERG # ^a	LERG #	BH12 equivalent limit mJy
3CRR	$S_{178\text{MHz}} \geq 10.9$	$0.0029 < z < 2.012$	135 ^b	37	$S_{1.4\text{GHz}} \geq 209$
2Jy	$S_{2.7\text{GHz}} \geq 2$	$0.05 < z < 0.7$	38 ^b	10	$S_{1.4\text{GHz}} \geq 338$
6CE	$2 \leq S_{151\text{MHz}} \leq 3.93$	$0.105 < z < 3.395$	37	19	$34 \leq S_{1.4\text{GHz}} \leq 66$
7CE	$S_{151\text{MHz}} \geq 0.5$	$0.086 < z < 2.982$	70	4	$8.42 \leq S_{1.4\text{GHz}} \leq 50$

^a ‘HERG’ here also includes narrow-line and broad-line radio galaxies and quasars.

^b Due to the absence of high powered HERGs in the BH12 catalogue only 44 HERGs are present to simulate the combined 3CRR and 2Jy equivalent samples. These 44 are distributed as 32 sources in the 2Jy equivalent sample and 12 in the 3CRR equivalent sample.

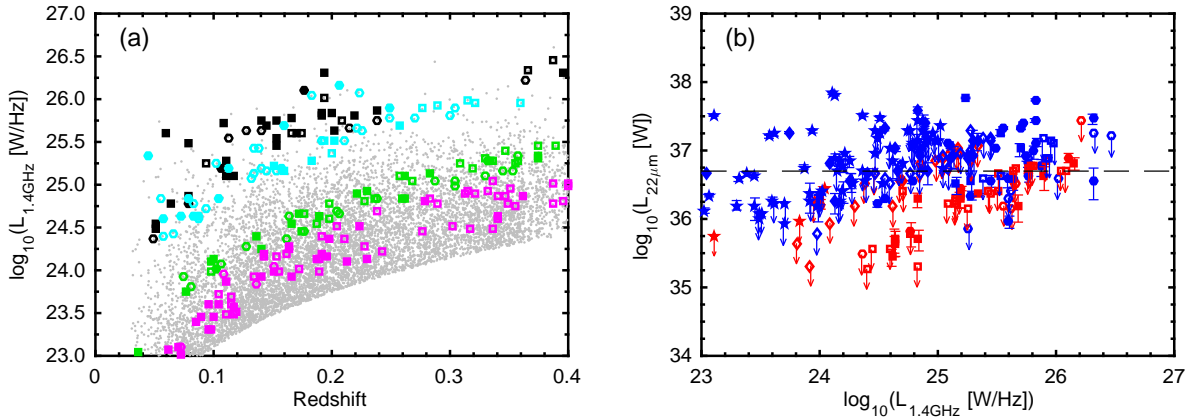


Figure A.2: (a) $L_{1.4\text{GHz}}$ as a function of redshift for the four dummy samples created from the BH12 radio-loud AGN sample. The four different colours indicate the subsample of G14 that is simulated (cyan: "3CRR", black: "2Jy", green: "6CE", magenta: "7CE"). HERGs are indicated by squares and LERGs by circles. Open symbols indicate that the $L_{22\mu\text{m}}$ measurement of this source is an upper limit, while filled symbols are $> 2\sigma$ detections. Grey dots show the entire BH12 sample in this plane. (b) 22 μm luminosity vs. 1.4 GHz radio luminosity for the LERG (red) and HERG (blue) in the four dummy samples (■: "3CRR", ●: "2Jy", ◆: "6CE", ★: "7CE"). Upper limits are indicated by a downwards pointing arrow and an open symbol. 1σ error bars are included for detections. The black dashed line is the G14 separation line.

selection of $L_{22\mu\text{m}}$ detections or upper-limits is made. Due to a lack of high powered HERGs in the BH12 sample, only 44 candidates were present to mimic the combined 3CRR and 2Jy samples. All these candidate sources are selected. We maximized the number of sources in the 2Jy equivalent sample and designated the remaining sources as the 3CRR equivalent sample.

Fig. A.2 shows the redshift, radio luminosity and mid-IR luminosity distribution of our mock samples. The left-hand side panel shows $L_{1.4\text{GHz}}$ as a function of redshift for the four dummy samples. The four different colours indicate the four subsamples and the different symbols indicate the differences in AGN excitation and $L_{22\mu\text{m}}$. In grey symbols all radio-loud AGN of the BH12 sample are displayed, which were not selected for one of the equivalent samples. It is clear from this figure that within each subsample a strong correlation between redshift and radio luminosity is introduced by the very narrow (implicit) flux limits. In contrast, the sample of local radio-loud AGN presented in this work has only a lower flux density limit, but at all relevant redshifts a radio luminosity can be defined on which it is volume limited, as shown by the grey dots in Fig. A.2(a). This reduces the redshift correlation between the mid-IR and radio luminosity and removes the diagonal sample boundaries seen in Fig. A.1.

The right-hand side panel of Fig. A.2 shows 22 μm luminosity vs. 1.4 GHz radio luminosity for the LERGs (red) and HERGs (blue) in the four dummy samples. Comparison

of Fig. A.1 and A.2(b) shows that the artificial subsamples reproduce the behaviour found by G14. The correlation between the two luminosities due to redshift is clearly visible. Observe the diagonal split between the high-flux (3CRR, 2Jy) and low-flux (6CE, 7CE) samples, which is introduced by the redshift. In addition, there does appear to be a mid-IR luminosity above which only HERGs and LERGs with upper limits are present, in particular at higher radio luminosities. This is the result of the low numbers of HERGs and LERGs. As can be seen in the right-hand side panel of Fig. 5.1 HERGs and LERGs have on average a different $L_{22\mu\text{m}}$. The empirical break found by G14 is located near the intersection of the two Gaussian distributions that describe the HERG and LERG population. By downsampling the number of sources it is therefore plausible to retrieve this separation. In addition, we expect only six LERGs with a $L_{22\mu\text{m}}$ detection, because of the high fraction of $L_{22\mu\text{m}}$ upper limits in the LERG population. This greatly increases the probability that there are only $L_{22\mu\text{m}}$ upper limits above the break. A.2(b) also shows that the contamination by weak HERGs without $L_{22\mu\text{m}}$ -excess increases at lower radio luminosity.

In conclusion, for a low number of high-power radio-loud AGN the fraction of HERGs will be high and these HERGs will be from the population that does have the excess $22\ \mu\text{m}$ luminosity. As a result the empirical separation criterion found by G14 works as a clean separator.

References

- [1] G. Gürkan, M. J. Hardcastle, and M. J. Jarvis, *The Wide-field Infrared Survey Explorer properties of complete samples of radio-loud active galactic nucleus*, Monthly Notices of the Royal Astronomical Society **438**, 1149 (2014).

Appendix B

Spherical coordinate systems

Within literature, computer programs and on the internet, many different definitions of the spherical coordinate system are used. While all cover the entire \mathbb{R}^3 there are subtle differences in their definition of the two spherical angles (θ, ϕ) . In this appendix the coordinate systems as defined by Wolfram MathWorld [1], Matlab [2] and CST MWS [3] are discussed. In the sections below a definition of each system is given using a description of θ and ϕ as well as the equations required to convert to Cartesian coordinates. For this conversion it is convenient to define the function “arctan2” as

$$\arctan2(y, x) = \begin{cases} \arctan(y/x) & \text{if } x \geq 0 \\ \arctan(y/x) + \pi & \text{if } x < 0 \text{ \& } y \geq 0 \\ \arctan(y/x) - \pi & \text{if } x < 0 \text{ \& } y < 0 \\ 0 & \text{if } x = 0 \\ \pi/2 & \text{if } x = 0 \text{ \& } y > 0 \\ -\pi/2 & \text{if } x = 0 \text{ \& } y < 0 \end{cases} \quad (\text{B.1})$$

Furthermore, for all these systems, their relation to the spherical coordinate system defined by the ISO80000 norm [4] is considered. The equations required to convert to and from the ISO-norm are given explicitly.

Besides the systems given below, many others are possible. When working in or reading literature in spherical coordinates, the definition of the system should always be checked.

B.1 ISO80000 definition

The ISO80000 [4] standard is commonly used in physics and defines the spherical coordinate system as:

- r is the radius or distance from the origin.
- θ is the angle running from the positive z-axis, where $\theta = 0$, through the (x,y)-plane ($\theta = \pi/2$) to the negative z-axis where $\theta = \pi$. Thus describing mainly the z-coordinate as it runs through its principle domain: $0 \leq \theta \leq \pi$.

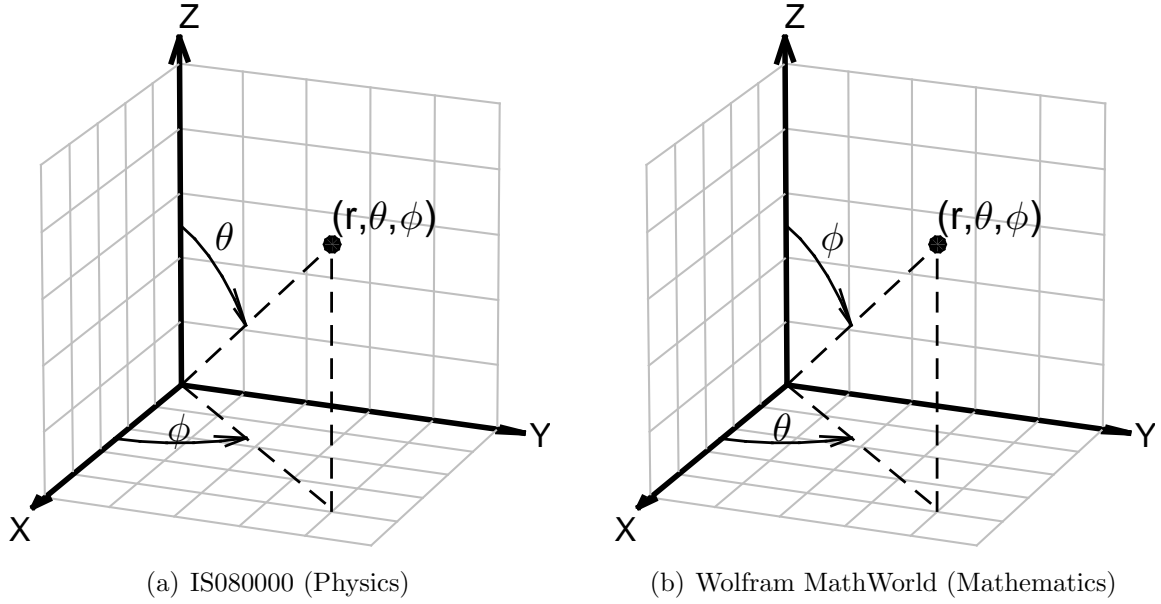


Figure B.1: The spherical coordinate systems as defined by the ISO80000 norm (a) and as defined by Wolfram MathWorld (b). The systems are identical with only the labels of the angles swapped. Note that the ISO norm is typically used in physics, while the Wolfram one is generally used in mathematics. Panel (a) also represents the default coordinate system for CST MWS. This system has the same origin and directionality for θ and ϕ as the ISO norm, but different principle domains.

- ϕ is the angle in the (x,y)-plane. The positive x-axis is located at $\phi = 0$ and ϕ increases towards the positive y-axis. The principle domain of ϕ is $0 \leq \phi < 2\pi$.

This system is illustrated in Fig. B.1(a). The equations that describe the conversion between Cartesian coordinates and the ISO80000 spherical coordinate system are given by

$$\begin{aligned}
 x &= r \cos \phi \sin \theta & r &= \sqrt{x^2 + y^2 + z^2} \\
 y &= r \sin \phi \sin \theta & \theta &= \arccos(z/r) \\
 z &= r \cos \theta & \phi &= \begin{cases} \arctan2(y, x) & \text{if } y \geq 0 \\ \arctan2(y, x) + 2\pi & \text{if } y < 0 \end{cases}
 \end{aligned} \tag{B.2}$$

B.2 Mathematics

Wolfram MathWold [1] defines the spherical coordinate system as often used in mathematics. In this coordinate system, which is shown in Fig. B.1(b), the coordinates are defined as:

- r is the radius or distance from the origin.

- θ is the angle in the (x,y)-plane. The positive x-axis is located at $\theta = 0$ and θ increases towards the positive y-axis. The principle domain of θ is $0 \leq \theta < 2\pi$.
- ϕ is the angle running from the positive z-axis, where $\phi = 0$, through the (x,y)-plane ($\phi = \pi/2$) to the negative z-axis where $\phi = \pi$. Thus describing mainly the z-coordinate as it runs through its principle domain: $0 \leq \phi \leq \pi$.

The equations that describe the conversion between Cartesian coordinates and the Wolfram spherical coordinate system are given by

$$\begin{aligned} x &= r \cos \theta \sin \phi & r &= \sqrt{x^2 + y^2 + z^2} \\ y &= r \sin \theta \sin \phi & \theta &= \begin{cases} \arctan2(y, x) & \text{if } y \geq 0 \\ \arctan2(y, x) + 2\pi & \text{if } y < 0 \end{cases} \\ z &= r \cos \phi & \phi &= \arccos(z/r) \end{aligned} \quad (\text{B.3})$$

B.2.1 Converting physics into math, and back

The conversion between the Wolfram, $(\theta_{\text{math}}, \phi_{\text{math}})$, and ISO80000, $(\theta_{\text{iso}}, \phi_{\text{iso}})$, coordinate systems is quite easy. As can be seen from Fig. B.1 it is only a change of label for the two angles. Hence the conversion equations are:

$$\begin{aligned} \theta_{\text{math}} &= \phi_{\text{iso}} \\ \phi_{\text{math}} &= \theta_{\text{iso}} \end{aligned} \quad (\text{B.4})$$

B.3 Matlab

The spherical coordinate system of Matlab [2] is defined along with the build in *sph2cart* and *cart2sph* routines. In the system of Matlab the azimuth, θ , and elevation, ϕ , angles are defined as:

- r is the radius or distance from the origin.
- θ is the azimuth angle in the (x,y)-plane. The positive x-axis is located at $\theta = 0$ and θ increases towards the positive y-axis. The principle domain of θ is $-\pi < \theta \leq \pi$.
- ϕ is the elevation angle running from the (x,y)-plane, where $\phi = 0$, towards the positive z-axis. Thus describing mainly the z-coordinate as it runs through its principle domain: $-0.5\pi \leq \phi \leq 0.5\pi$.

This is graphically represented in Fig. B.2(a) and mathematically by the equations given below.

$$\begin{aligned} x &= r \cos \phi \cos \theta & r &= \sqrt{x^2 + y^2 + z^2} \\ y &= r \cos \phi \sin \theta & \theta &= \arctan2(y, x) \\ z &= r \sin \phi & \phi &= \arcsin(z/r) \end{aligned} \quad (\text{B.5})$$

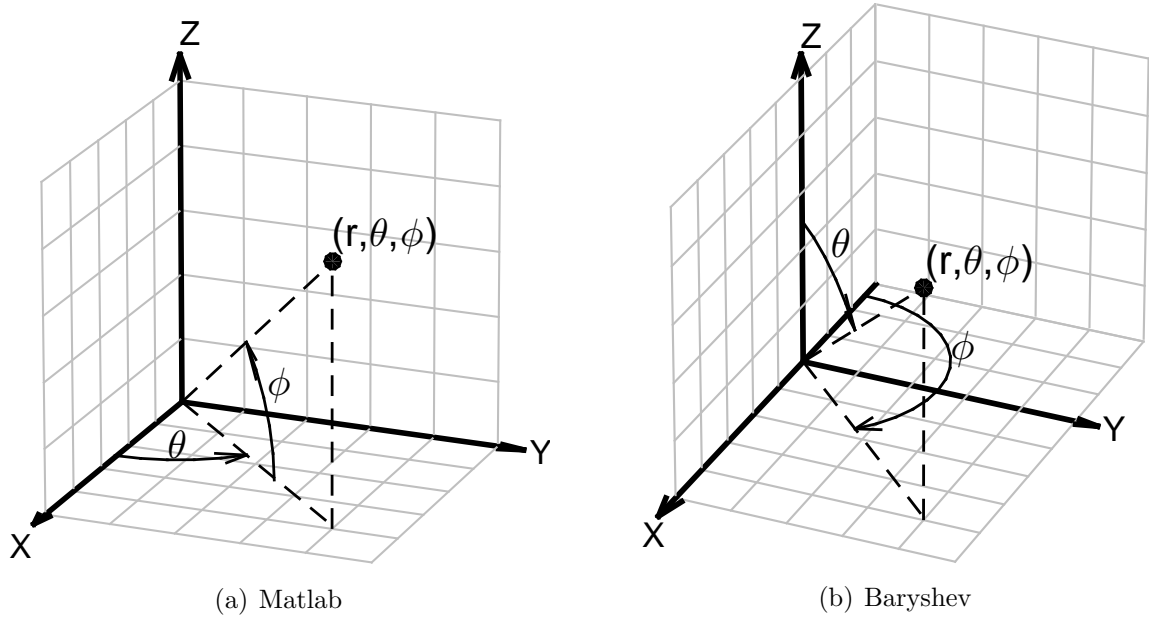


Figure B.2: The spherical coordinate systems as used in the computer software Matlab (a) and as defined by A.M. Baryshev (b) for antenna simulations in CST MWS. The systems are significantly different from each other and those commonly defined in physics and mathematics, which are shown in Fig. B.1.

B.3.1 Conversion between ISO and Matlab coordinates

To convert from the Matlab coordinate system to either that of the ISO norm or Wolfram MathWorld two operations need to be made. The first is flipping the direction of the elevation angle and the second is putting both angles into the right principle domain. This can be done using the mathematical operations given below.

$$\begin{aligned} \theta_{\text{iso}} &= \phi_{\text{math}} = \pi/2 - \phi_{\text{matlab}} \\ \phi_{\text{iso}} &= \theta_{\text{math}} = \begin{cases} \theta_{\text{matlab}} & \text{if } 0 \leq \theta_{\text{matlab}} \leq \pi \\ \theta_{\text{matlab}} + 2\pi & \text{if } -\pi < \theta_{\text{matlab}} < 0 \end{cases} \end{aligned} \quad (\text{B.6})$$

These equations can be inverted to obtain the conversion from ISO80000 coordinates to the Matlab system.

$$\begin{aligned} \theta_{\text{matlab}} &= \begin{cases} \phi_{\text{iso}} & \text{if } 0 \leq \phi_{\text{iso}} \leq \pi \\ \phi_{\text{iso}} - 2\pi & \text{if } \pi < \phi_{\text{iso}} < 2\pi \end{cases} \\ \phi_{\text{matlab}} &= \pi/2 - \theta_{\text{iso}} \end{aligned} \quad (\text{B.7})$$

The conversion from the Wolfram to the Matlab coordinate system can be obtained from by combining the above equations with Eq. B.4.

B.4 CST Microwave Studio

Beam pattern calculations are typically done in the Microwave Studio (MWS) software package of the Computer Simulation Technology (CST) company. Given the spherical nature of these beam patterns, CST MWS [3] has its own set of spherical coordinates in which it will output the beam patterns. In the system of CST MWS the azimuth, ϕ , and elevation, θ , are defined as:

- r is the radius or distance from the origin.
- θ is the elevation angle running down from the positive z-axis. It will increase to positive values for points with $x \geq 0$. The other half-space ($x < 0$) is covered by negative values of θ . The principle domain of θ is $-\pi \leq \theta < \pi$.
- ϕ is the azimuthal angle running in the (x,y)-plane. The positive x-axis is located at $\phi = 0$ and ϕ increases towards the positive y-axis. Note that in the half-space ($x < 0$) $\phi = 0$ is the negative x-axis and that ϕ increases in this half-space towards the negative y-axis. The principle domain of ϕ is $-\pi/2 \leq \phi \leq \pi/2$.

The angles θ and ϕ in the coordinate system of CST MWS have the same origin and directionality as those defined in the ISO80000 norm. As such the CST MWS coordinate system is graphically also represented by Fig. B.1(a). However, because CST MWS defines a different principle domain, it is mathematically given by the equations:

$$\begin{aligned} x &= r \cos \phi \sin \theta & r &= \sqrt{x^2 + y^2 + z^2} \\ y &= r \sin \phi \sin \theta & \theta &= \begin{cases} \arccos(z/r) & \text{if } x \geq 0 \\ -\arccos(z/r) & \text{if } x < 0 \end{cases} \\ z &= r \cos \theta & \phi &= \arctan(y/x) \end{aligned} \quad (\text{B.8})$$

B.4.1 Conversion between CST MWS and the ISO8000 norm

Given the significantly different definition of the elevation angle θ_{cst} the conversion to and from CST MWS coordinates is highly conditional. Therefore only the conversion to and from the ISO80000 coordinates (which for a physicist are most natural) is given. Further conversion to other systems can be obtained by sequentially applying this conversion and any other given in the other sections of this Appendix. Converting CST MWS to ISO80000 coordinates can be done using the following equations:

$$\begin{aligned} \theta_{\text{iso}} &= |\theta_{\text{cst}}| \\ \phi_{\text{iso}} &= \begin{cases} \phi_{\text{cst}} & \text{if } \phi_{\text{cst}} \geq 0 \text{ \& } \theta_{\text{cst}} \geq 0 \\ \phi_{\text{cst}} + \pi & \text{if } \theta_{\text{cst}} < 0 \\ \phi_{\text{cst}} + 2\pi & \text{if } \phi_{\text{cst}} < 0 \text{ \& } \theta_{\text{cst}} \geq 0 \end{cases} \end{aligned} \quad (\text{B.9})$$

Note that in the case of $\theta_{\text{cst}} = 0$ the determination of ϕ_{iso} is not unique. However, since in Cartesian coordinates $\theta_{\text{cst}} = 0$ can only mean $(x, y) = (0, 0)$ the value of ϕ_{iso} is

irrelevant. By inverting Eq. B.9 the conversion from ISO80000 coordinates to the CST system can be obtained.

$$\begin{aligned}\theta_{\text{cst}} &= \begin{cases} \theta_{\text{iso}} & \text{if } 0 \leq \phi_{\text{iso}} \leq \pi/2 \\ -\theta_{\text{iso}} & \text{if } \pi/2 < \phi_{\text{iso}} \leq 3\pi/2 \\ \theta_{\text{iso}} & \text{if } 3\pi/2 < \phi_{\text{iso}} < 2\pi \end{cases} \\ \phi_{\text{cst}} &= \begin{cases} \phi_{\text{iso}} & \text{if } 0 \leq \phi_{\text{iso}} \leq \pi/2 \\ \phi_{\text{iso}} - \pi & \text{if } \pi/2 < \phi_{\text{iso}} \leq 3\pi/2 \\ \phi_{\text{iso}} - 2\pi & \text{if } 3\pi/2 < \phi_{\text{iso}} < 2\pi \end{cases}\end{aligned}\quad (\text{B.10})$$

B.5 Alternative coordinate systems

There are a large number of possible definitions of the spherical coordinate system, which cover the 4π steradians solid angle of a complete sphere. As such, everyone might be used to a different definition and might think of a different system as logical. In this section a final coordinate system is discussed which was used by Baryshev [5] during his beam pattern simulations in CST MWS. In this system, coordinates are defined as:

- r is the radius or distance from the origin.
- θ is the angle running from the positive z-axis, where $\theta = 0$, through the (x,y)-plane ($\theta = \pi/2$) to the negative z-axis where $\theta = \pi$. Thus describing mainly the z-coordinate as it runs through its principle domain: $0 \leq \theta \leq \pi$.
- ϕ is the angle in the (x,y)-plane. The negative x-axis is located at $\phi = 0$ and ϕ increases towards the positive y-axis. The principle domain of ϕ is $0 \leq \phi < 2\pi$.

The AB coordinate system is graphically represented in Fig. B.2(b) and mathematically by the equations given below.

$$\begin{aligned}x &= -1 \times r \cos \phi \sin \theta & r &= \sqrt{x^2 + y^2 + z^2} \\ y &= r \sin \phi \sin \theta & \theta &= \arccos(z/r) \\ z &= r \cos \theta & \phi &= \pi - \arctan2(y, x)\end{aligned}\quad (\text{B.11})$$

The AB coordinate system converts readily to that of the ISO80000 norm using the following equations.

$$\begin{aligned}\theta_{\text{iso}} &= \theta_{\text{AB}} & \theta_{\text{AB}} &= \theta_{\text{iso}} \\ \phi_{\text{iso}} &= (\pi - \phi_{\text{AB}}) \text{ modulo } 2\pi & \phi_{\text{AB}} &= (\pi - \phi_{\text{iso}}) \text{ modulo } 2\pi\end{aligned}\quad (\text{B.12})$$

References

- [1] E. W. Weisstein, *Spherical Coordinates*, MathWorld – A Wolfram Web Resource (2015), <http://mathworld.wolfram.com/SphericalCoordinates.html>.

-
- [2] *MATLAB and Statistics Toolbox Release 2015b*, The MathWorks, Inc., Natick, Massachusetts, USA (2015), <http://nl.mathworks.com/help/matlab/ref/sph2cart.html>.
 - [3] *CST Microwave Studio*, Computer Simulation Technology, Darmstadt, Germany (2013), <http://www.cst.com>.
 - [4] International Organization for Standardization, *ISO 80000-2:2009 Quantities and units – Part 2: Mathematical signs and symbols to be used in natural sciences and technology*, International Organization for Standardization, Geneva, Switzerland (2009).
 - [5] A. M Baryshev, *private communication*, (2015).

Summary

Multiwavelength observations of active galactic nuclei

The galaxies we observe today in the local universe are the result of over 13 billion years of galaxy formation and evolution. A simple model to describe galaxy evolution is to see galaxies as a reservoir of stars and gas, where the inflow of gas is balanced by the formation of new stars. The inflow in most galaxies is governed by the gravitational attraction of cold gas from the dense filaments that make up the cosmic web. These slowly growing galaxies are associated with the main sequence of star formation: a relation between a galaxy's mass, M_* , (and therefore gravitational attraction on gas) and star formation rate (SFR). Alternatively, galaxies can grow through mergers. While major mergers are rare, they can result in a dramatic increase in stellar mass, a change in the morphology of a galaxy and trigger bursts of intense star formation.

However, using the above description large scale cosmological simulations overpredict the number of massive galaxies observed in the local universe. Furthermore, they predict that the most massive galaxies also have the highest SFR. This is in stark contrast with the strong bimodal distribution of galaxies observed in the local universe. Lower mass galaxies ($M_* \lesssim 10^{10.5} M_\odot$) typically are spiral galaxies with active star formation and a young stellar population. This young stellar population gives them a blue colour in the visible light. Blue spiral galaxies are generally located on the main sequence of star formation. The most massive ($M_* \gtrsim 10^{10.5} M_\odot$) galaxies on the other hand are large elliptical galaxies with an old stellar population and little star formation. The old stellar population gives them a red colour. Gas from the cosmic web that enters the gravitational influence of the elliptical galaxy joins its halo of hot X-ray gas. From there it does not continue to cool and the galaxy can not continue the formation of new stars.

To reproduce these observations simulations have nowadays implemented feedback mechanisms, which stop the inflow of cold gas, terminate star formation and continuously heat the hot halo gas. A prime candidate to provide this feedback in the real universe are active galactic nuclei (AGN). AGN are the result of matter being accreted by the super massive black hole thought to be present at the centre of every galaxy. In the local universe two populations of AGN have been identified: radiative-mode AGN and jet-mode AGN. Radiative-mode AGN are predominantly hosted by galaxies on the main sequence of star formation, which have a mass $10^{10.0} \lesssim M_*/M_\odot \lesssim 10^{11.0}$.

They are thought to accrete the cold gas in these galaxies at high rates (compared to the Eddington limit) in a radiatively efficient way. This results in emission across the entire electromagnetic (EM) spectrum: the collection of EM radiation (light) at all wavelengths, which includes radio, microwave, infrared (IR), visible (VIS), ultraviolet (UV), X-ray and gamma-rays. The high luminosity of these sources allows them to drive powerful winds by means of radiation pressure. These winds are thought to provide the quenching feedback that terminates the star formation in blue spiral galaxies and allows their stellar population to age. Roughly 5% of the radiative-mode AGN have a radio jet: a stream of ionized particles that are accelerated along magnetic field lines and emit synchrotron radiation in the process. This synchrotron emission can be observed at radio wavelengths and as such these AGN are classified as radio-loud. The radio jets of radio-loud AGN can reach up to several millions of light-years outside the AGN host galaxy.

The bulk of the local radio-loud AGN population are jet-mode AGN. Jet-mode AGN are preferentially hosted by the most massive red elliptical galaxies. They are thought to power themselves by accreting hot gas from the halo of these massive galaxies at low accretion rates in a radiatively inefficient process. As a result, jet-mode AGN lack the luminous emission lines, X-ray, UV and IR emission generally associated with radiative-mode AGN. However, models suggest that the radiatively inefficient accretion flow is favourable for the launching of a radio jet. Outside the massive elliptical galaxy radio jets collide with the hot halo gas. This collision heats the gas, thereby controlling the cooling of halo gas onto the massive elliptical. This prevents massive galaxies from a continued growth through steady star formation.

We investigate the properties of a (large) sample of approximately 7000 local radio-loud AGN, which have been identified in a sample of more than half a million galaxies observed by the Sloan Digital Sky Survey (SDSS). This has been achieved by cross-referencing the galaxy's position at visible (SDSS) wavelength with the location of radio emission in large area radio surveys (NVSS, FIRST). These radio-loud AGN were classified as radiative-mode (252 sources) or jet-mode (6691 sources) AGN based on their optical emission line properties. For these radio-loud AGN as well as a sample of 500,000 inactive galaxies we have collected flux density measurements at optical, infrared and radio wavelengths as well as derived quantities such as host galaxy stellar mass and star formation rate. Using this wealth of data we investigate the probability that a galaxy in the local universe hosts a jet-mode or radiative-mode radio-loud AGN as a function of the host galaxies stellar mass, star formation rate, optical colour and radio power (*Chapter 3*). We show that the fraction of galaxies with a jet-mode AGN strongly increases when the mass of the galaxy increases. Most of the jet-mode AGN (6157 out of 6328) are found in red galaxies. Radiative-mode AGN on the other hand are predominantly found in blue and green galaxies. These results are consistent with literature, but our large sample gives us the possibility to look in further detail. We show that the fraction of galaxies hosting a radio-loud radiative-mode AGN increases

with host galaxy mass. This is in contrast with radio-quiet radiative-mode AGN, for which the hosting probability shows no dependence on host galaxy mass. In addition, we identify 171 jet-mode AGN in massive blue galaxies. Given a red and a blue galaxy of the same mass, the probability of finding a jet-mode AGN in a blue galaxy is higher. These blue jet-mode AGN are generally also more powerful than their red counterparts. To discover the nature of the jet-mode AGN in massive blue host galaxies we take a closer look at the optical morphology of their hosts and radio morphology of the jets (*Chapter 4*). We have added to our catalogue of galaxies the morphological classification by Galaxy Zoo: an online citizen science project, in which the general public classifies the morphology of galaxies in SDSS. Our preliminary results show that blue galaxies with a jet-mode AGN have a significantly more elliptical morphology compared to inactive blue galaxies. They also have smaller radio jets compared to jet-mode AGN in red galaxies. We have obtained deep optical observations of the blue jet-mode AGN during two observation runs on the 4.2 meter William Herschel Telescope in La Palma as well as from public surveys. The increased image depth shows that at least 10 of the 24 galaxies show signs of mergers. Based on these initial results we speculate that a recent merger is responsible for both the increased star formation and AGN activity in blue jet-mode AGN.

In order to trace the co-evolution of the two AGN modes with the galaxy population we would like to extend the above analysis to the more distant universe (higher redshift). However, the spectroscopic observations, which are required to reliably classify AGN as radiative-mode or jet-mode, are observationally expensive (i.e. require lots of telescope time) and therefore limit number statistics. We investigate the potential of broadband mid-IR observations to distinguish the two AGN populations in *Chapter 5*. Radiative-mode AGN are expected to emit mid-IR radiation from their torus: gas and dust in the shape of a doughnut close to the accreting black hole. Jet-mode AGN are assumed not to have this torus. We show that jet-mode AGN have a mid-IR luminosity comparable to the general galaxy population, while at least 50% of the radiative-mode AGN show an excess mid-IR emission. Despite these trends we find that it is impossible to classify the two populations with a high completeness and reliability.

One of the main reasons for this poor differentiation is the large spread in mid-IR luminosities of both AGN populations. This is (at least partially) due to the emission of dust heated by young stars. Hence, the key to achieving a reliable classification will be constraining the mid-IR emission of dust. At far-IR wavelengths the contribution of both the radio jet and the torus emission is negligible compared to the dust emission of the host galaxy. Thus far-IR observations give an unbiased view of a galaxy's star formation and allows one to disentangle the contributions of AGN and stars to a galaxy's total emission across the EM spectrum. The total emission across the EM spectrum is also called the Spectral Energy Distribution (SED). Unfortunately, current far-IR and sub-mm surveys either lack the depth or the number statistics to perform SED fitting on a representative sample of local AGN and provide a calibration for higher redshifts.

Even the H-ATLAS survey by the Herschel Space Observatory, which is the largest survey of mid-IR/far-IR properties of galaxies in the local universe, only contains 9 radiative-mode and just over 250 jet-mode AGN from the sample studied in *Chapters 3 and 5*.

New large area surveys in the far-IR will require a new generation of large format far-IR cameras, which aim to fill the focal planes of telescopes like APEX, ASTE and the IRAM 30 meter. To achieve this, these cameras will require tens of thousands of pixels in combination with a high sensitivity and optical efficiency. The bolometer technology used in current instruments can achieve the latter. However, there is currently no viable way to build such large bolometer arrays. We show that Microwave Kinetic Inductance Detectors (MKIDs) can achieve the requirements of the next generation far-IR instruments (*Chapters 6–8*). MKIDs are superconducting resonators optimized for the detection of radiation. In a superconductor electrons form pairs, which allows them to carry a current without any resistance. When radiation is absorbed in the superconductor, these pairs are broken, thereby changing the electronic properties of the superconducting film. These changes can be observed in the transmission of the readout-line to which the resonator is coupled: the increased resistance reduces the depth of the resonance feature (amplitude readout) and the reduced number of pairs shifts the resonance frequency (phase readout). By designing each MKID with a slightly different resonance frequency thousands of MKIDs can be read out using a single pair of coaxial cables.

In this thesis we present both optical and thermal measurements on MKIDs made from a Niobium-Titanium-Nitrogen (NbTiN) alloy and Aluminium (Al). These MKIDs combine the low noise of the NbTiN with the high responsivity of the Al. We show that hybrid NbTiN-Al MKIDs are photon noise limited in both phase and amplitude readout when receiving a sub-mm power $P_{350\text{ GHz}} > 100\text{ fW}$ (*Chapter 7*). Through a detailed analysis of our optical system (*Chapter 6*), we demonstrate that this is achieved with an aperture efficiency of 75%, which is close to the theoretical maximum of 80%. Due to the high phase response of the NbTiN-Al the photon noise level is high enough to simultaneously monitor 1800 pixels using state-of-the-art electronics. Furthermore, we show that the response of NbTiN-Al MKIDs to temperature and sub-mm radiation is equivalent (*Chapter 8*). This will greatly simplify sensitivity measurements of large MKID arrays, because thermal sensitivity measurements can be performed in a closed cryostat in which disturbances can be more easily eliminated. We argue that the equivalent thermal and optical response is a property of the hybrid MKIDs and not a priori true for any MKID. In addition, the error on the optical sensitivity measurement described in *Chapters 6 and 7* is smaller than the error on the thermal sensitivity measurement. Given the performance presented above, hybrid NbTiN-Al MKIDs should enable astronomically usable kilopixel arrays for sub-mm imaging and moderate resolution spectroscopy. Thereby opening the far-IR sky to large scale observations and giving us a complete view of the co-evolution between AGN and their host galaxies.

Samenvatting

Observaties van actieve galactische kernen over het hele elektromagnetisch spectrum

De sterrenstelsels, die we in het lokale universum observeren, zijn het resultaat van meer dan 13 miljard jaar evolutie. Een simpel model om de evolutie van sterrenstelsels te beschrijven is door ze te zien als reservoirs van sterren en gas. In zo'n reservoir is de instroom van gas in balans met de formatie van nieuwe sterren. Continu stroomt nieuw gas het sterrenstelsel in doordat de zwaartekracht het gas aantrekt uit de omgeving van het sterrenstelsel. Van dit nieuwe gas worden nieuwe sterren gevormd. Dit creëert een relatie tussen de massa van een sterrenstelsel, M_* , en het tempo waarop nieuwe sterren worden gevormd. Deze relatie wordt ook wel de hoofdreeks van stervorming genoemd. Deze modus van stervorming door sterrenstelsels op de hoofdreeks is de dominante manier geweest waarop sterrenstelsels gegroeid zijn in de laatste 10 miljard jaar. Sterrenstelsels kunnen ook groeien door met elkaar te botsen. Hoewel botsingen tussen sterrenstelsels zeldzaam zijn, kunnen ze grote effecten hebben op de massa en morfologie van een sterrenstelsel en kunnen ze periodes van intense stervorming initiëren.

Als we het bovenstaande model gebruiken om de evolutie van het universum te simuleren dan wordt er een (te) hoog aantal massieve sterrenstelsels voorspeld. Ook voorspelt het model dat de meest massieve stelsels het hoogste stervormingstempo hebben. Deze resultaten komen echter niet overeen met observaties van sterrenstelsels in het lokale universum. In het lokale universum zien we een tweedeling in the populatie van sterrenstelsels. Sterrenstelsels met een lage massa ($M_* \lesssim 10^{10.5} M_\odot$) zijn over het algemeen spiraalvormige sterrenstelsels met actieve stervorming en een jonge sterpopulatie. Deze jonge sterpopulatie geeft spiraalvormige sterrenstelsels een blauwe kleur in het zichtbare licht. De massa en het stervormingstempo van blauwe spiraalvormige sterrenstelsels, een categorie waar ook de Melkweg toe behoort, zijn over het algemeen gerelateerd zoals voorspeld door de hoofdreeks van stervorming. Aan de andere kant zijn de meest massieve ($M_* \gtrsim 10^{10.5} M_\odot$) sterrenstelsels over het algemeen elliptische sterrenstelsels met een rode kleur in het zichtbare licht. Deze rode kleur is het gevolg van een oude ster populatie door het gebrek aan recente ster vorming. Gas dat door deze stelsels van buitenaf wordt aangetrokken, voegt zich bij een halo van heet gas rondom het sterrenstelsel. Deze halo is goed te zien in observaties van röntgenstraling. Vanuit deze halo

koelt het gas nauwelijks af en er is dus geen gas beschikbaar voor de meest massieve stelsels om verder te gaan met de formatie van sterren.

Om de observaties in het lokale universum te reproduceren worden er in moderne kosmologische simulaties mechanismen geïmplementeerd, die instroom van gas limiteren, stervorming stoppen en de röntgen halo verwarmen. Actieve galactische kernen (*Active Galactic Nuclei*, AGN) zijn een belangrijke kandidaat om de energie voor deze processen in werkelijkheid te leveren. AGN zijn het resultaat van materie die wordt verzwolgen door een zwart gat met een massa meer dan een miljoen keer die van de zon. Een dergelijk super massief zwart gat bevindt zich waarschijnlijk in het centrum van ieder sterrenstelsel. In het lokale universum zijn twee AGN populaties geïdentificeerd: *radiative-mode* en *jet-mode*. Radiative-mode AGN bevinden zich voornamelijk in sterrenstelsels aan het massieve einde ($M_* \sim 10^{10.5} M_\odot$) van de hoofdreeks. Gas en stof wordt op hoge snelheid (i.v.m. de Eddington limiet) door het zwarte gat aangetrokken. Dit gebeurt op een manier die efficiënt straling produceert en als gevolg daarvan is de emissie van radiative-mode AGN te zien in het hele elektromagnetische (EM) spectrum: de verzameling van alle EM straling (licht), waarin zich radiogolven, microgolven, infrarood (IR), zichtbaar (VIS) en ultraviolet (UV) licht en röntgen- en gammastraling bevinden. Deze extreem heldere bronnen kunnen sterke winden aandrijven door middel van stralingsdruk. Deze winden worden verantwoordelijk gehouden voor het beëindigen van de stervorming in blauwe spiraalvormige sterrenstelsels. Ongeveer 5% van de radiative-mode AGN hebben een *radio jet*: een stroom van geladen deeltjes die worden versneld in magneetvelden en in dit proces synchrotron straling uitzenden. Deze straling kan worden geobserveerd met radio telescopen. AGN met een radio jet worden dan ook wel *radio-loud* genoemd. De jets van radio-loud AGN kunnen miljoenen lichtjaren buiten het sterrenstelsel waarin de AGN huist, reiken.

Echter, de bulk van de lokale radio-loud AGN populatie zijn jet-mode AGN. Jet-mode AGN bevinden zich voornamelijk in massieve rode elliptische stelsels. AGN worden gedreven door de accretie van warm gas uit de röntgen halo. Dit gebeurt op een lage snelheid en op een manier die inefficiënt is in het produceren van straling. Jet-mode AGN missen daarom de emissielijnen, röntgen, UV en IR emissie die over het algemeen worden geassocieerd met radiative-mode AGN. Deze vorm van accretie is echter wel efficiënt in het produceren van radio jets. Deze jets botsen buiten het sterrenstelsel met de röntgen halo. Deze botsing verwarmt het gas en limiteert hoeveel gas er genoeg afkoelt om het sterrenstelsel te bereiken en sterren te vormen.

In dit proefschrift wordt onderzoek gedaan naar een verzameling van ongeveer 7000 lokale radio-loud AGN. Deze AGN zijn geïdentificeerd in een verzameling van meer dan een half miljoen sterrenstelsels geobserveerd door de Sloan Digital Sky Survey (SDSS). De radio-loud AGN worden geïdentificeerd door de positie van een sterrenstelsel in SDSS te vergelijken met de positie van radiobronnen in kaarten van de hemel gemaakt met radiotelescopie. De gevonden radio-loud AGN worden op basis van hun optische emissielijnen geclassificeerd als radiative-mode (252 bronnen) of jet-mode

(6691 bronnen). Voor deze 7000 AGN en de 500.000 inactieve sterrenstelsels hebben we intensiteitsmetingen van hun VIS-, IR- en radiostraling verzameld. Ook hebben we hun massa en stervormingstempo bepaald. Deze weelde aan informatie hebben we gebruikt om de waarschijnlijkheid te bepalen dat een sterrenstelsel in het lokale universum een radio-loud AGN bevat. In *Hoofdstuk 3* laten we zien dat de meeste (6157 van de 6328) jet-mode AGN worden gevonden in rode sterrenstelsels. De fractie van de sterrenstelsels met een jet-mode AGN neemt sterk toe voor stelsels met een hogere massa. Radiative-mode AGN worden daarentegen vooral in blauwe en groene sterrenstelsels gevonden. Deze resultaten zijn consistent met de literatuur, maar onze grote AGN catalogus geeft ons de mogelijkheid om in meer detail te kijken. Ook de fractie van sterrenstelsels met een radio-loud radiative-mode AGN neemt toe als de massa van het sterrenstelsel toeneemt. Dit is niet het geval voor hun tegenhangers zonder radio jets. Bovendien vinden we 171 jet-mode AGN in massieve blauwe sterrenstelsels. Indien de massa van een blauw en een rood sterrenstelsel hetzelfde is, dan is de kans om een jet-mode AGN te vinden hoger in het blauwe stelsel. De AGN in het blauwe stelsel zal naar alle waarschijnlijkheid ook nog krachtiger zijn.

Om te ontdekken wat de jet-mode AGN in blauwe sterrenstelsels drijft, onderzoeken we de morfologie van de sterrenstelsels en de radio jets (*Hoofdstuk 4*). We hebben de morfologische classificatie van het Galaxy Zoo project aan onze catalogus toegevoegd. Galaxy Zoo is een project waarin vrijwilligers middels een speciale website astronomen helpen om de morfologie van sterrenstelsels te classificeren. Wij hebben deze data gecombineerd met diepere observaties verkregen gedurende twee observatie campagnes met de 4.2 meter William Herschel Telescope in La Palma en uit publieke hemelkaarten. Onze voorlopige resultaten laten zien dat blauwe sterrenstelsels met een jet-mode AGN een meer elliptische vorm hebben dan inactieve blauwe sterrenstelsels. Ook hebben ze kleinere radio jets dan jet-mode AGN in een rood sterrenstelsel. De diepere observaties laten zien dat minimaal 10 van de 24 blauwe sterrenstelsels tekenen van een botsing hebben. Op basis van deze eerste resultaten denken wij dat de extra AGN activiteit het resultaat is van een recente botsing tussen sterrenstelsel.

Om de evolutie van radio-loud AGN te kunnen bepalen willen we het bovenstaande onderzoek uitbreiden naar het verdere universum (hogere roodverschuiving). Echter, de spectroscopische observaties die nodig zijn om AGN betrouwbaar als radiative-mode of jet-mode te classificeren, vereisen veel telescoop tijd. Omdat de totale telescoop-tijd gelimiteerd is, beperkt dit de statistieken. In *Hoofdstuk 5* onderzoeken we of IR observaties kunnen helpen om radiative-mode en jet-mode AGN betrouwbaar te classificeren. De verwachting is dat radiative-mode AGN meer IR emissie hebben als gevolg van hun torus: een donut van gas en stof nabij het zwarte gat. Jet-mode AGN hebben deze torus zeer waarschijnlijk niet. Wij hebben laten zien dat jet-mode AGN dezelfde IR helderheid hebben als de algemene populatie van sterrenstelsels. Daarentegen heeft minimaal 50% van de radiative-mode AGN een overschot aan IR emissie. Ondanks deze trends hebben we geen robuuste methode kunnen ontwikkelen voor het classificeren van

AGN.

Een van de belangrijkste redenen dat dit niet gelukt is, is de inherente spreiding in de IR emissie van beide AGN populaties. Deze spreiding is ten dele het gevolg van de emissie van stof dat verwarmd is door jonge sterren. Het is dus belangrijk te weten hoeveel van deze emissie aanwezig is in een sterrenstelsel, alvorens AGN betrouwbaar kunnen worden geclassificeerd. Observaties met ver-IR telescopen kunnen worden gebruikt om te bepalen hoeveel emissie afkomstig is van stof verwarmd door jonge sterren. In het ver-IR is de emissie van de torus en de radio jet namelijk nihil in vergelijking met de emissie van het door sterren opgewarmde stof. Op basis van ver-IR observaties is dan ook de contributie op kortere golflengten te bepalen. Helaas missen de huidige hemelkaarten in het ver-IR en sub-mm de diepte of de oppervlakte om genoeg statistiek te krijgen en deze methode te kalibreren. Zelfs in H-ATLAS, de grootste census van IR en ver-IR eigenschappen van sterrenstelsels in het lokale universum, bevinden zich slechts 9 radiative-mode en 250 jet-mode AGN uit de populatie bestudeerd in *Hoofdstukken 3 en 5*.

Om nieuwe en grotere hemelkaarten in het ver-IR te maken is er een nieuwe generatie ver-IR camera's nodig, die het complete blikveld vullen van telescopen zoals APEX, ASTE en de IRAM 30 meter. Dit vereist tienduizenden pixels die ieder een hoge gevoeligheid en optische efficiëntie hebben. De bolometer technologie die gebruikt wordt in de huidige generatie camera's kan aan de laatste twee eisen voldoen. Er is echter geen praktische manier om zulke grote bolometer camera's te maken. Bolometers opereren namelijk in koelers met een temperatuur van $-272\text{ }^{\circ}\text{C}$. Het aantal kabels dat van $-272\text{ }^{\circ}\text{C}$ naar kamertemperatuur moet lopen om een tienduizend pixel camera te laten werken, veroorzaakt een te grote aanvoer van warmte om de koeler op temperatuur te kunnen houden.

Wij laten zien dat kinetische inductie detectoren (KIDs) wel aan de eisen van de volgende generatie ver-IR camera's kunnen voldoen (*Hoofdstukken 6–8*). KIDs zijn microgolf resonatoren gemaakt van een supergeleidend materiaal en geoptimaliseerd voor het detecteren van straling. In een supergeleider vormen elektronen paren die stroom kunnen geleiden zonder weerstand. Als straling wordt geabsorbeerd in een supergeleider worden deze paren gebroken. Dit verandert de elektrische eigenschappen van de supergeleider en dus ook die van de supergeleidende resonator. Als de resonator is gekoppeld aan een uitleeslijn dan zijn deze veranderingen als gevolg van straling zichtbaar in de resonantie signatuur: een sterke reductie in de transmissie van de uitleeslijn in een kleine frequentieband rond de resonantiefrequentie. Straling zal de diepte (amplitude) van de transmissie-dip verminderen en de frequentie (fase) verlagen. Door iedere KID een andere resonantiefrequentie te geven kunnen duizenden KIDs worden uitgelezen met een paar coaxkabels.

In dit proefschrift presenteren we optische en thermische metingen van KIDs gemaakt van aluminium (Al) en een Niobium-Titanium-Stikstof (NbTiN) legering. Deze KIDs combineren de lage ruis van NbTiN met de hoge respons van Al. We laten zien dat

NbTiN-Al KIDs gelimiteerd worden door de ruis inherent aan het observeren van fotonen (lichtdeeltjes) voor een stralingsvermogen > 100 fW. Zoals te zien in *Hoofdstuk 7* is dit bereikt in de ruis van zowel de amplitude als fase van de resonantie signatuur. Met behulp van een gedetailleerde studie van ons optische systeem (*Hoofdstuk 6*) hebben we laten zien dat we dit bereiken met een *aperture efficiency* van 75%. Dit is nabij het theoretische maximum van 80%. De fase verandering als gevolg van een kleine intensiteitsverandering is bij NbTiN-Al KIDs hoog genoeg om 1800 pixels simultaan te volgen met moderne elektronica. Bovendien is de thermische en optische respons van NbTiN-Al KIDs equivalent (*Hoofdstuk 8*). Dit vereenvoudigt de metingen die nodig zijn om de gevoeligheid van een KID te bepalen, omdat ze kunnen worden uitgevoerd in een dichte cryostaat waarin verstoringen makkelijk kunnen worden geëlimineerd. Deze equivalentie is echter een eigenschap van NbTiN-Al resonatoren en niet in het algemeen geldig voor KIDs. Bovendien is de onzekerheid in de thermische gevoeligheid meting groter dan die van de optische meting beschreven in *Hoofdstukken 6* en *7*. Op basis van de in dit proefschrift gepresenteerde eigenschappen, zouden NbTiN-Al KIDs bruikbare ver-IR camera's en spectroscopen mogelijk moeten maken. Dit maakt de weg vrij voor grootschalige observaties met ver-IR telescopen en zal ons een compleet beeld geven van de gezamenlijke evolutie van AGN en de sterrenstelsels waarin zij zich bevinden.

Curriculum Vitae

Reinier Maarten Johannes Janssen

- 02–08–1985 Born in Delft, The Netherlands
- 1997–2003 Grammar school
St. Stanislas College, Delft
- 2003–2007 B. Sc. Applied Physics at Delft University of Technology
Minor in Astronomy and Instrumentation at Leiden University
Bachelor Thesis: *Vortex unbinding in NbN thin film superconductors*
Supervisor: Dr. D. Ludkov
- 2006–2011 M. Sc. Applied Physics at Delft University of Technology
Master Thesis: *Submicron kinetic inductance detectors for SAFARI*
Supervisor: Dr. A. Endo
- 2007–2009 Suspension Engineer at DUTracing, Delft
- 2008–2011 M. Sc. Astronomy at Leiden University
Master Thesis: *Host galaxies of radio-loud active galactic nuclei*
Supervisor: Prof. dr. H. J. A. Röttgering
- 2011–2017 Ph. D. Research at Delft University of Technology
Thesis: *Multiwavelength observations of active galactic nuclei: Using current facilities and development of enabling technologies*
Supervisors: Prof. dr. ir. T. M. Klapwijk (promotor), Prof. dr. H. J. A. Röttgering (promotor) and Dr. ir. J. J. A. Baselmans (copromotor)

List of publications

1. *A kilo-pixel imaging system for future space based far-infrared observatories using microwave kinetic inductance detectors*
J. J. A. Baselmans, J. Bueno, S. J. C. Yates, O. Yurduseven, N. Llombart, K. Karatsu, A. M. Baryshev, L. Ferrari, A. Endo, D. J. Thoen, P. J. de Visser, R. M. J. Janssen, V. Murugesan, E. F. C. Driessen, G. Coiffard, J. Martin-Pintado, P. Hargrave, M. Griffin
submitted for publication
2. *Classification of radio galaxies using broadband mid-infrared observations*
R. M. J. Janssen, A. O. Farrish, E. E. Rigby and H. J. A. Röttgering
submitted for publication
3. *Equivalence of optical and electrical noise equivalent power of hybrid NbTiN-Al microwave kinetic inductance detectors*
R. M. J. Janssen, A. Endo, P. J. de Visser, T. M. Klapwijk and J. J. A. Baselmans
Applied Physics Letters **105**, 193504 (2014)
4. *Performance of hybrid NbTiN-Al microwave kinetic inductance detectors as direct detectors for sub-millimeter astronomy*
R. M. J. Janssen, J. J. A. Baselmans, A. Endo, L. Ferrari, S. J. C. Yates, A. M. Baryshev and T. M. Klapwijk
Proceedings of the SPIE **9153**, 91530T (2014)
5. *High optical efficiency and photon noise limited performance of microwave kinetic inductance detectors using phase readout*
R. M. J. Janssen, J. J. A. Baselmans, A. Endo, L. Ferrari, S. J. C. Yates, A. M. Baryshev and T. M. Klapwijk
Applied Physics Letters **103**, 203503 (2013)
6. *The triggering probability of radio-loud AGN: A comparison of high and low excitation radio galaxies in hosts of different colors*
R. M. J. Janssen, H. J. A. Röttgering, P. N. Best and J. Brinchmann
Astronomy & Astrophysics **541**, A62 (2012)

7. *Power handling and responsivity of submicron wide superconducting coplanar waveguide resonators*
R. M. J. Janssen, A. Endo, J. J. A. Baselmans, P. J. de Visser, R. Barends and T. M. Klapwijk
Journal of Low Temperature Physics **167**, 354-359 (2012)
8. *Development of DESHIMA: A redshift machine based on a superconducting on-chip filterbank*
A. Endo, J. J. A. Baselmans, P. P. van der Werf, B. Knoors, S. M. H. Javadzadeh, S. J. C. Yates, D. J. Thoen, L. Ferrari, A. M. Baryshev, Y. J. Y. Lankwarden, P. J. de Visser, R. M. J. Janssen and T. M. Klapwijk
Proceedings of the SPIE **8452**, 84520X (2012)
9. *Design of an integrated filterbank for DESHIMA: On-chip submillimeter imaging spectrograph based on superconducting resonators*
A. Endo, P. van der Werf, R. M. J. Janssen, P. J. de Visser, T. M. Klapwijk, J. J. A. Baselmans, L. Ferrari, A. M. Baryshev and S. J. C. Yates
Journal of Low Temperature Physics **167**, 341-346 (2012)
10. *Photon noise limited radiation detection with lens-antenna coupled microwave kinetic inductance detectors*
S. J. C. Yates, J. J. A. Baselmans, A. Endo, R. M. J. Janssen, L. Ferrari, P. Diener and A. M. Baryshev
Applied Physics Letters **99**, 073505 (2011)

Acknowledgements

“Home is people. Not a place.” — The Fool
Robin Hobb, Fool’s Fate

Over the past five years I have had many homes and had the privilege of collaborating with many people. I am grateful for the people at the Cosmonanoscience group in Delft and the astronomical observatory in Leiden for providing a stimulating and supportive daily work environment. Furthermore, the broad range of research topics I pursued has allowed me to get to know many people in the fields of galaxy evolution and astronomical instrumentation both nationally and internationally. Here I would like to thank everyone who supported me during my PhD both professionally and personally.

First of all I would like to thank my (co)promotors Teun, Huub and Jochem. You have been a very diverse team of supervisors each with your very own knowledge and management style. Teun thank you for giving me the opportunity to pursue a wide range of topics in both my research and broader professional career. Reflecting with you upon these matters has been a very valuable part of my PhD. I am very grateful for all the guidance you have provided me over the past decade and it has been a pleasure to see how much you enjoy your ‘retirement’. Huub thank you for supporting my astronomical research ambitions. Your encouragement and large network within the astronomical community has enabled me to meet many people and your ‘statement of facts’ communication style has more than once been an efficient way to kick-start me again. Jochem, your endless energy, enthusiasm and wide range of interests made you a great supervisor. Thank you for all the support over the last years. It was a privilege to benefit from your extensive knowledge both of the physics and instrument design required to make individual detectors into promising astronomical instrumentation.

In Delft I had the honour of being part of the close-knit Cosmonanoscience group. I would like to thank my roommates Pieter, Nathan and Eduard for providing a homely and supportive working environment. Pieter, for more than a decade we have walked the path of astronomy and instrumentation together and it has always been a pleasure working with you. It is good to see that your in-depth knowledge of superconducting resonators continues to bear fruit in a wide community. Nathan, you were a driving force for the many social events of the group even after you formally left it. The gatherings you organised will always be a good memory and your birthday trip to Belgium was exceptional. Eduard, you were always very kind and supportive. You always had

valuable input for the many discussions within the group regardless of the topic. I would also like to thank Akira for our many discussions on physics, astronomy, teaching, attracting new students, living in Nootdorp or virtually any other topic. I wish you all the best in the continued development of DESHIMA and I am looking forward to my first application for DESHIMA time. David, thanks for keeping the cleanroom in working order and for the many films of high quality NbTiN that came out of it. I would also like to thank you for keeping the group lively at the times that it was shrinking. In this respect, I would also like to remember Niels. Your three o'clock tea was a defining characteristic that bound the group together. I would like to thank Rik, Pieter-Jan, Alessandro, Gao, Yuan, Rami, Cristina, Tom, Bastian, Nuri, Rutger, Robbert-Jan, Werner, Boy, Chris, Masato, Mohammed, Jing, Jaime, Marc, Matvey, Holger, Benham, Allard, David, Peng, Mihai, Morris, Alibey, Maria, Dorine and Irma and all other current and former group members for all professional discussions and support as well as the many lunches, dinners, movie nights, sports tournaments, pub quizzes, pub visits and many other enjoyable times together.

During my entire time at the Leiden observatory I have only met helpful and friendly people. However, I would like to especially name a few who have directly supported me during my PhD research. Jarle, thank you for all the guidance in the use of SDSS data and pointers with regards to the subtleties of optical astronomy. I will never forget our late night, last-minute effort to prepare a proposal for observation time on the William Herschel Telescope and I am very grateful for your support there. Leah thank you for your help in preparing for the actual observations and getting me up to speed on the mountain. Emma, Wendy and Gaby thank you for our many discussions on AGN, infrared emission and the morphology of radio sources. I would also like to thank Gilles, Stephanie and Gerard for our discussions on the more instrumentation-oriented subjects.

During my PhD I have also been able to benefit from the strong collaboration between SRON and the TU Delft. Juan and Stephen, thank you for all your support during the measurements at SRON as well as providing a friendly welcome whenever I visited Utrecht or Groningen. Jan Joost and Vignesh, thank you for all the work in the cleanroom that made this research possible. Lorenza, thanks for your assistance in obtaining the beam patterns and for cheering me up with a familiar face and a nice dinner after a rough and rainy day in Kyoto. With many other SRON colleagues I have visited various conferences and I would like to thank them for the many enjoyable lunches and dinners we had together. I would also like to thank the members of the Terahertz sensing group for adopting me as part of the group in the last years of my PhD and the fruitful discussions to further my understanding of antennae. In this respect, I would especially like to mention Ozan for answering many of my trivial questions.

During my PhD I have also discovered both how much I like teaching and how difficult it can be. I would like to thank Bernhard for having me as a teaching assistant in the 'Introduction to Astronomy' course. I have really enjoyed redeveloping the course and

undertaking the grassroots proposal together. I would also like to thank all students for allowing me to practise my teaching skills. In particular those whom I was allowed to guide during their BSc thesis or first year project.

Ik wil ook mijn vrienden en familie bedanken. Jullie waren er altijd om mij te steunen en een overvloed aan afleiding te verstrekken. Marieke bedankt voor al je zorgen en het grote aantal taarten dat je voor mij hebt gebakken. Het aantal dankwoorden waarin deze staan vermeld is nog maar net op één hand te tellen. Teun, bedankt voor al je wiskundige hulp en de vele filosofische discussies over onze gezamenlijke hobby's. Maar vooral ook veel dank voor de schop die mij heeft aangezet weer te gaan spelen en schilderen, en tijd te maken om mooie ideeën daadwerkelijk tot uitvoering te brengen. Mama, bedankt dat je er altijd voor mij bent en voor een thuis zorgt waar ik altijd naar terug kan. Papa, in de laatste jaren van je leven hebben gezamenlijke interesses er voor gezorgd dat ik je niet alleen als vader maar ook als vriend heb mogen ervaren. Je afwezigheid is nog steeds een groot gemis. Miranda, bedankt voor al je feedback op dit boekwerk. Zonder jou oog voor detail zouden er aanzienlijk meer spelfouten en slordigheden in dit boek hebben gezeten. Ik wil je echter vooral danken voor al je steun, warmte en liefde, die ik gedurende mijn hele promotie van je heb mogen ontvangen.

Reinier Janssen
Delft, December 2016

